Design of a piezoelectric actuation system for movement functions of optical elements in automotive environment

Santiago Venegas Bayona

Par **Santiago VENEGAS BAYONA**

Design of a piezoelectric actuation system for movement functions of optical elements in automotive environment

Thèse présentée
pour l'obtention du grade
de Docteur de l'UTC

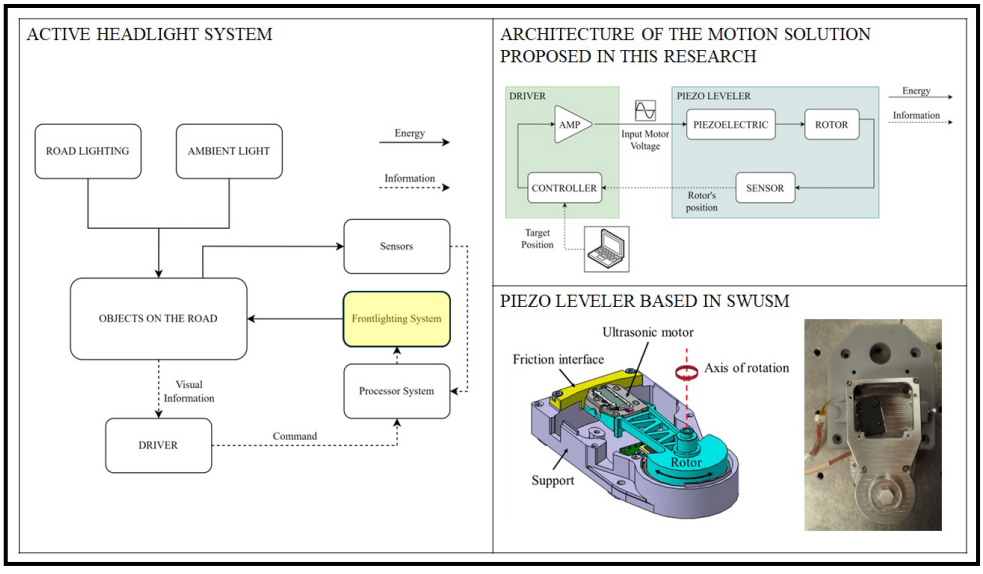

Soutenue le 12 janvier 2024
Spécialité : Mécatronique, Photonique et Systèmes : Unité de recherche en Mécanique - Laboratoire Roberval (FRE UTC - CNRS 2012)

D2789

UNIVERSITE DE TECHNOLOGIE DE COMPIEGNE

CNRS Roberval Laboratory
Department of Mechanical Engineering
Mechatronics, Energy, Electricity & Integration Research Unit
PhD Dissertation

Design of a piezoelectric actuation system for movement functions of optical elements in automotive environment

Spécialité : Mécatronique, Photonique et Systèmes

Par **Santiago VENEGAS BAYONA**

Soutenue le 12 janvier 2024 devant le jury composé de :

Reviewer: Prof. Dr. Eric BIDEAUX, INSA Lyon

Reviewer: Prof. Dr. Marc BUDINGER, INSA Toulouse

Jury member: Prof. Dr. Jérôme FAVERGEON, UTC

Advisor: Prof. Dr. Christine PRELLE, UTC

Invited: Hassan KOULOUH, AML Systems

ACKNOWLEDGMENTS

Here are the last words I write in this thesis. As I do so, countless memories of moments I experienced throughout my doctorate flood my mind, along with the people who supported me over the years to successfully complete this project, to which I devoted all my talent and energy.

I want to start by thanking my friends, whose loyalty in the most difficult times reflected the great love they have for me. It's no secret to anyone that a doctorate pushes the spirit to its limits, and in those moments of darkness, the word of a good friend translates into another ray of light to keep going. To them, from GINSA School, EAFIT University, Université de Technologie de Compiègne, known in Medellín and in Compiègne, my beloved cities, this humble paragraph of acknowledgment. To Mateo, Daniel B, Daniel R, Emilie, Federico, Juan, Nicolas, Louise, Natalia, Mariana, Julio, Maxime, Hénoik, Aurélien, Laure, Franco, María, Céline, Xiangjun, Jessica, Camila, Francesca, Louis, Margot, Florian, Daniel S, Felipe, Juanes, Jerónimo, Alexandra, Manuel, Victoria, Nicolas, Alexandre, Rolex, Carole, Juan Simón, Juan Manuel, Simón, Sergio, Juan Pablo, Verónica, Marco, Alejandro, Diego. To you, thank you.

To my professors, Frédéric, Laurent, Hani, Erwan, Muneeb, and Philippe. Because their wisdom and knowledge are only matched by their humility and kindness.

To Hassan, Anderson, and my colleagues at AML Systems, for the coffee breaks and good vibes. For being part of my very first professional experience and treating me as an equal despite my youth.

To Christine, who was an absolute guide and a thesis advisor who not only clarified my scientific doubts but believed in me at all times, and thanks to her support, I have the immense honor of writing these words with a sense of victory that undoubtedly, thanks to her, stopped being a dream and became a reality. Thank you, Christine, eternally, because your patience, humility, wisdom, and trust were undoubtedly indispensable and invaluable.

Finally, to my four pillars. To Victoria and Alejandro, my parents; and to Caro and Isa, my sisters. You are my very life. And for you, this victory.

During the years I dedicated to this research project, there were moments of great uncertainty and frustration that now seem insignificant. Let there be no doubt, this thesis exists not only because of my talent but because of the absolute richness I possess in having the love of so many people.

And remember, the parallelepiped is your friend.

AGRADECIMIENTOS

Estas son las últimas palabras que escribo en esta tesis. Mientras lo hago, innumerables recuerdos de momentos que viví a lo largo de mi doctorado llegan a mi mente, y con ellos, las personas que durante todos estos años me brindaron su apoyo para llevar a cabo con éxito este proyecto en el que invertí todo mi talento y energía.

Quiero empezar dándole las gracias a mis amigos, cuya lealtad en los momentos más difíciles reflejó el gran amor que tienen por mí. No es un secreto para nadie, que un doctorado lleva al límite el espíritu y es en esos instantes de oscuridad, es la palabra de un buen amigo que se traduce en un rayo más de luz para seguir adelante. A ellos, del colegio GINSA, de la Universidad EAFIT, de la Université de Technologie de Compiègne, conocidos en Medellín y en Compiègne, mis ciudades amadas, este humilde párrafo de reconocimiento. A los Mateo, Daniel B, Daniel R, Emilie, Federico, Juan, Nicolas, Louise, Natalia, Mariana, Julio, Maxime, Hénoik, Aurélien, Laure, Franco, María, Céline, Xiangjun, Jessica, Camila, Francesca, Louis, Margot, Florian, Daniel S, Felipe, Juanes, Jerónimo, Alexandra, Manuel, Victoria, Nicolas, Alexandre, Rolex, Carole, Juan Simón, Juan Manuel, Simón, Sergio, Juan Pablo, Verónica, Marco, Alejandro, Diego. A ustedes, gracias.

A mis profesores, Frédéric, Laurent, Hani, Erwan, Muneeb y Philippe. Porque su conocimiento y experiencia solo es comparable a su humildad.

A Hassan, Anderson y mis demás colegas de AML Systems, por los cafecitos y la buena onda. Por hacer parte de mi primera experiencia profesional real y haberme tratado como igual a pesar de mi juventud.

A Christine, quien fue una guía absoluta y una directora de tesis que no solo aclaró mis dudas científicas, sino que creyó en mi en todo momento, y que, gracias a su apoyo, tengo el inmenso honor de redactar estas palabras con una sensación de victoria que indudablemente, gracias a ella, pasó de ser un sueño a una realidad. Gracias Christine, eternas, porque tu paciencia, humildad, sabiduría y confianza fueron sin duda imprescindibles e invaluables.

Finalmente, a mis cuatro pilares. A Victoria y Alejandro, mis padres; y a Caro e Isa, mis hermanas. Ustedes son mi vida misma. Y para ustedes esta victoria.

Durante los años que dediqué a este proyecto de investigación, hubo momentos de mucha incertidumbre y frustración que hoy parecen ínfimos. Que no quede la menor duda, esta tesis existe no solo por mi talento, sino por la absoluta riqueza que poseo en contar con el amor de tantas personas.

Y recuerda, el paralelepípedo es tu amigo.

ABSTRACT

When a vehicle is in motion, its orientation changes due to irregularities on the ground or driving maneuvers such as braking, accelerating, or changing direction. Affected by these variations, headlights may illuminate an area that is not the one toward which the vehicle is heading. The same observation can be made for sensors in an autonomous vehicle, which are responsible for detecting obstacles in its path. Furthermore, as the distance to illuminate (or detect) increases, the headlight (or sensor) must be precisely positioned so that obstacles are detected early enough.

It is therefore necessary to be able to adjust the angular orientation so that the beam remains aligned despite road irregularities and driving maneuvers. This leveling function, which is mandatory in headlights, is not just a matter of making the environment visible but also of doing so in such a way that these changes do not result in undesirable or abrupt movements of the headlights. It is about ensuring safety by maximizing comfort.

The actuators currently available in the market range from less performing versions of open-loop static type to more robust versions of closed-loop dynamic type, all based on the use of a conventional electromagnetic motor to drive a mechanism to transform the rotary motion of the motors into longitudinal motion of a rod (which is ultimately responsible for the leveling). Nevertheless, these actuators reach their limits as new technologies increase the requirements, especially in terms of miniaturization and precision.

Piezoelectric technologies with a strong advantage in terms of size and precision compared to conventional technologies (such as electromagnetic motors) have the potential to find their place and bring added value to headlight leveling. This thesis addresses the design of a piezoelectric actuator for adjusting the orientation of an optical device in a vehicle.

CONTENTS

INTRODUCTION

Road safety involves a series of elements among which visibility is at the core for all users on the road, that is, being able to perceive and be perceived with the enough time and space to avoid potential risks that may come in a highly changing activity as is to drive.

For over one hundred years automotive lighting has been improved: gas lights were used on the first car headlamps before the introduction of electrical light sources in 1908. The implementation of rear lamps arrived shortly after, and in the 20's differencing of high and dipped beam was possible thanks to the use of double filament sources. With the creation of new functions as the flashing turn signal and the improvements on filament sources, headlamps finally were integrated to the vehicle body in the mid 40's.

Visibility when driving has an enormous impact on comfort and risk-avoidance and headlamps are typically considered as one of the most important safety devices in automobiles as they are responsible of enhancing the visual range of the driver in obscured light conditions. Among the total of fatal accidents, around the 40% occur at night [1] when visual performance is highly impacted by the absence of light. Hence the use of more powerful sources in the second half of XX century was at least logical, especially when driving in geographical zones where no public illumination was still developed or climatic conditions were more exigent.

Headlamps provide illumination on the road in the direction of movement during periods of low visibility. The projected beam of light (headlight) can be described by the cut-off line, which divides the visual panorama into two parts: a bright area below that provides visual information to the driver and a dark area above that prevents glaring on oncoming traffic. In addition to this, headlamps should make the vehicle easily visible for other road users.

In Europe, high intensity discharge sources (Xenon) were implemented in the early 90's bringing tremendous performance enhancement of forward lighting (better illuminance to size ratio) as well as much cooler light temperature compared to halogen sources. Nevertheless, as the use of these high-power sources became a trend on headlamps design, glare appeared as an urgent problem to solve.

Glare is the sense of discomfort associated with a reduction in visibility caused by scattered light in the eye producing reduced retinal image contrast. When driving, it is most likely to occur when the distance between the source and the receptor, i.e. the driver, reduces. It is evident that headlights of an approaching vehicle are the most obvious source of glare and some of the consequences are discomfort, distraction and reduction of visibility on oncoming drivers which causes a huge reduction in their ability to detect targets with enough time, as exposed by Helmers and Rumar [2].

In their experiments, they showed how the maximal detection distance of 220m with no opposite vehicle reduced to only 80m when an opposing vehicle is present. If we take into account that for a 110km/h speed the stopping distance is around 100m, that is, the distance travelled by the vehicle from the moment a target is identified until the moment the vehicle has completely stopped, it is clear that high range is uncompleted with no control.

From a rather philosophical point of view, the current paradigm is to well illuminate and not just simply increase output power as it used to be in most part of the XX century. This new perspective gave origin to the concept of Front Lighting System (FLS) so headlamps are no longer a merely light source integrated to vehicle's body but rather a mechatronic system mainly focused on safety improvement.

Particularly, the positioning of the cut-off line, called leveling, has great importance and imposes a trade-off on headlamp systems between maximizing visibility and minimizing glare on oncoming traffic (or even pedestrians). Taken to the extreme, good visibility for the driver can be achieved by allowing

the headlights emit the maximum possible amount of light, while avoidance of glare is just the opposite: no light from the headlight at all [3].

To respond to this need, headlamp actuation systems appeared in the 90s adding new functions to headlamps. Particularly, the use of headlamp levelers, which are devices able to modify the angular positioning of the cut-off line, became mandatory and nowadays all vehicles in Europe are equipped with them. Nevertheless, latest trends on automobile lighting are starting to overpass the capabilities of current devices, overly based on electromagnetic technologies, in terms of precision, response time and miniaturization potential, as electric motors are the best choice at a macro scale but present significant challenges when used on a confined space.

With this in mind, this CIFRE research focuses on the design of a piezoelectric device for headlamp leveling, given their intrinsic characteristics of higher precision and greater force-volume ratio and giving a first step on the implementation of piezoelectric technologies for automobile lighting.

- The first chapter gives a general description of headlamp actuation systems and allows the reader to have a general sight of current problematics.

- The state of art on piezoelectric actuation is developed in chapter II. In it, a global basis about piezoelectricity and piezoelectric materials is given in order to introduce the different architectures found on piezoelectric actuation, needed to select the most adequate given the conditions of our application, a standing wave ultrasonic motor

- Chapter III shows the design of the prototype.

- As one of the main objectives of this thesis, a dynamic model of the whole actuator has been formulated and chapter IV details how this model has been made and why it is useful regarding future designs for levelers based on multilayer linear piezoelectric motors.

- Chapter V shows the assembly of the leveler and the experiments driven for its characterization and the dynamic model validation.

- Conclusions and future work

I. BACKGROUND ON HEADLAMP ACTUATION

I.1. Introduction

The development of new light sources with higher luminous flux has been a usual solution to improve driver's visual range. These great advancements, as the use of LED headlamps, even if enhancing the quantity of light, have increased the risk of affecting other road users, especially oncoming drivers, who might get momentarily blinded if there is no correct aiming of the headlamp beam. The constant perturbation of external vibrations, the added load on the vehicle, road surface quality and the different phases of acceleration have also an impact on the pitch of the cut-off line.

Regulation No. 48 of the Economic Commission for Europe of the United Nations stipulates that every vehicle must be equipped with a Headlamp Leveling Device (HLD) to compensate the change of pitch angle and it has to be of automatic type when the light source exceed 2000 lm [4].

In this chapter we will see the outline of automotive lighting and how mechatronics has enabled its evolution making an emphasis on the headlamps and the existing actuators needed to fulfill the current market demands. With this, we can summarize the specifications that we search to satisfy with our actuator and why we have chosen piezoelectric principle as the core of our actuation device.

I.2. Automotive Lighting

The most important elements for good detection at nighttime are the headlamps, easily described by the cut-off line, which divides the panorama into two parts: the bright area below that provides visibility to the driver, called headlight, and a dark area above that prevents glaring on oncoming traffic [5]. We can find two different techniques to produce the light distribution: reflection and projection.

For the first technique, the light of the bulb is distributed according to the geometry of a reflector and the pattern designed on the cover lens. The use of computational design has made possible the step from strictly parabolic reflectors to computer-calculated free-form surfaces. On the other hand, second method consists in the projection of focused light onto a convex lens. Although these techniques produce slightly different beams in terms of optical aberrations and energy distribution, they are both globally described by the schema shown in the Figure I.2-1. For the scope of our research, we will work on the positioning of a given cut-off line independently on how is it generated.

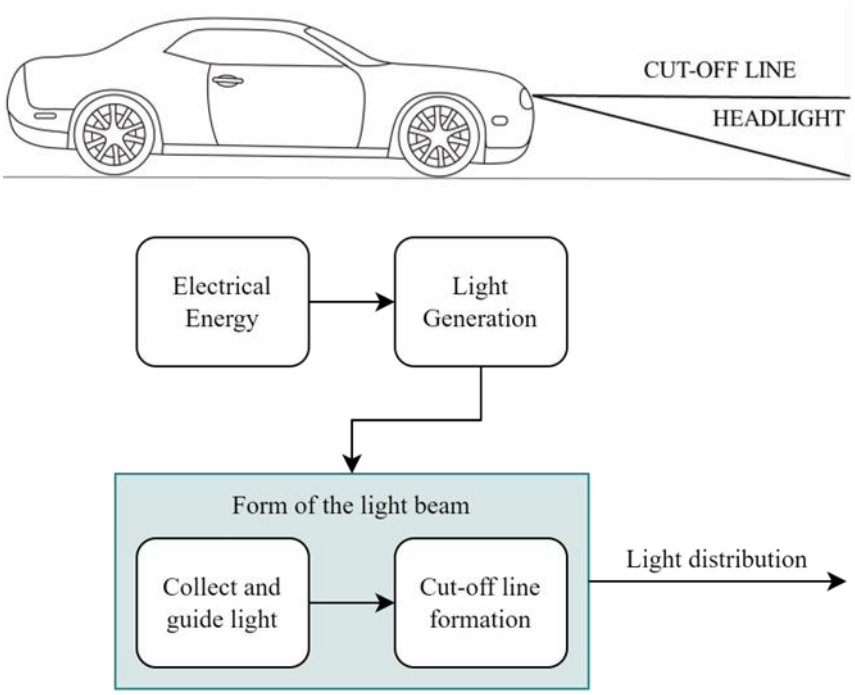

Figure I.2-1. Light distribution and generation of the cut-off line.

Once the problem of glare became of interest, the design conflict was initially solved by using passive systems. As long as no external information other than the driver's perception, either about the system itself or the environment is considered, the system is passive.

For example, the modification of the light pattern, i.e. the dipped beam, appeared as a passive solution. Seen from the driver's perspective, dipped beam lighting pattern is shown in Figure I.2-2. It consists on a modification of the entirely horizontal cut-off line, keeping high luminance on driver's lane and simultaneously, avoiding glare on oncoming lane by reducing light projected on it.

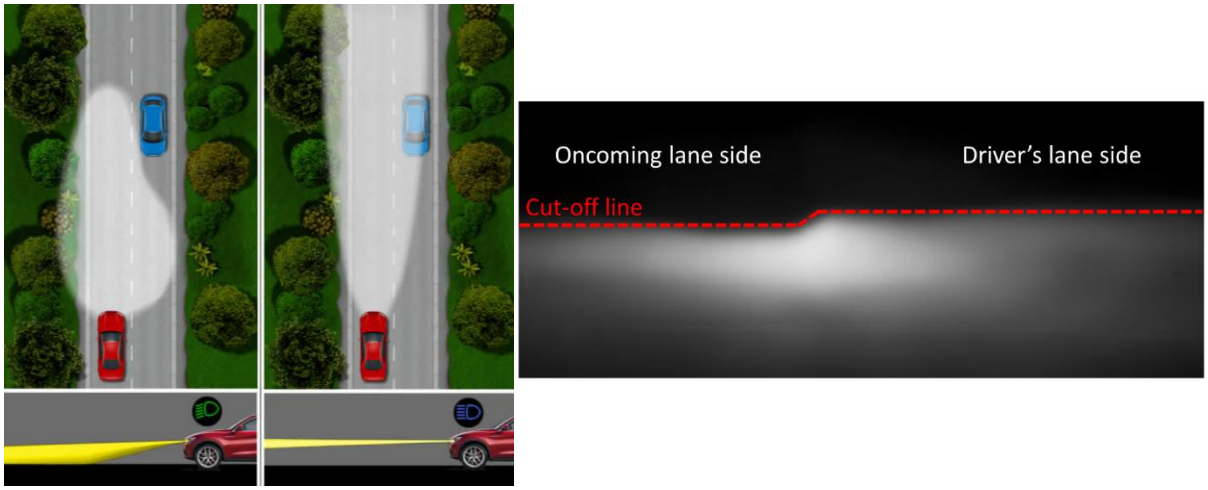

Figure I.2-2. Left: Dipped beam and high beam comparison. Right: Driver's perspective of a dipped beam projected on a wall at 10m [6].

Nowadays other patterns may be found that are more proper to a given traffic situation or climatic condition, as it happens with fog lights. Nevertheless, a greater limitation on passive systems remains present as they relay on the driver who directly commands the headlamps based on the visual information he acquires when the objects on the road are illuminated by the headlights or other external sources as public lighting (Figure I.2-3). Hence, the selection of the correct light pattern is rarely done as reported by Sullivan et al. in their work, they noticed an underuse of high beam because drivers hesitate to activate them, as they might forgot to switch them off and glare oncoming traffic, hence sacrificing their vision field even though high beam was the most adequate light distribution on that precise scenario [7] but this also results in potential hazards, given that low beam cut-off reduces the visibility range so the ability to detect obstacles with enough time is compromised.

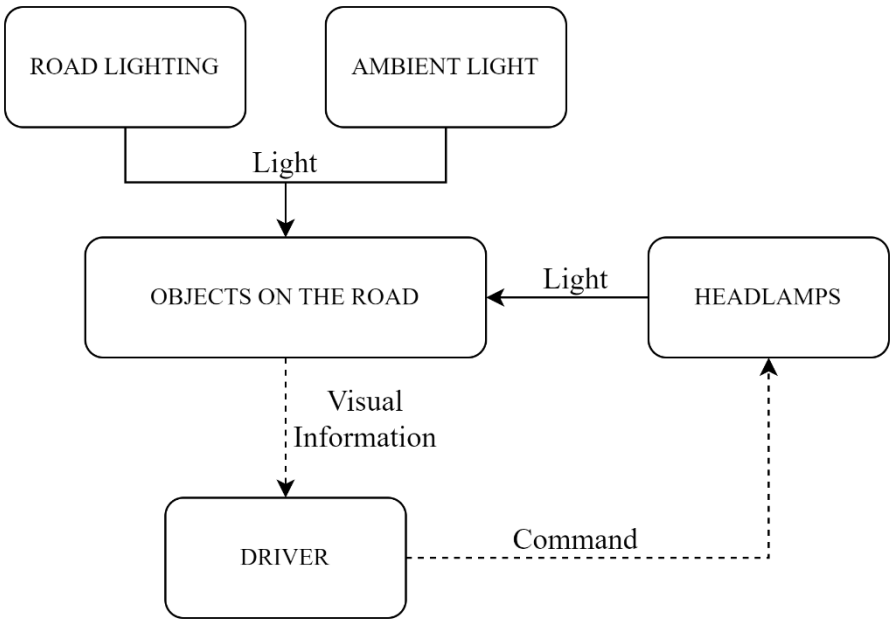

Figure I.2-3. Energy and information flow on passive headlight systems

I.3. Active Lighting Systems

During the last decades, mechatronics has been present as a powerful tool necessary in the design and development of more complex systems either to perform an already existing task more precisely or even adding new functions to them. Mechatronic systems are based on the integration of sensors and actuators to provide the systems with a certain degree of adaptability so they are able to react to changes and with this, a step forward from passive to smarter active systems capable of compensate external perturbations (Figure I.3-1).

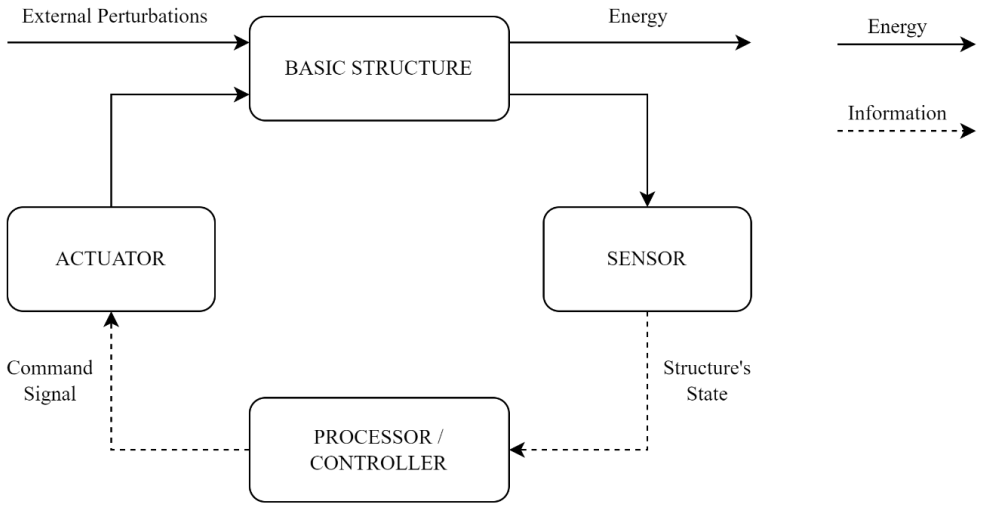

Figure I.3-1. Mechatronics system structure

Automotive industry has beneficiated from this trend and lighting has experienced important changes. This new perspective gave origin to the concept of Adaptive Front-Lighting System (AFS) so headlamps are no longer a merely light source integrated to vehicle's body but rather a mechatronic system focused on safety improvement.

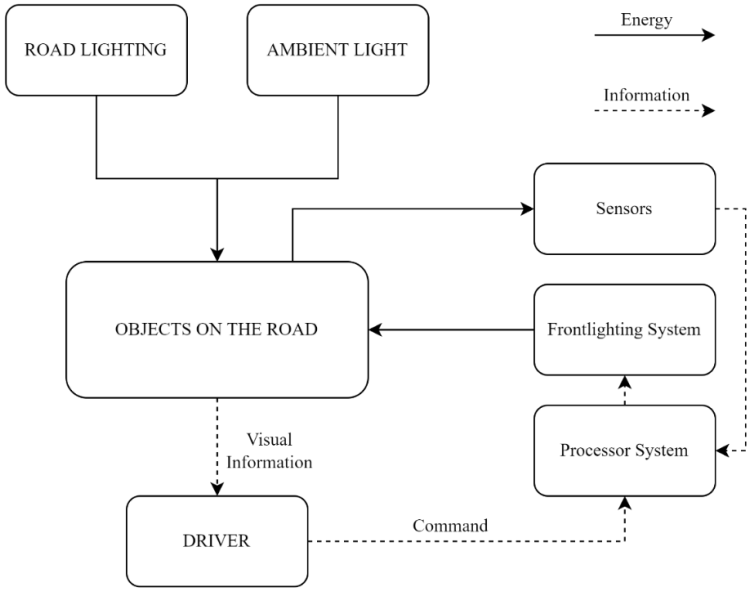

Figure I.3-2. Energy and information flow on active headlight systems

The basic idea behind AFS is to use information from the car and the environment and thus adapt the lighting pattern to the actual situation. The basic structure of such a AFS is shown in Figure I.3-2.

As we can see, sensors for both the surroundings and the system are necessary to sample information of the environment and vehicle sensors which provide information about the vehicle state such as speed, steering angle, pitch, etc. After processing, an actuator receives a proper command that allows the adaptation of the headlight to a given scenario. In general, the more the headlights are adapted to the actual driving situation e.g., to the pitch angle of the car, to the curvature of the road or to the position of other traffic participants etc., the better the conditions of perception for drivers will be. This will lead to more safety and comfort as well as to a reduced accident risk during trips at night.

The first AFS consisted in the automatic selection between full and dipped beam depending on the traffic situation. By moving a shutter placed between the lights source and the lenses, the cut-off line is modified, so with one single source both dipped and full beam can be generated.

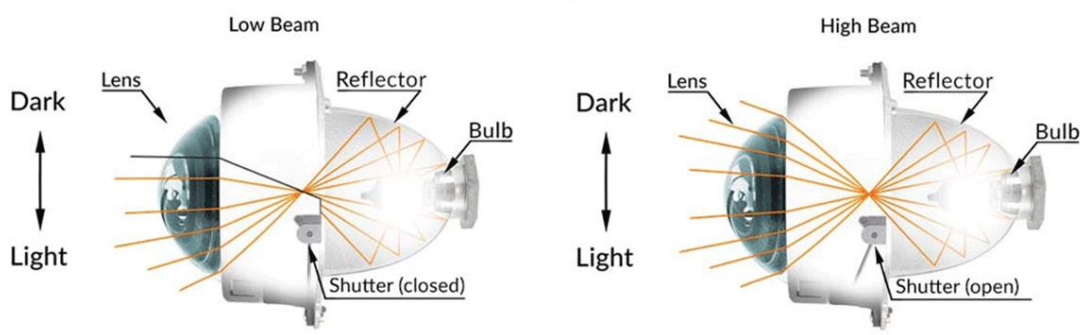

Figure I.3-3. Shutter actuator for dipped and full beam automatic selection. Image taken from [8].

As more light distributions were designed, a better compromise between visibility and glare was possible and nowadays the concept of a movable shutter has evolved. As shown in the figure Figure I.3-4, new profiles have been designed and the selection of a given configuration depends on the constant lecture of road conditions, weather, traffic and vehicle's speed. Between the light source and the lens, there is a shaft that can be rotated around its longitudinal axis and every profile is modeled on the outer surface of the shaft that allow the generation of different light distributions on the road.

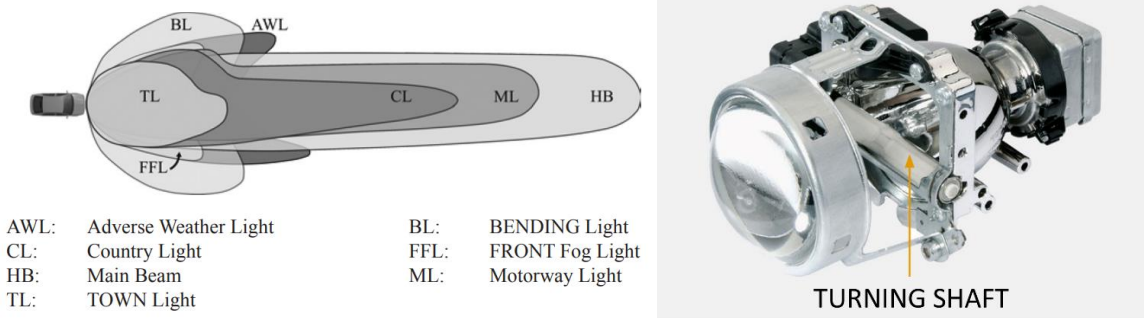

Figure I.3-4. AFS Light distributions. Image taken from [9]

With the use of steering angle sensors, another improvement was possible: the concept of bending light. It consists in the lighting of corners and turns by swiveling the headlamp so that the light distribution

follows the road. For this, the projector is installed in a frame able to rotate around the vertical axis operated by an electric motor.

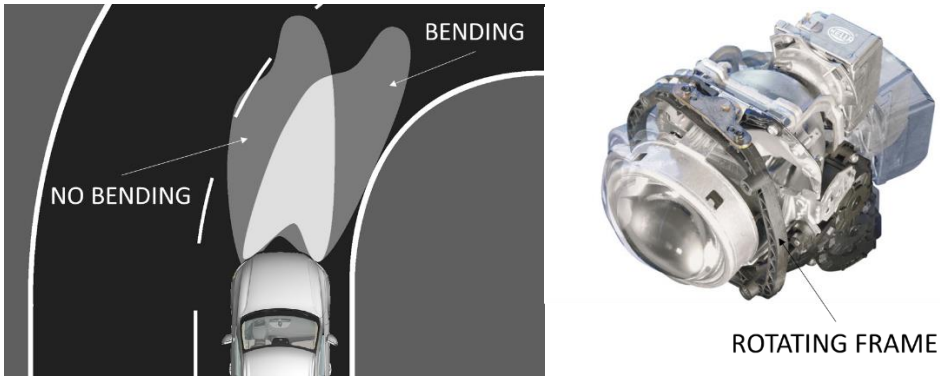

Figure I.3-5. Bending light actuation; Image taken from [10]

I.4. Headlamp Leveling

When driving, the constant change in road conditions, together with the variable loads on the vehicle, have a direct effect on the inclination of the cut-off line. For instance, the vehicle tends to go up when more passengers are inside it or when the driver accelerates and to go down when the brakes are hit. This clearly impacts the detection capabilities and safety: if the cut-off line rises above a certain height, then glare may be caused on other drivers. On the other hand, if it goes down, the range of visibility of the driver is compromised.

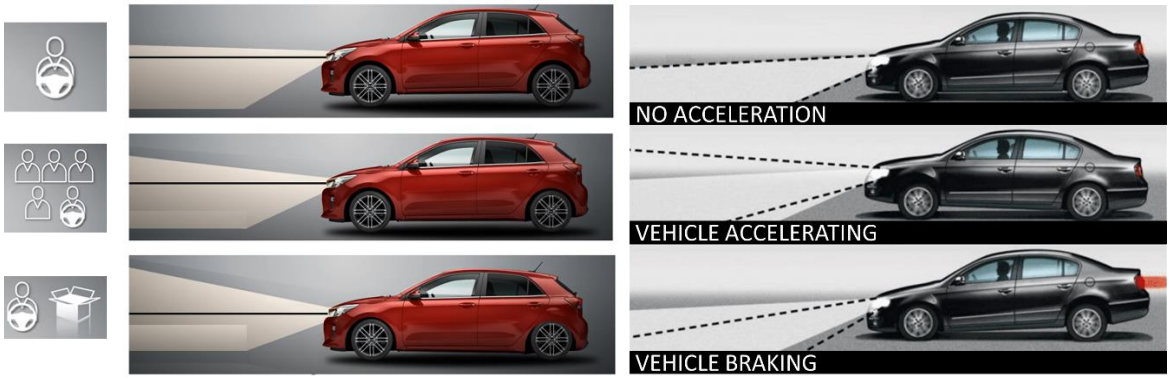

Figure I.4-1. Cut-off line inclination changes. Snapshot taken from video [11]

This constantly changing context creates a scenario where illuminating as much as possible without perturbing the other drivers is of vital importance for the security of all the users of the road. The ideal case would be to permanently have a maximum emission of the headlights while avoiding glare.

Levelers are devices that adjust the height of the cut-off line regarding the pitch angle of the vehicle. We distinguish two kinds of levelers: manual and automatic. In the former, the driver adjusts the inclination of the beam by using a graduated interrupter that ultimately controls the leveller. These systems need the user to be constantly checking and variating the inclination, even while driving. As stated before, this kind of passive systems fail to perform as it is the driver who ultimately decides the

aiming of the light beam and often it is not accomplished with great precision, especially when acting on a highly changing environment.

The compromise between glare and high illumination is at the core of automobile lighting knowing that it does exist a technological gap between light generation and glare avoidance, the first one being much more advanced thanks to the rise of LED technology and the interest in using alternative sources as laser light. For instance, after the introduction of high-intensity-discharge (HID) lamps for cars, automatic headlamp leveling (AHL) became mandatory as manual type was not enough to maintain the light beam positioned according to regulation ECE R48 [12].

An active system can compensate dynamic changes of the pitch angle, for example during acceleration, or as caused by bumps in the road and they appeared as a solution with an actuator changing the inclination of the headlamp. The actuation system consists typically of a stepper motor combined with a lead screw in such a way that a linear output movement is generated. A plastic shaft, joined to the screw, serves as interface between the actuator and the headlamp. The leveller pushes or pulls the whole projector which in the end results in a change of its inclination by means of a pivot point as seen in Figure I.4-2.

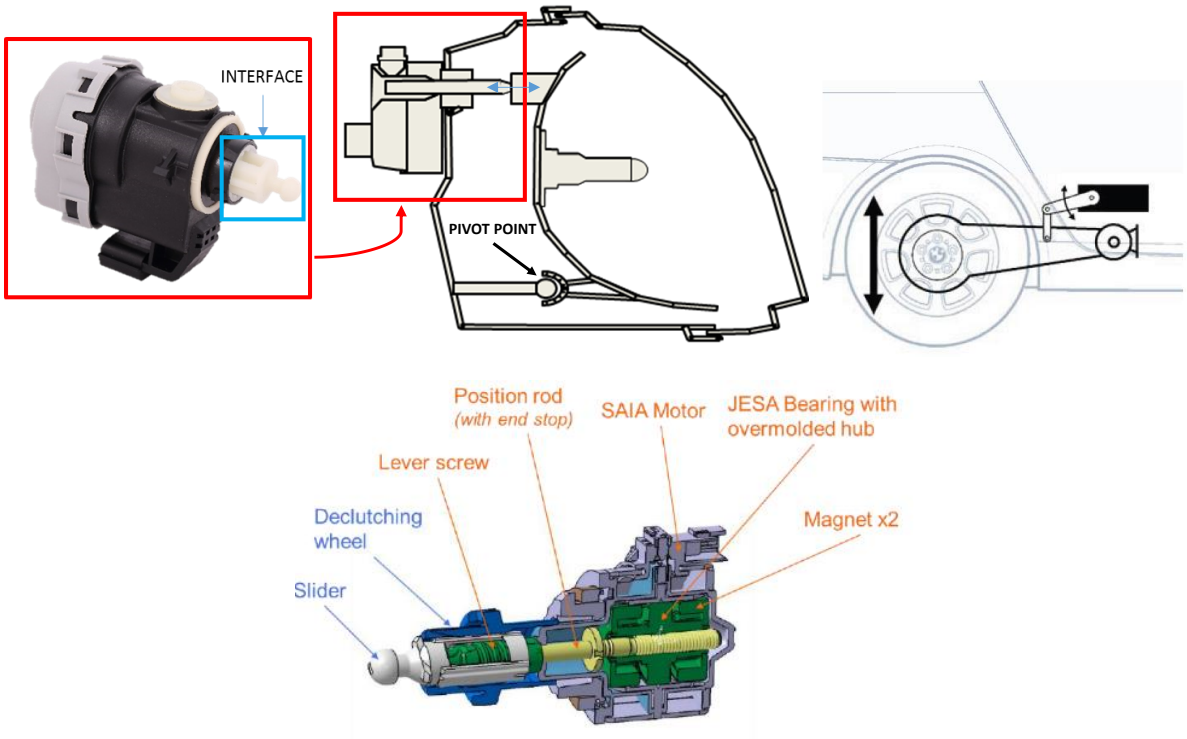

Figure I.4-2. Right: Automatic Headlamp Leveller. Left: Pitch sensor attached to vehicle's body. Down: Detail on a typical leveller mechanism.

These actuators do not integrate a feedback sensor. Instead, a pitch sensor, usually placed in the vehicle body, provides the information necessary to estimate the inclination of the vehicle. On the other hand, the actuator is operated in feed-forward mode, hence the step size must be known to such a point of certainty that any value of inclination has its corresponding number of linear steps of the shaft.

The leveling requires a rotational final output which, in these systems, is obtained throughout a mechanism of power transmission. The presence of such mechanisms induces play that may allow undesirable movements to occur under external loads, loss of repeatability and has great influence in

the final precision of the leveller. This degraded precision limits the maximum range of vision of the headlamp, i.e., the circular arc corresponding to a given angle increases with the range and any error can easily significate a difference of several tens of centimeters on the reaction distance, a major drawback in ultra-long range applications (at 100 m, 0.1° corresponds to 17 cm height).

The reaction distance is defined as the distance traveled by the vehicle between the moment an obstacle is detected and the brake is activated. The stopping distance is the actual distance traveled once the brakes have been pressed. For example, when driving at 100 km/h, the former distance is around 40m and the latter 100m.

Consider the scenario in Figure I.4-3. θ is the angle formed by the vertical h and the cut-off line that lies at a distance x from the front of the vehicle.

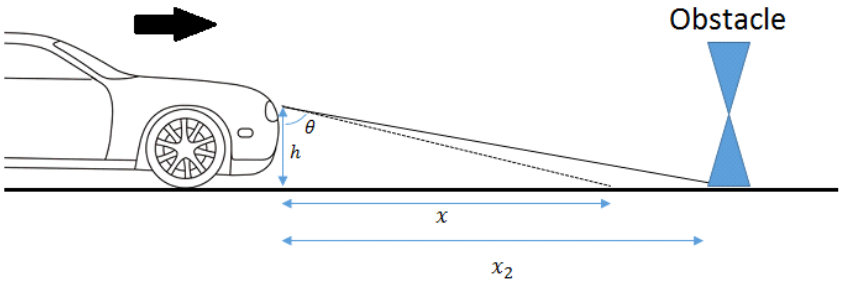

Figure I.4-3. The importance of precision during obstacle detection.

We can easily deduce that, for a given value of angular precision δ and a stopping distance x_2

$$x = h\left(\frac{x_2 - h\tan\delta}{h + x_2\tan\delta}\right) \qquad \textit{Eq. I.4.1}$$

Classic levelers have a precision δ in the range of $\pm 0.1°$. Under these conditions, x corresponds to 80 m. So additional 20 m are needed to perceive the obstacle and the minimum 100 m needed to stop the vehicle, are no longer suitable, ultimately requiring more effort on the brakes to avoid collision.

Now, suppose a light source of luminous intensity sufficiently high so visibility is possible at 200 m in front of the vehicle. At this distance, the aforementioned precision represents 0.35 m of vertical precision, hence the source may produce glare on an oncoming car that makes contact with the cut-off line. And this becomes even more critical if a more powerful light source is used. In other words, in order to implement sources of high power and range, the requirement on precision at the time of situating the cut-off line arises tremendously.

Both examples are a basic exemplification of how higher precision will always benefit the performance of the headlamps. Besides, a tendency to miniaturization makes difficult the integration of actuators based on electric motors on more compacts spaces and a general trend on resolution increasement imposes new constraints, particularly in terms of positioning. This is the case for led matrix lighting which consists on the discretization of the visual field on portions that are individually controlled so a particular section can be dimmed while maintaining full beam on the rest as shown in the figure below.

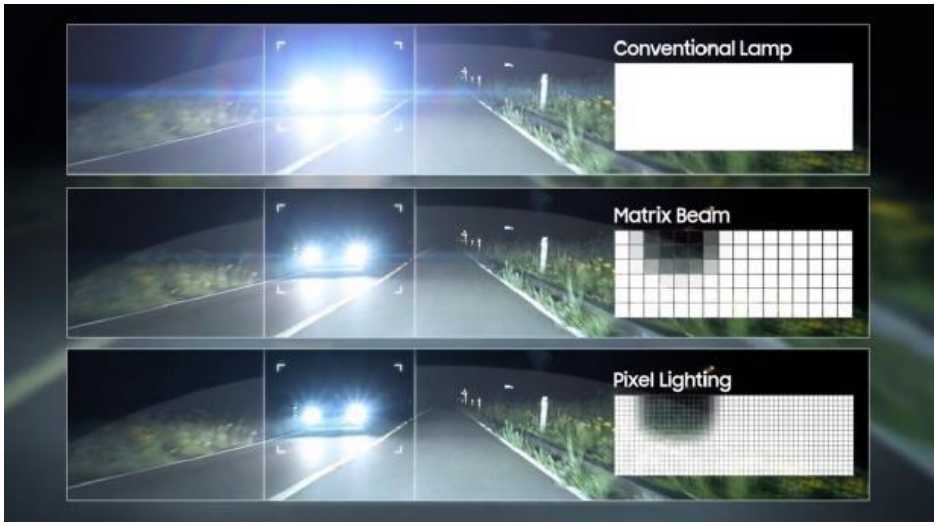

Figure I.4-4. Comparison on conventional, matrix and pixel lighting.

For this reason, it is appropriate to think about piezoelectric actuation as the next step on AHL because their great better power to volume ratio, miniaturization capabilities, a tremendous precision compared to electric motors and the direct actuation possibilities (no need of gearbox or whatsoever).

II. STATE OF ART

II.1. Introduction

A general scope about piezoelectricity will be given and in a much deeper way, piezoelectric actuation will be discussed, in order to give a solid basis for the subsequent chapter of Mathematical Modeling and simulation. This chapter will also allow the reader to have a clearer sight about the different types of piezoelectric actuation and will facilitate the understanding about the choice made when selecting the type of actuator for a leveling application given the constraints and capabilities of the different piezoelectric architectures.

Starting by an overview of piezoelectricity, we will give a general classification of piezoelectric actuation based on the type of movement executed and some applications where each of them are classically used.

We will also see the outline on automotive lighting and how mechatronics has enabled its evolution making an emphasis on the headlamps and the existing actuators needed to fulfill the current market demands. With this, we can summarize the specifications that we search to satisfy with our actuator and why we have chosen a piezoelectric motor as the core of our actuation device.

Finally, we will show the latest trends on this kind of actuators as they also possess several types of architectures, which will ultimately allow us to justify the use of a Standing Wave Ultrasonic Motor (SWUSM) as a potential solution for high precision headlamp leveling.

II.2. Piezoelectricity

In 1880, Jacques and Pierre Curie discovered the presence of induced electric charges when applying a mechanical stress on pieces of quartz, topaz, and other crystals. Derived from Greek work *Piezo,* which means pressure; they called this phenomenon piezoelectricity, based on an analog phenomenon already known at that time called pyroelectricity, the polarization of a material by means of changes on the temperature.

The opposite effect, that is, the deformation of a material when submitted to an electric field, would have to wait until 1881 when Lippman mathematically deduced its existence and the Curie brothers demonstrated it experimentally [13].

Hence, we differentiate two types of energy conversion within piezoelectricity: the direct and the inverse piezoelectric effect.

Direct Piezoelectric Effect

It is the effect by which electric charges accumulate in certain materials in response to an applied mechanical stress. This phenomenon is useful for the creation of sensors as we obtain an electric response proportional to the force applied on the material, that is, mechanical energy is transformed to electrical energy. One of the first applications dates from 1917 when Paul Langevin developed the first sonar using quartz crystals for submarine survey [14].

Inverse Piezoelectric Effect

As follows from the works of Lippman on thermodynamics, all piezoelectric materials are also capable of showing inverse piezoelectric effect which is the deformation of a body in the presence of an electric field. The sense of the energy transformation is inversed when compared with the direct effect and a proportional mechanical response is obtained for a given electrical stimulus within the crystalline structure, so this phenomenon is related to our case of study, the actuation applications.

II.3. Piezoelectric Materials

Polarity of a molecule is a property of the bonds between the atoms leading to the apparition of a dipole. It refers to the uneven distribution of the positive and negative electric charges of the molecules due to some atoms that exert significantly more pull on the charges than others. In nonpolar molecules, the center of these charges coincides and therefore, no dipole is present in the molecule. This is caused, among other things, by the symmetry of the crystal network.

Most frequently used piezoelectrics are ceramics with a perovskite structure that don't exhibit a net dipole moment $\vec{p}$ above a critical temperature known as Curie Temperature T_C. On the other hand, at temperatures below T_C, the material is characterized by the existence of a net polarity within their crystal structure (Figure II.3-1).

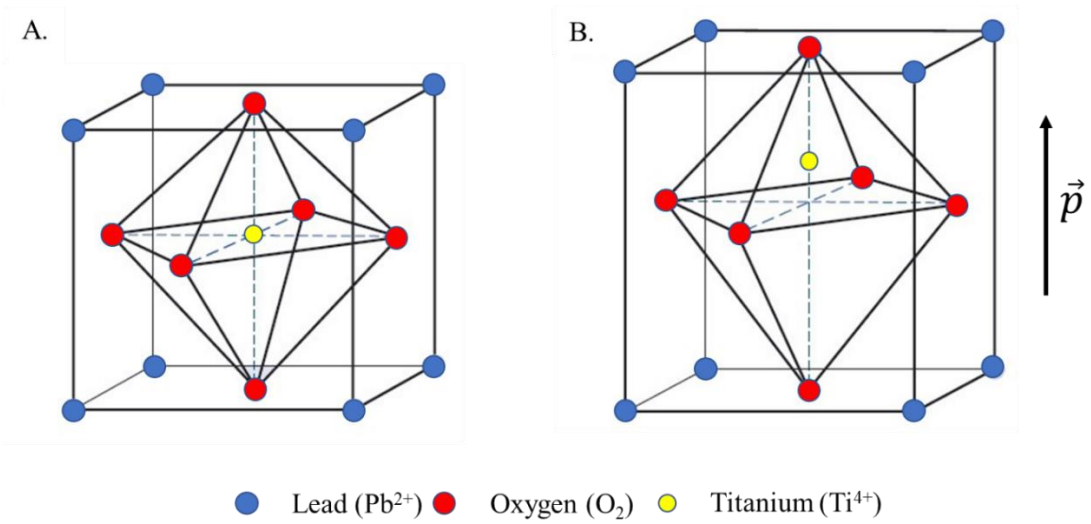

Figure II.3-1. A perovskite structure. A. Above Curie Temperature. B. The crystal already polarized.

Adjacent dipoles in small regions form domains in the material. Each domain has a net dipole moment itself which is randomly oriented so the overall polarization at a macro scale is zero. In order to obtain macroscopic piezoelectricity, the material must undergo a poling process in which the solid is put in a sufficiently strong electric field at a temperature close to T_C. In response to this external perturbation, the dipoles align to the electric field and once it is removed, most of the domains will keep aligned in the same direction.

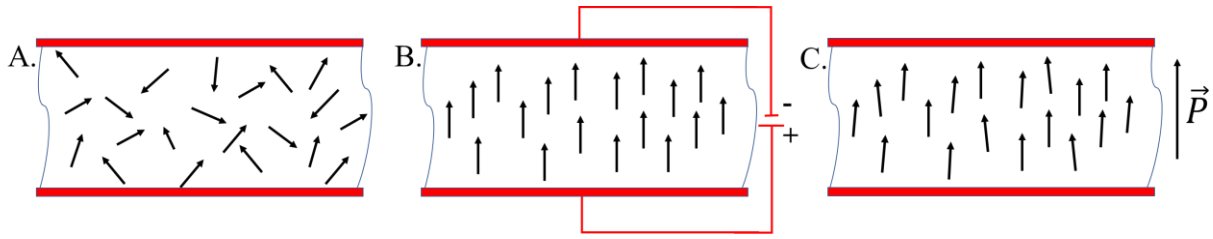

Figure II.3-2. Poling process of a piezoelectric ceramic.

We say then that the material has been polarized and the total electric polarization per unit volume $\vec{P}$ is equal to the vector sum of each dipole moment $\vec{p}$

$$\vec{P} = \frac{1}{V}\sum_{k=0}^{N}\overrightarrow{p_k} \qquad \textit{Eq. II.3.1}$$

Mechanical or electric perturbation will modify the dipole moment in different ways regarding the direction of the axis of polarization of the material.

When a constant electric field is applied in the direction of $\vec{P}$, the element will grow along the axis of the polarization and will shrink in the directions perpendicular to it. Analogically, if the electric field is opposite to $\vec{P}$, then the element will be shorter and broader. For an alternating electric field, the element will shrink and grow at the frequency of the applied electric field.

Similarly, if compression is applied along the axis of polarization, a voltage with the same polarity as the one used in the poling process will be generated and vice versa, i.e., the electric field generated when applying tension will be contrary to $\vec{P}$.

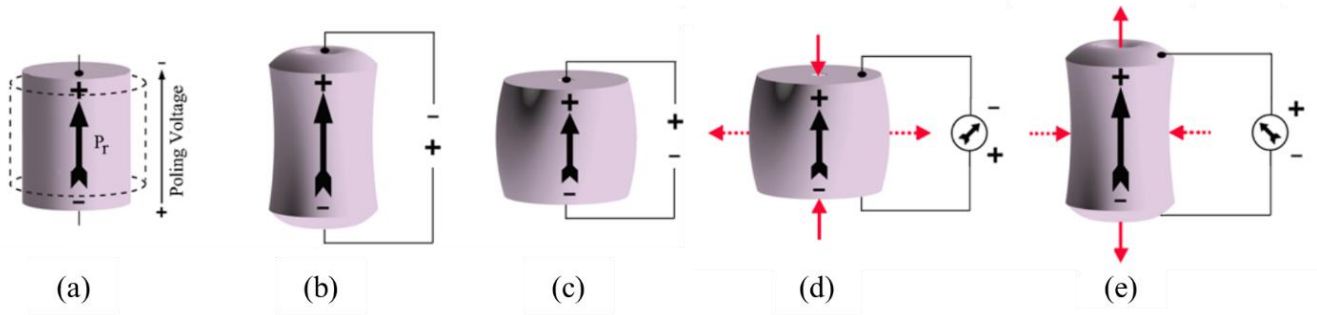

Figure II.3-3. Direct (b), (c) and inverse (d), (e) piezoelectric effect and the different responses to different perturbations along the polarization axis. (a) No perturbation, (b) positive voltage as a response to tension, (c) negative voltage as a response to compression, (d) shrinking under a positive electric field, (e) expansion under a negative electric field. Image taken from [15]

II.4. Piezoelectric Equations

Piezoelectricity bridges electrical and mechanical energy transformations. In practice, it is modeled as the coupling between mechanical variables, stress T and strain S, and electric variables, electric displacement D and electric field E. In the direct effect, D is related to an external stress T by the piezoelectric constant d. The same constant links the strain S caused by an external electric field E. Because we can relate two pairs of variables, three other constants are needed to describe the different piezoelectric outputs.

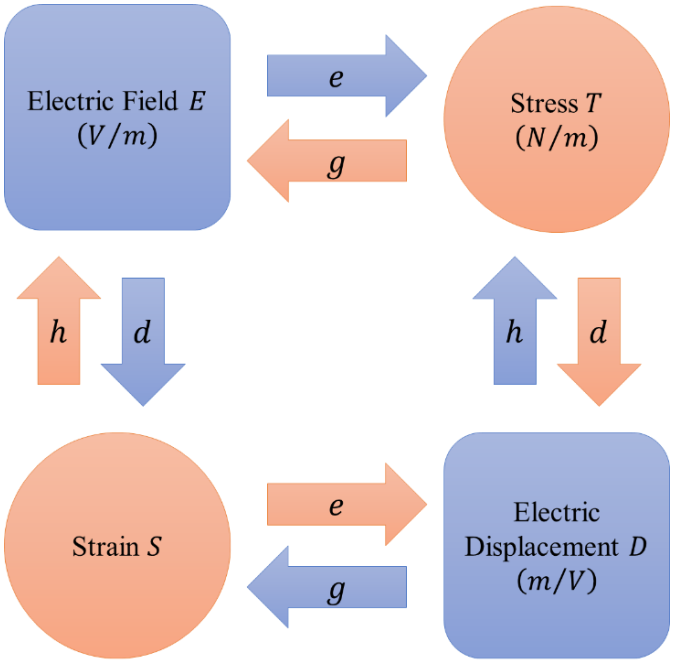

Figure II.4-1. Piezoelectric constants based on the direction of energy transformation.

Hence, for a given piezoelectric ceramic we will have two basic equations describing the direct and the inverse effect.

Table II.4-1. Linear piezoelectric equations.

Direct Effect	Inverse Effect
$D = \varepsilon^T \cdot E + d \cdot T$	$S = s^E \cdot T + d \cdot E$
$E = \beta^T \cdot D - g \cdot T$	$S = s^D \cdot T + g \cdot D$
$D = \varepsilon^S \cdot E + e \cdot S$	$T = c^E \cdot S - e \cdot E$
$E = \beta^S \cdot D - h \cdot S$	$T = c^D \cdot S - h \cdot D$

The superscript indicates that the constant it goes with is considered at a constant value of that superscript, ultimately defining the boundary conditions. These boundary conditions depend on the scenario where the piezoelectric is being operated. For example, if the electrodes are short-circuited, the electric field through the piezoelectric body will remain constant and hence s^E will be the elastic compliance in that particular scenario.

Then we can identify two mechanical boundary conditions:

- Stress-free mechanical condition; ε^T and β^T.
- Clamped (displacement constraint) condition; ε^S and β^S.

And two electrical one:

- Short-circuit condition; s^E and c^E.
- Open circuit condition; s^D and c^D.

This work focusing on the design of a piezoelectric actuator, the equation of interest will be

$$T = c^E \cdot S - e \cdot E \qquad \textit{Eq. II.4.1}$$

II.5. Properties of piezoactuators

Actuators are characterized by their displacement, force, frequency, size, power consumption where the ideal architecture points towards high displacement and force on a broad range of frequencies while energy consumption is kept to a minimum level. Regarding the application, a given type of actuator will better perform than other one as, in general, every kind of actuation method cover some of the previous categories and their shortcomings have not great impact on the environment they are used. For example, hydraulic actuators are a good choice when the application requires high force and displacement capabilities but only at low speeds. Electromagnetic actuators can operate at a much better speed range but they are heavier and require significant electrical current.

As with conventional actuation, the same applies for smart material actuators. Since the apparition of MEMS in the 80s and the interest on lighter devices, piezoactuators have earned a significant place on precision applications thanks to their great ability to generate precision motion as well as their flexibility to integrate with other subsystems and miniaturization capabilities. Besides, piezoelectric actuators are known for their excellent operating bandwidth and can generate large forces in a compact size. Nevertheless, they are characterized by a very short inherent displacement [16]. To better illustrate this, consider a piezoelectric material as shown in the figure Figure II.5-1.

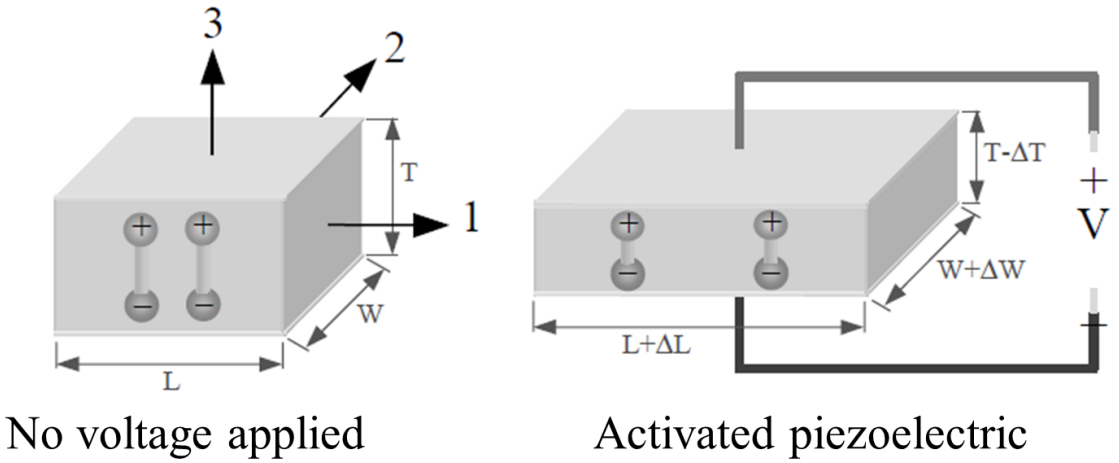

Figure II.5-1. Typical piezoelectric deformation.

We know that, when applying a constant voltage V in absence of mechanical perturbation, the strain S on the material depends on the piezoelectric constant d and the applied electric field E.

$$S = d \cdot E \qquad \textit{Eq. II.5.1}$$

The electric field through the piezoelectric is uniform since piezoelectric materials are dielectric and the electrodes are parallel. The strain is defined as the ratio of total deformation Δx to the initial dimension x and ignoring the boundary effects near the edges, the previous expression can be transformed into

$$\frac{\Delta x}{x} = \frac{d \cdot V}{x} \qquad \textit{Eq. II.5.2}$$

$$\Delta x = d \cdot V \qquad \textit{Eq. II.5.3}$$

It is clear that the stroke does not depend on the size of the material. Classical values of d constant are of order of $10^{-12}\ m/V$. So if we suppose a 1000 V/m electric field and for $d = 500\ pm/V$ then $\Delta x = 500\ nm$. This tiny deformation is generally not useful in most actual applications as it is the case for dynamic leveling. Because of this, piezoelectrics cannot often be used on a raw form and amplification is necessary to take advantage of their tremendous precision capabilities.

It is worth making a small review on the different forms a piezoelectric can be operated regarding their innate anisotropy. Indeed, use of piezoelectrics as actuators depends on both the direction of polarization and the electric field, resulting in three different modes which are longitudinal, transverse and shear mode.

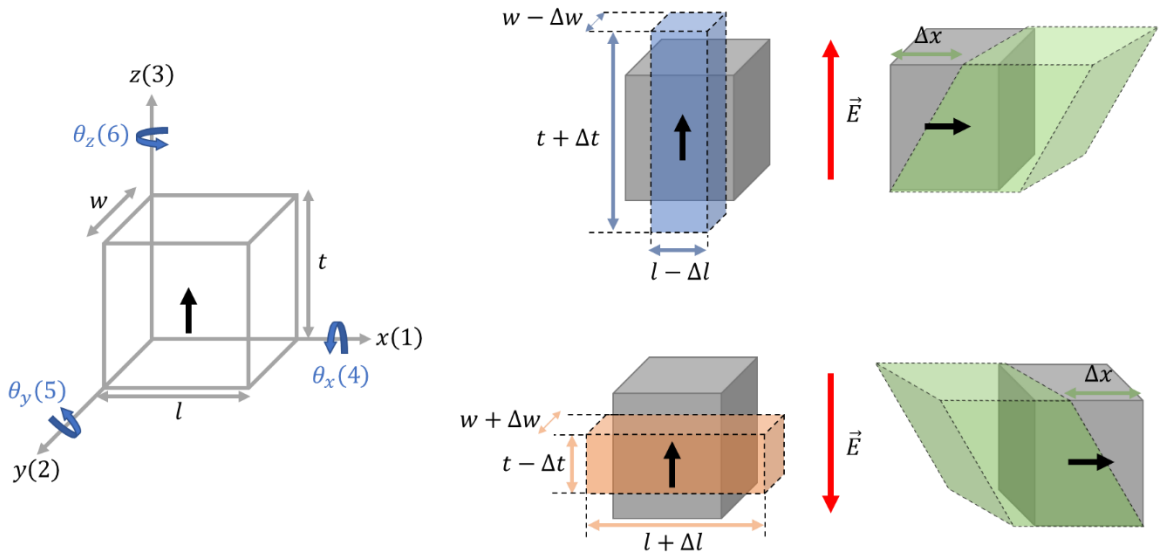

Figure II.5-2. Different modes of actuation of piezoelectric materials.

The direction of positive polarization $\vec{P}$, represented by the bold black arrow in Figure II.5-2 is usually chosen to coincide with the z-axis of a rectangular system of crystallographic axes x, y, z, denoted by 1, 2 and 3, and the shear planes are indicated by 4, 5, 6 and are perpendicular to the directions 1, 2, 3 respectively. So, when applying an electric field $\vec{E}$, depicted by the red arrow, that is parallel to the polarization, growth in that dimension will occur. Consequently, because of the Poisson effect, reduction of both perpendicular dimensions will be observed on the material. So longitudinal extension and transverse contraction are taking place in the piezoelectric material. The exact opposite will occur when $\vec{E}$ is antiparallel to $\vec{P}$. The shear mode occurs when $\vec{E} \perp \vec{P}$.

The utilization of a given mode of actuation majorly depends on the type of precision motion required in the concerned application [17]. From *Eq. II.5.4*, regarding exclusively piezoelectric contribution, we can calculate the longitudinal strain S_3, the transverses S_1, S_2 and shear strain S_5 for the cases shown at right hand side of the previous figure.

$$S_p = S_{pq} T_q + d_{pk} E_k \qquad \textit{Eq. II.5.4}$$

$$\begin{cases} S_1 = d_{31} E_3 \\ S_2 = d_{32} E_3 \\ S_3 = d_{33} E_3 \\ S_5 = d_{15} E_1 \end{cases} \qquad \textit{Eq. II.5.5}$$

Due to the anisotropy of the piezoelectric, longitudinal mode is sometimes chosen, as the deformation along that axis is significantly more important compared to transverse deformation because $d_{33} > d_{31}$.

For evaluating their performance, piezoelectric actuators are treated in terms of the free deflection, that is, the amplitude of the stroke when the actuator is free to move and the blocking force F_B that corresponds to the force exerted at maximum voltage. This force appears when the actuator works against a load of infinite stiffness[1].

[1] Such a stiffness is impossible to exist. F_B is then obtained as the force required to push back to its original dimensions an actuator at maximal voltage with no load.

In most cases, the relation between force and deflection at a fixed voltage can be considered linear: the displacement reduces as the load increases until reaching the maximal force of the actuator F_B. Contrarywise, at free deflection, the output force of the actuator is zero. For an ideal transfer of energy to happen, the difference of stiffness, between the actuator and the system where it will operate, and the free play of the actuator must be as minimum as possible [18], [19].

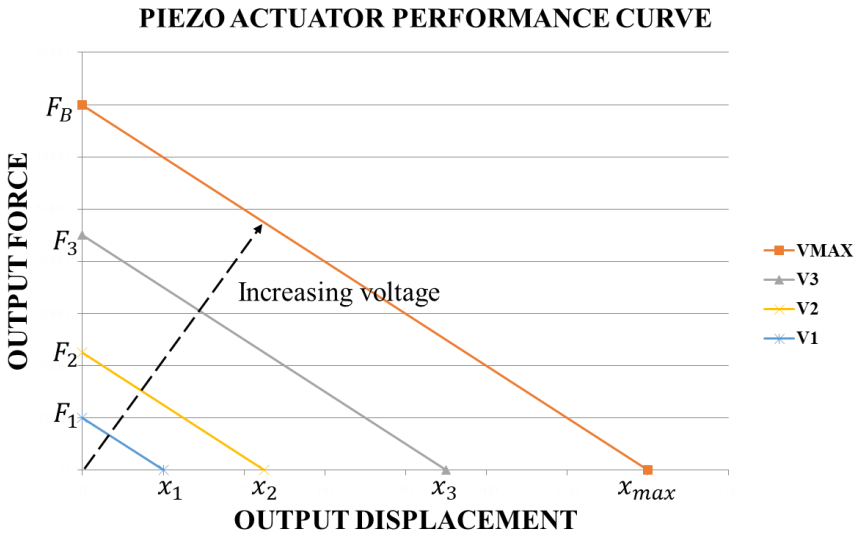

Figure II.5-3. Performance of a piezoelectric actuator for different voltages $V1 < V2 < V3 < VMAX$.

As piezoactuators are brittle, tensile strength is low and preload is necessary for their operation. We illustrate two scenarios on the next figure.

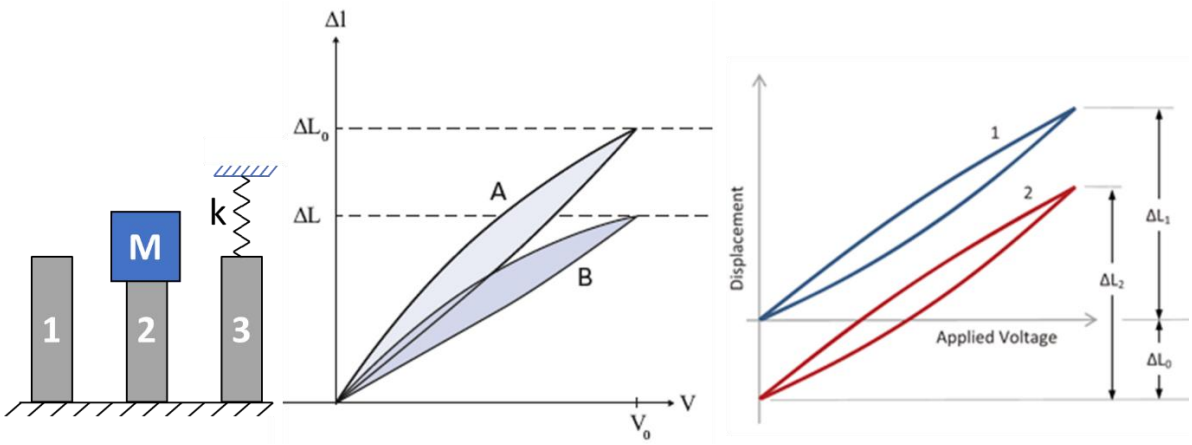

Figure II.5-4. Preloading of piezoactuators. Images taken from [19].

In the case of an actuator of stiffness k_p with an external constant load due to a mass m, the deflection is given by

$$\Delta l_0 = \frac{F}{k_p} = \frac{mg}{k_p} \qquad \textit{Eq. II.5.6}$$

The stroke of the actuator under these conditions won't be different to the stroke of the unloaded case. However, if the external load is no longer constant, as it would be the case with a spring, the piezo actuator stiffness k_p is in series with the external stiffness k_e and the overall stroke will be reduced to

$$\Delta l_2 = \frac{\Delta l_1 k_p}{k_p + k_e} \qquad \textit{Eq. II.5.7}$$

Figure II.5-4 shows another important characteristic of piezoelectric actuators, hysteresis. Due to their dielectric nature, hysteresis on piezoelectric materials is one of the major contributors to nonlinearity. The material properties that cause hysteresis are also responsible for creep. When applying an electric field in open loop, the creep is an undesirable behavior due to the much faster response time of the material than the reorientation time of its individual dipoles. Hence by applying a constant electric field to a piezoceramic, the later will first make the corresponding displacement and afterwards, it will continue to move slowly as the dipoles reorient. It could take several minutes to reach the steady final state (1% to 5% more than the initial strained position)[2].

Piezoactuators are mostly used on closed loop so hysteresis, creep and other non-linearities can be compensated. Controllers depend on the mathematical model which also depends on the structure that amplifies the piezoelectric deformation [20]. Given the large diversity of devices, the next section aims to give an overall view on the numerous ingenious concepts that have been created on an attempt to amplify the typical tiny deformations of piezoelectric materials and transform them into useful actuators. They can be categorized based on how the amplification is done: of type external, internal and frequential.

II.6. Internally amplified piezoactuators

We talk about Internally Amplified Piezoactuators (IPA) when the amplification is obtained without the use of an external mechanical structure. In fact, they rely on the material's anisotropy by disposing the electrodes and choosing geometries that take advantage of this.

II.6.1. Stacks

It might be the simplest way to produce amplification. The typical maximal free strains induced in a piezoceramic at fields of some hundreds of kV/m is on the order of 0.1% to 0.2% of its length [21].

The longitudinal deformation of a piezoelectric crystal is independent of its dimensions. Thus, considering the scenario depicted on the left side of Figure II.6.1-1 and from *Eq. II.5.2* and *Eq. II.5.5*, we know that, for a piezo d_{33} of length w under a voltage V, the displacement is

$$\Delta w = d_{33} \cdot V$$

[2] For periodic motion, creep and hysteresis have only a minimal effect on repeatability.

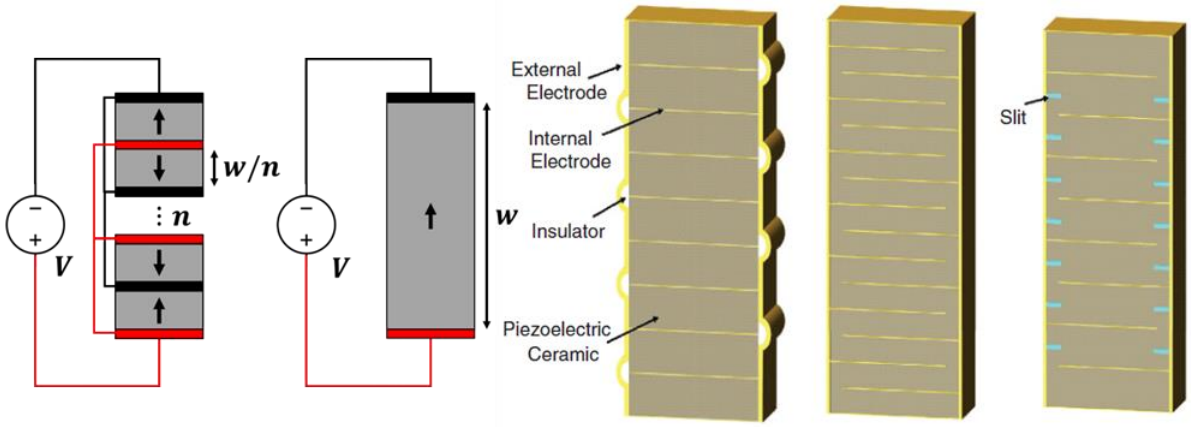

Figure II.6.1-1. Piezoelectric stack for longitudinal deformation. Right hand side: Electrode configuration

If now, the same voltage is applied to a stack of n layers of the same material, each of them of longitude w/n then, we obtain a more general expression for *Eq. II.5.3*

$$\Delta w = n \cdot d_{33} \cdot V \qquad \textit{Eq. II.6.1.1}$$

So, the total deformation of this kind of actuator will be n times higher than the one of a piezo block of the same dimensions. On the other hand, there is no loss of force as it depends on the cross-sectional area of the actuator. Of course, for this to be possible, the layers that compose the stack must be arranged in a proper way, for example, by alternating a positive and a negative polarized layer as shown in the Figure II.6.1-2. The electrodes of each layer are also alternated and interconnected in such a way that one single voltage source can operate the actuator.

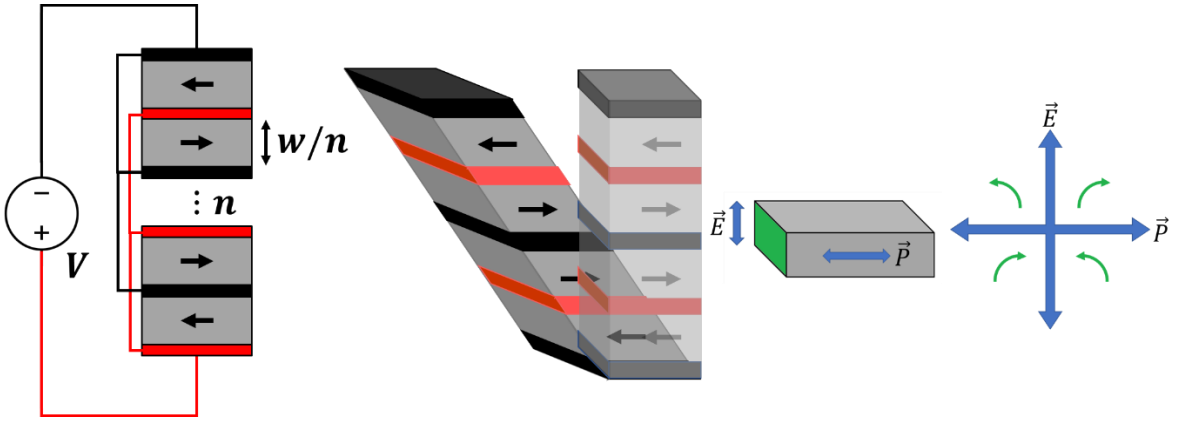

Figure II.6.1-2. Shear piezoelectric stack. Right: green surface displacement regarding polarization and electric field directions.

Stack amplification is also possible to enhance shear displacement n times as shown in the figure above.

$$\Delta x = n \cdot d_{15} \cdot V \qquad \textit{Eq. II.6.1.2}$$

In fact, shear piezoelectric coefficient d_{51} is usually the highest, so they are preferred for some applications. Nevertheless, preload cannot compensate shear stress which limits the height of shear stacks, and so, the quantity of layers.

Today, stacks of tenths of layers of some hundreds of μm thick exist in the market which allow to operate them at relatively low voltages of some hundreds of volts. Nevertheless, the characteristic displacement of these type of actuators is about a few μm which is still rather low for macro applications but combined with other structures, they have become the base on some of the externally amplified architectures as the lever arm actuators (LAA) and the parallel pre-stressed actuators (PPA).

They display great output force and high resonant frequencies which demonstrate great applicability on vibration control of structures and machines. For example, by connecting a piezo stack on a host structure, parallel to the main axis, vibration damping or even bending moment compensation is possible [22].

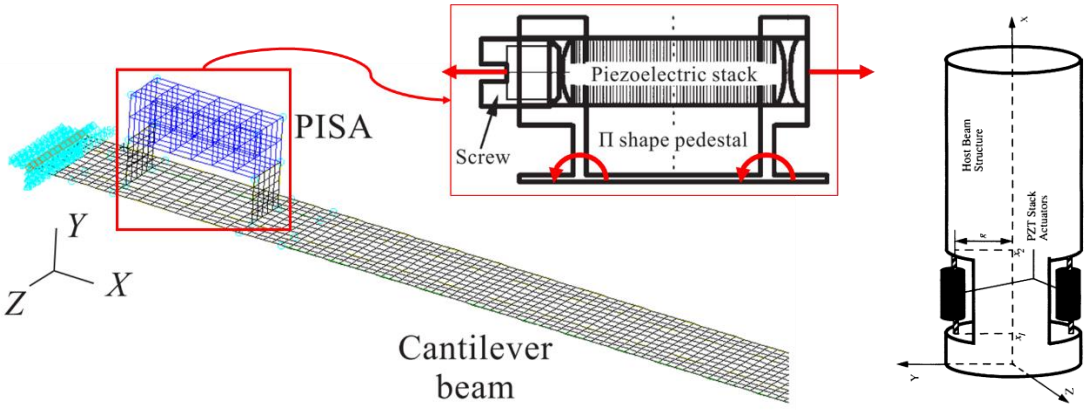

Figure II.6.1-3. Piezoelectric stack on host structures. Left: First bending mode control of a cantilever structure [23]. Right: Damping enhancement of bending vibrations on a thick beam [24].

II.6.2. Piezoelectric tube actuators

A classic piezo tube consists in a thin cylinder polarized along the radial direction and an arrangement of electrodes on the interior and exterior surfaces. Two different modes are possible: radial, due to the longitudinal elongation or contraction in the axial direction; and bending mode, a lateral mode of actuation where electric potential of different polarity is applied on diametrically opposed electrodes as shown in Figure II.6.2-1.

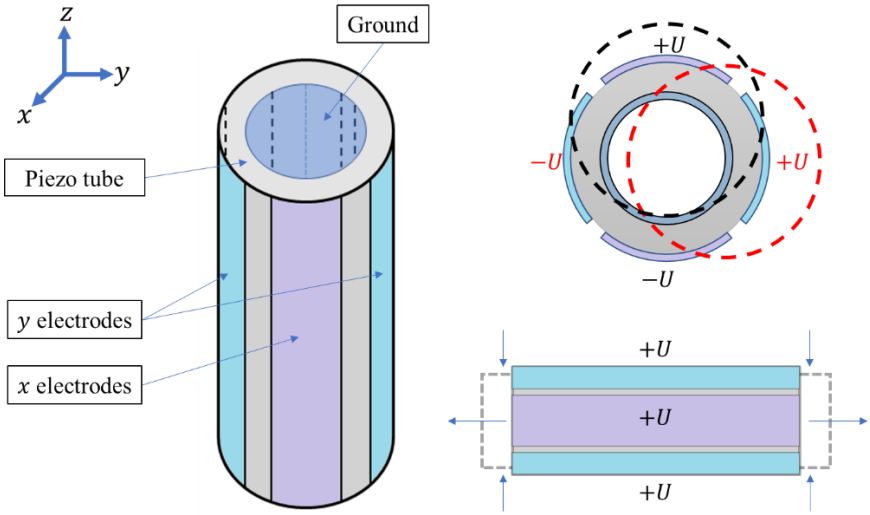

Figure II.6.2-1. Piezo tube actuator.

It is possible to obtain multi-axis motion as the actuator can bend in different directions. For example, consider the case depicted on the right-hand side of the figure Figure II.6.2-1. For it to move on $+y$ direction, a positive voltage $+U$ is applied on the right electrode while a same voltage of inverse polarity is applied on the counterpart electrode. Same principle applies for bending the tube along the x axis, applying a positive voltage on the electrode situated towards the desired direction and a negative voltage on its counterpart. Voltages of the same sign on the four electrodes activate the radial/axial displacement mode. The more segmented the tube is, the better the accuracy of motion will be [17].

Because of their great flexibility, they are the main type of actuator found in Atomic Force Microscopy (AFM) [25] which are extensively used in crystallography, biology (study of virus, proteins, DNA), pharmaceutics, etc. as they allow the visualization of solid surfaces at micro to atomic resolution.

By measuring micro contact forces between a probe and the sample it is possible to obtain the morphology of the sample's surface. For this, a probe, placed a few nanometers apart, interacts with the region of interest of the sample by scanning the surface thanks to the relative motion of both parts. The widely applied scan trajectory is the back-and-forth raster pattern which actually is executed by a piezoelectric tube actuator. A diagram of the basic functioning of AFM is shown in Figure II.6.2-2.

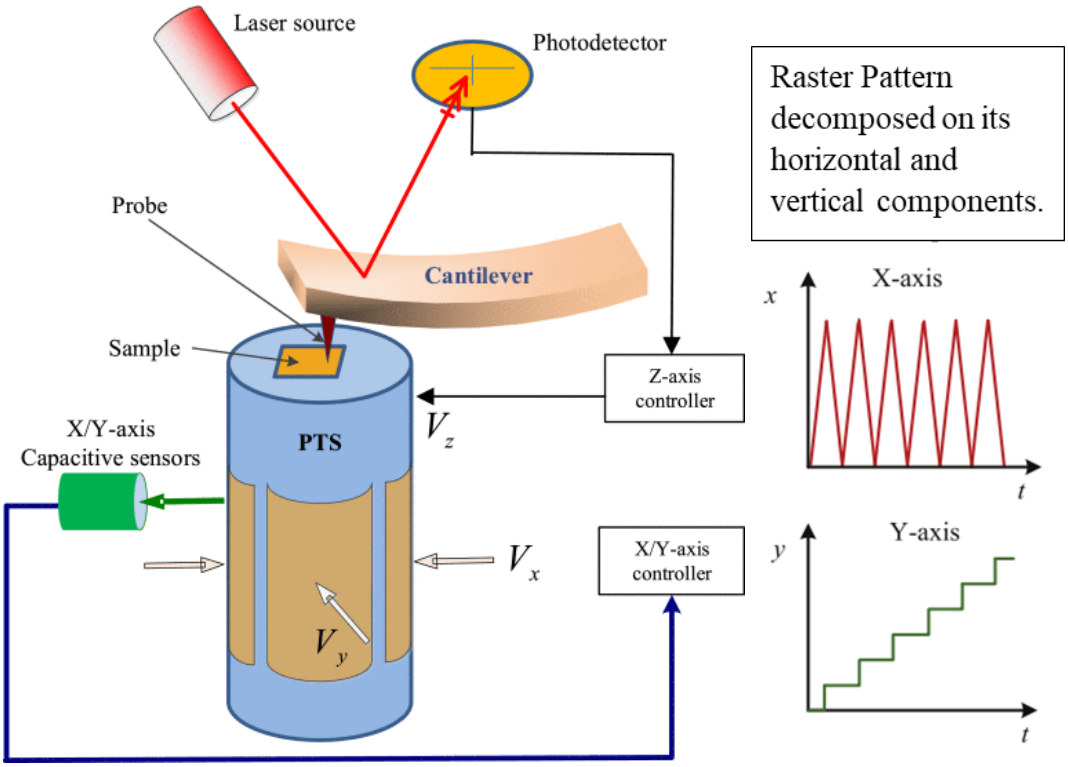

Figure II.6.2-2. Piezo tube actuator on an AFM. Images taken from [26].

II.6.3. Bender Actuators

They are based on the strain differences of two or more layers to indirectly induce bending motion. We can basically distinguish two types of benders: unimorph and bimorph. Both configurations are characterized by a great length to thickness ratio, so longitudinal deformation is insignificant compared to transverse deformation, and the dominant piezoelectric coefficient on the actuator is d_{31}.

Unimorph benders consist in one active layer of piezoelectric material constrained by a substrate layer made of an elastic material, such as steel, bonded together by an adhesive. On the other hand, bimorphs consist of two piezoelectric layers that are arranged so their polarization vectors, either point in the same direction, and we say it is a parallel bimorph; or point towards each other, in which case they are in series. Sometimes inactive substrates may be included for structural stability of the actuator [27].

As it was explained in Figure II.5-2, once an electric field is applied along the thickness, expansion in the poling direction and contraction on the plane perpendicular to that direction takes place and inversely, thickness contraction generates expansion of that same plane. The functioning of these actuators is based on the restriction for the piezo material to suffer deformation in the thickness direction z and the constrains resulting from opposing strain at both sides of the neutral surface, which generates an internal bending moment that causes the whole structure to flex in the z direction.

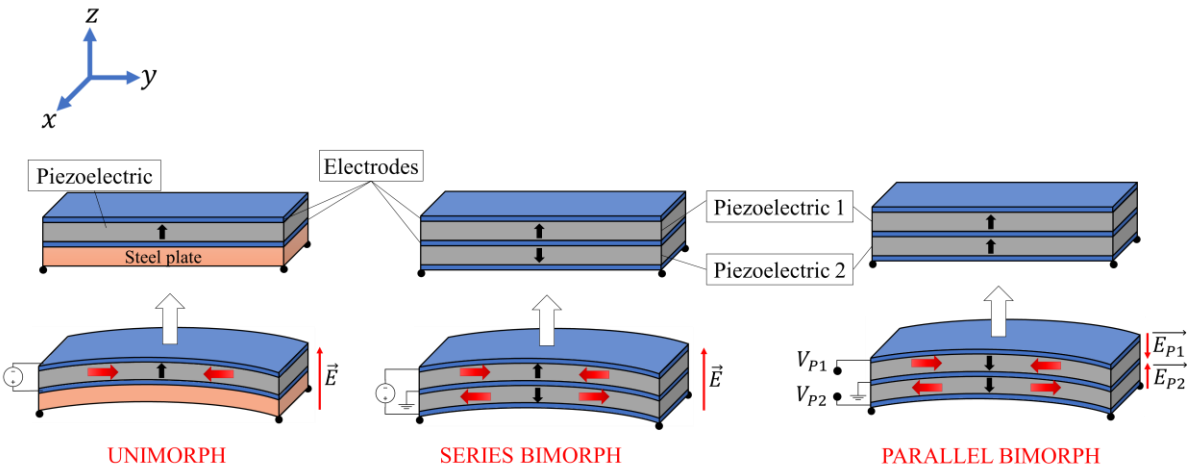

Figure II.6.3-1. Piezoelectric benders. Left side: unimorph structure. Center: series bimorph structure. Right side: parallel bimorph structure.

In Figure II.6.3-1, unimorph displacement coincides with the direction of the electric field. Bimorphs, on the other hand, may be electrically more complex: they output positive displacement when the poling direction of the upper's piezo layer is parallel to the electric field. It is common to use the bender actuators on a cantilever configuration, in order to use exclusively the tip displacement as shown in the figure Figure II.6.3-2.

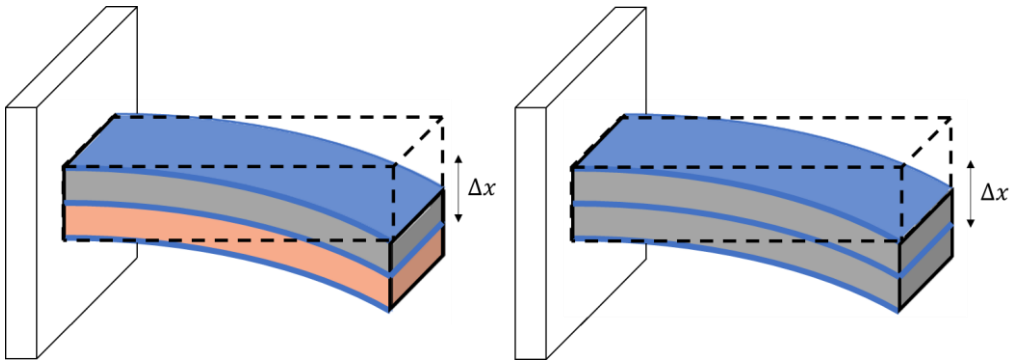

Figure II.6.3-2. Piezoelectric benders. Left side: unimorph structure. Right side: series bimorph structure.

RAINBOW (Reduced And Internally Biased Oxide Wafer) actuators are considered a specific case of unimorph benders. Invented by Haertling [28], they are operated similarly to the unimorphs but instead

of a layered structure, RAINBOW consists in a monolithic structure, obtained by a chemical process, of piezoelectric and electrode material, usually at the bottom, which ultimately, is the responsible of exerting an internal compressive stress which gives the actuator a dome appearance at rest position.

RAINBOW actuators present great mechanical resistance due to their intrinsic prestress condition and can generate larger displacements compared to unimorphs of the same dimensions [29]. Besides, they offer the possibility of stacking several actuators to even enhance the output displacement.

Benders have much bigger output displacement (ranging from several μm to a few mm) at the expense of losing force capacity when compared to stacks. They are frequently used in energy harvesting applications, micro switching and micro pumping. One example developed by Takasago ® is shown in Figure II.6.3-4.

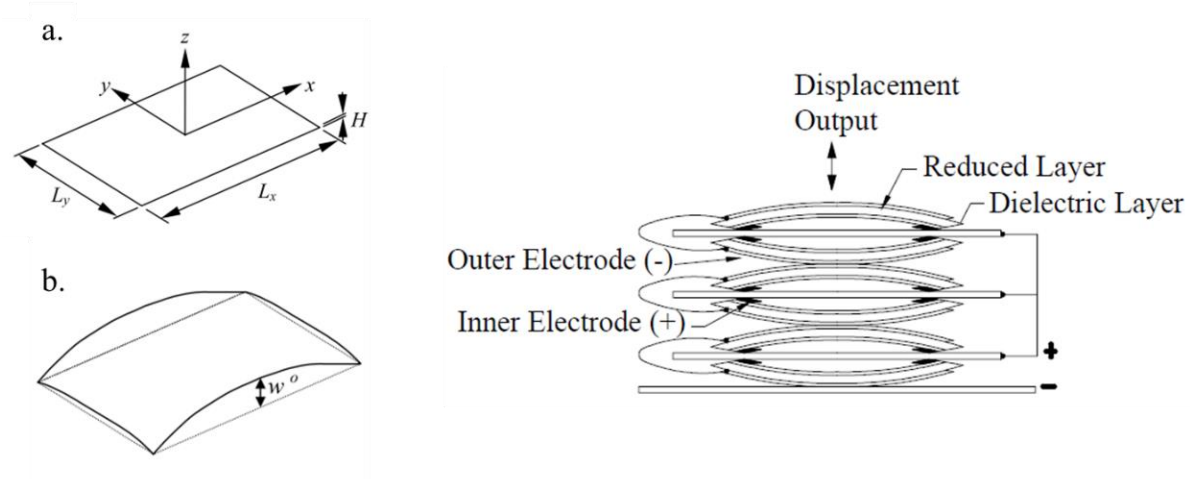

Figure II.6.3-3. RAINBOW actuator. a. Initial shape before fabrication. b. Final shape after fabrication.

Figure II.6.3-4. Takasago ® piezoelectric micropump [30].

II.7. Externally amplified piezoactuators

Externally leveraged actuators rely on an external mechanical component for their actuating ability. In general, they consist in the integration of a piezo stack into a flexible structure, and, at the expense of their force output, displacement is highly increased. The motion is achieved by a piezo stack that bends a monolithic compliant structure, which differs from classic mechanisms in that the amplification is caused by the deformation of their parts rather than the change of position of rigid joints. The use of

compliant mechanisms over stiff components has great advantages for miniaturization because it allows operation without friction and wear. Besides, it requires no assembly offering the possibility of fabricating complete systems using few mask layers [31].

As they can be tailor-made for a specific scenario, there is a tremendous diversity of compliant mechanisms. The difficulty lies in the design of an optimal topology, as predicting how a force applied on a point in the structure would move another point in the same structure is not evident.

In general, the design of such mechanisms passes through two stages:

- First, topology synthesis that is the generation of a basic geometry that satisfies the desired output movement direction when subjected to prescribed input forces [32]. Sometimes, it is useful to start with classic rigid mechanisms and transform them in compliant mechanisms.

- Then an optimization phase, where the previous structure is size and shape optimized: optimum number of holes placed at the most appropriate locations along with the optimal shapes and sizes for all its features [33]. As there is a trade-off between force and displacement, the goal is also to maximize output displacement by keeping output force as high as possible.

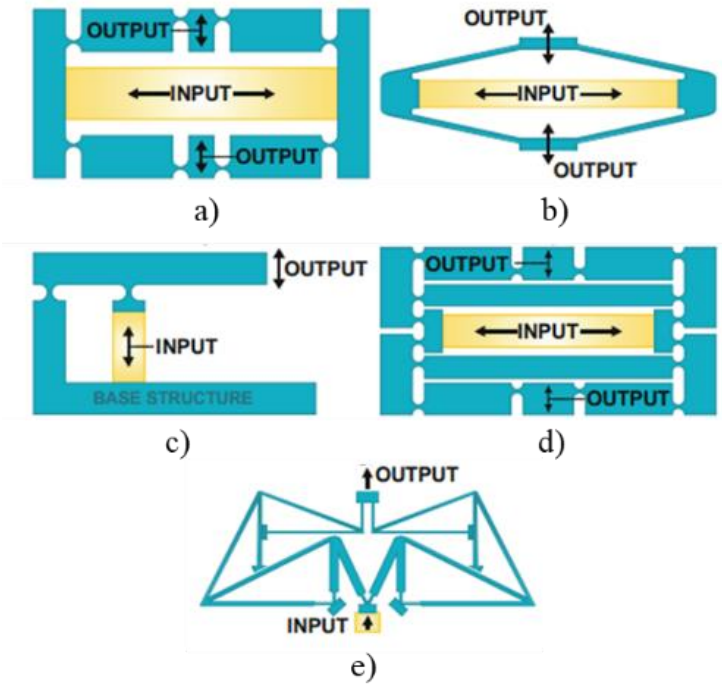

Figure II.7-1. a) bridge-type. b) rhombus type. c) lever mechanism. d) bridge-lever-type amplifier. e) 20:1 stroke amplification mechanism.

Figure II.7-1 shows different Displacement-Amplifying Compliant Mechanisms (DACM). This was taken from an article made by Hricko and Havlík [34] that presents compliant structures (colored in blue) of some of the mechanical amplifiers most frequently applied in small positioning devices. The depicted topologies are compared in static condition regarding their amplification ratio, and some drawbacks proper to each topology were discussed:

- Bridge and rhombus type: they are well suited for microscale applications as they exhibit compact symmetrical structures, but they have one of the smallest amplification ratios among compliant structures.

- Lever mechanism: It is one of the easiest compliant structures to fabricate, together with the linear relation between input and output for displacement-force relations that maximizes accuracy, which makes them of great use in micro-robotics. Their main drawback is the great cumulation of stress in the joints.

- 20:1 stroke amplification mechanism: It provides the largest amplification ratio of the analysis made by Hricko and Havlík and was used to multiply in a factor of 20 the displacement of an integrated piezoelectric actuator [35].

II.7.1. Lever Arm Actuators

The amplification structure consists of 4 parts: lever arm, anchor (fulcrum), the input and the output systems. In single stage mechanisms, as in their rigid equivalent simple machine, three configurations are possible based on the relative position of the input and the output with respect to the anchor (Figure II.7.1-1).

Given that piezo stacks have large force and low displacement, class I (for $l < L$) and class III are the useful ones, as their geometric advantage is greater than one. An actual example found in the industry is the piezo lever actuator P-604 fabricated by Physik Instrumente ®, which uses a stack of 8 µm maximal output on a compliant lever class III whose amplification ratio rounds 37, hence a travel range of up to 300 µm is possible [36].

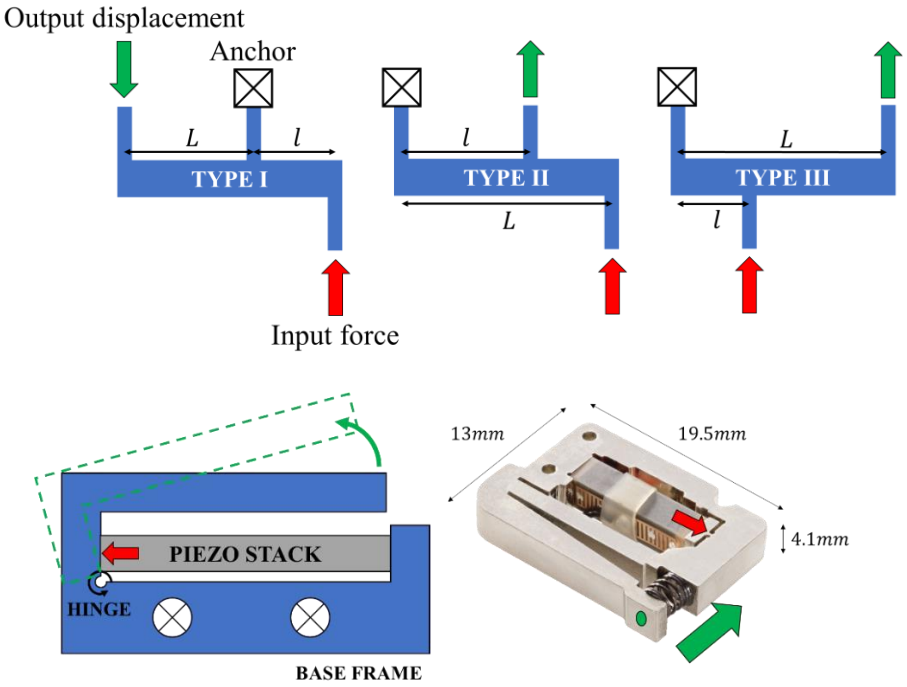

Figure II.7.1-1. Up: Types of levers on compliant mechanisms. Down: A class III piezo lever actuator. The red and green arrow indicates the input and output displacement direction respectively.

The simplicity of design and machining makes of lever type mechanisms a very popular option on piezo actuation [37]. Regarding their analysis, a conservator enough approach is to calculate the amplified displacement by simple geometry. For example, for the piezo pump shown in Figure II.7.1-2, the amplified displacement S is obtained as follows

$$S = L'_y - L_y = L\left[\sin(a_p + b) - \sin b\right]$$

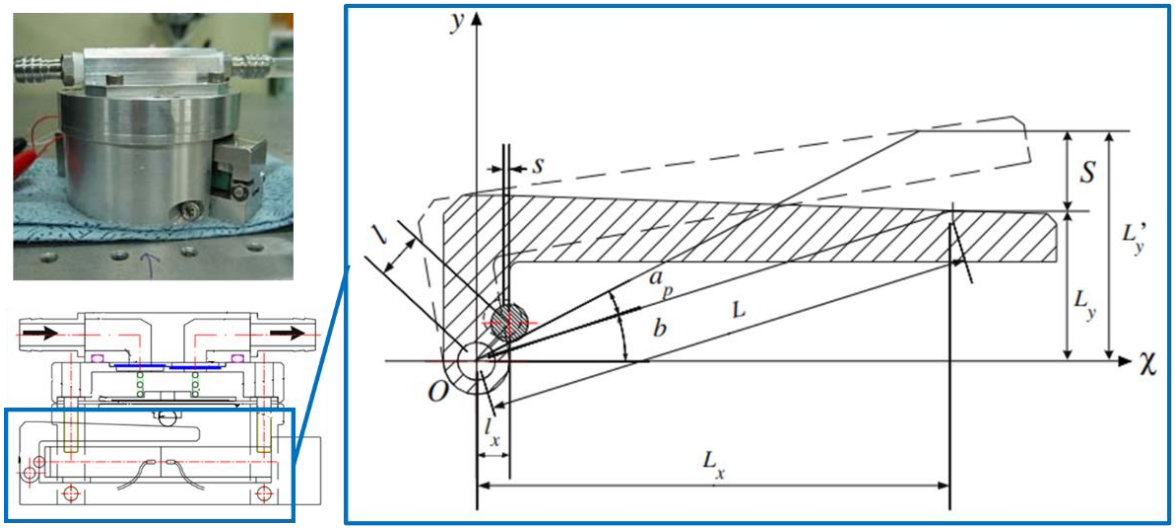

Figure II.7.1-2. Piezo lever pump designed by Ham et al [38].

These piezoactuators present great amplification ratios but their size is somewhat a tradeoff, as for obtaining a high gain, the length of the lever must be elevated as well. Nevertheless, this architecture allows the multi-stage amplification by connecting the output of a lever to the input of another one. As a result, bigger amplification ratios are possible with a more compact packaging (Figure II.7.1-3 B)

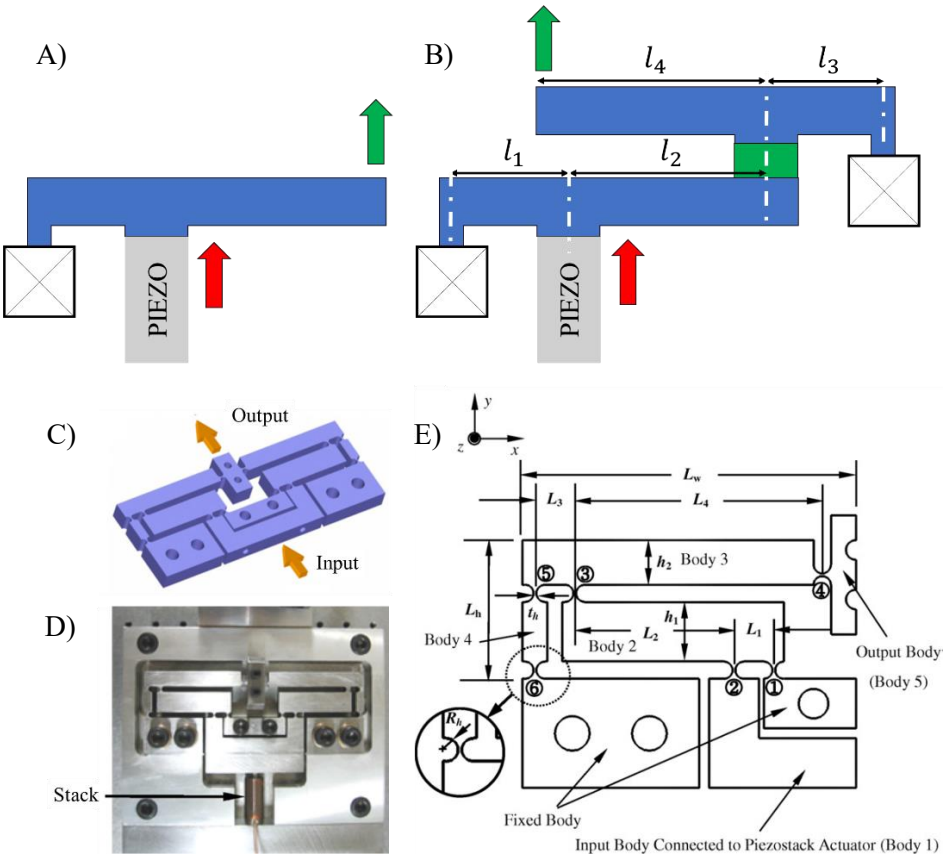

Figure II.7.1-3. A) Single Lever Amplification. B) Multistage amplification. C) Magnification compliant mechanism based on two-stage lever. D) Piezo lever actuator fabricated by Choi et al. E) The two-stage amplification.

Choi et al. [39] designed a positioning actuator based on a two-stage lever (Figure II.7.1-3. C, D). Based on the diagram shown in Figure II.7.1-3. E) a piezo stack acts on Input Body (Body 1) which transmits force to a first lever (Body 2) through ②. The output displacement then moves the second lever (Body 3) through ③, and the final output is obtained at Output Body (Body 5). Hence for a input displacement s, an output displacement S may be obtained through

$$S = s \times \frac{L_2}{L_1} \times \frac{L_4}{L_3}; A_{tot} \approx \frac{L_2 L_4}{L_1 L_3}$$

Where the total amplification may be approximated as the product of the amplification of each lever.

II.7.2. Moonie and cymbal actuators

These compliant actuators are characterized by a stack and a mechanism that transforms its deformation on motion in the transverse direction. The most basic are the Moonie and the cymbal architectures.

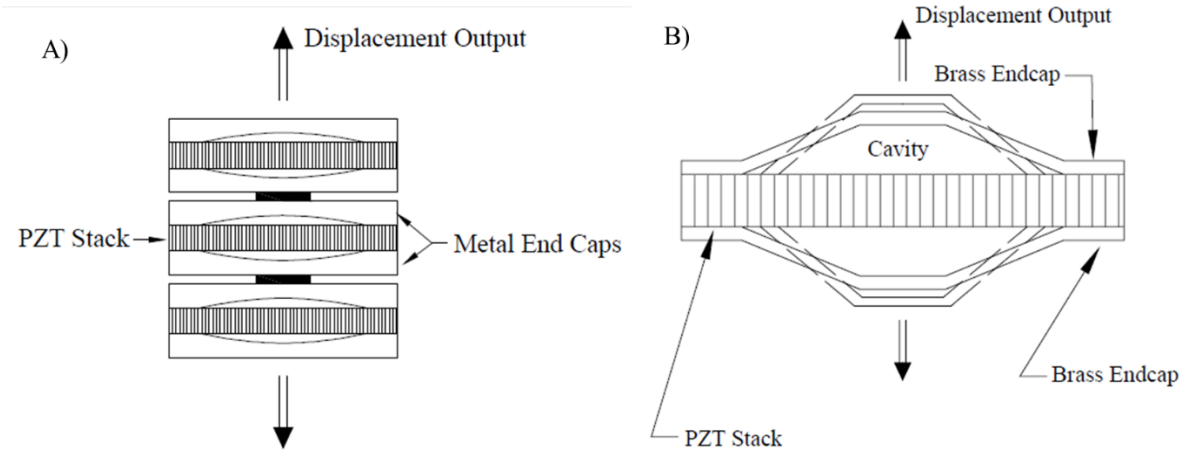

Figure II.7.2-1. A) Moonie actuator. B) Cymbal actuator.

A moonie consists of two metal endcaps, each having a crescent-moon-shaped cavity on its inner surface (hence the name moonie) and because its geometry, this actuator can generate higher forces than a bimorph plus the amplification of a piezo stack stroke (it greatly increases with cavity diameter and depth and it is inversely proportional to endcap thickness) and offers the possibility of stacking them as shown in the figure above.

The cymbal appeared as a solution to the high stresses that appear near the bonding layer of the moonies. With a renewed endcap, the cymbal actuator eliminates the stress concentration and the position-dependent displacement behavior, i.e. on moonies, the displacement amplitude decreases when moving approaching the edge of the endcap [40].

The external structures not only help with the displacement amplification, but they could also be used to apply a force constraint on the piezoelectric, which allows to overcome tensile stress limitation and enhances the piezoelectric deformation. Other structures have been designed to accomplish this with great results and are commercialized by Cedrat ®.

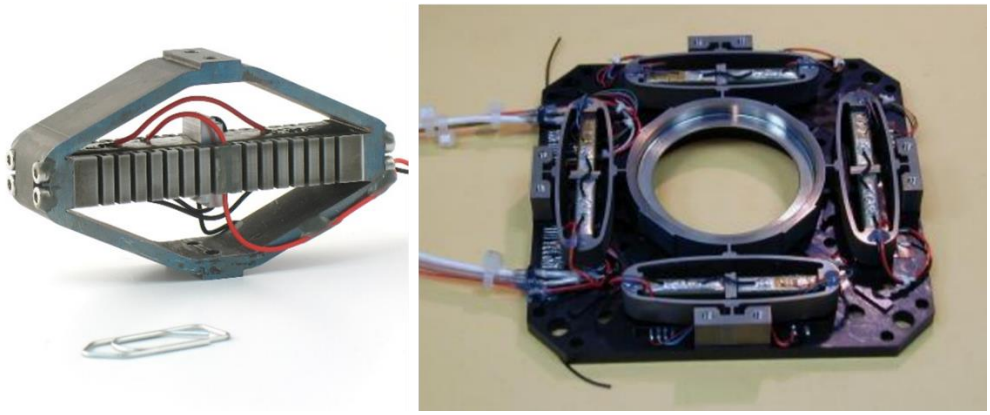

Figure II.7.2-2. Cedrat piezoelectric actuator.

II.8. Frequency Operated Actuators

The movement is obtained through the continuous repetition of small steps in a given direction. As piezoelectric materials have great reaction time, this type of architecture takes advantage of small response time of piezo materials to generate stroke only limited by the track on which the actuator operates, thanks to a moving element driven by the accumulation of micro displacements over many periods of the driving voltage applied on the piezo material. We can distinguish two groups: stepping (quasi-static) motors and ultrasonic motors.

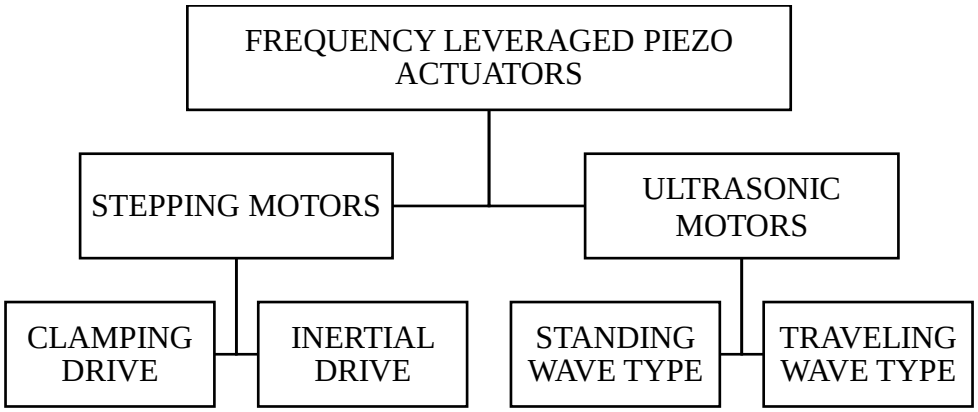

Figure II.8-1. Classification of frequency operated actuators.

II.8.1. Stepping motors

A. Clamping drive (inchworm, walking)

These actuators are based on the sequence of a clamping and a feeding phase, mechanisms that provide these actuators with typically high forces and efficiencies at low speeds and low frequencies as they

operated in a quasi-static state. Clamping drive piezo actuators need, at least, one clamping mechanism and one feeding mechanism to work.

The first type of motors relies on the repetition of clamping and feeding of a series of piezo material that imitate the movement of inchworms in nature. For this reason, they are also known as inchworm actuators.

They normally consist in a system of three coordinated piezo materials: two at the sides (1 and 3 in Figure II.8.1-1) that are in charge of clamping and one at the center (number 2 in Figure II.8.1-1) that is used as a feeding mechanism. In turn, inchworms can be subdivided in two groups based on whether the piezo actuator is moving: They are *walker* type when the actuator itself moves through a fixed guide. On the other hand, the *pusher* type consists in a shaft that is pushed by a fixed piezo actuator. The main difference is their cycle of operation.

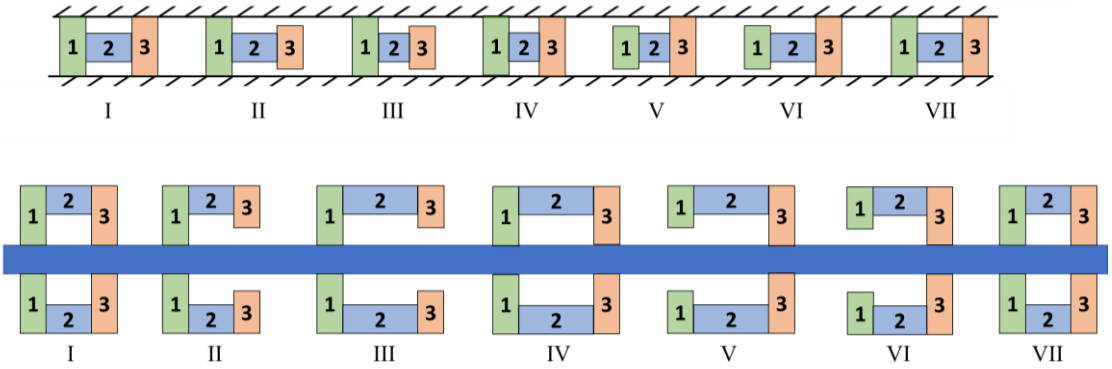

Figure II.8.1-1. Inchworm piezo actuator.

From the previous figure, starting from phase I towards phase VII of movement, one complete cycle of the walker is: PZ3 is released (II), PZ2 contracts (III), PZ3 recovers its form and clamps (IV), PZ1 is contracted (V), PZ2 recovers its form (VI) and finally PZ1 recovers its form (VII). In this scenario, the actuator moves toward the left and inversing the sequence would result on a movement on the opposite direction.

Analogously, for the pusher, one cycle is as follows: PZ3 separates from the shaft, then PZ2 expands and moves the shaft towards the left, PZ3 recovers and clamps the shaft, PZ1 releases the shaft, PZ2 contracts to feed the shaft another step to the left and finally PZ1 recovers and clamps the shaft. Of course, for this to happen, the piezo actuator is fixed to the base.

The stroke of each cycle is limited by the maximum displacement of the central piezoelectric and the total range it can moves depends strictly on the length of the guide or the shaft.

Another type of clamping and feeding motor is the piezo walker which simulates the walking of human beings. They are formed by at least, two legs that can both clamp and feed the moving element independently.

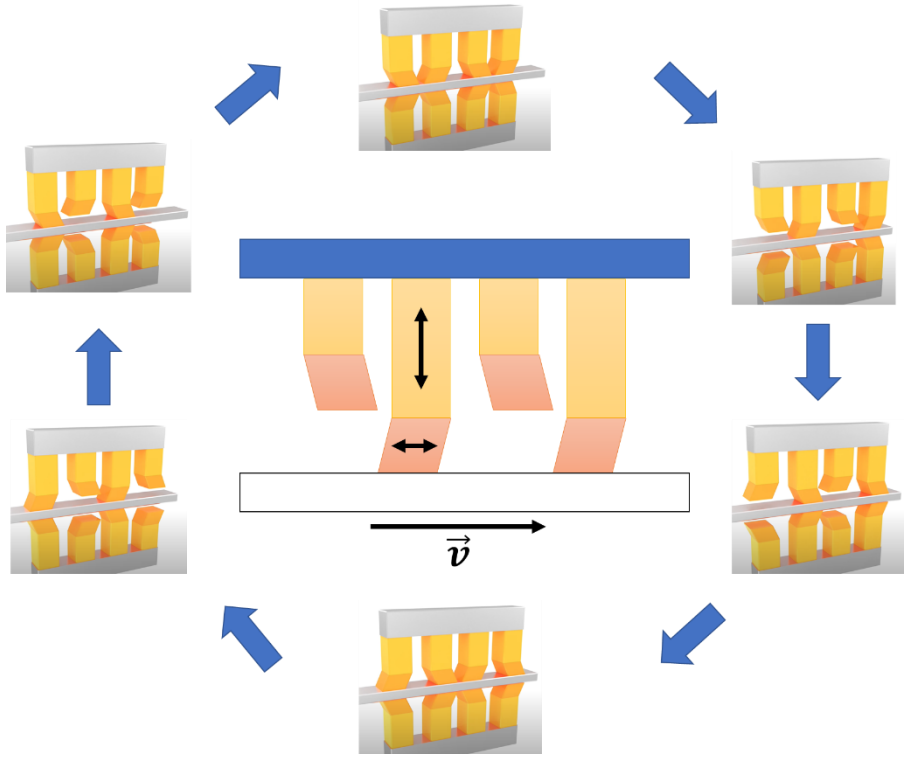

Figure II.8.1-2. Piezo walker by PI ®.

Because there are at least two legs, their respective cycles are out of phase, in such a way that one leg can feed while the other prepares to do it. For example, the piezo walker shown in Figure II.8.1-2 consists of two groups of legs, both formed by a longitudinal piezo (shown in yellow) which enables the clamp, and one shear piezo responsible of the feeding (in orange) [41].

Inchworms present simpler structures, but their motion is intermittent because there is only one feeding actuator that must stop for changing between clamping and feeding state. On the other hand, one leg of a piezo walker may be carried out during its feeding phase and therefore, the movement can be done continuously and smoothly without loss of rigidity.

B. Inertial drive

The cycle of operation for one step goes from a inertial force to a friction force between the driver part and a stator, both forces generated by means of piezoelectric deformation. They generally use a sawtooth signal with different duty ratios to alternate between slow and rapid deformation. There are two main types of inertial piezo actuators: impact-inertial drive and friction-inertial [42].

i. Impact drive type

Figure II.8.1-3 shows the principle of these type of actuator, which consist mainly of three parts: a main body, a piezo actuator and an inertial mass. Only the main body is in contact with the surface and to make a step, the actuator goes through two phases:

i. The piezo actuator slowly increases until the end of the first part of a sawtooth input signal. With it, the inertial mass is moved while the main body remains in the same position due to friction force with the contact surface.

ii. The fast decrease of the electric signal causes a sudden contraction of the piezoelectric generating an inertial force. Because of this, the main body acquires a momentum that overcomes the static friction with the contact surface and so, the actuator moves one step forward.

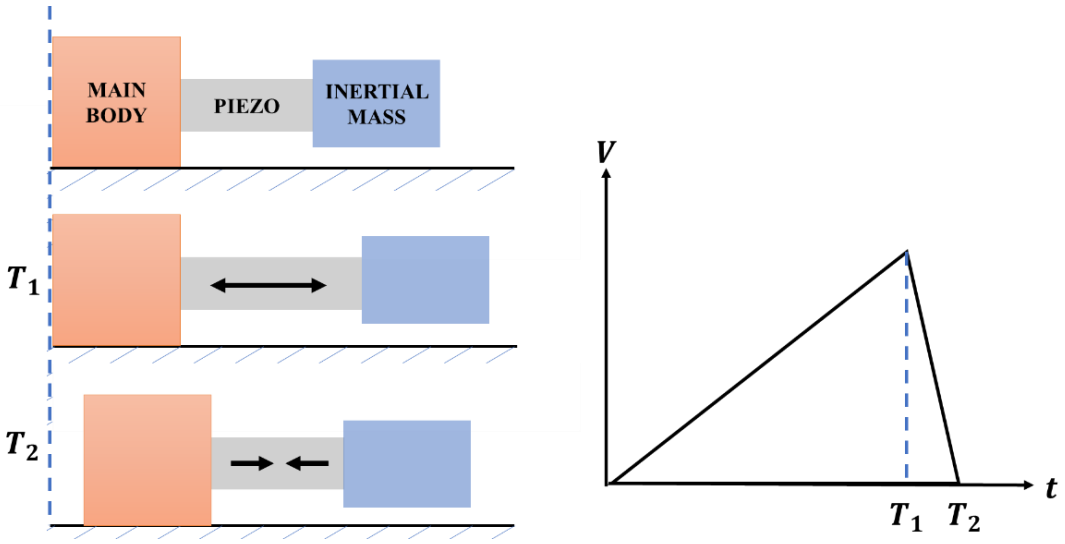

Figure II.8.1-3. Inertial type piezoelectric motor.

The piezoelectric cannot move the main body by itself and of course, for the movement to occur, the inertial mass must be large so the transmission of inertia to the main body is effective enough to overcome its static friction. It is possible to use externally amplified piezoactuators to enlarge the step size of inertial motors.

A good example of this is the actuator designed by Cedrat Technologies for which, instead of using a piezo stack, the inertia is generated by an amplified piezo actuator (APA). As explained before, there is a phase of slow contraction of the APA which moves the mass, before a phase of fast expansion where the mass stands still and the inertia is transmitted to the rod, enough to displace it by overcoming the friction between it and the clamp [43]. As seen in Figure II.8.1-4, this architecture offers great miniaturization possibilities.

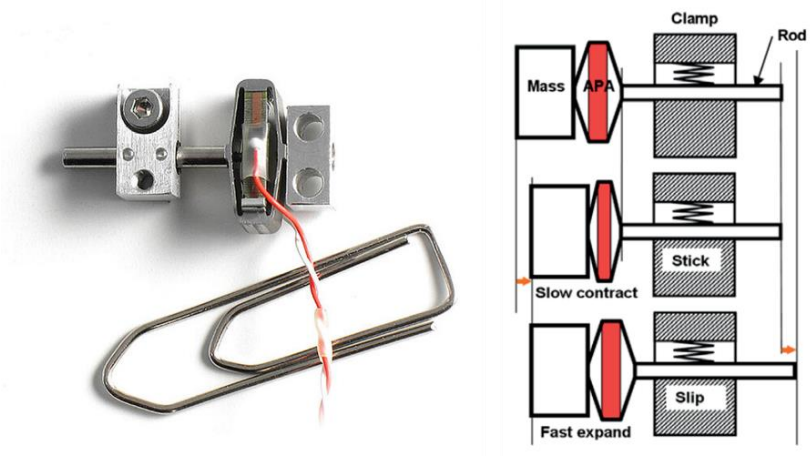

Figure II.8.1-4. CEDRAT ® Inertial motor.

ii. Friction drive type

Starting from an impact drive actuator, Yoshida et al. modified the architecture by replacing the inertial mass with a friction interface and putting in it in contact with a moving element by means of a preload mechanism [44](Figure II.8.1-5).

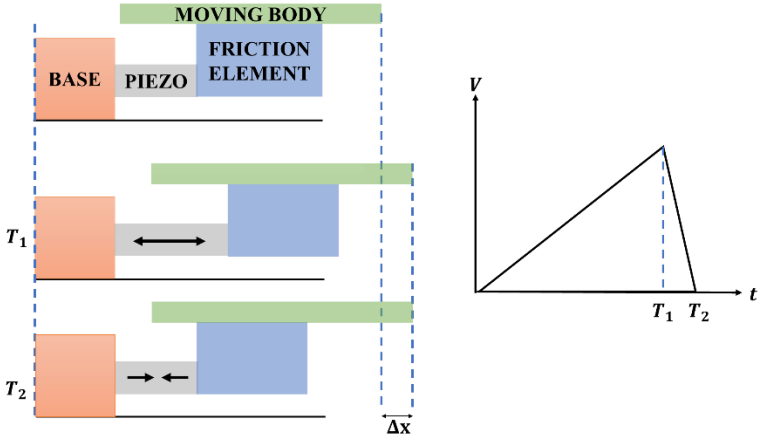

Figure II.8.1-5. Friction type piezoelectric motor.

Also based on a sawtooth electric signal, the first phase of the movement is based on a slowly applied frictional force that moves forward the moving body. At T_1 the piezo shrinks very fast and due to its inertia, the moving element is not able to follow the friction element maintaining its position thanks to its inertia, and as result, a step Δx is accomplished. By continuously repeating these two phases, the whole length of the moving body can be travelled.

Again, it is possible to use a leveraged compliant actuator as input. By using a system of a threaded jaw clamped on a precision screw (Figure II.8.1-6) it is possible to generate high precision motion by friction and obtain force amplification at the expense of velocity compared to a linear slider [45]: slow piezo movement will make the screw to rotate due to static friction (phase I on the figure) and because the screw's inertia, it will hold its position when a fast electric signal makes the piezoelectric to recover its form (phase II) [46]. These mechanisms are found on actuators designed by PI and Newport ® and show practical use on optical positioning when using a high pitch screw.

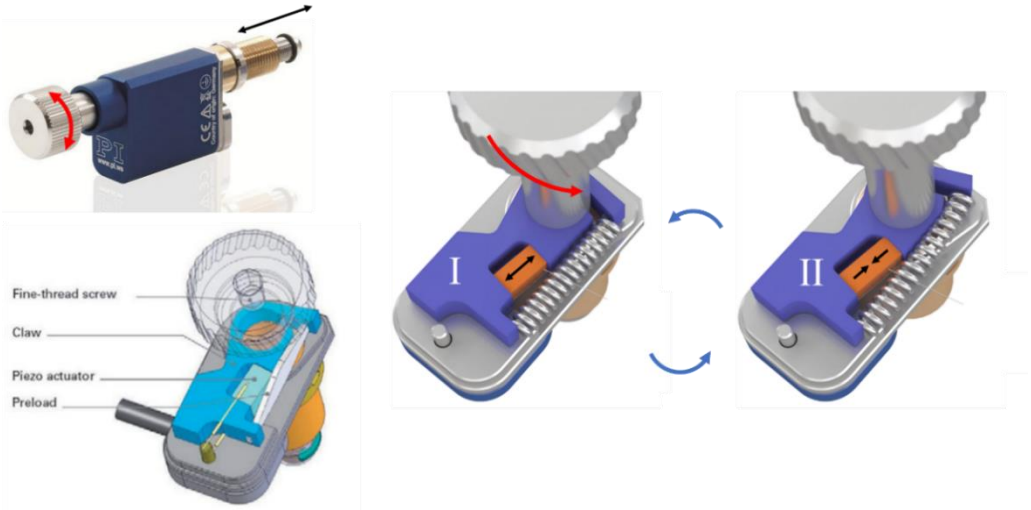

Figure II.8.1-6. PI friction linear motor [47].

II.8.2. Ultrasonic Motors

Even if there is a tremendous diversity in ultrasonic motors (USM), and that they can be classified based on different criteria (see Table II.8.2-1), two characteristics remain constant in ultrasonic piezoelectric motors. They are, the use of a piezoelectric body in a resonant mode at ultrasonic frequency (>20 kHz) and the macro-output movement of the rotor is the result of moment transmission, by friction, of micro-steps of the stator. As USM are based on the vibration modes of a continuous body, the shape and volume of it, is strictly related to the design of the actuator. The large number of different eigenmodes for a given geometry, the possibility to combine modes of vibration and how the frictional contact is done explain why it may be difficult to categorize all USM upon just one criterion [48]. Nevertheless, it is important, for every USM, to have a clear vision about:

- The number of vibrating bodies.
- Which modes of vibration are excited.
- The number of driving signals.
- The method of change of direction (frequency, phase, or excited part).

Table II.8.2-1. Piezoelectric ultrasonic motors classification.

Classification criteria	**Type**
Wave propagation method	Traveling or standing wave
Movement output	Rotary or linear
Degree of freedom	Single or multi-degree of freedom
Geometry of the stator	Disk, Ring, Bar, Shell

This thesis focuses on the wave propagation method to classify the different architectures.

A. Traveling Wave Ultrasonic Motors (TWUSM)

The motion is the result of a wave that, at all points of the resonant body's surface (the stator), generates an elliptical trajectory as it travels along the material. Because of the friction force, a slider pressed against said surface will experience movement in the opposite direction of the traveling wave.

The most known USM that is based on this principle is the rotary type motor, an example of which is shown in the figure below.

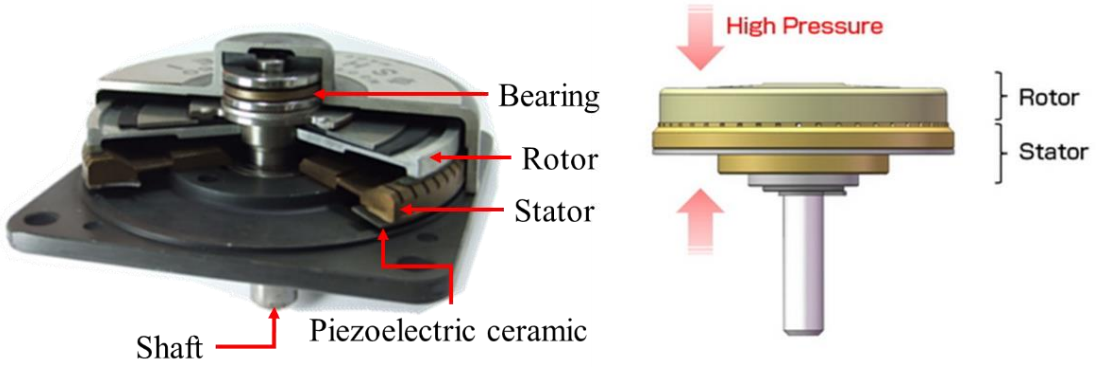

Figure II.8.2-1. Traveling Wave Rotary Ultrasonic Motor (TRUM) from Shinsei® [49].

In this kind of motors, the ring shape stator is composed of an elastic body and a bonded piezoelectric ceramic situated beneath, and a disc shape rotor is pressed against to guarantee permanent contact. Under Kirchhoff assumptions, considering free boundary conditions on the stator, the transverse displacement w of a point in its middle plane is given by

$$w(r,\theta,t) = W(m\theta)\cos(\omega t)\,^{3} \qquad \textit{Eq. II.8.2.1}$$

Which clearly denotes a standing wave of angular frequency ω. Axial symmetry leads to degenerate modes of vibration, which means that for every eigenfrequency it is possible to excite two independent modes of vibration

$$\begin{aligned} W_1(m\theta) &= R(r)\cos(m\theta) \\ W_2(m\theta) &= R(r)\sin(m\theta) \end{aligned} \qquad \textit{Eq. II.8.2.2}$$

Where $R(r)$ is the radial distribution function, $\cos(m\theta)$ and $\sin(m\theta)$ are the distribution functions along the circumferential direction and m denotes the number of nodal diameters.

But it was said that the working principle of this motor is based on the existence of a travelling wave in the stator. For this, the piezoceramic induces two *free* vibrations of the type

$$\begin{aligned} w_1(r,\theta,t) &= AR(r)\cos(m\theta)\cos(\omega t) \\ w_2(r,\theta,t) &= BR(r)\sin(m\theta)\sin(\omega t+\alpha) \end{aligned} \qquad \textit{Eq. II.8.2.3}$$

Adding both we obtain

$$\begin{aligned} w(r,\theta,t) = \frac{1}{2}R(r)[&(A+B\cos\alpha)\cos(m\theta-\omega t)+(A-B\cos\alpha)\cos(m\theta+\omega t) \\ &+2B\sin\alpha\sin m\theta\cos\omega t] \end{aligned} \qquad \textit{Eq. II.8.2.4}$$

Kinematically, the previous expression can be seen as two traveling waves moving on opposite θ directions and one standing wave of amplitude $2B\sin\alpha$. Based in this, the piezoceramic is correctly positioned under the elastic body so the phase difference of the time-dependent term α is zero and both amplitudes A, B are equal. Then, *Eq. II.8.2.4* is reduced to

$$w(r,\theta,t) = AR(r)\cos(m\theta-\omega t) \qquad \textit{Eq. II.8.2.5}$$

And we get our traveling wave moving in the positive θ direction by superimposing two standing waves of the same form, amplitude and frequency. For inversing the direction, a phase difference α of $\pi/2$ is caused. In practice, the piezoelectrics are continuously vibrating since the actual stator does not *freely* vibrate and is transmitting mechanical power to the rotor. The later will move in the direction opposite to the traveling wave, at angular speed Ω given by

$$\Omega = -\omega m\frac{a}{r}\frac{R(r)}{r}$$

Where a is the distance between the surface and the mid plane of the stator.

An example of how the piezoelectrics are arranged under the elastic body is shown in Figure II.8.2-2.

[3] In polar coordinates.

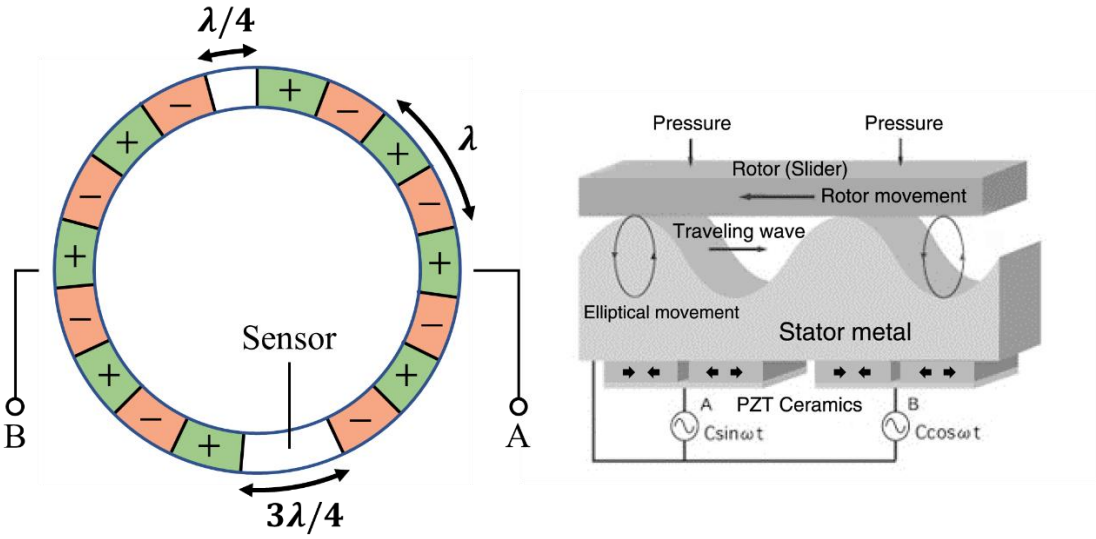

Figure II.8.2-2. Left: Piezoceramic ring detail of a TRUM The signs + and – indicate their direction of polarisation. Right: the rotor (slider) travels in the opposite direction of the traveling wave.

As shown above, the piezoceramic ring consist of two groups of segments A and B separated by a single element that serves as sensor. These two groups are spatially separated one quarter of wavelength λ and this way, the group A of elements excites the cosine degenerated mode while group B excites the sinusoidal degenerated mode (w_1, w_2 in *Eq. II.8.2.3*). Furthermore, the transverse deformation of the elastic body is in fact due to shear stress generated by the piezoceramics operating in d_{31} mode: alternating one positive and negative polarized piezoelectric (green and red in the figure respectively), and in-plane deformation is generated when the respective sinusoidal voltage is applied to group A and B.

Then, segments A and B would each generate a standing wave A_{SW} and B_{SW} given by

$$A_{SW} = C\cos(kx)\sin(\omega t)$$

$$B_{SW} = C\cos\left(kx + \frac{k\lambda}{4}\right)\cos(\omega t)\,;\frac{k\lambda}{4} = \frac{\pi}{2} \qquad \textit{Eq. II.8.2.6}$$

Which is equivalent to the expressions on *Eq. II.8.2.3*, so their interference on the stator would result in the traveling wave AB_{TW}

$$AB_{TW} = Csin(kx - \omega t)$$

The sensor is used to check the temporal phase shift and the amplitude of the input voltages of group A and B.

Traveling waves cannot be generated on a finite length beam under normal circumstances because vibrations are reflected on boundaries and there would be energy transport in two opposite directions. Therefore, linear motors based on traveling waves are not common as it would require a beam-shape stator where the standing waves would have to be generated at one end and absorbed at the other which is not energetically efficient [50]. An example of this is the ring-shape linear motor designed by Kuribayashi et al. [51] and Seeman [52]

B. Standing Wave Ultrasonic Motors (SWUSM)

Contrary to TWUSM, there is only one single point of contact between the stator and the rotor at a time. This point also moves in an elliptical trajectory but not as the result of two standing waves constructively interfering but rather, due to the properly tuned movement of two orthogonal axis. Thus, the output movement is the result of the summation of micro-impulses at a high rate, i.e., ultrasonic frequency.

As standing waves are easily obtained on finite mediums, it is possible to obtain the elliptical trajectory with only one mode of vibration which are known as single-mode motors. On the other hand, it is common when designing SWUSM to obtain the elliptical trajectory as the result of two different modes of vibration, one per axis, and these are referred as bimodal or hybrid motors (HUSM).

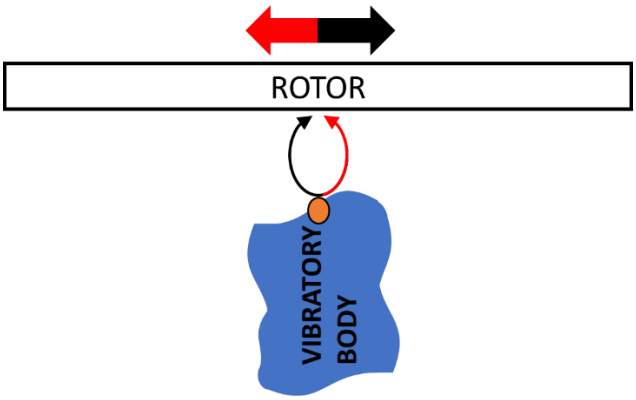

Figure II.8.2-3. Standing Wave Ultrasonic Motors.

Because elastic bodies present infinite natural frequencies, once the applied electric field matches one of them, the body will resonate. Vibration types are defined by the relation between polarization and deformation direction, in accordance with the different modes of actuation of piezoelectric materials mentioned in section II.5 and depicted in the figure below for some typical resonant bodies used as resonators.

LONGITUDINAL VIBRATION		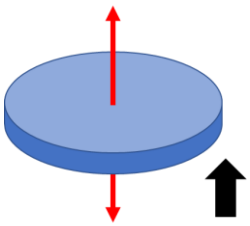	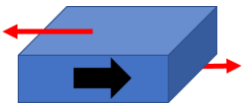
TRANVERSE VIBRATION		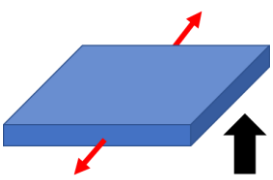	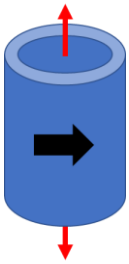

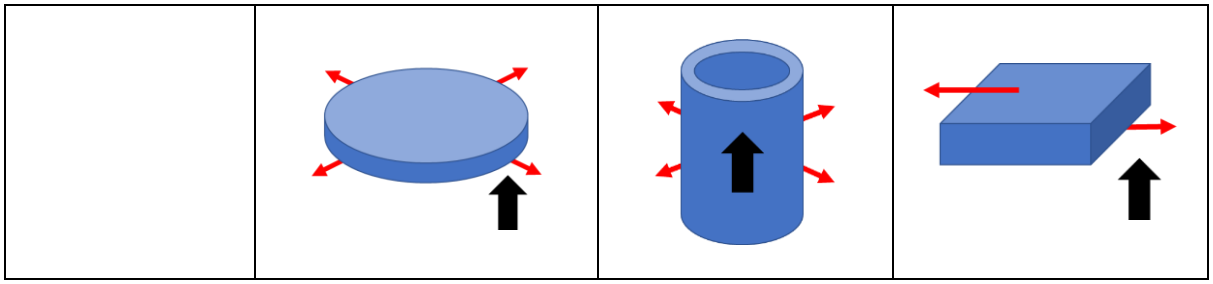

Figure II.8.2-4. Several vibration types observed from some regular vibrators, where the bolt arrow represents the polarization direction and the solid arrows point to the vibrating directions.

If multivibrators are used, like in bimodal motors, then either their orientation or the vibration must be orthogonal, together with a proper phase shift of their respective driving signal, in order to obtain the elliptical motion. A good example of the latter are the motors based on longitudinal vibration (Figure II.8.2-5), as they decomposed the ellipse in a normal and tangential component, each generated by a different vibrator [53].

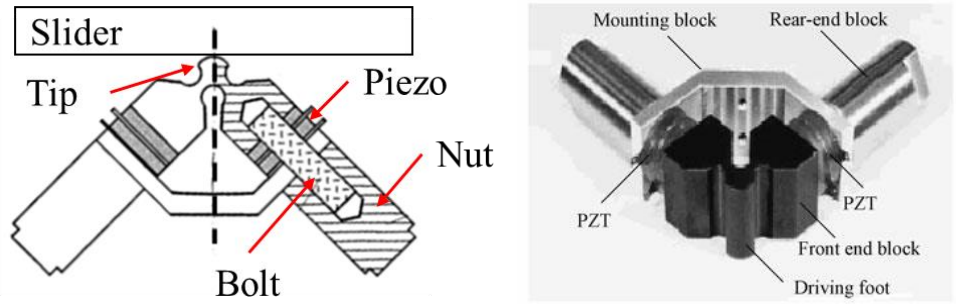

Figure II.8.2-5. Ultrasonic motor based on two longitudinal vibrators designed by Kurosawa et al [54].

Based on the orthogonal arrangement of two separate longitudinal vibrators, each excited to resonance frequency so they generate a normal and a tangential vibration component. The vibrators usually consist of a sandwich type transducer (Langevin) of a bolt-nut system that compress a piezo actuator inserted into the vibrating structure. These systems are known as bolt-clamped.

When the vibrators are in phase, the tip of the transducer moves normal to a driving surface (slider) and movement tangential to the surface is produced when both vibrators are in antiphase. The two vibrators are then driven by two electrical sources of same frequency, tuned to the resonance of the transducer and 90 degrees phase shift so both vibration modes are excited hence generating the elliptical motion of the tip.

The concept designed by Kurosawa et al, inspired a huge quantity of researchers in seek of optimizing the structure of the actuator, the positioning of the vibrators, the material of the tip, stress concentration robustness, etc. For instance, Liu et al designed a high power USM optimizing structural parameters in order to match the frequencies of the two vibration modes, obtaining a no-load speed of 1160 mm/s and a maximum thrust force of 20 N at a voltage of 200 Vrms [55].

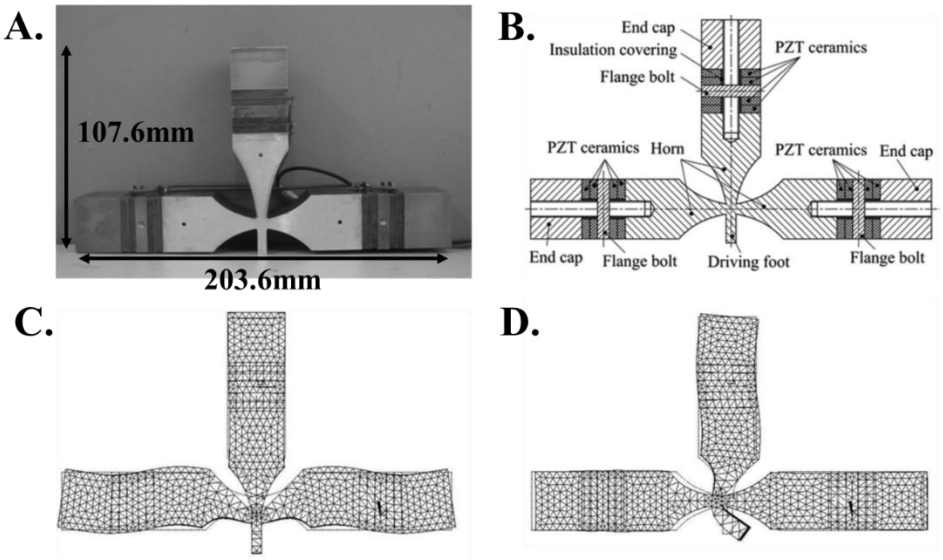

Figure II.8.2-6. Ultrasonic motor by Liu et al [55]. A. The designed actuator. B. Detail on the components. C. First vibration mode for the normal output movement. D. Second vibration mode for the tangential output movement

Given that it is theoretically possible to use any geometry as the vibratory body, exciting at least two orthogonal resonance modes of the stator generates elliptical motion on single vibrators. According to the shape of the stator (see Figure II.8.2-4), a given resonant mode will be more suitable to induce than other.

Excitation of two different groups of electrodes (one at a time) or tuning one single frequency to induce two different orthogonal frequency pair on the structure, are two ways of obtaining the elliptic output characteristic in SWUSM. Hence, degenerated modes obtained from two bending-modes, a longitudinal and bending mode, longitudinal and torsional mode and so on, may be used for obtaining the desired elliptic motion.

Bending USM by Uchino et al. [53]	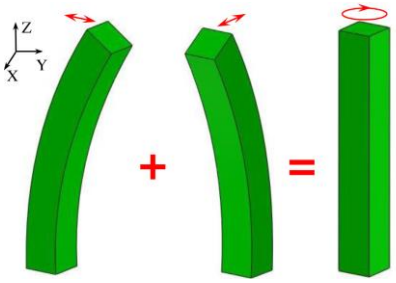	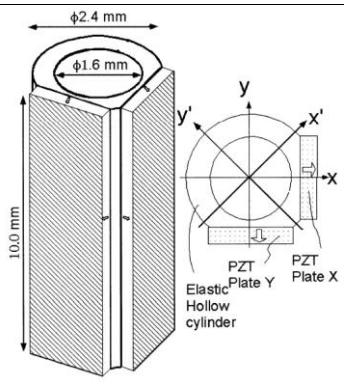
Longitudinal Bending by Nanomotion [56].	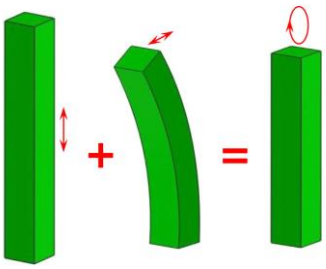	

Longitudinal Torsional by Yang and Zhao [57].	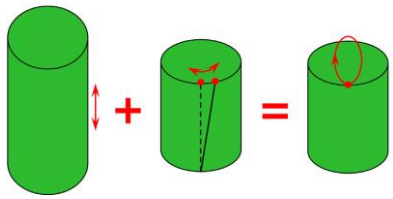	

Figure II.8.2-7. SWUSM based on single vibrators and degenerated modes from two different orthogonal modes.

II.9. Comparison of the performance of different piezoelectric actuator architectures

Because of their tremendous variety, piezoelectric actuators provide a broad range of possibilities, hence the selection of a specific architecture is defined by the application requirements. Regarding their performance, internal and external architectures can be compared regarding their free deflection and their blocked force.

In their research, Mohith et al [17], compared different types of architectures following the aforementioned criteria as shown in Figure II.9-1. Based on their results, we can see that internally amplified actuators, as for instance the stacks, offer higher blocked force at low free deflection while externally amplified actuators develop a higher range of motion and lower blocked force. A compromise is found when stacks are integrated in flexible amplifiers but this reduces the response time and stiffness of the actuators as a whole when compared to the piezoelectric stacks.

On the other hand, free deflection is not a relevant feature when comparing frequency operated actuators and instead, output maximal velocity becomes the feature of interest together with their blocked force. Mohit et al compared three architectures in both linear and rotary configurations and the results show that the inchworm, a clamping drive architecture, are capable of generating higher force and torque but because the complexity of motion (alternately changing between clamping and driving), the output speed is lower than the other two architectures. Ultrasonic motors instead present greater output speeds and lower output force.

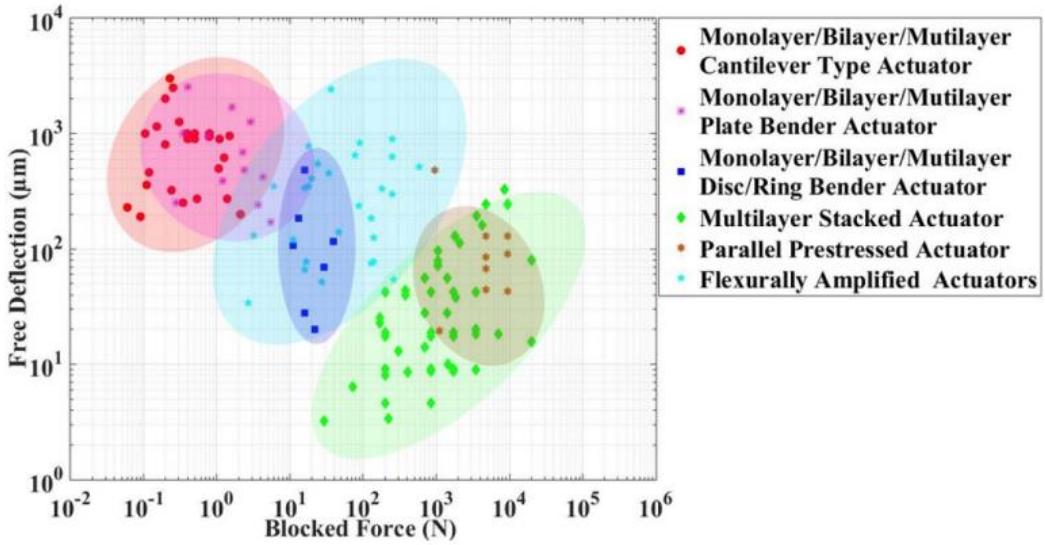

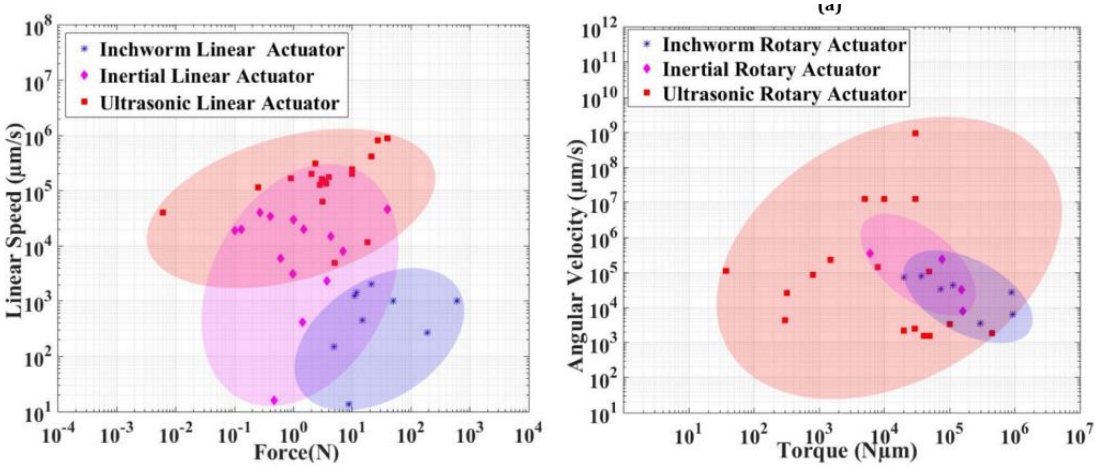

Figure II.9-1. Comparison of different types of the piezoelectric actuators. Plots published by Mohid et al [17].

II.10. Conclusion

The vast diversity in piezoelectric actuation can be divided in three families regarding how the deformation is amplified in order to get more useful displacements. Because there is no trace of the use of piezoelectric materials in leveling applications, it is important to have an overall view of these main architecture families and the subgroups that compose them, before deciding which is the most suitable for the scope of the thesis objective.

We add some examples so the reader can see some practical uses of these architectures, some of them are even found on a more industrial level, as it is the case of PI® and Cedrat®, that commercialize different piezoelectric actuators based on standard architectures reviewed along this chapter.

From this, we can do a conscious choice and justify it based on the advantages and drawbacks that every architecture exhibits. This will be presented in the next chapter.

III. DESIGN OF THE ACTUATOR

III.1. Introduction and application requirements

In this application, the final desired movement is a rotative one. Today's leveling is achieved by producing a torque with a linear actuator that pushes the lighting module at a certain distance of a pivot point as shown in Figure III.1-1.

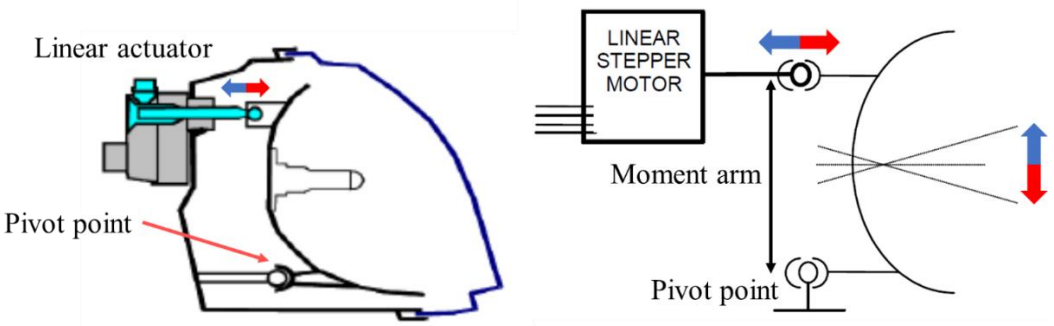

Figure III.1-1. Leveling by means of linear actuators.

Current levellers have a stroke of 8 to 10mm at about 70 to 80mm of moment arm hence, as shown in Figure III.1-1, the total angle is given by

$$\tan^{-1}\left(\frac{linear\ stroke}{moment\ arm}\right) \approx 7°$$

Table III.1-1 highlights some Externally Leveraged Piezoelectric actuators (ELP) and their characteristics. Although these actuators present great amplification ratio, loss of stiffness and low resonant frequency appears as a tradeoff. Besides, getting a millimetric stroke implies the use of both a large piezoelectric stack together with big compliant structures, as piezo stacks maximal displacement is around 0.1% the value of their length.

Knowing that the characteristic stroke of ELPs is only of hundreds of micrometers, replacing current linear actuators with an ELPs that pushes and pulls the projector around a pivot point is not suitable as these actuators have a trade-off between amplification ratio and size, that is, the more the amplification needed for a same input, the bigger footprint of the amplification structure. A 7° movement would require an ELP too big to fit in as well as the use of high voltage sources for operating the piezo stack.

In this thesis, a new concept for leveling is proposed, and instead of a linear output we decided to design a rotary actuator that directly operates on the rotation axis. This decision seeks not only to reduce the space needed for a leveller to operate but also to avoid the use of gear box as it affects the accuracy. As the application addresses a rotary motion, the moment of inertia of the projector is a variable of interest more representative than the mass itself. Nevertheless, projectors are a part of the vehicle that varies among car makers and even differs from model to model. As the moment of inertia depends on both the mass and its distribution when rotating about a given axis, it is difficult to set a specific value of moment inertia that remains true for every projector. For this reason, in order to simplify this study, we take a parallelepiped of 0.5 kg that rotates around an axis parallel to an axis through the center of mass at a distance d as a representative body of the projector. The distance d can be thought of as the contribution of the asymmetry and use of different materials to the moment of inertia of the projector I (Figure III.1-2).

Table III.1-1. ELPs

Author	Year	Reference	ELP Architecture	Stack dimension (mm^3)	Operation Voltage (V)	Stack's stroke (µm)	Amplification ratio	Actuator stroke (µm)	Actuator size (mm^3)	Application
CEDRAT APA 1000XL		[58]	Flextensional		-20 - 150			990	214x57x25	
PI P-621		[59]	Flextensional					500	60x32x16	
Ling et al.	2019	[60]	Rhombus	36x10x10	0 - 120	38	32	1250	160x160	XY Stage
Dsouza	2018	[61]	Lever	20x5x5	0 - 160	10	7.8	78	50	
Pant et al.	2015	[62]	Cymbal	18x10x10	1400	17.3	4.6	160	65x30x12	
Haller et al.	2011	[63]	Cymbal		0 - 150			65	50x30	Control of airfoils
Muraoka, Sanada	2010	[64]	Honeycomb	40x5x5	0 - 150	41	10	410	55x13	XY Stage

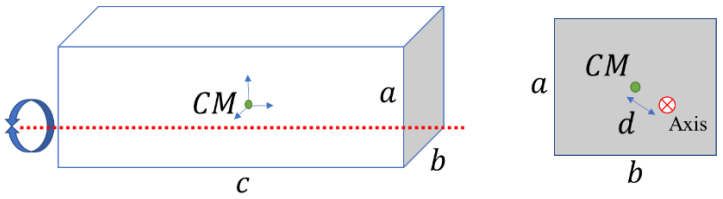

Figure III.1-2. Required moment of inertia is supposed as a parallelepiped that turns around an axis at a distance d of its center of mass.

$$I_{Axis} = \frac{M}{12}(a^2 + b^2 + 12d^2) \qquad \textit{Eq. III.1.1}$$

Hence based in the knowledge of AML Systems, the requirements the actuator must satisfy are:

- Operational range $\pm 10°$
- Maximal velocity $10°/s$
- Temperature range $-40°C$ to $105°C$
- Precision 0.05°
- Moment of inertia 0.8 $g.m^2$
- Operational voltage < 20V

III.2. The proposed actuator architecture

To achieve this, the architecture proposed in this thesis is shown in Figure III.2-1. Because the desired output is rotational, the leveller consists in a proper stator-rotor configuration driven by a piezoelectric actuator, the electronic driver and a motion controller with a closed loop angular position signal measured by an encoder.

Piezoelectric actuators present several nonlinearities and hysteresis proper to the piezoelectric materials. Besides, output characteristics of the actuator vary according to temperature, prestress, exciting frequency, etc., which for high precision applications, makes difficult their operation in open loop. In general, closed loop is often used to fully exploit the potential of piezoelectric materials, and with this, control of position, velocity or torque is necessary to operate the actuator.

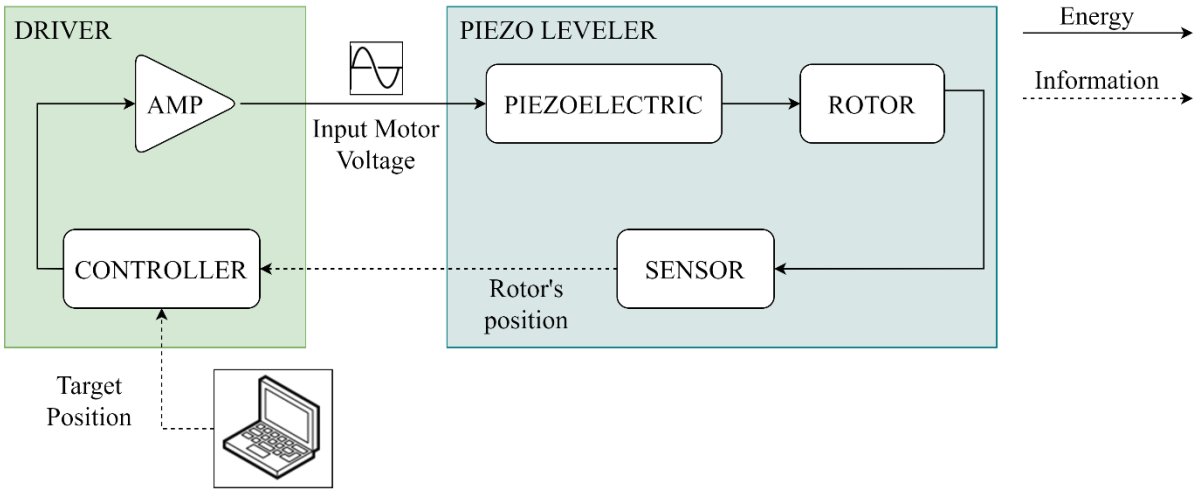

Figure III.2-1. Architecture of the motion solution proposed in this research.

A target position is defined and the controller adjusts the control signal based on the target position and the position feedback of the rotor, the position of the latter being constantly measured by the sensor. The control signal is applied to the amplifier which in turn applies the proper voltage to the piezoelectric material which ultimately causes the rotor to move with a minimal error between the desired and the actual angular position. The position error of course depends on the actuator and the sensor resolution, the controller bandwidth, etc. [65]

In this thesis, we exclusively focused on the design of the leveller, which also includes the selection of an adequate piezoelectric actuator among the architectures seen in chapter II and the integration of an existing piezoelectric actuator, the goal and market strategy for AML Systems being the design of complete motion solutions and not the fabrication of piezoelectrics.

This chapter continues with the choice of the piezoelectric architecture in III.3, the design of the piezoelectric actuator after selection in III.4 and its use as the core of a leveling actuator III.5.

III.3. Choice of Piezoelectric architecture

$\pm 10°$ is a large enough displacement to avoid the use of some piezoelectric architectures because, in order to get such a displacement, the size of the actuator would not be suitable for the application. Such is the case for internally and externally leveraged architectures.

The use of a frequency leveraged piezo actuator presents reasonable advantages when a considerable high stroke is needed as these kind of actuators are only limited by the size of the guide they are moving on. Their inherent power-off break becomes useful for maintaining a position with no energy consumption. Based on the two types of motor architectures of section II.8, ultrasonic motors present a broader range of velocity when compared with piezo steppers which in turn tend to present higher output force. As velocity and response time are key characteristics for leveling application, the use of an ultrasonic motor is adequate given that stationary behavior is achieved in several milliseconds and brake even faster due to the frictional contact between the stator and the rotor [66].

Ultrasonic motors can be compact due to the possibility to dismiss a gear box which also reduces vibrations caused by transmission mechanisms, ultimately resulting in accuracy positioning improvement. Besides this, the high variety in terms of resonant body to use and the frequency modes to be excited have led to a wide variety of motor designs, some of which are mentioned in Table III.3-1 along their main features. From a theoretical point of view, it is not designing the geometry of the resonant body but being able to excite modes of vibration which lies as the most important thing to do. Still simple geometries such as rings, beams, discs or plates are preferred for the USM stator in order to simplify their polarization, electrode location, assembly and miniaturization possibilities.

As seen in chapter II, Traveling Wave Ultrasonic Motors (TWUSM) generate an elliptical movement on the stator's surface when a traveling wave propagates through it as a result of two standing waves properly excited. To get such a wave on a rod-type structure is difficult because the side effects caused by the wave reflection on both ends of the body, hence TWUSM tend to use a disc or a cylinder as vibrator and so, they are more suitable as rotary motors.

On the other hand, Standing Wave Ultrasonic Motors (SWUSM) are shape independent, which results in a greater variety of structures to use as vibrator body and hence rotary or linear output only depends on whether if a rotor or a slider is in contact with it. Bidirectional movement is obtained by either:

- Exciting a single different mode of vibration for each sense of movement. This can be achieved by variating the frequency of the exciting signal, or the activation of a particular subgroup of electrodes. These motors are known as Single Mode motors.

- Based in Lissajous curve theory, inverting the phase difference δ of two perpendicular oscillations ϕ_1, ϕ_2 that are in superposition. This working principle has been applied in many SWUSM, often called Hybrid Ultrasonic Motors (HUSM) as they are characterized by the use of two modes of vibration, for example, by combining two first order longitudinal modes that are perpendicular to each other, or by the coupling of a longitudinal vibration mode with either a bending vibration or a torsional vibration mode [67].

We decided to design a leveller actuator based on the use of a HUSM because the output speed can be controlled by voltage amplitude. Besides it presents similar motion characteristics in forward and

backward directions contrary to single mode SWUSM and their structure being simpler than a TWUSM, might lead to future prototypes more compact and easier to integrate.

Because they involve two different modes, HUSM need that both resonant frequencies are as close as possible so a given point on the vibrating body exhibits elliptical motion as efficiently as possible. Such a point will afterward be used as the contact point with the rotor. By means of Finite Element Method (FEM), sensitivity analysis is carried out so that the relation between modes of vibration and a set of structural parameters can be obtained, which seeks to answer the question about which parameters have the most influence on the resonant frequency of a particular mode. Modal analysis allows to obtain the values of resonant frequency and the parameters are adjusted in an iterative process that ends when both calculated values of frequency are close enough, leading to a phase of prototyping. Because stator modeling is often idealized during the design process, together with the errors due to its fabrication, the actual modal frequencies of the vibrator deviate from the calculated and a final tuning is necessary. For this reason, a set of geometric parameters is chosen as design variables whereas the material properties are preferred to be fixed since the beginning, as it is easier to deal with dimension adaptations than material properties in this prototyping phase. By using Doppler laser vibrometer or impedance analyzer, the modal frequencies of the prototype are experimentally measured and thanks to the sensitivity analysis, it is possible to know which geometric parameter slightly adjust, usually by griding. The previous design methodology (Figure III.3-1) has been applied to address different problems, as it is configuration synthesis, which often results on novel stator geometries; or stator geometry optimization [68].

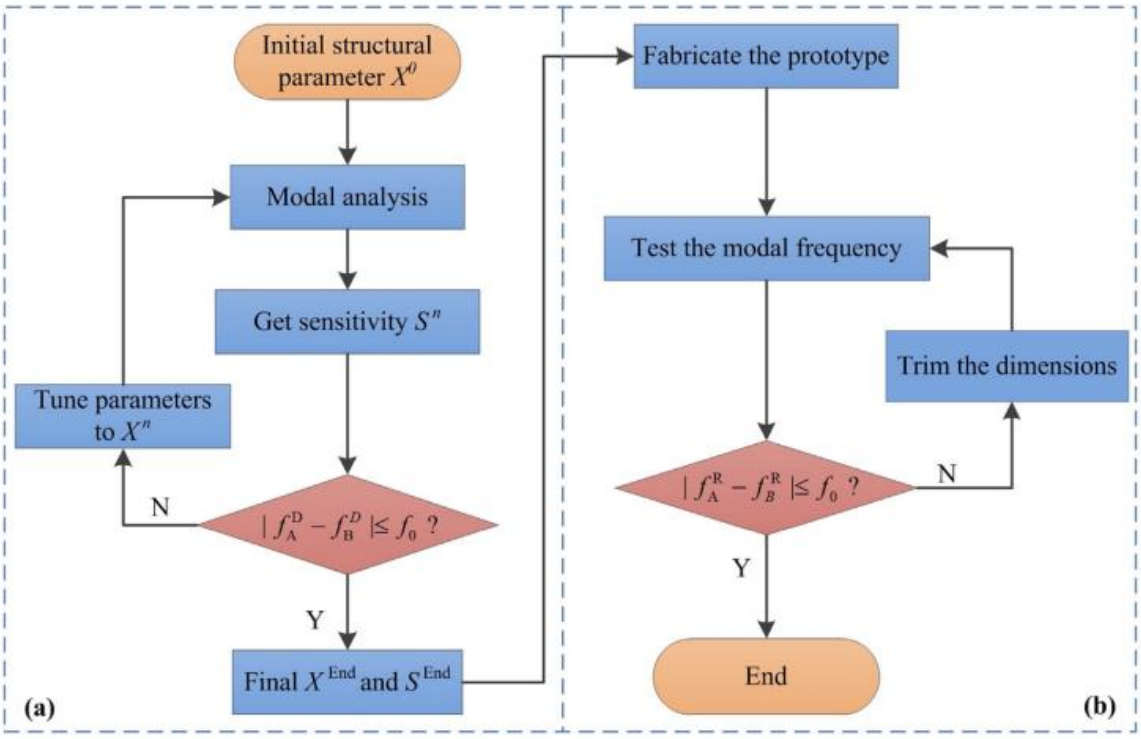

Figure III.3-1. Ultrasonic motors design methodology [69].

Table III.3-1. Details of different ultrasonic piezoelectric motors.

Manufacturer/ Researcher	Reference	Year	Type	Vibrating Body	Modes of vibration	Output Motion	Size (mm)	Max. Voltage	Max. Speed	Max. Force/ Torque
Shinsei	[70]		Traveling Wave	Disc	Axial bending	Rotary	30×40×25*	110V RMS	300 RPM	100 mN.m
PI	[71], [72]		Standing Wave	Plate		Linear	35×14×6*	42V RMS	500 mm/s	2 N
Nanomotion EDGE4X	[73]		Hybrid Modes	Beam	Longitudinal - Bending	Linear	23×12×4*	14V RMS	180 mm/s	1.3 N
Squiggle	[74]		Hybrid Modes	Hollow cylinder	Bending - Bending	Linear	3×3×6	3.3V	<18 mm/s	<0.6 N
Zhang et al	[75]	2021	Hybrid Modes	Beam	Longitudinal - Bending	Linear	3.93×1.63×1.12	20V P-P	81 mm/s	56 mN
Lu et al	[76]	2020	Single mode	Beam	Bending	Linear	28×10×5	300 V	120 mm/s	0.85 N
Wang et al	[77]	2019	Traveling Wave	Disc		Rotary		152 V	112 RPM	780 mN.m
Izuhara and Mashimo	[78]	2018	Hybrid Modes	Hollow cuboid	Longitudinal - Longitudinal	Linear	2.6×2.6×2.2	150V P-P	140mm/s	20mN
Dabbagh et al	[79]	2017	Hybrid Modes	Beam	Bending - Bending	Rotary	49×14×2	50 V	122 RPM	0.32 mN.m
Liu et al	[80]	2016	Hybrid Modes	Beam	Bending - Bending	Rotary	53×12.8×10	100V RMS	158 RPM	53 mN.m
Zhou and Yao	[81]	2014	Hybrid Modes	PG**	Longitudinal - Longitudinal	Linear	130×88×12*	200V P-P	430 mm/s	47 N
Park and He	[82]	2012	Hybrid Modes	Square tube	Bending - Bending	Rotary	3.975×3.975×16	50 V	1000 RPM	370 µN.m
Shi and Zhao	[83]	2011	Hybrid Modes	Beam	Longitudinal - Bending	Linear	55×26×14	400V P-P	98 mm/s	3.2 N
Wang et al	[84]	2010	Hybrid Modes	PG**	In plane modes	Linear		200V P-P	245 mm/s	1.6 N
Vyshnevskyy et al	[85]	2005	Hybrid Modes	Hollow cylinder	Longitudinal - Bending	Rotary	Φ20×20	15V RMS	400 RPM	40 mN.m

* Size of the overall actuator.

** Particular vibrator geometry.

Although HUSM based on longitudinal modes can achieve several tens of newtons, their use is problematic for leveling application as they tend to have more complex structures and relatively larger sizes compared to other hybrid configurations. In contrast, motors based in longitudinal and bending modes (LB motors) bring particular interest from the industrial point of view and among them, the ones based on a rectangular plate vibrator are popular due to the advantages such as simple structure which simplifies fabrication, assembly and miniaturization [86]. Even though it exists a certain variance between LB rectangular motors, regarding which modes to excite, the positioning of the driving tip, the piezoelectric mode of actuation, etc., we encounter several characteristics that are usually find on this particular kind of motor:

1. One mode of vibration is in charge of exerting the normal force and the other is used for pushing the load.

2. There is a plane where nodes of both modes overlap so support elements, needed for clamping the stator and providing the pre-stress force, can be positioned all by reducing their influence on the modes of vibration.

3. The driving tip is usually located near a wave crest of one of the modes.

4. Excitation of the vibrator is achieved by the action of forces applied in accordance with the mode shape that is pretended to be generated.

Among the motors described in Table III.3-1, the EDGE4X motor is a motor that brings special interest to AML SYSTEMS for the leveling application and has been chosen as the USM of this research, as it is already manufactured and commercialized by Nanomotion®, and in seek of maximizing industrial advantages, is well suited for production possibilities [87]. As shown in Figure III.3-2, the operational point is computed after the requirements of moment of inertia and angular speed (defined in section III.1) and plotted in the performance curve of the EDGE4X motor as presented in the datasheet [73]. As the point lays inside the area delimited by the line of no-load angular speed and the blocking torque, the power required for the application is satisfied by this ultrasonic motor.

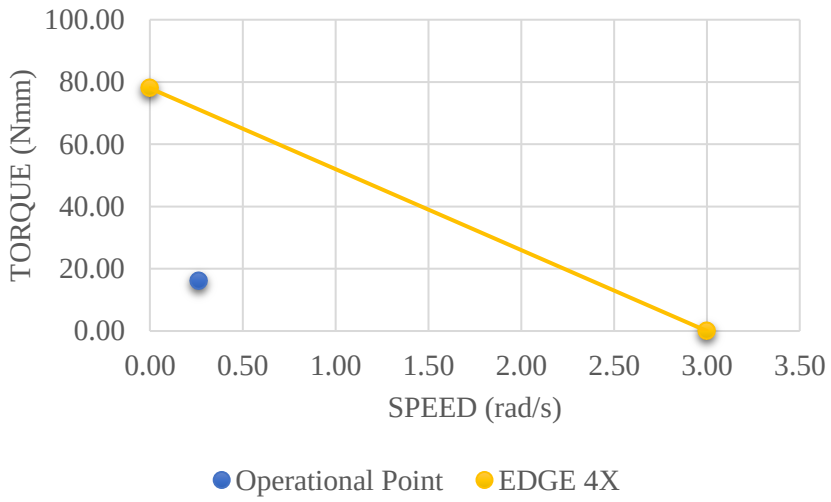

Figure III.3-2. Performance of the EDGE4X Nanomotion motor and the point of operation of the application.

III.4. The piezoelectric motor

For the leveling actuator, we actually chose the vibrating body of the EDGE4X motor for creating our rotational output concept. The vibrating body is placed within a frame that clamps it and allows the positioning of several springs, which in turn apply preload, needed for the motor to operate, as well as preventing the ceramic to break. The output movement of the actuator is achieved thanks to the transmission of force by friction between a bonded tip in one end of the vibrating body in contact with a friction interface.

Further aspects concerning the USM elements are discussed next, before dealing with the whole actuator design.

III.4.1. The vibrating body

The vibrating body is a parallelepiped 15×4×2 mm beam made of lead zirconate titanate $PbZr_xTi_{1-x}O_3$, one of the most widely used piezoelectric ceramic materials. With the objective of understanding how the vibrating body would be supported and to model and simulate the behavior of the actuator in the next chapters, we were interested in knowing which modes of vibration are excited and for this we used Finite Element Simulation on COMSOL®. Since the exact PZT material properties are not communicated by Nanomotion company, we assumed PZT5A material for running the simulation and we considered the beam under free-free constraints. Then, we obtained the contours of displacement and the respective eigenfrequencies for the first several modes above 20kHz bringing special interest the 800Hz gap between the first longitudinal mode (L1) and the second bending mode (B2). Even though this simulation is not a perfect description of the vibrating body as the actual ceramic is not an ideal parallelepiped and the exact PZT material properties values may deviate from the simulated ones, the results are accurate enough to conclude that the EDGE4X is based on the combination of the first longitudinal and second bending modes (L1B2 motor). An instant of both modes is shown in Figure III.4-1.

The low voltage operation of this motor (14V RMS) is possible thanks to the multilayer structure of the ceramic. Several researches have shown that it is possible to create USM based on multilayer structures, and when compared with a bulk ceramic of the same dimensions, driving voltage is much lower at the expense of a greater heat productivity [88], [89], [90], [91].

A schema of the structure of the vibrator in the EDGE4X is shown in Figure III.4-2. It consists in a stack of 11 layers of piezoelectric material, colored in gray, each one positioned between two planes of electrodes in a pattern such that upside and downside polarization layers are intercalated. We distinguish five different electrodes: the ground electrode, colored in black, which covers almost completely one side of the PZT layer, and the remaining four covering the opposite side. These four electrodes are disposed in four quadrants, separated in two independent groups I and II, differentiated by colors green and red in Figure III.4-1 and Figure III.4-2. When AC voltage with the correct value of frequency f_{res}, is applied to group I while keeping II disabled, piezoelectric layers being polarized in the z direction will undergo deformation on the XY plane and L1 and B2 in-plane modes are excited, and consequently, the driving tip will experience elliptical movement. In an analogous way, when group II is activated, the sense of movement is inverted so bidirectional output is possible with one single signal. In this case, the motor operates in the d_{31} mode which compared to d_{33} L1B2 motors, it presents a more compact and simple structure which facilitates miniaturization at the expense of less thrust because electro-mechanical transformation efficiency is lower for the d_{31} effect [92].

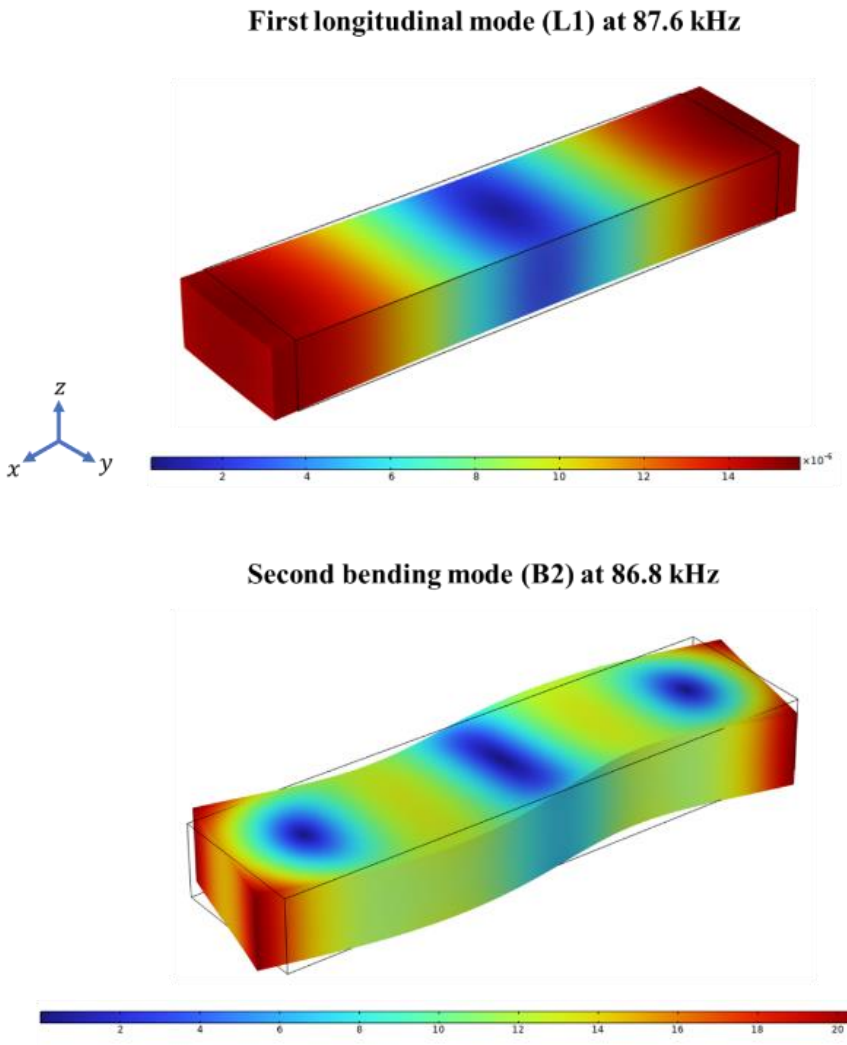

Figure III.4-1. Contours of displacement of the EDGE4X beam.

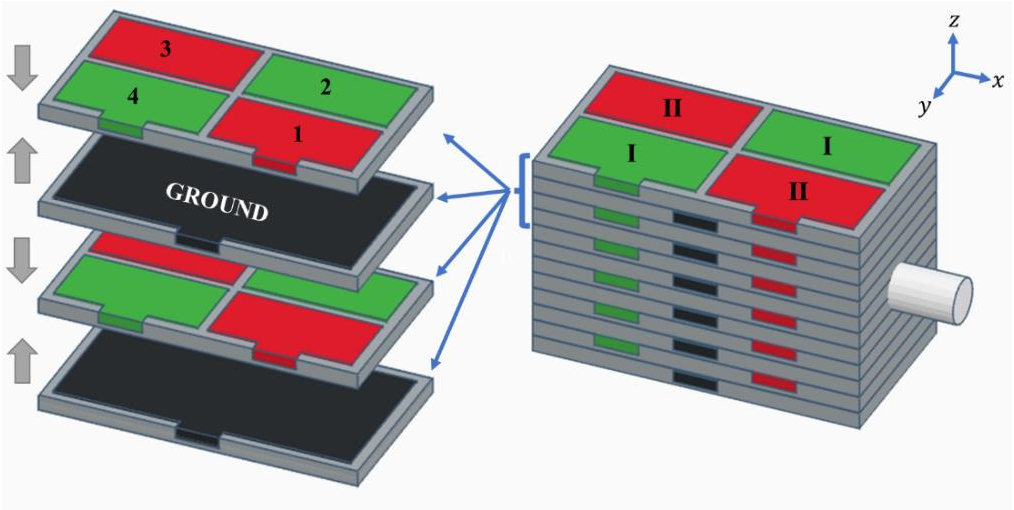

Figure III.4-2. Schema of the structure of the vibrating body.

All groups of electrodes of the different layers must be connected to each other so each electrode possesses a small rib that extends until one side of the ceramic. Once stacked, all the ribs of a same group are interconnected by means of a conductive coating. This can be appreciated in figure Figure III.4-3 where the coating of group I and ground electrodes has been peel off so their respective ribs can be appreciated with a Leica M205C.

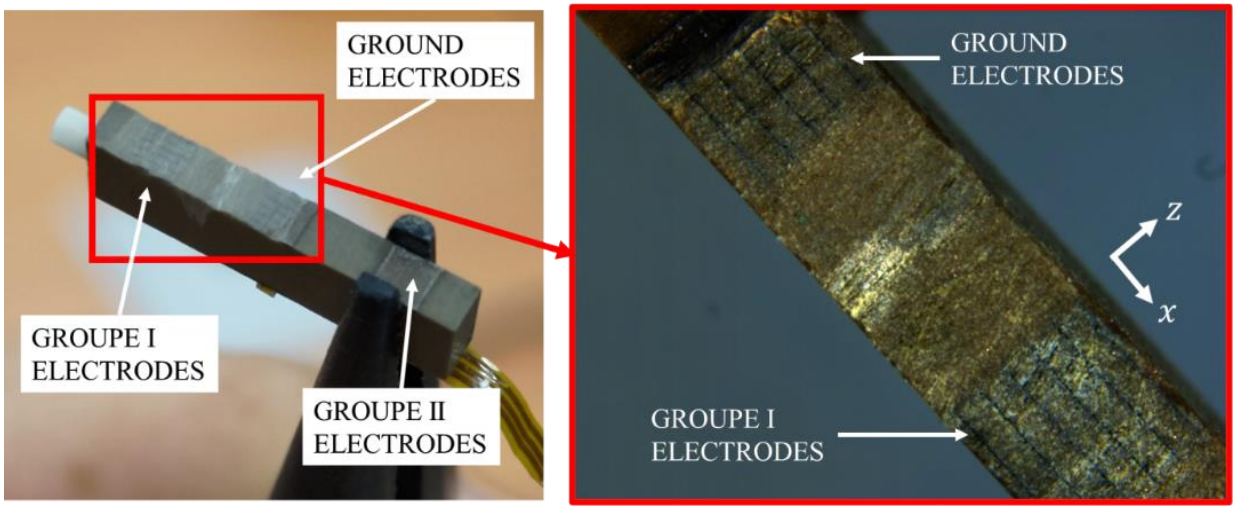

Figure III.4-3. Macroscopic image of the multilayered piezoelectric vibrating body of the motor.

III.4.2. The driving tip

Ultrasonic motors are characterized by two stages of energy conversion, the first one being the generation of vibration mode shapes thanks to the piezoelectric effect and the second one about how this vibration energy on the vibrating body is transmitted to the load by means of friction contact between the stator and the rotor. This last conversion requires stable and relatively high friction force at the contact interface, hence high wear resistance materials are mostly used in order to avoid changes in the contact condition between the stator and the rotor which ultimately leads to losses on accuracy and lifespan of the actuator [66]. In our case, the driving tip is made of alumina Al_2O_3 which typically is selected due to its combination of high hardness, inertness, low wear rate and a relatively high coefficient of friction [93].

In Figure III.4-4, normalized displacement amplitudes of both L1 and B2 modes are plotted against the normalized length. When group I electrodes is excited, both modes of deformation make the end of the vibrator to undergo negative deformation along the x axis while deformation is negative along the y axis and a clockwise movement is generated in the rotor. On the other hand, activation of group II electrodes causes the B2 mode to be reversed in phase causing the rotor to turn in clockwise direction.

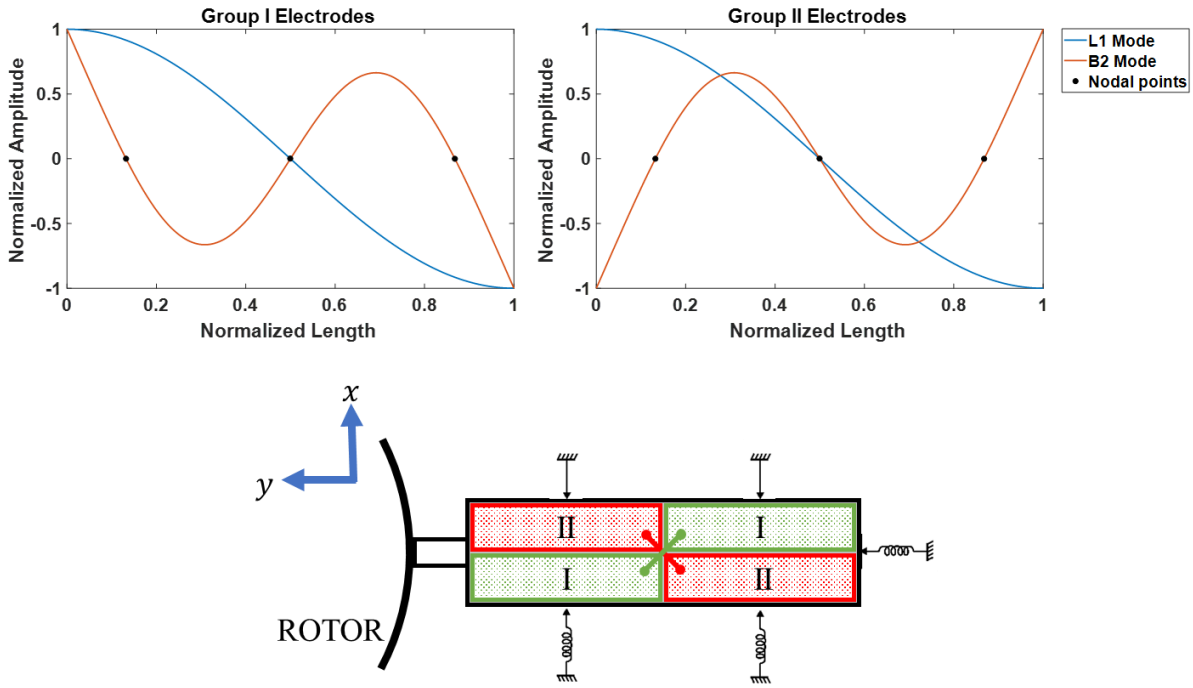

Figure III.4-4. Normalized displacement of L1 and B2 mode of the vibrating body.

The driving tip is conveniently placed in this position, a location that yields an elliptical trajectory with the greatest longitudinal deformation amplitude. This choice is also related to how the vibrating body contacts the stator at different moments of a vibrating period, corresponding to which mode exerts a normal force needed to support the load and a tangential force that impulses the load. In our actuator, L1 mode is the vibration component of the elliptical motion that is perpendicular to the moving direction of the rotor, and it changes the normal force between the rotor and the hard tip periodically while B2 mode is the vibration component parallel to the moving direction of the runner and it pushes the runner with the friction force.

If a sinusoidal voltage of frequency f_{res} is applied to group I, the x and y components of the elliptical movement can be described by

$$x(t) = \phi_{B2} \sin 2\pi f_{res} t$$
$$y(t) = \phi_{L1} \sin 2\pi f_{res} t \qquad \textit{Eq. III.4.1}$$

Where ϕ_{L1} and ϕ_{B2} are the amplitudes of the L1 and B2 modes excited on the vibrator. Considering Figure III.4-5, the cycle of movement is decomposed in four fractions of the period $T = 1/f_{res}$

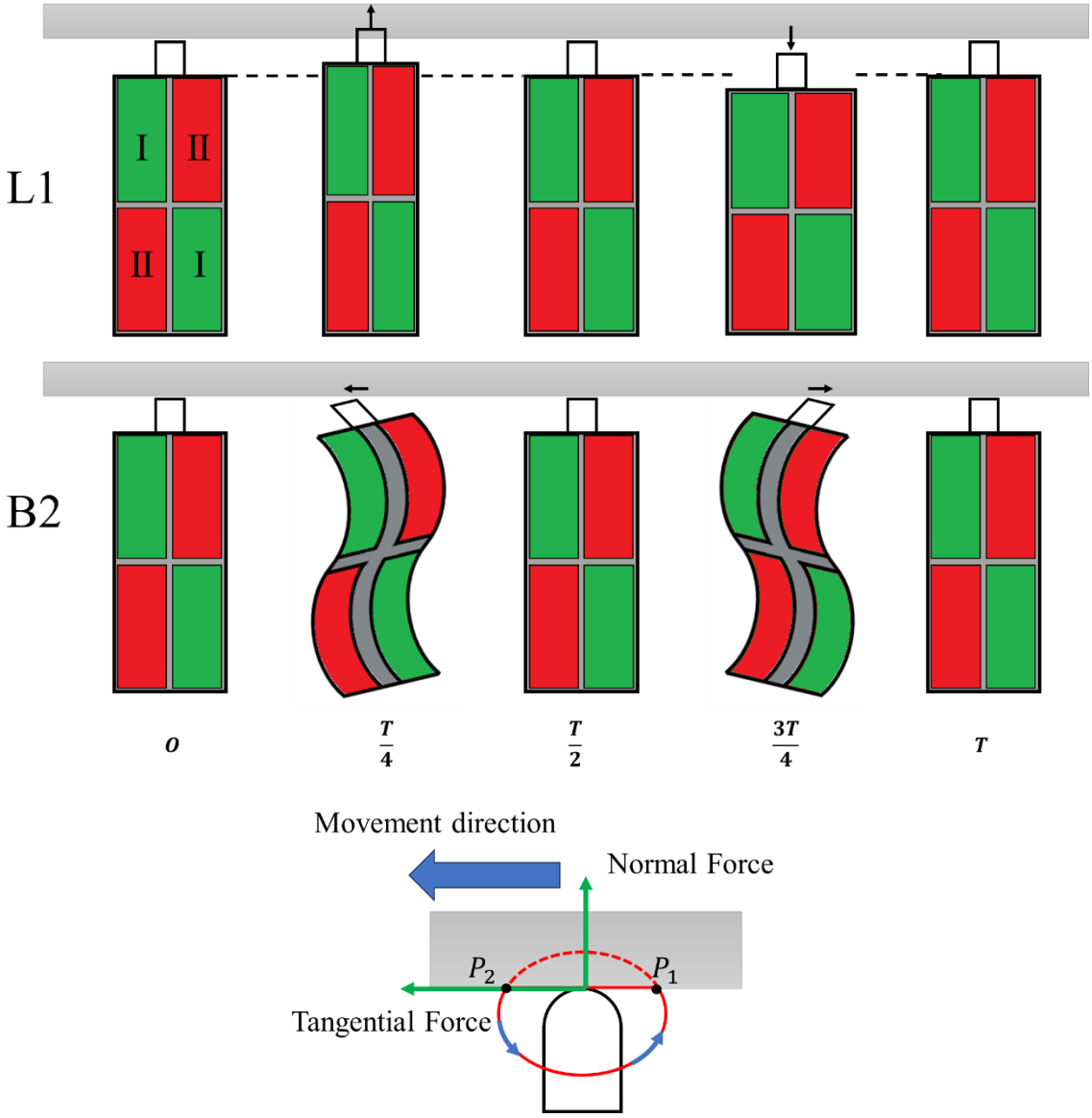

Figure III.4-5. Elliptic trajectory and forces exerted by the driving tip when group I electrodes are activated.

Because L1 is excited, the stator expands during $[0; T/4]$, and the driving tip will exert pressure onto the slider until $T/2$. Then contraction will begin and smaller pressure or even separation from the slider will occur. At the same time, B2 is being excited, and the stator will produce a periodic vibration along the horizontal direction deforming towards the left in the first half of the cycle $[0; T/2]$ and to the right in the second half $[T/2; T]$. The driving tip is in contact with the slider once per cycle, between P1 and P2 points, and will move it towards left. Because there is not enough normal force when the vibrator is deformed towards the right, no force in this direction is transmitted. In order to inverse the output direction of movement, the group II electrodes needs to be activated so the vibrator is deformed towards the right when the tip makes contact with the slider.

The elliptical motion of the hard tip moves the rotor periodically in this way and the pressing component and the pushing component of the elliptical motion have primary influences on the thrust and the speed of the motor, respectively [69], [94].

III.4.3. The support frame

As it is shown in Figure III.4-4, in the B2 mode we can distinguish three nodes that are situated along the length L of the vibrator at $0.13L$, $0.5L$ and $0.87L$, where the vibration amplitude is zero. These three points are important as they can be used to support the vibrator by means of a clamping frame. This strategy is used in other architectures as it reduces the influence of the mounting on the vibration modes to a minimum. For example, Shi et al took advantage of two nodal points for the mounting of their butterfly-shaped USM (Figure III.4-6)

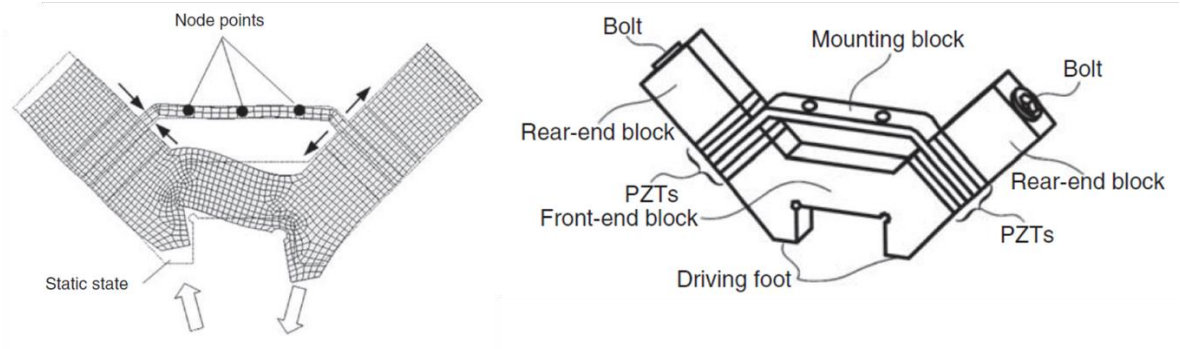

Figure III.4-6. The use of nodes for clamping and mounting is frequently used when designing USM. In this actuator designed by Shi et al [95] the modal study allowed the researchers to find three nodes at the operation frequency, two of which were used for the mounting the actuator.

Yet it is important to consider the long-term damage that the structure can suffer due to the B2 vibration mode as it was shown by Yuan et al [96]. In their research, they concluded that a L1B2 piezoelectric vibrator tends to fracture at one of the crests of the B2 mode while being mechanically free as shown in the figure below.

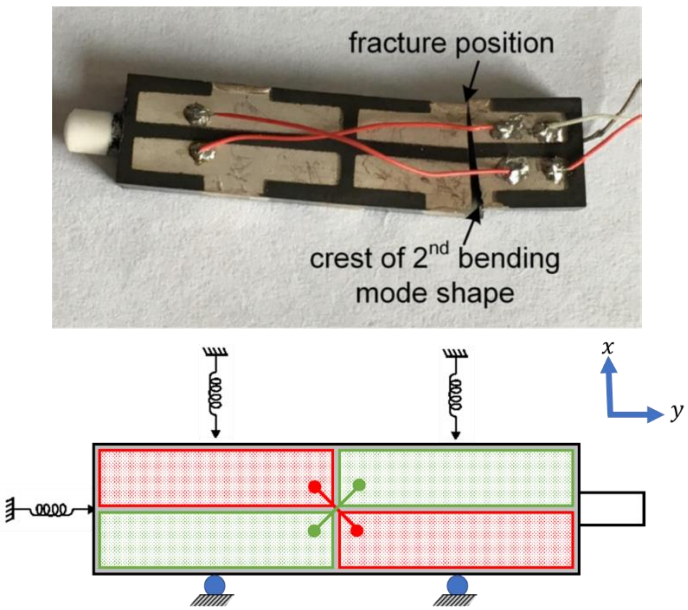

Figure III.4-7. Fracture of a mechanically free L1B2 vibrator (image taken from [96]) and the diagram of the vibrator when subjected to the lateral springs and supported by the frame.

For this reason, the clamping frame is designed to fit into the housing and allow the positioning of two lateral springs which help to reduce the effects of wear and provide a degree of shock protection for the piezoelectric ceramic which is still capable of sliding in y direction. Figure III.4-8 shows in detail these main components and their resulting design after positioned in the USM housing.

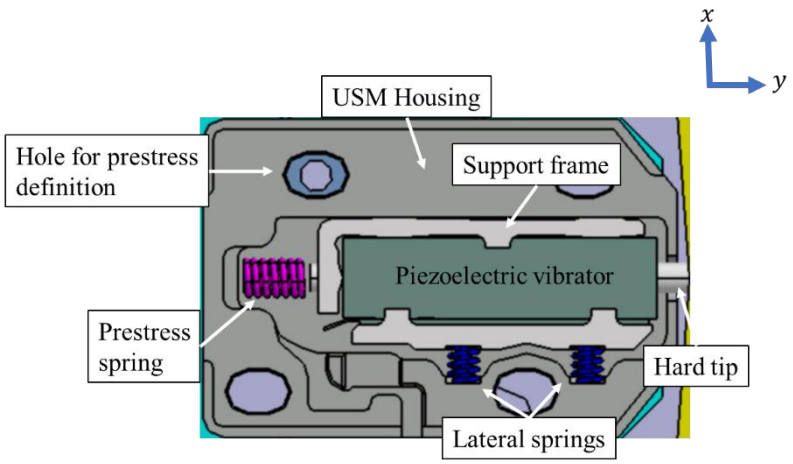

Figure III.4-8. Ultrasonic motor.

III.5. The leveling actuator

Figure III.5-1 shows the leveller actuator. Both covers of the actuator and the USM are not shown so we can appreciate the rotor-stator configuration: a support that remains fixed to the vehicle and secures a friction interface, which acts as the stator, and a second support, which acts as the rotor and can rotates about an axis of rotation. The USM is mounted on the rotor, so the hard tip is in contact with the friction interface. The latter has an arc shape, its axis of revolution coincides with the axis of rotation. The rotor is intended to be secured to the projector, so it is possible to change its angular position relative to the vehicle.

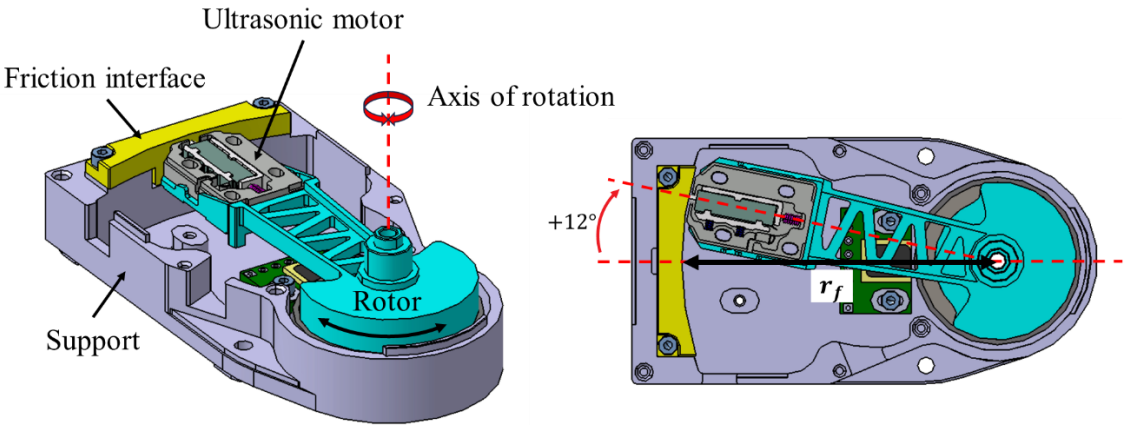

Figure III.5-1. The designed leveller based on USM actuation.

We set the radius of the friction interface r_f to such a value that the torque and rotational speed generated by the friction force between the hard tip of the ultrasonic motor and the surface of contact meet the requirements mentioned at the beginning of this chapter. From the top view, we can distinguish the axial

symmetry and the range of movement the actuator has. The application requiring 10° on both directions, we decided to add 2° degrees more in order to avoid runout problems or collisions between the rotor and the support.

III.5.1. The prestress and bearing configuration.

As explained in section II.5, piezoelectric actuators need to be operated under prestress. This is related to the properties of piezoelectric ceramics which work great when subjected to compressive stress but brittle under tensile stress. During the L1 mode, there are moments where the body expands and undergoes tension. If it were not to be a counter force, the ceramic may break. So, the selection of a proper pre-stress force allows to maintain a state of compressive stress for the full duration of the L1 periodic motion, which is desirable for reliability and longevity of the stator [97].

In our design, this force is given by the compression of a preload spring, situated in the opposite side of the hard tip, when the USM is mounted. In fact, the radius of the friction interface r_f being fixed, the spring is compressed a distance defined by the separation between the edge of the housing of the USM and the surface of contact of the friction interface. It is important to know that this compressive force also influences the normal force F_N exerted on the friction interface and how long the tip is in contact with the stator in every period T, and consequently the output torque and speed of the actuator. These relations are treated in the mathematical model of the actuator in chapter IV.

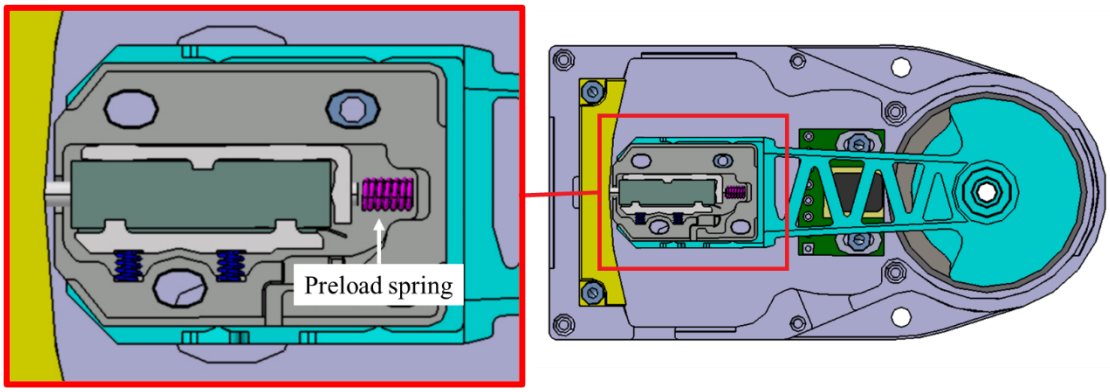

Figure III.5-2. Applying the prestress on the piezoelectric ceramic.

A proper bearing configuration is required so output movement is smooth as insufficient stiffness of the bearing structure could lead to vibration, noise, or excessive wear. For this reason we decided to use a fixed-end and free-end bearing arrangement of two single-row deep groove ball bearings B1 and B2, this configuration sustains both axial and radial loads, allows us to axially position the rotor R1 and helps the shaft to relieve when thermal elongation and contraction takes place. The size of both bearings has been chosen in accordance with the size limitations of the overall actuator rather than based in force or speed calculations. This is because our application is far from the magnitude that bearings can withstand in either force or speed, in the ranges of kN and kHz.

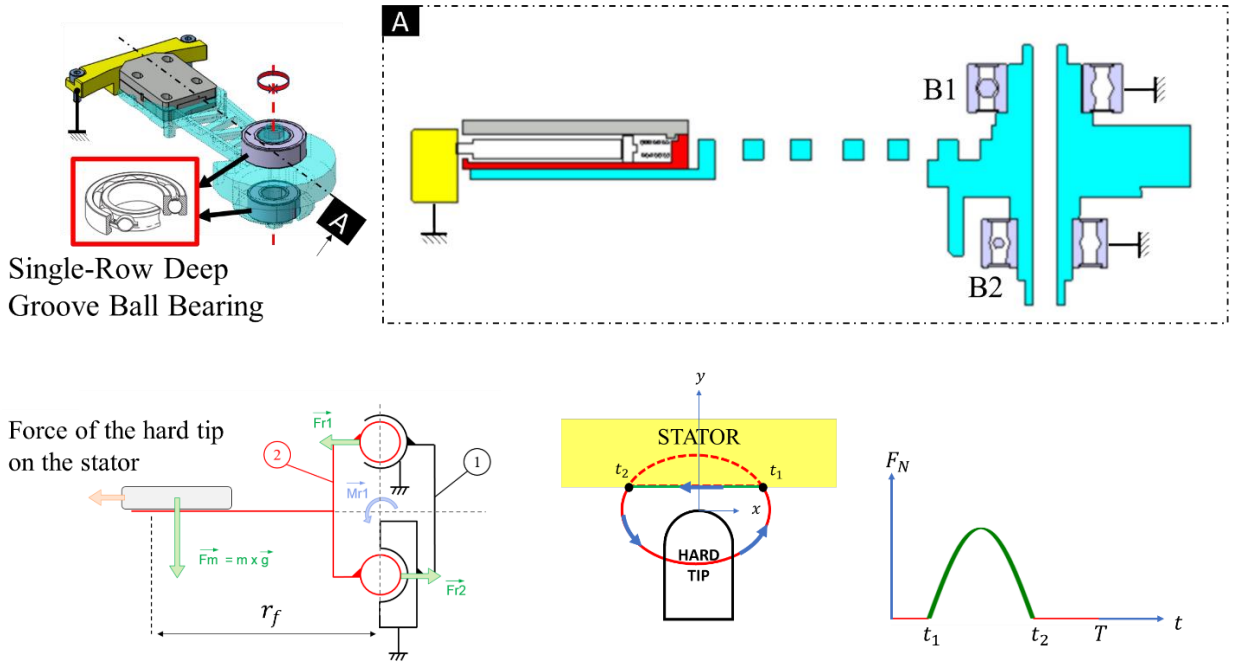

Figure III.5-3. Bearing configuration.

Besides, it is important to stablish which ring in the bearing remains static and which rotates to the housing so the fitting of the internal and external rings of each bearing can be defined. This depends on whether the load applied to the inner and outer ring is rotating or stationary. In general, the ring that supports a rotating load should be mounted with interference fit because looseness in such a case may cause the ring to slip (creep) yet overtightening the ring has an impact on the life expectancy of the bearing and the mounting easiness. In the other hand, there is no problem when slipping occurs for a ring on which a stationary load is applied so a loose fit can be used [98].

Once per cycle, the hard tip contacts the friction interface, during which, for simplicity; it is assumed that the longitudinal deformation is zero and a corresponding normal force pushes the friction interface resulting in a reaction force that is transmitted to the rotor. Based on Figure III.5-3, we can conclude that the inner rings of both bearings shall be mounted with interference on the rotor and the outer rings a loose fit on the actuator's housing.

Preload is often useful to optimize the bearing's performance as well as increase their stiffness, minimize noise due to axial vibration, prevent sliding between the balls and the raceways, etc [99]. Hence, after axially positioning the bearing B1, a star spring washer and nut is used to apply preload on its outer ring.

Finally, the actuator's housing (split in support S1 and cover C1) and the rotor shaft R1 were designed so the mounting of stator, rotor and bearings respects the following criteria (see Figure III.5-4):

- The shaft has a shoulder whose height and filler radius are designed for axially supporting the inner ring of both bearings B1 and B2.
- The inner ring fitting of both bearings in the shaft is k5 (tight fit).
- The outer ring fitting of both bearings in the cages of the support S1 and cover C1 is H7 (loose fit).
- Star spring washer applies uniform pressure on the whole outer ring of the bearing in C1.

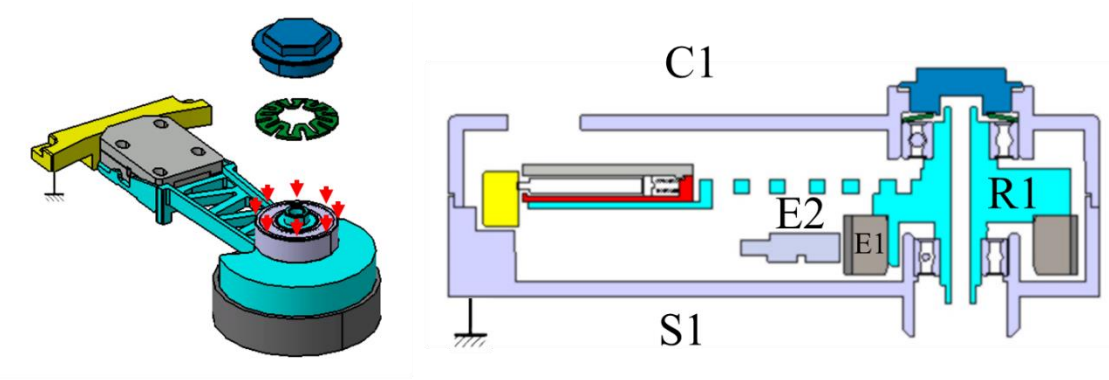

Figure III.5-4. Bearing fitting on actuator's shaft and housing.

III.5.2. The sensing system

In the Figure III.5-4, we can see two elements E1 and E2 that have not been mentioned yet. They form the sensing system chosen for monitoring the angular position of the actuator's shaft. We decided to use an incremental rotary encoder sensor system comprising a magnetic ring of 50 poles E1 and a PCB sensor E2. The poles in E1 consist of an elastoferrite layer firmly bonded on a stainless-steel hub. The layer is magnetized with 2 mm long alternating magnetic poles forming an incremental magnetic pattern along the circumference of the ring and it also includes a "U" shaped mark that is used as a reference, as shown in Figure III.5-5.

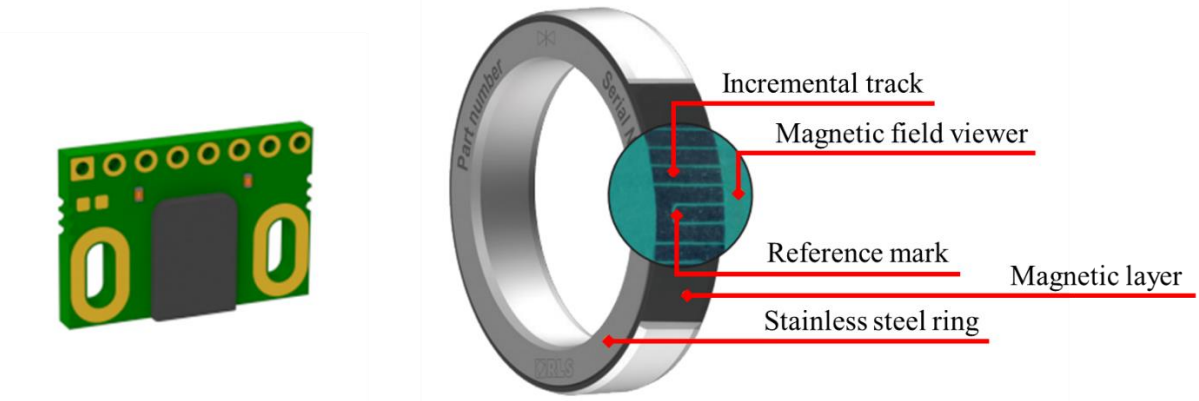

Figure III.5-5. The 50 poles magnetic ring and the PCB sensor for the encoding system. Images taken from RLS® [100].

With an interpolation factor of 2^{13}, the final resolution in PPR is given by *Eq. III.5.1*

$$PPR = \frac{N_P \times 2^{13}}{4} = 102400 \approx 0.003\,\text{deg/rev} \qquad \textit{Eq. III.5.1}$$

The actuator's support S1 includes a specific place for mounting the PCB sensor by means of small screws M2 such that the alignment and the perpendicular distance respects the builder

recommendations. Then the inner diameter of magnetic ring is slip onto to the rotor's shaft with a loose fit, the axis of revolution coinciding with the axis of rotation of the rotor, the ring is then secured by gluing it to the shoulder designed for its integration. Because only an arc of 20 degrees is needed for monitoring the whole actuators range, the only condition when mounting the magnetic ring is to orient it in such a way that the reference mark points towards the hard tip of the motor and fully passes by the PCB sensor which allows us to use it for the zero homing of the actuator.

The whole design of the actuator is shown in Figure III.5-6. Some details are worth mentioning for further understanding of how the leveller shall be operated:

- The leveller housing counts with a planar surface in S1 for ensuring perpendicularity between the axis of rotation and the radius of the friction interface. This surface is meant to face the projector and to be fixed relative to the vehicle by means of the two mounting holes.

- The actuator's output is found at the end of the rotor's shaft, on the opposite side of the preload nut. The shaft can be used either as a female connector introducing a external shaft in it or as a male connector taking advantage of the standard hex geometry.

- The cover has a slot that makes possible the measurement of the prestress distance of the USM and to slightly modify it without having to dismount the actuator.

- Leveller stiffness can also be modified by turning the preload nut. This will compress or release the tightening of the bearing B1.

- Cables for driving the vibrator and the sensor (not shown) pass through corresponding slots designed for this purpose.

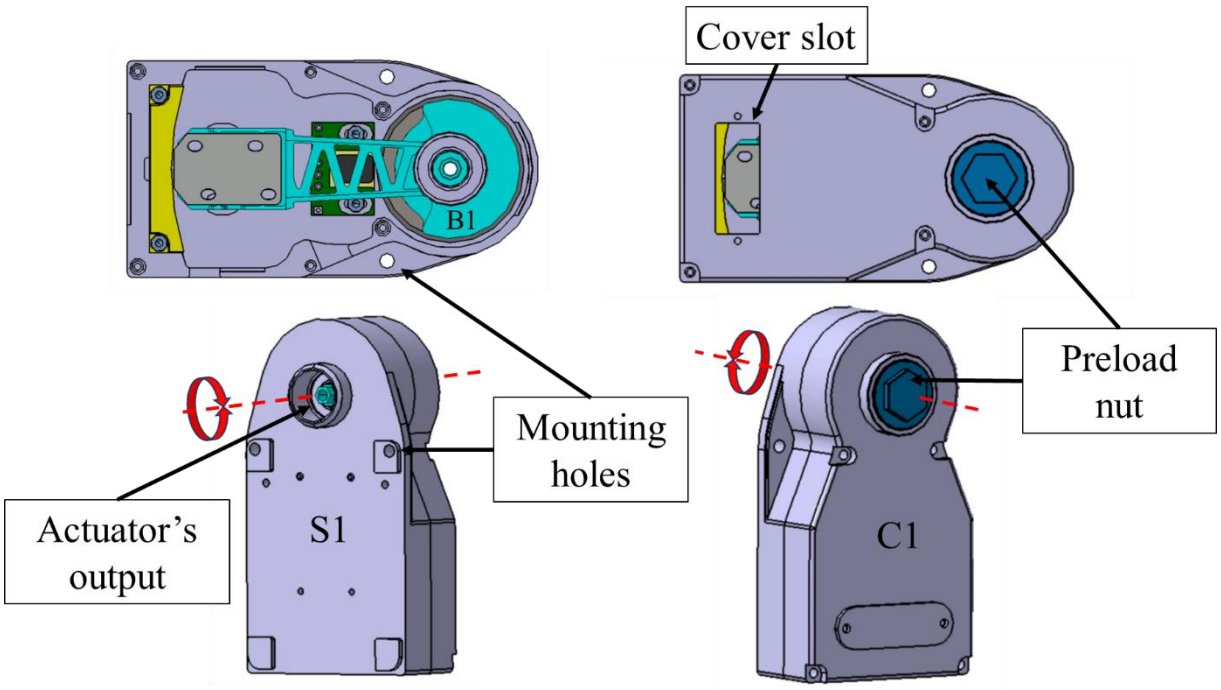

Figure III.5-6. The complete actuator design for leveling applications.

III.6. Conclusion

Using finite element analysis, the modes of vibration and their frequencies were calculated, treating the vibrating body as a parallelepiped geometry in free-free condition. The coincidence of the first longitudinal mode L1 and the second bending mode B2 at around 89 kHz is at the core of our actuator and the operating principle shares some similarities with other actuators found in the literature and described in chapter II. For instance, the resonance frequency depends on the size of the vibrating body and some material properties as the stiffness and density of the material. This imposes the frequency of the driver to be used, as it must generates an AC voltage with this value of frequency. Nevertheless, it is possible to excite the same modes of vibration at lower frequencies by either using a piezoelectric material less stiff or a bigger parallelepiped vibrating body. Even though USM allow the use of virtually any geometry for the vibrating body, from an industrial point of view, it is advantageous to keep working with simple structures, as it is the parallelepiped geometry, since they are easier and cheaper to fabricate than more complex structures.

On the other hand, our actuator presents some differences with which is classically found when using this kind of actuators.

The first, and maybe the most important one, is that we were interested on creating a complete motion solution, so the need of integrating a sensor inside the actuator motivates us to seek a solution accurate enough that can still be used in automotive headlight context. Indeed, the magnetic encoder system lacks the resolution that traditionally sensor systems as interferometers or doppler vibrometers exhibit but the reader will understand the current shortcomings that these measuring methods imply when small spaces are available for their integration. Besides, we must take into account that both technologies are used in rather static environments, as it is the case of optical tables or laboratories, because they are highly affected by surrounding vibrations. The rather harsh environment in which the leveling takes place, makes of the magnetic encoder a good solution.

Our actuator is characterized by a rotor-stator configuration in which the USM is situated in the rotor and not the friction interface, like it is usually find in the literature. This configuration actually allowed us to save space as the USM is placed inside the circumference described by the radius of the friction interface, contrary to place it outside of it. This implied the correct configuration and choice of bearings to ensure perpendicularity between the hard tip of the USM and the surface on which it contacts the friction interface.

It is worth mentioning that the designed concept was delivered a patent during the realization of this thesis and stands out above previous concepts found in the competition that lack in detail and just mention the use of piezoelectrics without going further in the selection of a specific architecture, measuring system, rotor-stator configuration, driving technique, desired mechanical output, etc.

Because the scope of this project leaves outside the design of the driver, we decided to use an XCD Nanomotion driver which is able to furnish an AC driving voltage with the correct frequency for the vibrator to resonate in L1B2 mode. By modifying the duty cycle of a square signal, it is possible to modify the amplitude of the sinusoidal voltage that comes into the vibrator. The output speed of the vibrator is then based on voltage control. Other drivers use frequency control, which is based in the modification of the output speed by changes in the frequency of the driving voltage; or phase control, which modify the phase difference between two driving signals.

Because we privileged the use of voltage control, the goal in the next chapter is to obtain a relation between the RMS value of the input signal and the output velocity of the actuator, and to look deeper in the dynamics of the actuator.

IV. DYNAMIC MODELING OF THE PIEZOELECTRIC LEVELER

IV.1. Introduction

One of the goals of this CIFRE thesis includes the construction of a functional prototype and its respective dynamic modeling for evaluation of the actuator's mechanical output (angular velocity $\vec{\omega}$ for instance) as a function of voltage input V in a given time t.

On the other hand, and taking into account that the industrial capabilities and objectives of AML Systems do not include the production of piezoelectrics but rather complete actuation solutions for automotive lighting, a mathematical model including the behavior of the piezoelectric vibrator brings interest in a long-term perspective as it allows us:

- To evaluate the impact that different parameters (piezoelectric coefficient, prestress, number of layers in piezoelectric, etc.) have in the actuator's performance.
- To simulate this actuation system based in L1B2 piezo vibrators in a rapid way, which makes part of a digital twin strategy for the company.

The mathematical modeling is the subsequent phase of the application definition stage, where the parameters, on which the model will be based, have also been defined and includes:

Table IV.1-1. Parameters for the dynamic model based on the design described in chapter III.

CHARACTERISTICS		PARAMETER FOR THE MODEL
Selection of ultrasonic structure	Beam-shaped piezoelectric	Length l, width w and height h of the beam
	L1 ϕ_{L1} and B2 ϕ_{B2} modes of vibration	
Electrodes configuration	Multilayer	Number of layers N
	Four quadrants and ground electrode	
	Sinusoidal voltage input	Voltage amplitude V and frequency f
Rotor-stator configuration	The USM moves with the rotor	
Components in contact with the stator	Prestress spring, hard tip, bearings	Preload force F_P
Geometrical parameters	Arc shape stator	Radius of the friction interface R
	Overall maximal dimension of the actuator	
Material properties	Piezoelectric coefficient	e_{31}
	Permittivity	ε
	Stiffness	c_{11}, c_{66}
	Coefficient of friction	μ
Actuator Performance	Moment of inertia of the load	I_{CM}
	Mass of the load	M
	Decentering of the load	d

The design of the actual piezoelectric material does not make part of the scope of this research and is not part of AML Systems business model, yet the proposed model seeks to facilitate the design of future leveling prototypes based in L1B2 piezoelectric vibrators which may be characterized by a different set of material properties, driving voltages or sizes.

Due to the tremendous variety on vibrator geometries and electrode configuration, it is not a realistic objective of this chapter to declare a general model for ultrasonic actuators but rather to apply a methodology that may be useful in dynamic modeling for a great variety of actuators based on SWUSM, based in the fact that they do tend to share a characteristic independent of the stator-rotor configuration or the vibration modes utilized: the two-stage energy conversion [101]. As we know, most of these actuators are vibratory coupler type, where a flat-elliptical movement on a hard tip positioned on the piezoelectric vibrator can be generated by a given actuated method (in our case this was explained in section III.4.1 The vibrating body), followed by the passage from small orthogonal deformations ($\sim \mu m$) into macroscopic rotary output of the slider (deg/s in rotary case) as a result of the cyclical contact of the USM's hard tip and the friction interface, as seen in section III.4.2 The driving tip, for our design.

Based on this common feature, it is reasonable to model such an actuator as a series of interconnected subsystems, as seen in Figure IV.1-1, one of them transforming the input electrical energy into output mechanical vibrations of the piezoelectric and another subsystem that deals with how the vibration energy is delivered to the load by frictional coupling between stator and rotor.

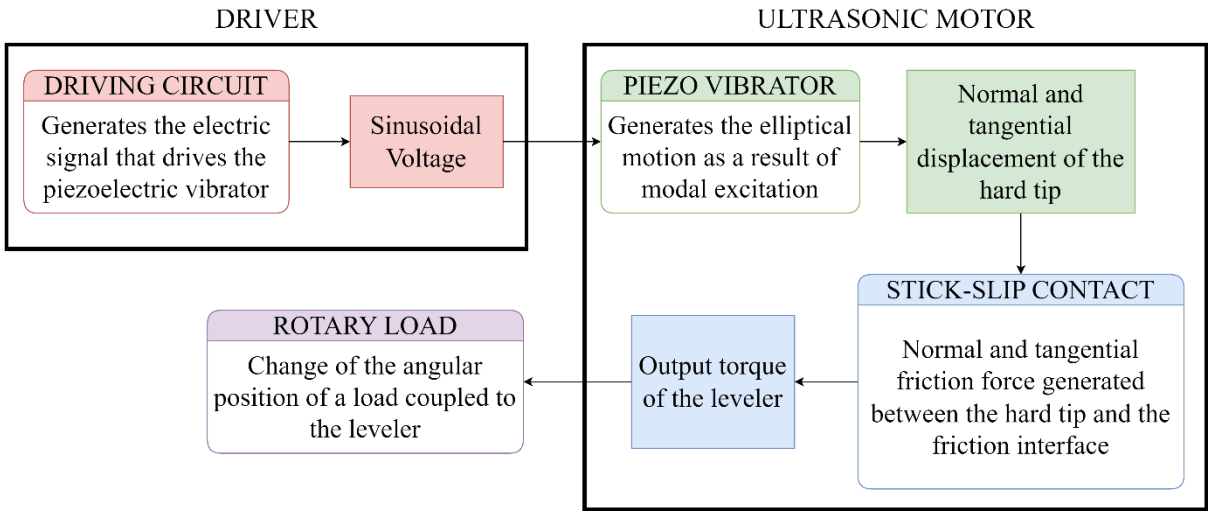

Figure IV.1-1. Piezo leveler's subsystems.

IV.2. *Driving circuit* subsystem

Based on the USM design seen in chapter III, and the assembly shown in Figure III.4-8, a schema of the piezo vibrator is shown in Figure IV.3.1-1, where the polarization direction is defined by the blue bolt arrow parallel to z axis. Because the design of the electric driver is not part of this thesis, the driving circuit subsystem is modeled as a sinusoidal function $V(f,t)$

$$V(f,t) = V \cdot n \cdot \sin(2\pi f t) \qquad \textit{Eq. IV.2.1}$$

This electric signal drives the vibrating body as described in chapter III, where V is the voltage amplitude sent by the driver, n the number of layers, f a proper selected frequency based on the L1 and B2 modes and t the time.

IV.3. *Piezo vibrator* subsystem

We model the mechanical vibrations obtained through electrical excitation of the piezo vibrator. This corresponds to the second subsystem of Figure IV.1-1 whose input is the electric field described by *Eq. IV.3.1.1* and the output is the elliptic movement generated in the hard tip decomposed in the orthogonal components of normal displacement u and tangential displacement v. In this work, both the longitudinal and bending vibrations will be respectively treated as the longitudinal and bending vibration of a beam in free-free boundary conditions.

The field variables are the stress components (T_i), strain components (S_i), electric field components (E_k), and the electric displacement components (D_k). In chapter II (Table II.4 1), we saw that the standard form of the piezoelectric constitutive equations can be given in four different forms regarding the chosen independent variables. Considering the strain components and the electric field components as the independent variables, the piezoelectric constitutive equations in matrix form are

$$\begin{bmatrix} \boldsymbol{T} \\ \boldsymbol{D} \end{bmatrix} = \begin{bmatrix} \boldsymbol{c^E} & -\boldsymbol{e}^* \\ \boldsymbol{e} & \boldsymbol{\varepsilon^S} \end{bmatrix} \begin{bmatrix} \boldsymbol{S} \\ \boldsymbol{E} \end{bmatrix} \qquad \textit{Eq. IV.3.1}$$

where $\boldsymbol{c^E}$ denotes that the compliance matrix is evaluated at constant electric field, $\boldsymbol{\varepsilon^S}$ denotes that the electric permittivity was obtained at constant strain and $\boldsymbol{e}^*$ is the transpose of the piezoelectric matrix $\boldsymbol{e}$. In general, poled piezoceramics (such as PZT-5A and PZT-5H) are transversely isotropic materials (the plane of isotropy is defined by the xy-plane) and therefore the piezoelectric material exhibits symmetry about the poling axis of the material (z axis). Due to this symmetry some constants of *Eq. IV.3.1* are equal, for example $c_{11}^E = c_{22}^E$, $c_{12}^E = c_{21}^E$, $e_{31} = e_{32}$, etc. which in the expanded form results in 11 different non-zero constants, 6 from the compliance matrix $\boldsymbol{c^E}$, 2 from the permittivity matrix $\boldsymbol{\varepsilon^S}$ and 3 from the piezoelectric matrix $\boldsymbol{e}$

$$\begin{bmatrix} T_1 \\ T_2 \\ T_3 \\ T_4 \\ T_5 \\ T_6 \\ D_1 \\ D_2 \\ D_3 \end{bmatrix} = \left[\begin{array}{cccccc|ccc} c_{11}^E & c_{12}^E & c_{13}^E & 0 & 0 & 0 & 0 & 0 & -e_{31} \\ c_{12}^E & c_{11}^E & c_{13}^E & 0 & 0 & 0 & 0 & 0 & -e_{31} \\ c_{13}^E & c_{13}^E & c_{33}^E & 0 & 0 & 0 & 0 & 0 & -e_{33} \\ 0 & 0 & 0 & c_{44}^E & 0 & 0 & 0 & -e_{15} & 0 \\ 0 & 0 & 0 & 0 & c_{44}^E & 0 & -e_{15} & 0 & 0 \\ 0 & 0 & 0 & 0 & 0 & c_{66}^E & 0 & 0 & 0 \\ \hline 0 & 0 & 0 & 0 & e_{15} & 0 & \varepsilon_{11}^S & 0 & 0 \\ 0 & 0 & 0 & e_{15} & 0 & 0 & 0 & \varepsilon_{11}^S & 0 \\ e_{31} & e_{31} & e_{33} & 0 & 0 & 0 & 0 & 0 & \varepsilon_{33}^S \end{array}\right] \begin{bmatrix} S_1 \\ S_2 \\ S_3 \\ S_4 \\ S_5 \\ S_6 \\ E_1 \\ E_2 \\ E_3 \end{bmatrix} \qquad \textit{Eq. IV.3.2}$$

We can reduce this matrix by considering the geometry of the vibrating body and the placement of the electrodes.

IV.3.1. Reduction of the constitutive equations

As shown in Figure IV.3.1-1, we assume that Group I and II electrodes cover the totality of the surface, hence the electric field components parallel to x axis E_1 and parallel to y axis E_2 will be zero and the remaining component E_3 parallel to z axis will be defined by

$$E_1 = E_2 = 0 \qquad E_3 = \frac{V \cdot n}{h} \cdot \sin(2\pi f t) \qquad \textit{Eq. IV.3.1.1}$$

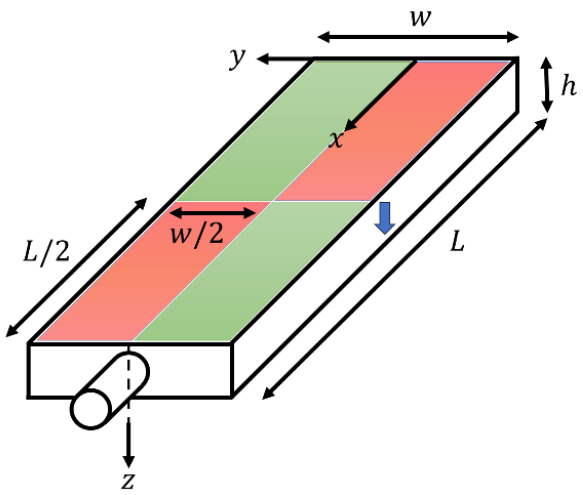

Figure IV.3.1-1. Schematic of the vibrating body.

The multilayer structure of the vibrator will be assumed to be a Timoshenko Beam and the hard tip is assumed to be rigid. Because the clamping structure supports the vibrator in nodal points, its effects on the modes of vibration will be neglected [102]. The beam of length L, width w and thickness h, is under both axial and shear stress due to the normal force F_N and tangential force F_T generated by the contact with the friction interface and F_1 and F_2 are the reaction forces caused by the clamping structure when the vibrator is in B2 mode.

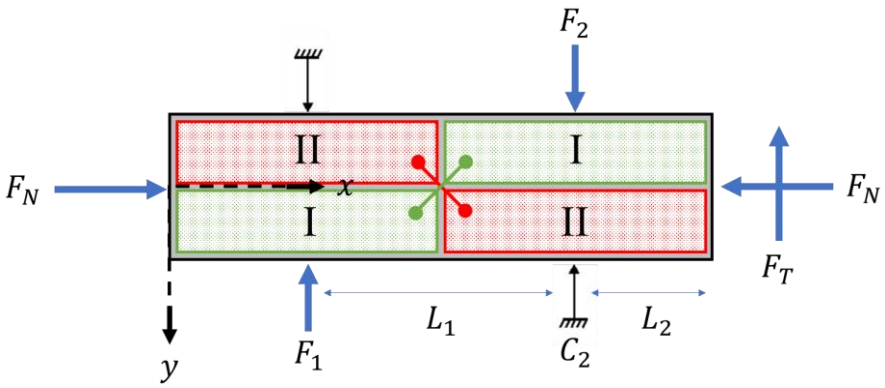

Figure IV.3.1-2. Forces acting on the vibrating body.

In Timoshenko theory, the centerline of the beam, shown in red in Figure IV.3.1-3 and Figure IV.3.1-4 coincides with the x axis in absence of deformation. This theory takes into account the effects of both shear and bending.

First, considering only the effects of shear deformation (Figure IV.3.1-3), we suppose any vertical section $\overline{PQ}$ before deformation will remain vertical $\overline{P'Q'}$ after deformation regarding x and displaced by a distance $v_s(x,t)$ along the y axis. Shear does not produce axial strain and hence, for any point in the beam, the components of its displacement parallel to x, y and z are respectively u, v, w and are defined as,

$$u = 0 \qquad v = v_s(x,t) \qquad w = 0 \qquad \textit{Eq. IV.3.1.2}$$

And consequently, the components of strain ϵ are given by,

$$\epsilon_{xx} = \frac{\partial u}{\partial x} \quad \epsilon_{yy} = \frac{\partial v}{\partial y} \quad \epsilon_{zz} = \frac{\partial w}{\partial z} \quad \epsilon_{xy} = \frac{\partial u}{\partial y} + \frac{\partial v}{\partial x} \quad \epsilon_{yz} = \frac{\partial v}{\partial z} + \frac{\partial w}{\partial y} \quad \epsilon_{zx} = \frac{\partial u}{\partial z} + \frac{\partial w}{\partial x} \qquad \textit{Eq. IV.3.1.3}$$

The only non-zero component of strain is the shear strain $\epsilon_{xy} = \partial v_s/\partial x$, which is the rotation that any parallel to the centerline will suffer after deformation as shown in Figure IV.3.1-3

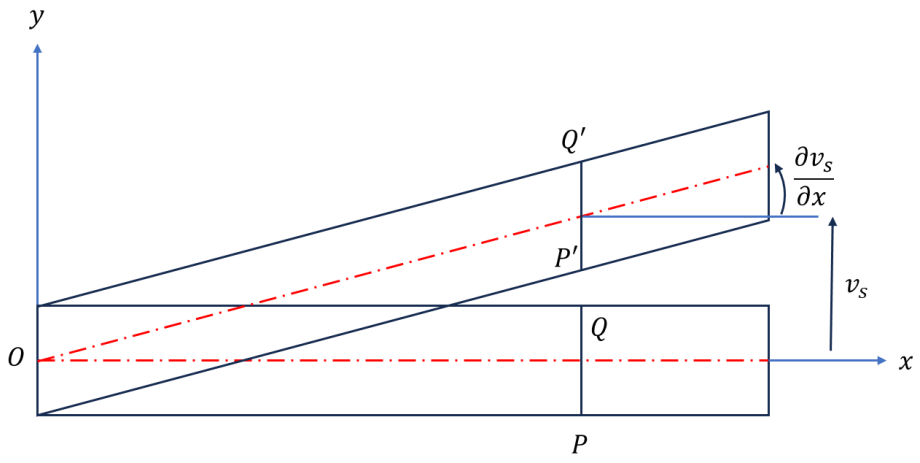

Figure IV.3.1-3. Shear deformation of the piezoelectric vibrator.

At this point, we have only considered the deformation caused by shearing, but the total vertical displacement v must also include the curvature effect of the beam due to bending moment. We approximate this by adding to *Eq. IV.3.1.2*, the individual contributions of bending v_b to the vertical displacement v,

$$v = v_s + v_b \qquad \textit{Eq. IV.3.1.4}$$

From the previous equation, the total slope of the beam $\partial v/\partial x$ is given by,

$$\frac{\partial v}{\partial x} = \frac{\partial v_s}{\partial x} + \frac{\partial v_b}{\partial x} \qquad \textit{Eq. IV.3.1.5}$$

Where $\partial v_b/\partial x$ is the slope of a tangent to the centerline at a point R'' defined by the intersection of the centerline $\overline{OO''}$ and the vertical section after bending deformation $\overline{P''Q''}$ as shown in Figure IV.3.1-4

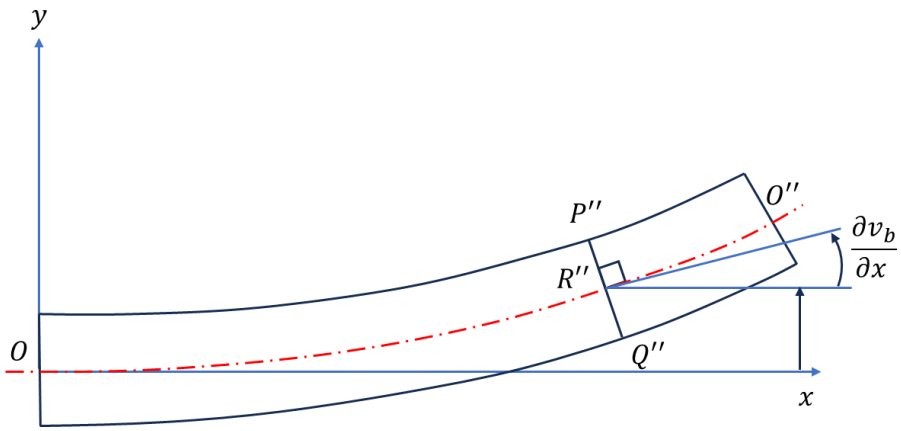

Figure IV.3.1-4. Bending deformation of the piezoelectric vibrator.

It is worth mentioning that regarding bending case, the assumption of perpendicularity of a section before and after deformation is slightly modified when compared with shear deformation case. In the first case, the vertical section $\overline{PQ}$ rotates an angle $\partial v_b/\partial x$ and remains perpendicular to the centerline $\overline{P''Q''} \perp \overline{OO''}$ but not to the x axis, while in the shear deformation case, $\overline{P'Q'} \perp x$ axis given that there is no rotation of the vertical section $\overline{PQ}$, which instead, will form an angle $\partial v_s/\partial x = \beta$ with the centerline known as shear angle.

From *Eq. IV.3.1.5*, the rotation of $\overline{PQ}$ is then,

$$\frac{\partial v_b}{\partial x} = \frac{\partial v}{\partial x} - \beta = \psi(x,t) \qquad \textit{Eq. IV.3.1.6}$$

This rotation $\psi(x,t)$ produces a corresponding axial strain on an element fiber located at a distance y from the centerline. Finally, the components of displacement u, v, w including shear and bending effects on the piezoelectric vibrator are defined as follows

$$u = u(x,t) - y\psi(x,t) \qquad v = v(x,t) \qquad w = 0 \qquad \textit{Eq. IV.3.1.7}$$

Where the contribution $u(x,t)$ of the axial forces F_N appears exclusively on the horizontal component of the movement u. From *Eq. IV.3.1.3*, the strain components are

$$\epsilon_{yy} = \epsilon_{zz} = \epsilon_{yz} = \epsilon_{zx} = 0;$$

$$\epsilon_{xx} = \frac{\partial u}{\partial x} = \frac{\partial u}{\partial x} - y\frac{\partial \psi}{\partial x};\ \epsilon_{xy} = \frac{\partial u}{\partial y} + \frac{\partial v}{\partial x} = -\psi(x,t) + \frac{\partial v}{\partial x} \qquad \textit{Eq. IV.3.1.8}$$

From the above expressions, we observe that there are only two non-zero components of the strain and together with *Eq. IV.3.1.1*, the piezoelectric equations of *Eq. IV.3.2* for our piezo vibrator are simplified to

$$\begin{bmatrix} T_1 \\ T_6 \\ D_3 \end{bmatrix} = \begin{bmatrix} c_{11} & 0 & -e_{31} \\ 0 & c_{66} & 0 \\ e_{31} & 0 & \epsilon_{33} \end{bmatrix} \begin{bmatrix} S_1 \\ S_6 \\ E_3 \end{bmatrix} \qquad \textit{Eq. IV.3.1.9}$$

Where the stress (σ_{ij}) and strain components (ϵ_{ij}) have been contracted according to Voigt's notation, specifically,

$$\begin{bmatrix} T_1 \\ T_2 \\ T_3 \\ T_4 \\ T_5 \\ T_6 \end{bmatrix} = \begin{bmatrix} \sigma_{xx} \\ \sigma_{yy} \\ \sigma_{zz} \\ \sigma_{yz} \\ \sigma_{xz} \\ \sigma_{yz} \end{bmatrix} \qquad \begin{bmatrix} S_1 \\ S_2 \\ S_3 \\ S_4 \\ S_5 \\ S_6 \end{bmatrix} = \begin{bmatrix} \epsilon_{xx} \\ \epsilon_{yy} \\ \epsilon_{zz} \\ 2\epsilon_{yz} \\ 2\epsilon_{xz} \\ 2\epsilon_{yz} \end{bmatrix} \qquad \textit{Eq. IV.3.1.10}$$

This great reduction of the complete set of equations is possible due to the previous assumptions, i.e. the electrodes disposition and the Timoshenko Beam. These assumptions can be applied to future leveler models as long as they are based on a moderately thick piezoelectric beam made of a transversely isotropic material poled along the z axis.

Unlike rigid body systems, the piezoelectric ceramic is a spatially deformable body (it occupies a volume V delimited by a surface area S) and yet it has an infinite number of degrees of freedom. We will use the Euler-Lagrange equations to obtain the equations of motion of the ceramic. The Lagrangian $\mathcal{L}$ is expressed by [103]

$$\mathcal{L} = K - H \qquad \textit{Eq. IV.3.1.11}$$

Where K is the kinetic energy and H is the electrical enthalpy. For classical mechanical systems, we know that the Lagrangian $\mathcal{L}$ is given by the difference of the kinetic energy and the potential energy U. On the other hand, when it comes to a piezoelectric material, it exists coupling between mechanical deformation and electrical polarization: The stored potential energy is decomposed into a part associated with mechanical deformation and another linked to the electrical movement of charges. In order to include this coupled behavior, the use of electrical enthalpy H instead of potential energy U in the Lagrangian $\mathcal{L}$ allows these two contributions, together with the piezoelectric effect, to be taken into account.

The kinetic energy depends on the density of the piezoelectric material ρ, the cross section of the stator A and its second moment of area I. We assume these three quantities as constants, then the volume integral becomes an ordinary integral:

$$K = \frac{\rho}{2}\int_V \dot{u}\cdot\dot{u}dV = \frac{\rho}{2}\int_0^l \left[A\left(\frac{\partial u(x,t)}{\partial t}\right)^2 + A\left(\frac{\partial v(x,t)}{\partial t}\right)^2 + I\left(\frac{\partial \psi(x,t)}{\partial t}\right)^2\right]dx \qquad \textit{Eq. IV.3.1.12}$$

We assume that we operate far from the plastic zone of the material and knowing that the piezoelectric ceramic is a dielectric material between metal electrodes (as described in the previous section) we can define H as [4]

$$H = \frac{1}{2}\int_V (\sigma_{xx}\epsilon_{xx} + 2\sigma_{xy}\epsilon_{xy} - E_3D_3)dV = \frac{1}{2}\int_V (T_1S_1 + T_6S_6 - E_3D_3)dV \qquad \textit{Eq. IV.3.1.13}$$

Using *Eq. IV.3.1.8* and the piezoelectricity relations of *Eq. IV.3.1.9*, we obtain

$$H = \frac{1}{2}\int_V \left[c_{11}\left(\frac{\partial u(x,t)}{\partial x} - y\frac{\partial \psi(x,t)}{\partial x}\right)^2 + c_{66}\left(\frac{\partial v(x,t)}{\partial x} - \psi(x,t)\right)^2 - 2e_{31}\left(\frac{\partial u(x,t)}{\partial x} - y\frac{\partial \psi(x,t)}{\partial x}\right)E_3 - \varepsilon_{33}E_3^2 \right] dV \qquad \textit{Eq. IV.3.1.14}$$

It should be noted that in the previous expressions, all the variables linked to the mechanical behavior only take into account the displacement in the plane, unlike the electrical variables which are spatially dependent on the direction of the polarization of the material z.

The electrodes are diagonally connected, then the electric field in the direction of polarization of the material E_3, ignoring the effect due to thickness, is given by

$$E_3 = \begin{cases} -\dfrac{V(f,t)}{h} & \text{when} \quad 0 < x < \dfrac{L}{2}; -\dfrac{w}{2} < y < 0 \\ -\dfrac{V(f,t)}{h} & \text{when} \quad \dfrac{L}{2} < x < L; 0 < y < \dfrac{w}{2} \\ 0 & \text{elsewhere} \end{cases} \qquad \textit{Eq. IV.3.1.15}$$

Under this electric input, the displacements $u(x,t), v(x,t), \psi(x,t)$ in *Eq. IV.3.1.7* can be decomposed into their spatial and temporal components as

$$\begin{aligned} u(x,t) &= u(t)\phi_u(x) \\ v(x,t) &= v(t)\phi_v(x) \\ \psi(x,t) &= \psi(t)\phi_\psi(x) \end{aligned} \qquad \textit{Eq. IV.3.1.16}$$

The frequency value of $V(f,t)$ is equal to the mean value f_r of the resonance frequencies of these two modes,

$$V_p(t) = V(f_r,t) \qquad f_r = \frac{f_{L1} + f_{B2}}{2} \qquad \textit{Eq. IV.3.1.17}$$

We assume that the resonant frequencies f_{L1}, f_{B2} of the first longitudinal mode L1 and the second bending mode B2 are close enough, then these two modes will be excited in the, hence the spatial components of $u(x,t)$, $v(x,t)$ and $\psi(x,t)$ in *Eq. IV.3.1.6* are described by

$$\begin{aligned} u(x,t) &= u(t)\phi_L(x) \\ v(x,t) &= v(t)\phi_B(x) \\ \psi(x,t) &= \psi(t)\phi_\psi(x) \end{aligned} \qquad \textit{Eq. IV.3.1.18}$$

Where we take ϕ_L, ϕ_B and ϕ_ψ as the vibrational mode functions of an Euler-Bernoulli beam under free-free boundary condition.

$$\phi_L(x) = \cos\left(\frac{\pi x}{L}\right)$$
$$\phi_B(x) = \alpha(\cos\beta x + \cosh\beta x) + \sinh\beta x + \sin\beta x \qquad \textit{Eq. IV.3.1.19}$$
$$\phi_\psi(x) = \frac{d\phi_B(x)}{dx}$$

Where α and β are values numerically obtained and depend on the excited mode, the dimensions of the beam and the boundary conditions [104]. In our case

$$\alpha = \frac{sin(\beta L) - sinh(\beta L)}{cosh(\beta L) - cos(\beta L)} \qquad \beta = \frac{2.4997\pi}{L} \qquad \textit{Eq. IV.3.1.20}$$

By replacing the functions of the modes of *Eq. IV.3.1.19* in the expressions for K of *Eq. IV.3.1.12* we get

$$K = \frac{\dot{u}_L^2 \rho A}{2}\int_0^l \phi_L^2 dx + \frac{\dot{v}_B^2 \rho A}{2}\int_0^l \phi_B^2 dx + \frac{\dot{\psi}_R^2 \rho I}{2}\int_0^l \phi_\psi^2 dx$$
$$K = \frac{1}{2}\left[m_{11}\dot{u}_L^2 + m_{22}\dot{v}_B^2 + m_{33}\dot{\psi}_R^2\right] \qquad \textit{Eq. IV.3.1.21}$$

Where $\dot{u}_L, \dot{v}_B, \dot{\psi}_R$, are the time derivatives of the temporal part of u, v and ψ. Applying the same process to H, after expanding and simplifying *Eq. IV.3.1.14*

$$H = \frac{1}{2}\Bigg[u_L^2 c_{11} A\int_0^l {\phi'}_L^2 dx + v_B^2 c_{66} A\int_0^l {\phi'}_B^2 dx - 2\psi_R v_B c_{66} A\int_0^l \phi_\psi {\phi'}_B dx$$
$$+\psi_R^2\left(c_{11} I\int_0^l \phi_\psi'^2 dx + c_{66} A\int_0^l \phi_\psi^2 dx\right)\Bigg]$$
$$-\frac{e_{31} V_p}{2}\Bigg[-\psi_R\left(\frac{w}{2}\right)^2\int_0^{l/2} {\phi'}_\psi dx + \psi_R\left(\frac{w}{2}\right)^2\int_{l/2}^l {\phi'}_\psi dx$$
$$- w u_L\int_0^l \phi_L' dx\Bigg] - \frac{1}{4}\frac{A\varepsilon_{33} V_p^2}{h}$$
$$H = (k_{11}u_L^2 + k_{22}v_B^2 + k_{23}\psi_R v_B + k_{33}\psi_R^2) + V_p(b_{11}u_L + b_{31}\psi_R) - \frac{1}{2}E_{CA} \qquad \textit{Eq. IV.3.1.22}$$

It remains to specify the energy brought to the system δW linked to the normal forces F_N and tangential forces F_T that act on the ceramic. From the free body diagram of Figure IV.3.1-2, we can obtain the expression for the mechanical work as

$$\delta W = F_N \cdot \delta u|_{x=0} - F_N \cdot \delta u|_{x=l} + F_T \cdot \delta v|_{x=l} + M_l \cdot \delta\psi \qquad \textit{Eq. IV.3.1.23}$$

From the sum of moments about the clamping point C_2 in Figure IV.3.1-2,

$$M_l = F_T L_2 - F_1 L_1 = 0; F_2 = F_T + F_1 \qquad \textit{Eq. IV.3.1.24}$$

Replacing in *Eq. IV.3.1.23* we get

$$\delta W = F_N \cdot \left(\phi_L(0) - \phi_L(L)\right) + F_T \cdot \phi_B(L) + F_T L_2 \phi_\psi(L) - F_1 L_1 \phi_\psi(L_2)$$

$$\delta W = F_N b_{12} + F_T b_{23} + F_T b_{33} \qquad \textit{Eq. IV.3.1.25}$$

The definition of the coefficients in *Eq. IV.3.1.21*, *Eq. IV.3.1.22* and *Eq. IV.3.1.25* is given in Appendix A. Then Euler-Lagrange equation allows us to obtain the equations of motion by applying

$$\frac{d}{dt}\frac{\partial \mathcal{L}}{\partial \dot{q}} - \frac{\partial \mathcal{L}}{\partial q} = Q \qquad \textit{Eq. IV.3.1.26}$$

on the Lagrangian $\mathcal{L}$ defined in *Eq. IV.3.1.11* and replacing K, H and Q with the expressions obtained in *Eq. IV.3.1.21*, *Eq. IV.3.1.22* and *Eq. IV.3.1.25*. In matrix form, we obtain

$$\begin{bmatrix} m_{11} & 0 & 0 \\ 0 & m_{22} & 0 \\ 0 & 0 & m_{33} \end{bmatrix} \begin{bmatrix} \ddot{u}_L^2 \\ \ddot{v}_B^2 \\ \ddot{\psi}_R^2 \end{bmatrix} - \begin{bmatrix} 2k_{11} & 0 & 0 \\ 0 & 2k_{22} & k_{23} \\ 0 & k_{23} & 2k_{33} \end{bmatrix} \begin{bmatrix} u_L \\ v_B \\ \psi_R \end{bmatrix} = \begin{bmatrix} b_{11} & b_{12} & 0 \\ 0 & 0 & b_{23} \\ b_{31} & 0 & b_{33} \end{bmatrix} \begin{bmatrix} V_p \\ F_N \\ F_T \end{bmatrix} \qquad \textit{Eq. IV.3.1.27}$$

$$\mathrm{M}\ddot{X} + \mathrm{K}X = \mathrm{B}F$$

Which is a coupled system of equations, as the temporal components v_B and ψ_R have crossed terms, i.e., the matrix K is not diagonal. The coupling depends on the coordinates used but it is not an inherent property of a system [105].

Since both M and K are positive definite matrix, the solution of the associated eigenvalue problem generates 3 eigenvectors which constitute a transformation matrix Δ to transform the vector of coordinates X of the original system of coupled equations into a vector of generalized coordinates Q of a decoupled system of equations, such that.

$$X = \Delta Q \qquad\qquad Q = \Delta^{-1} X \qquad \textit{Eq. IV.3.1.28}$$

This relates to finding the vector X that satisfies.

$$\lambda \mathrm{M}X = \mathrm{K}X$$

$$[\mathrm{K} - \lambda \mathrm{M}]X = 0$$

For the problem to have a non-trivial solution, it must satisfy.

$$\det(\mathrm{K} - \lambda \mathrm{M}) = \det(\mathrm{K} - \omega^2 \mathrm{M}) = 0$$

As K and M are symmetric with real elements, all the eigenvalues λ_i are real and correspond to the squares of the resonance frequencies $\omega_L, \omega_B, \omega_\psi$ of each vibration mode u_L, v_B, ψ_R. We can finally construct Δ as

$$\Delta = [X_L \quad X_B \quad X_\psi]$$

With X_i the eigenvectors corresponding to each resonance frequency. Applying this process using the material parameters of Table IV.3.1-1, we get the three eigenvalues ω_i^2 and its respective eigenvector associated to each mode of vibration,

$$\omega = 2\pi \begin{bmatrix} 91057.353 \\ 91084.006 \\ 274309.584 \end{bmatrix} = 2\pi \begin{bmatrix} f_{L1} \\ f_{B2} \\ f_{\psi} \end{bmatrix} \qquad \Delta = \begin{bmatrix} 0 & 1 & 0 \\ 0.6099 & 0 & 1 \\ 1 & 0 & -0.3936 \end{bmatrix} \qquad \textit{Eq. IV.3.1.29}$$

Table IV.3.1-1. Parameters of piezo vibrator model.

Parameter	Symbol	Value	Units
Density	ρ	7500	kg/m^3
Length	L	15.2	mm
Width	w	3.9	
Thickness	h	2	
Transversal section	A	$w \cdot h$	mm^2
Second moment of area about x axis	I	$\frac{2h}{3}\left(\frac{w}{2}\right)^3$	mm^4
Elastic compliance	c_{11}	5.6×10^{10}	N/m^2
	c_{66}	2.6 ×10^{10}	
Piezoelectric coefficient	e_{31}	25.8	N/Vm
Dielectric coefficient	ε	3442	

Moreover, as all the eigenvalues are positive, the eigenvectors are M and K orthogonal, which is useful to test that the process has been correctly applied.

$$X_i^T \mathrm{M} X_j = 0$$

$$X_i^T \mathrm{K} X_j = 0$$

Then, replacing $X = \Delta Q$ in *Eq. IV.3.1.27* we get

$$\begin{bmatrix} \widehat{m_{11}} & 0 & 0 \\ 0 & \widehat{m_{22}} & 0 \\ 0 & 0 & \widehat{m_{33}} \end{bmatrix} \begin{bmatrix} \ddot{q}_L^2 \\ \ddot{q}_B^2 \\ \ddot{q}_R^2 \end{bmatrix} - \begin{bmatrix} \widehat{k_{11}} & 0 & 0 \\ 0 & \widehat{k_{22}} & 0 \\ 0 & 0 & \widehat{k_{33}} \end{bmatrix} \begin{bmatrix} q_L \\ q_B \\ q_R \end{bmatrix} = \begin{bmatrix} \widehat{b_{11}} & \widehat{b_{12}} & 0 \\ 0 & 0 & \widehat{b_{23}} \\ \widehat{b_{31}} & 0 & \widehat{b_{33}} \end{bmatrix} \begin{bmatrix} V_p \\ F_N \\ F_T \end{bmatrix} \qquad \textit{Eq. IV.3.1.30}$$

$$\widehat{\mathrm{M}}\ddot{Q} + \widehat{\mathrm{K}}Q = \widehat{\mathrm{B}}F;$$

And $\widehat{\mathrm{M}}$, $\widehat{\mathrm{K}}$ are now diagonal matrix, hence the system of equations is now decoupled. From *Eq. IV.3.1.29*, two important conclusions can be made:

- The resonance frequencies f_{L1} and f_{B2} of the L1 mode and B2 mode are very close.
- The value of frequency f_{ψ} is far greater than the other two.

If the frequency of driving voltage V_p is properly chosen, following *Eq. IV.3.1.17*,

$$f_r = \frac{f_B + f_L}{2} \ll f_\psi \qquad \textit{Eq. IV.3.1.31}$$

Only the L1 and B2 modes will be excited by and we can eliminate the equation of motion of ψ_R associated to the generalized coordinate q_R in *Eq. IV.3.1.30*, given that its frequency f_ψ, and therefore is mode of vibration $\phi_\psi(x)$, will not be excited by f_r. Finally, transforming back to the original coordinates by using $Q = \Delta^{-1}X$, and adding linear damping associated to each mode C_L, C_B, which has proven to give accurate results for describing the damping behavior for piezo-beam systems [106], we get a systems of ordinary differential equations from which we can obtain the temporal description of *Eq. IV.3.1.18* for the axial and transversal movement of the beam $u(x,t), v(x,t)$ under the first longitudinal and the second bending mode of vibration.

$$\begin{aligned} M_L\ddot{u}(t) + C_L\dot{u}(t) + K_L u(t) &= \alpha_N V_p + \eta_N F_N \\ M_B\ddot{v}(t) + C_B\dot{v}(t) + K_B v(t) &= \alpha_T V_p + \eta_T F_T \end{aligned} \qquad \textit{Eq. IV.3.1.32}$$

M_i and K_i are the modal mass and modal rigidity and the subindex L, B associates them with the longitudinal and transverse modes respectively. F_N denotes the axial force on the stator and includes the normal force, resulting from the action of the spring and the axial deformation of the ceramic as a consequence of the piezoelectric effect. F_T is the tangential force responsible for the transverse component of the movement, also linked to the transverse deformation, to the friction between the stator and the rotor and to the relative speed between the stator and the rotor as we will see in the next section.

IV.4. Normal and tangential force: *The stick-slip contact* subsystem.

The contact dynamics between the hard tip and the friction interface are determined by the normal force F_N and the tangential force F_T generated by the ceramic. An important assumption made here is that the hard tip is perfectly bonded to the piezo vibrator at the point $x = L$, so

$$\begin{aligned} x_{hardtip} &= u(t)\phi_L(L) \\ y_{hardtip} &= v(t)\phi_B(L) \end{aligned} \qquad \textit{Eq. IV.4.1}$$

At the time of its integration, the motor is positioned and pressed against a spacer which ensures a distance between the front end of the USM and the friction interface, such that the spring of stiffness k and length l_{s0} is compressed to a length L_{SP_0} which gives as a result the preload force F_P necessary for the operation of the motor.

$$F_P = k\left(l_{S_0} - l_{SP_0}\right) = k\Delta l \qquad \textit{Eq. IV.4.2}$$

The piezovibrator will also generate force as a result of inverse piezoelectric effect. Thus, when the voltage V_p value is zero, the deformation due to mechanical stress L_{st} is determined using

$$L_{st} = \frac{F_P}{k_c} \qquad \textit{Eq. IV.4.3}$$

Where k_c is an equivalent contact stiffness, which is equal to $E_{FI}A_{FI}/h_{FI}$, with E_{FI} the elastic modulus of the friction interface, A_{FI} the contact area, defined by the intersection of the hard tip and the friction interface and h_{FI} the thickness of the friction interface, as shown in Figure IV.4-1 [101].

Once a non-zero V_p is applied, dynamic deformation L_d will take place and the hard tip will dynamically change its position in the normal direction, along the x axis.

$$L_d = u(t)\big(\phi_L(L) - \phi_L(0)\big) \qquad \textit{Eq. IV.4.4}$$

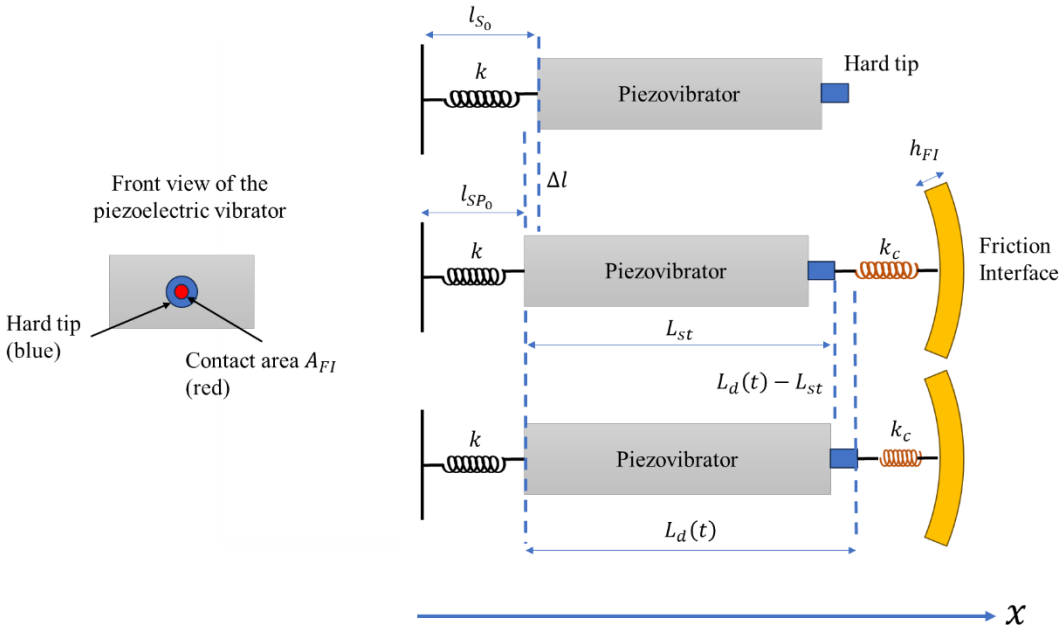

Figure IV.4-1. Normal dynamic force diagram.

The normal force F_N is therefore proportional to the prestress force F_P, and includes a dynamic component which depends on the L1 vibration mode

$$F_N = F_P + k_c(L_d - L_{st}) \qquad \textit{Eq. IV.4.5}$$

We see that the normal force is zero when

$$L_d = L_{st} - \frac{F_P}{k_c}$$

Likewise, if $F_P + k(L_d - L_{st}) < 0$, the normal force will be zero and the end will not be in contact with the rotor. Then

$$F_N = \begin{cases} F_P + k_c(L_d - L_{st}) & \text{when} \quad F_P + k_c(L_d - L_{st}) > 0 \\ 0 & \text{otherwise} \end{cases} \qquad \textit{Eq. IV.4.6}$$

The cyclical behavior of the dynamic force is due to the periodicity of the L1 mode. Every period, the dynamic deformation L_d will vary between the points of maximal and minimal longitudinal deformation, respectively caused by the mechanical tension and compression of the piezovibrator because of the piezoelectric effect.

The tangential force F_T is in turn dependent of the normal force, the friction coefficient μ, and the relative tangential speed between the hard tip velocity $\dot{v}$ and the rotor tangential velocity ωR. We can distinguish 3 stages that depends on the contact state of the hard tip with the friction interface: stick, slip and separation as

$$F_T = \begin{cases} F_{stick} \in [-\mu_s F_N, \mu_s F_N] & \text{when} \quad F_N > 0 \text{ and } \dot{v} - \omega R = 0 \\ F_{slip} = sign(\omega - \omega_R)\mu_d F_N & \text{when} \quad F_N > 0 \text{ and } \dot{v} - \omega R \neq 0 \\ 0 & \text{when} \quad F_N \leq 0 \end{cases} \qquad \textit{Eq. IV.4.7}$$

The coefficient of static friction only appears in stick phase and is responsible of the stick force. From the moment there is non-zero tangential relative velocity between the hard tip and the rotor, coefficient of dynamic friction appears and slip force takes place. It is possible to obtain the stick force considering that while it occurs, the acceleration of $\ddot{y}_{hardtip} = \dot{\omega}_{rotor}$

IV.5. *The rotary load* subsystem

The angular acceleration α of a body with a moment of inertia I_M about an axis passing through its center of mass is equal to the sum of torques about that axis. In our case, the load is linked to the rotor and besides its moment of inertia, we must consider possible decentering between the axis of rotation of the rotor and the center of mass of the load. The perpendicular distance defined by such offset will generate a torque τ_d that the actuator must compensate. Then according to Newton's equation for rotational motion,

$$I_M \alpha = F_T R - \tau_d \qquad \textit{Eq. IV.5.1}$$

Where R is the radius of curvature of the arc interface that is in contact with the hard tip of the USM.

IV.6. Conclusions of this chapter

In conclusion, this chapter has provided a comprehensive overview of the mathematical model developed for our piezoelectric leveler. The modeling process has been a critical step in understanding the complex dynamics and behavior by discussing the underlying principles of ultrasonic actuation based on L1B2 beam vibrators and highlighting the importance of modeling in gaining insights into its performance. This included the wave equations governing the propagation of ultrasonic waves and the piezoelectric equations that define the actuator's response to sinusoidal excitation at a proper value of frequency throughout various mathematical techniques, including modal decomposition, matrix methods and analytical approximations.

We explored the assumptions and simplifications made during the modeling process, which are necessary to create a dynamic model that could be used for simulation and analysis together with the key parameters and variables that play a crucial role in the model, such as material properties, geometry, and boundary conditions. The discussion on how variations in these parameters can impact the actuator's performance will be treated with more emphasis in the next chapter where the provided equations will serve for simulating the actuator's behavior under different operating conditions.

Finally, we highlight the importance of model validation with experimental data. This process will allow us to assess the model's accuracy and make refinements where necessary, ensuring that it closely represents the real-world behavior of the designed piezo leveler.

In summary, the mathematical model developed in this chapter provides a base for AML in the design of future rotative actuators based in standing wave ultrasonics.

V. EXPERIMENTS AND SIMULATION

V.1. Introduction

The definition of the piezo actuator and the design of the leveler, both explained in chapter II, allowed us to build a prototype. Before presenting the result of the leveler prototype, the different steps necessary for the assembly of the ultrasonic motor are described, and some useful remarks will be discussed. This seeks to familiarize the reader with the handling of the different components needed in standing wave ultrasonic motors.

This chapter also focuses on the numerical simulations performed to validate the dynamic model developed in chapter IV. A Runge–Kutta integration scheme is employed to solve the differential equations in the model by using Simulink software (MathWorks, Natick, MA). The parameters used in the simulation are defined by the design choices made and explained in chapter III.

V.2. The Standing Wave Ultrasonic Motor (SWUSM) assembly

As described in chapter III, the prototype of the USM is based on the L1B2 piezoelectric vibrator of EDGE4X by Nanomotion. Its operating principle is briefly recalled here:

Sinusoidal voltages are applied to diagonally opposed electrodes on the piezo vibrator which is polarized along its thickness. The first longitudinal mode (L1 mode) and the second bending mode (B2 mode) of the piezo vibrator are excited when the frequency of the input voltage is close to the natural frequencies of these two vibration modes. Consequently, a clockwise elliptic motion is formed at the alumina (Al2O3) hard tip, which can be reversed by changing the active electrodes from group I to group II. In Figure V.2-1, we show the piezo vibrator used for the realization of this prototype and its main dimensions (length and width of the piezo vibrator and length of the hard tip) taken with a Leica Microscope M205C

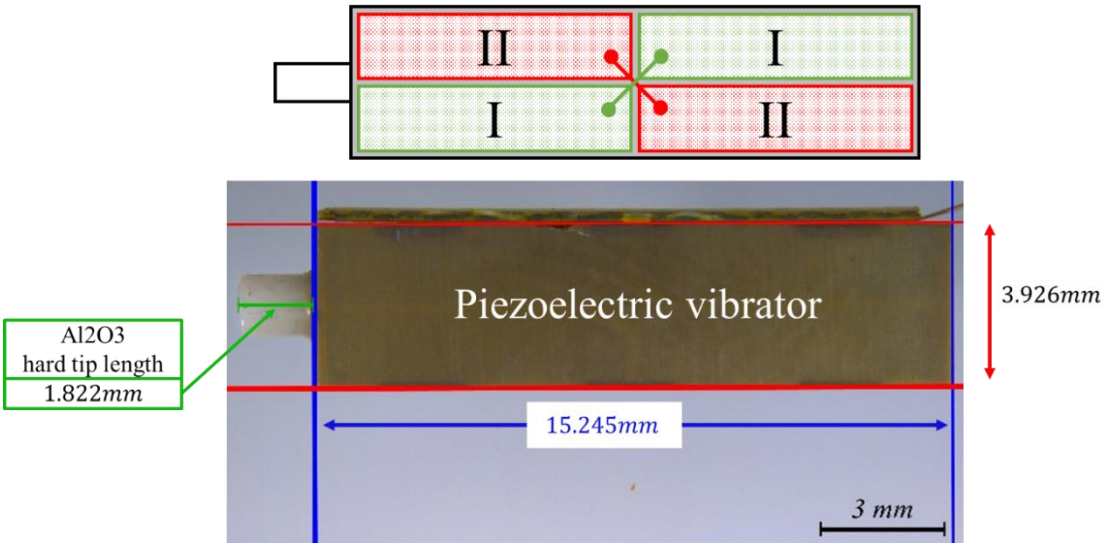

Figure V.2-1. Piezoelectric vibrator, taken from the EDGE4X USM.

The two symmetrical nodes of B2 mode facilitate the fixation of the piezo vibrator in its housing box, and together with the clamping structure, the lateral springs and the preload spring compose the SWUSM. The springs has been chosen following Nanomotion guidelines according to the size of the piezo vibrator of the EDGE4X USM. These components (Figure V.2-2) are all manually assembled following the next steps:

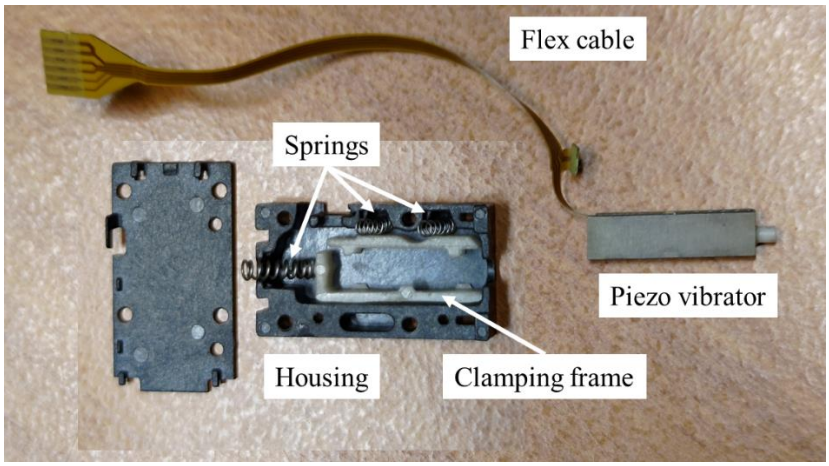

Figure V.2-2. Components of the SWUSM.

1. We started by inserting the piezo vibrator in the clamping frame.

2. Then, with the flex cable oriented towards the slit designed for its passage, we put the ensemble inside the housing. The hard tip must pass through the frontal hole as shown in Figure V.2-3.

3. We continued with the insertion of the lateral springs in the lateral cavities designed for them. Given their small length and diameter, of some millimeters, and the compression needed for placing them inside the lateral cavities, we decided to use precision tweezers, usually used in electronics assembly tasks. In order to facilitate the insertion of these springs, the clamping frame is also designed with small extrusions around which the spring diameter can be secured.

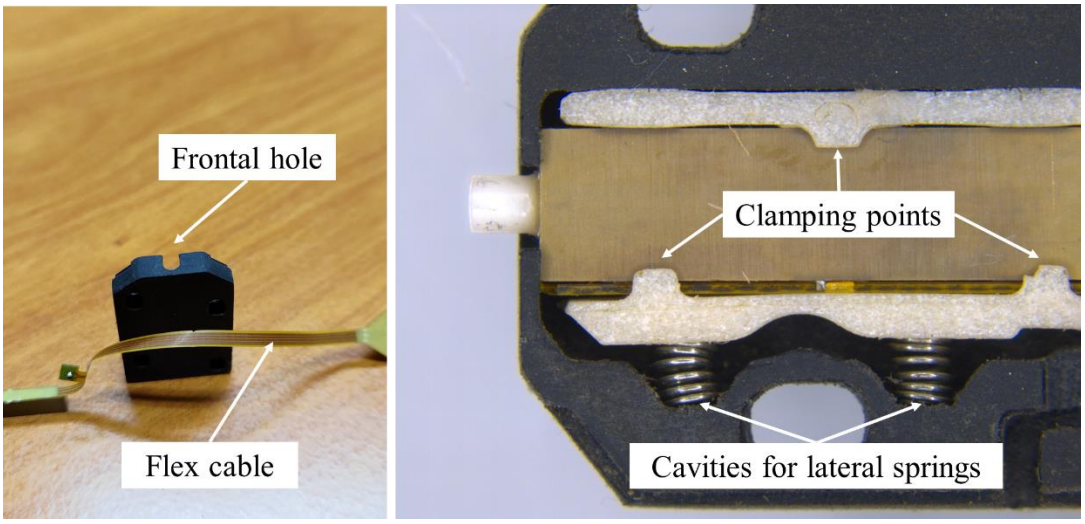

Figure V.2-3. Lateral springs assembly in the USM housing. Right image taken with Leica M205C.

4. After the previous step, the piezo vibrator will be more firmly restrained in the housing cavity which will facilitate the insertion of the preload spring (shown in Figure V.2-4.A) in the opposite side of the hard tip in a similar way to the lateral springs.

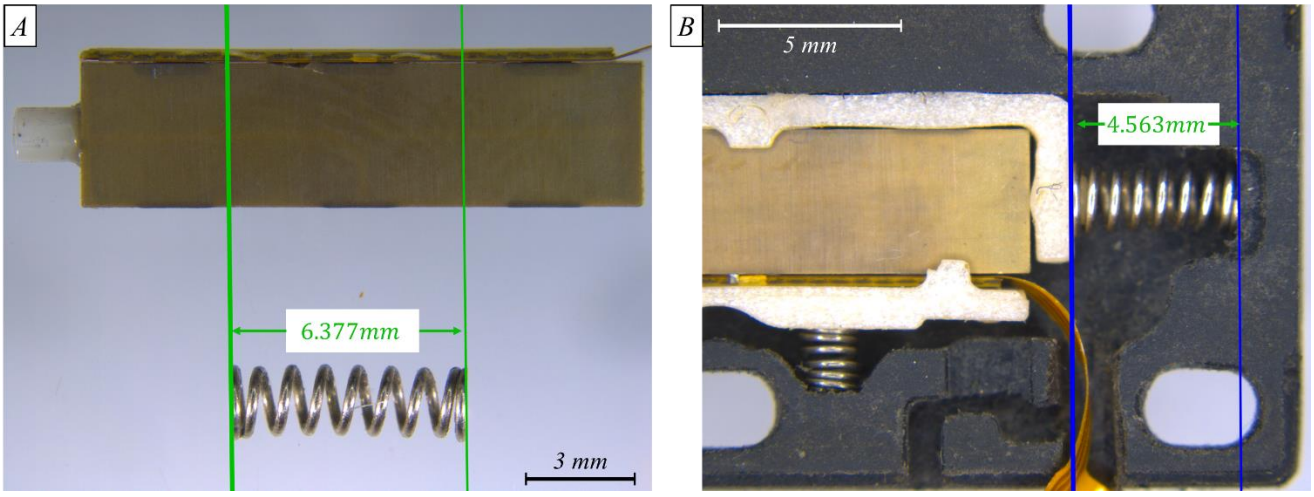

Figure V.2-4. A. Measurement of the preload spring. B. Preload spring after assembly in the USM housing.

Figure V.2-5.A shows the internal structure of the SWUM once assembled, where the stator is fixed at the nodes of the second bending vibration by the three ribs ① ② ③ found on the clamping frame.

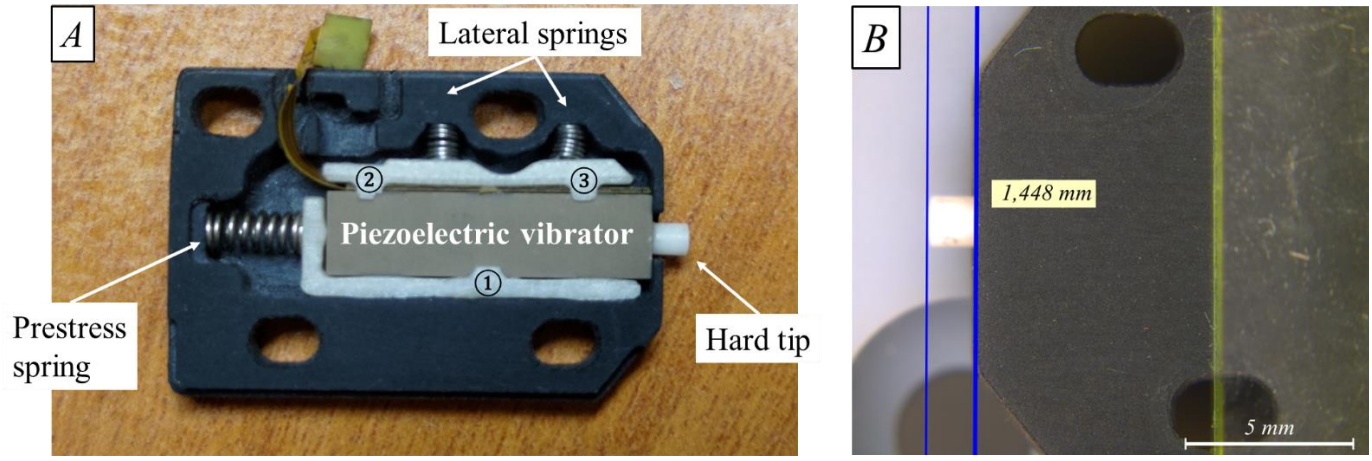

Figure V.2-5. A. The internal structure of the assembled SWUSM. B. Measurement of the hard tip distance

The Nanomotion piezo vibrator can be used at temperatures ranging from -10°C to 60°C thus according to these limits, Polypropylene Homopolymer is selected for the frame and the housing material as it is appropriate for applications at 82°C. In seek of keeping tolerances, this material is convenient for CNC milling [107].

In Figure V.2-4, we show two length measurements of the preload spring before and after its insertion. The latter is related to the hard tip length, shown in Figure V.2-5.B, when no preload is applied on the USM. These lengths are necessary for calculating the preload force F_P once the USM is put against the friction interface.

Table V.2-1. Length measurements of preload spring and hard tip.

Length of the preload spring under no constraint	l_{s0}	6.377mm
Length of the preload spring after USM mounting	l_{s1}	4.563mm
Length of the hard tip under no constraint	l_{t1}	1.448mm

V.3. The Leveler prototype assembly

Figure V.3-1 shows the different parts constituting the actuator. All these pieces were made with CNC machining because some dimensions were defined to respect tolerances regarding assembly easiness and precision. For example, the radius of the internal surface of the friction interface was set to $60 \pm 0.05mm$ and the diameter tolerances regarding bearing mounting in the housing, cover and rotor's shaft was set according to what was explained in section *III.6.1. The prestress and bearing configuration*. Concerning the material choice of these parts, all of them but the friction interface are made of Aluminum 6082.

Because hardness is important for the best force transmission between the hard tip and the friction interface, the best material for it would be the same as the hard tip material, alumina AL_2O_3. Nevertheless, this material is expensive and more difficult to machine when more complex geometries are needed. For these reasons, we decided to use Stainless Steel 304. This material choice is suitable in short term solutions but we know beforehand that the hard tip will tend to wear the metal so for longer

lifetime scenarios, ceramic materials as alumina need to be privileged. There are several aspects that we took into account for the assembly of the actuator that are detailed next.

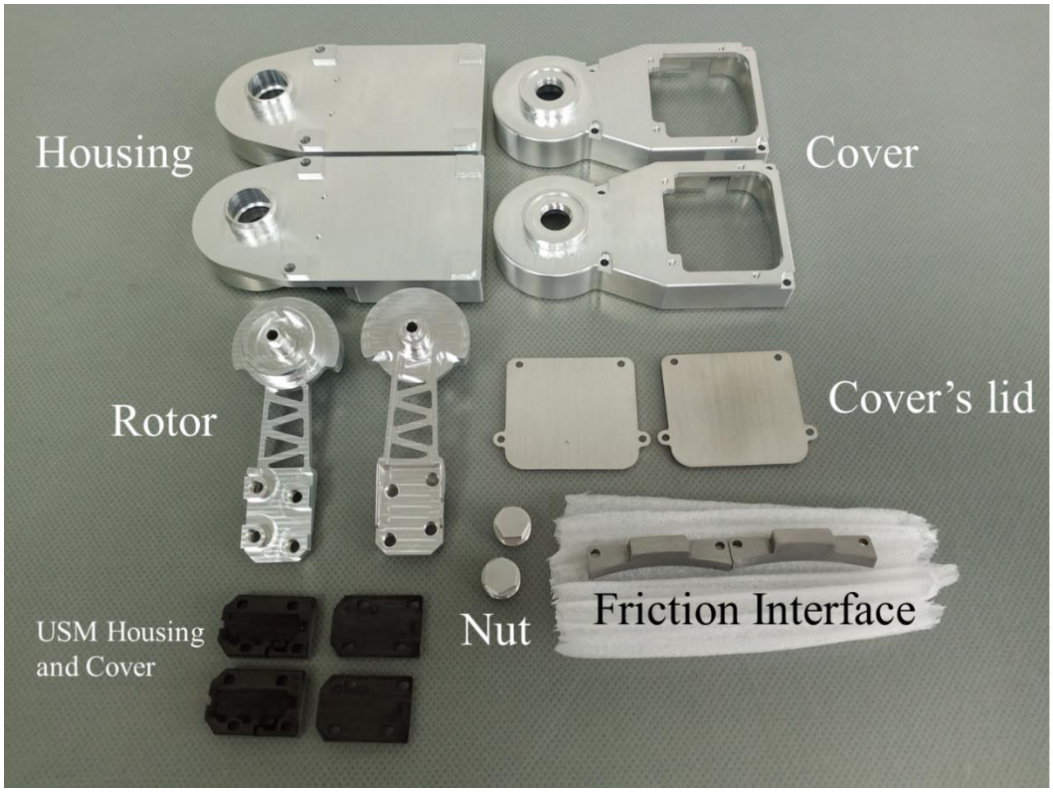

Figure V.3-1. Actuator mechanical components.

V.3.1. Bearing mounting on the rotor's shaft

Our actuator uses two bearings, both inner rings with k5 fitting (fit tight) on the aluminum shaft of the rotor and outer ring with H7 (loose fit) on their respective cages in the actuator's housing and cover. We privileged temperature mounting method over hammering mounting methods, which reduces the risk of bearing or shaft damage during installation as it makes easier sliding the bearing onto the shaft. A temperature differential is obtained by uniformly heating the bearings in an oven at 70°C and cooling the rotor at -5°C for 10 minutes. Then, the bearings were mounted by soft pressing on the inner ring by means of a mounting fixture and a press.

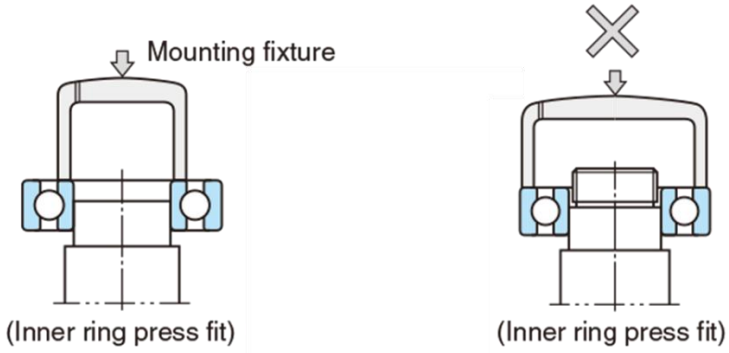

Figure V.3.1-1. When mounting the inner ring with tight fitting, apply pressure to the inner ring only as rolling elements are easily damaged. Image taken from [108]

V.3.2. Encoder and magnetic ring mounting

Our measure system based on a 31mm magnetic ring and the RLC2IC encoder from RLS® must respect the mounting tolerances shown in Figure V.3.2-1.

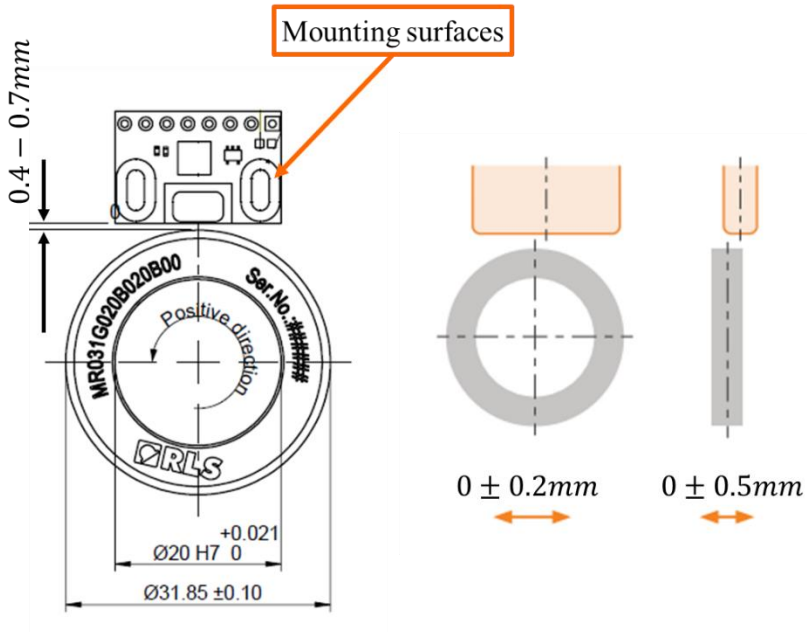

Figure V.3.2-1. Mounting tolerances of the sensing system.

The PCB encoder is positioned in the housing, on two supports similar to the mounting surfaces of the PCB designed so the height tolerance of $0 \pm 0.5mm$ is respected. Then a template that has the same footprint of the magnetic ring is slip into the cavity. This template facilitates the fixation of the encoder so the lateral tolerance of $0 \pm 0.2mm$ and the ride height of $0.4 - 0.7mm$ are respected. Finally, two M2 screws maintain the encoder in place.

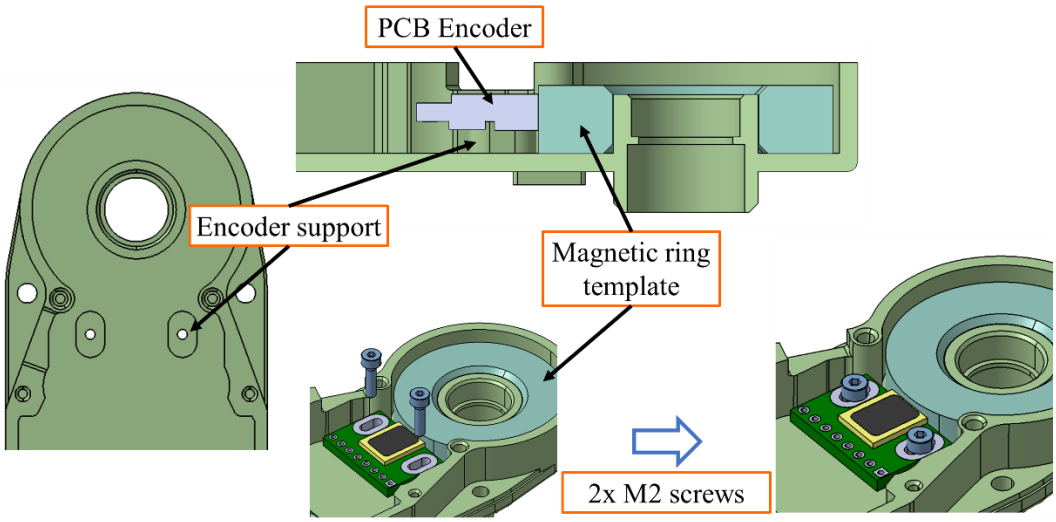

Figure V.3.2-2. Mounting the encoder.

As explained in *III.6.2. The sensing system*, the magnetic ring is slip and glued onto the rotor's shaft with the reference mark pointing towards the encoder as we will use this mark for the zero homing of the actuator.

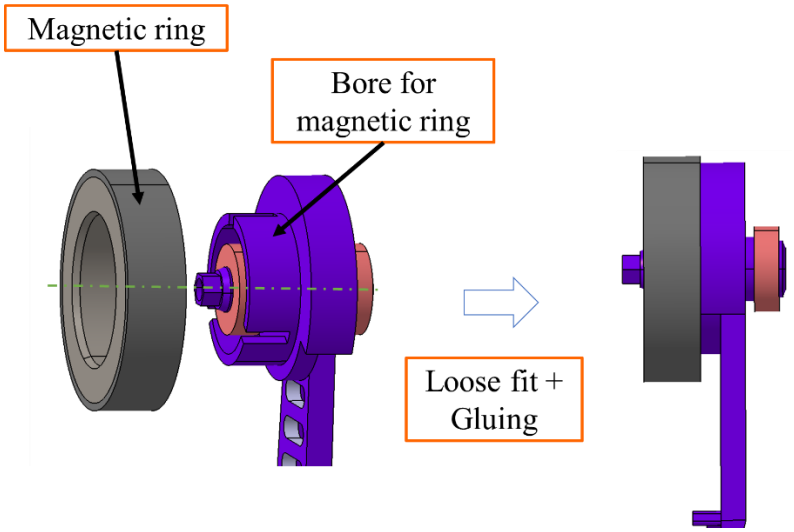

Figure V.3.2-3. Mounting the magnetic ring.

V.3.3. Friction interface mounting and USM mounting.

In a previous design prototype (Figure V.3.3-1), the mounting of the friction interface was designed to be glued in the slit designed in the housing for it. This approach aimed to simplify the friction interface structure and hence reduce its cost production by implementing an arc strip of 60mm inner radius, 2mm thickness and 4mm height.

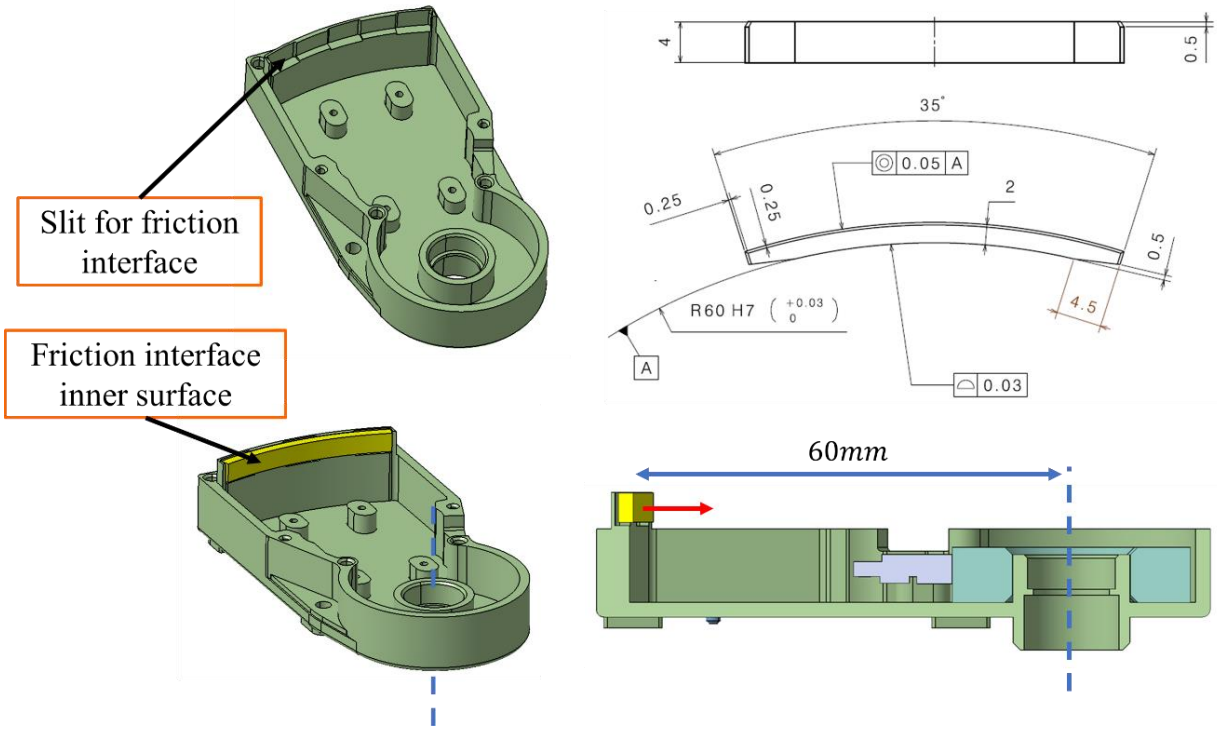

Figure V.3.3-1. Gluing friction interface on housing slit.

Nevertheless, this design concept presented a drawback. Assuring proper surface contact between the friction interface outer surface and the slit proved to be difficult which resulted in a non-coaxiality between the axis of revolution of the friction interface and the axis of rotation of the actuator, i.e. non perpendicularity between the normal to the inner surface of the friction interface (represented by a red arrow in Figure V.3.3-1) and the axis of rotation. After mounting the USM, a reaction force on the whole rotor causes static tilt δ_t which in consequence over constrains the bearings internal clearance, reduces the total range of movement of the actuator and produces high vibrations and wear debris which affects the smoothness of the output movement.

Theoretical: No misalignment	Real: Angular deviation δ_t of the axis.
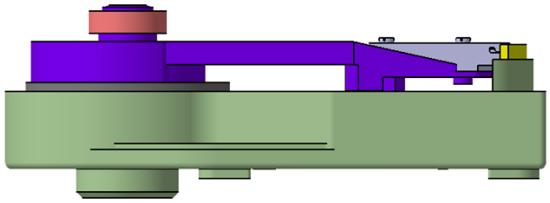	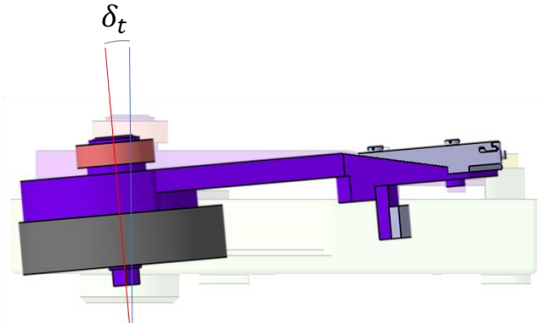

For this reason, we redesigned the friction interface and decided to avoid the use of non-planar surfaces as a reference for mounting. Instead, the perpendicularity is assured by planar contact of flat supports in the friction interface and the slit in the housing. This new concept makes easier the mounting of the friction interface which is done by means of two M2 screws.

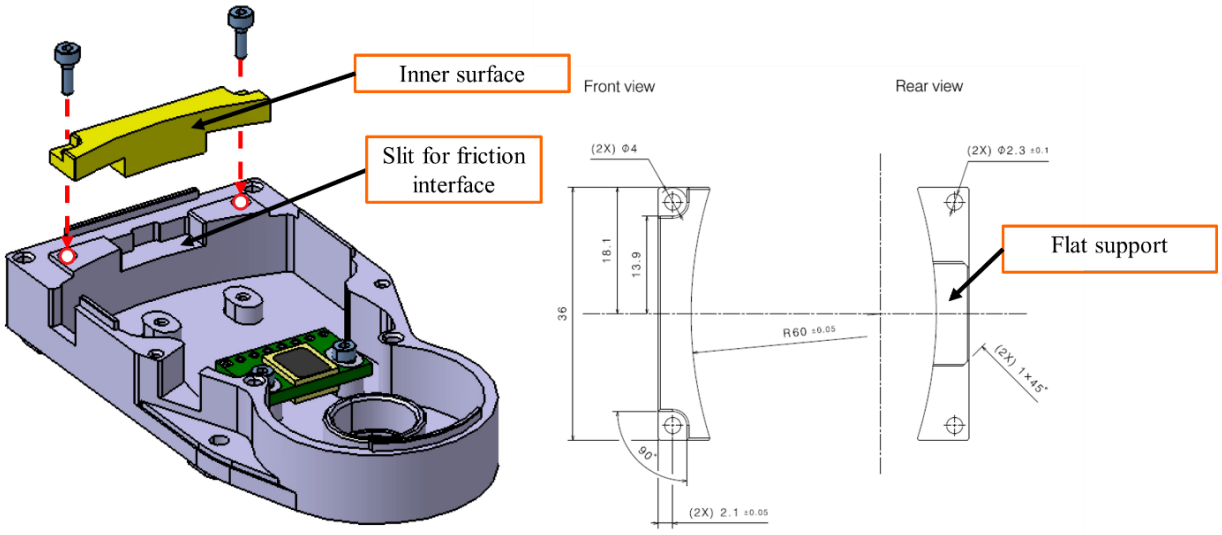

Figure V.3.3-2. Assembly of the redesigned friction interface with screws.

After this, the rotor's shaft is inserted in the cavity of the housing and a preload can be applied by adjusting the distance between the USM front and the friction interface by means of a spacer of thickness. After setting in place the motor on the rotor, we positioned the spacer between the motor and the friction interface as shown in Figure V.3.3-3. Then, while manually holding the motor against the spacer, we fasten the four screws in the four mounting holes of the USM's cover in a diagonal sequence.

The USM is now mounted and the resulting distance between the front of the USM and the friction interface is defined as the preload distance d_P, which is shown in Figure V.3.3-4 and is equal to 0.745mm. Due to the length difference between the mounting slot in the USM and the mounting hole in the rotor, there is a small degree of freedom so d_P can be modified using another spacer of different thickness.

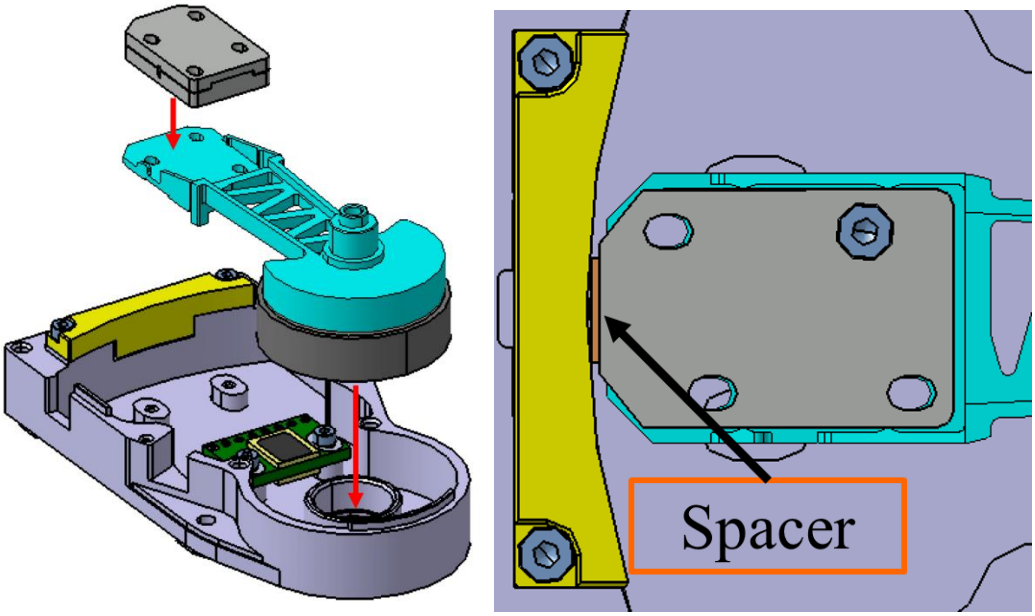

Figure V.3.3-3. Fixing the motor and setting the preload distance.

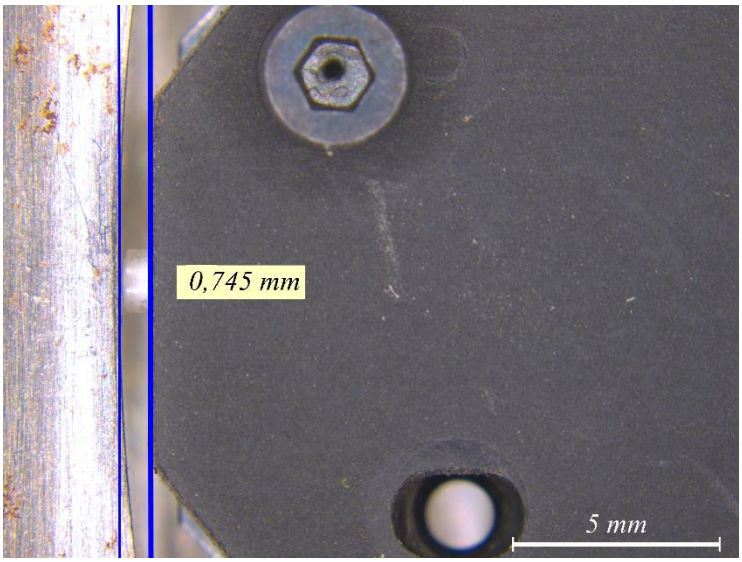

Figure V.3.3-4. Measaurement of preload distance d_P.

After measuring d_P, and the lengths of the preload spring and the hard tip (listed in Table V.2-1), we can calculate the preload force F_P exerted by the preload spring of stiffness k

$$F_P = k \cdot \left(l_{s0} - l_{s1} + (d_P - l_{t1})\right)$$
$$F_P = F_{P0} + k \cdot d_P; F_{P0} = k \cdot (l_{s0} - l_{s1} - l_{t1}) \qquad \textit{Eq. V.3.3.1}$$

Finally, the rest of the components are assembled. The covers lid allows access to the USM, so preload distance d_P can be adjusted and measured without needing covers removal.

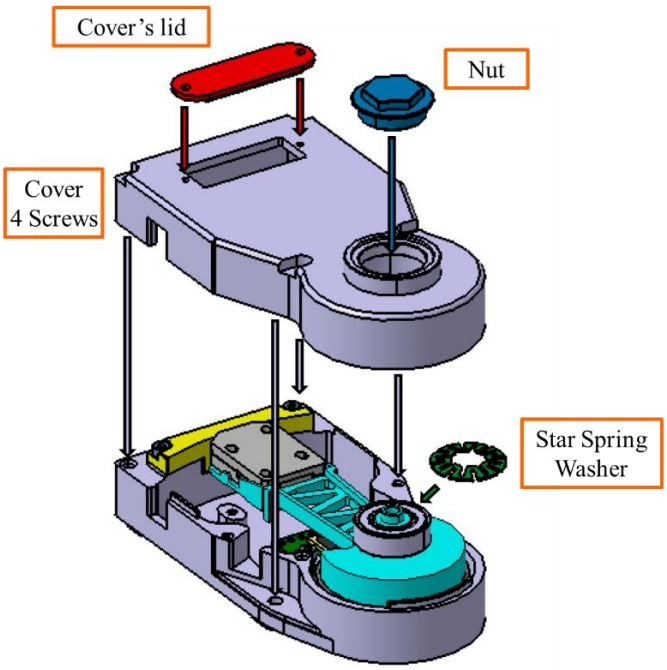

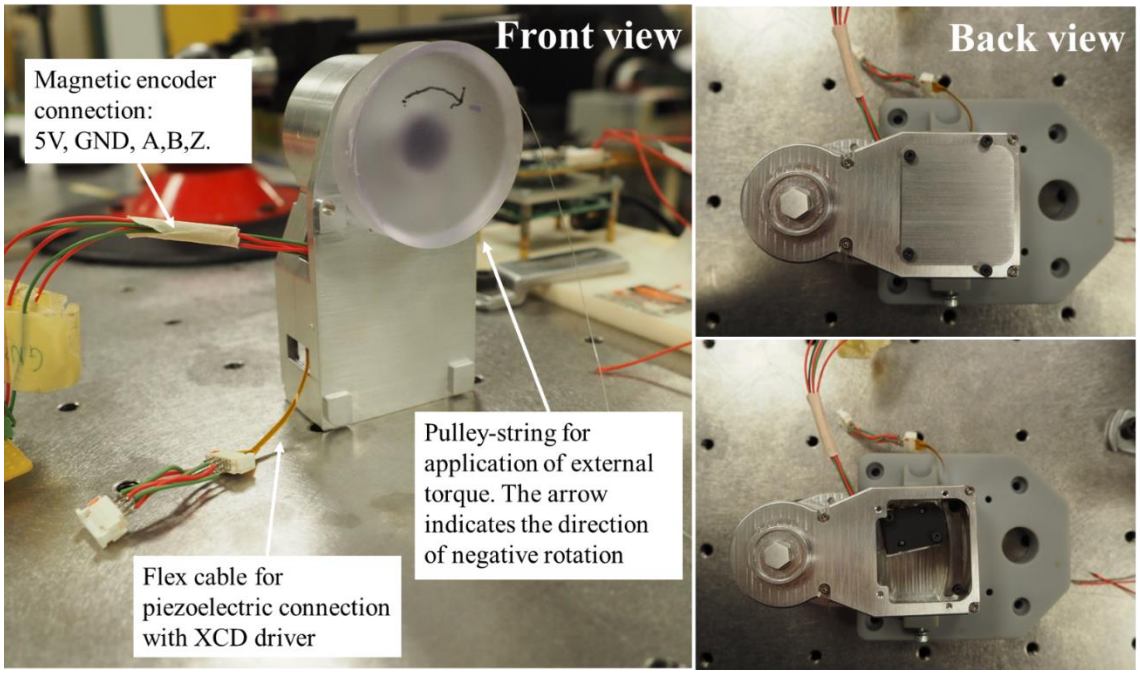

Figure V.3.3-5. Final assembly of the piezoelectric leveler and front view of the actuator in standing position. The back side of the actuator is shown with and without the cover's lid.

V.4. Numerical simulation

In chapter IV, dynamic modeling was explained by taking the whole actuator as a series of interconnected subsystems. Following this strategy, we decided to perform numerical simulations of the piezo leveler to evaluate the performance and dynamics of the actuator and the impact that a given parameter have on the behavior of the actuator, especially in the steady-state output of the actuator. For

this, we divided the piezo leveler in four subsystems as shown in the flowchart of Figure V.4.1-1. Each subsystem is characterized by a main equation, all previously obtained from the dynamic modeling discussed in chapter IV.

1. The driver, which is the electrical input characterized by a sinusoidal voltage V of amplitude V_{DC} and frequency f.

$$V_P = V_{DC}\sin(2\pi f t) \qquad \textit{Eq. V.4.1}$$

2. The piezoelectric ceramic, where the longitudinal displacement $u(x,t)$ and transverse displacements $v(x,t)$ are decomposed in a temporal component and a spatial component as

$$\begin{aligned} u(x,t) &= u(t)\phi_L(x) \\ v(x,t) &= v(t)\phi_B(x) \end{aligned} \qquad \textit{Eq. V.4.2}$$

By solving *Eq. IV.3.1.32* (here renamed *Eq. V.4.3)*, we can obtain the temporal component of equation *Eq. V.4.2*, while *Eq. IV.3.1.19* (renamed *Eq. V.4.4*) allows us to obtain the spatial component

$$\begin{aligned} M_L\ddot{u}(t) + C_L\dot{u}(t) + K_L u(t) &= \alpha_N V_p + \eta_N F_N \\ M_B\ddot{v}(t) + C_B\dot{v}(t) + K_B v(t) &= \alpha_T V_p + \eta_T F_T \end{aligned} \qquad \textit{Eq. V.4.3}$$

$$\begin{aligned} \phi_L(x) &= \cos\left(\frac{\pi x}{L}\right) \\ \phi_B(x) &= \alpha(\cos\beta x + \cosh\beta x) + \sinh\beta x + \sin\beta x \end{aligned} \qquad \textit{Eq. V.4.4}$$

As we are particularly interested in the friction contact between the hard tip and the friction interface, *Eq. IV.3.1.19* is computed for $x = L$

$$\begin{aligned} \phi_L(L) &= \cos(\pi) \\ \phi_B(L) &= \alpha(\cos\beta L + \cosh\beta L) + \sinh\beta L + \sin\beta L \end{aligned} \qquad \textit{Eq. V.4.5}$$

3. The interface model, that is the rotor-stator interaction and the resulting forces described by *Eq. IV.4.6* and *Eq. IV.4.7* here renamed *Eq. V.4.6* and *Eq. V.4.7* respectively.

$$F_N = \begin{cases} F_P + k_c(L_d - L_{st}) & \text{when} \quad F_P + k_c(L_d - L_{st}) > 0 \\ 0 & \text{otherwise} \end{cases} \qquad \textit{Eq. V.4.6}$$

$$F_T = \begin{cases} F_{stick} \in [-\mu_s F_N, \mu_s F_N] & \text{when} \quad F_N > 0 \text{ and } \dot{v} - \omega R = 0 \\ F_{slip} = sign(\omega - \omega_R)\mu_d F_N & \text{when} \quad F_N > 0 \text{ and } \dot{v} - \omega R \neq 0 \\ 0 & \text{when} \quad F_N \leq 0 \end{cases} \qquad \textit{Eq. V.4.7}$$

4. The rotational output under a given load which applies a couple τ_d defined by

$$I_M\alpha = F_T R - \tau_d \qquad \textit{Eq. V.4.8}$$

V.4.1. Inputs and parameters in the simulation

The simulation is implemented in Matlab Simulink software where the Runge–Kutta solver is used for numerically solving the previous equations. Because of the high frequency dynamics of the piezo

vibrator (in the order of 90kHz), the simulation time step Δt is fixed to 0.5 μs, a step resolution that allows us to obtain the vibration responses of the piezo vibrator $u(x,t), w(x,t)$, the cyclical contact dynamics described by the normal force F_N and the tangential force F_T and the steady-state output of the piezo leveler.

To the parameters mentioned in Table IV.3.1-1 necessary for the computation of the constants $M_L, M_B, K_L, K_B, \alpha_N, \alpha_T, \eta_N, \eta_T$, we add the parameters defined in Table V.4.1-1 to simulate the designed piezo leveler actuator. The damping coefficients C_L, C_B were determined experimentally by curve fitting.

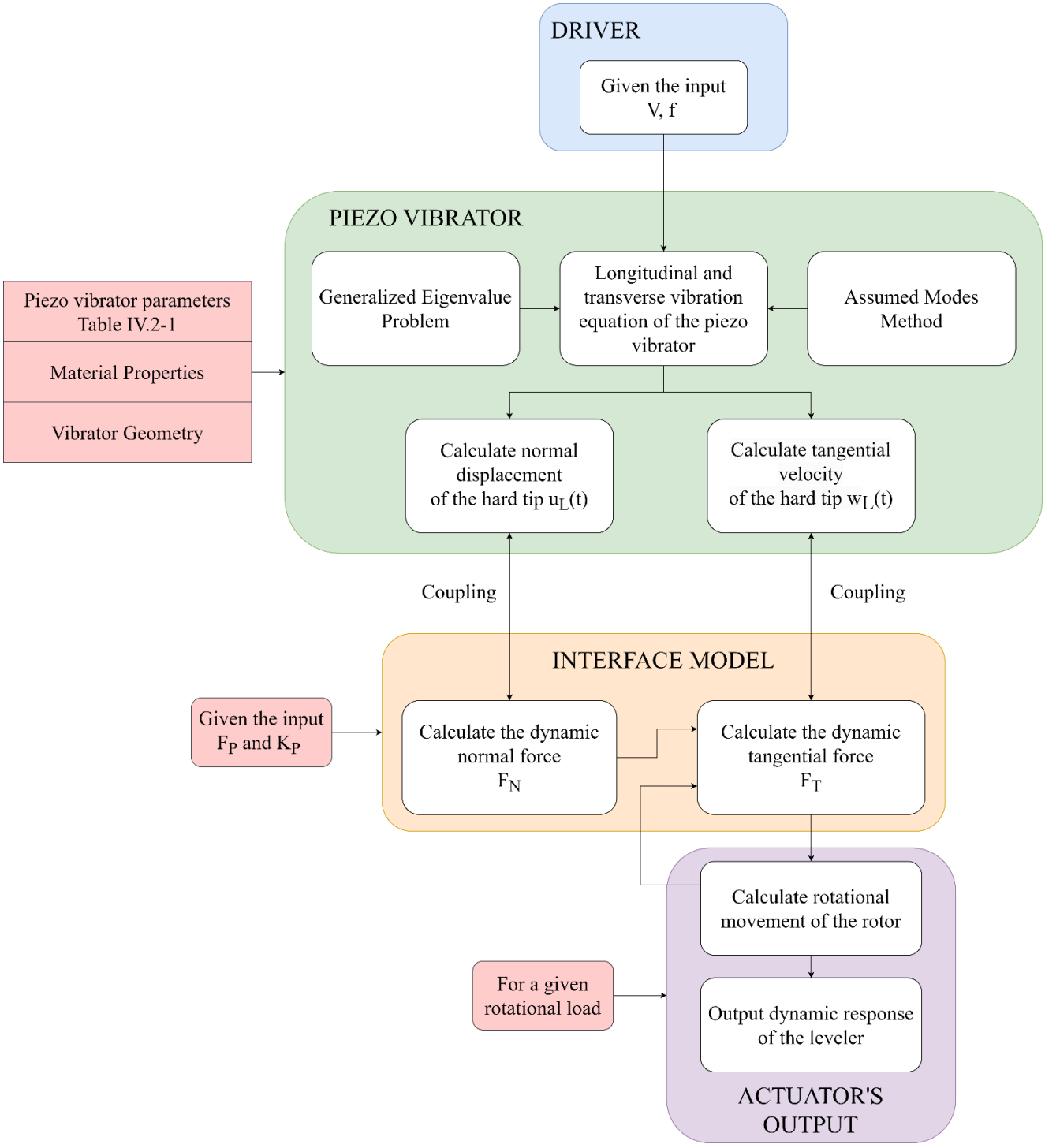

Figure V.4.1-1. Simulation flowchart

Table V.4.1-1. Parameters of the simulation.

Parameter	Symbol	Value	Units
Voltage frequency	f	89015	Hz
Modal mass	M_L	4×10^{-4}	kg
	M_B	4×10^{-4}	
Modal damping	C_L	20	Ns/m
	C_B	28	
Modal stiffness	K_L	1.42×10^8	N/m
	K_B	2.72×10^8	
Electromechanical coupling factor	α_N	0.0979	N/V
	α_T	-0.104	N/V
Load factor	η_N	2	
	η_T	2.74	
Preload force*	F_P	4	N
Interface stiffness*	k_P	1.73×10^7	N/m
Friction coefficient*	μ_s	0.35	
Actuation radius*	R	60×10^{-3}	m
Rotor inertia*	I_M	5×10^{-5}	kg.m^2

*Parameters calculated for the prototype

V.5. Experiment set-up

Corresponding experiments were conducted to validate the simulation results. A schema of the experimental set-up is shown in Figure V.5-1. The experimental set-up comprises two parts, the driving and acquisition system, and the test system.

As mentioned in chapter III, the scope of this project does not include the design of the driver, hence the driving system consists of an XCD Nanomotion driver which is able to furnish an AC voltage at a given frequency for the vibrator to resonate in L1B2 mode. It also comprises a port for the encoder connection and two analog outputs from 0 to 3.3V that we connect to a National Instruments USB 6002 DAQ to acquire the position data of the encoder.

On the other hand the test system includes the assembled piezo leveler with encoder sensor that measures the position of the rotor as described in chapter III. Additionally, a string-pulley-weight system is used to apply a load torque on the piezo leveler which is defined by the suspended masses and the radius of the pulley of 20mm, whose axis of rotation coincides with the output axis of the piezo leveler. The tangential force is calculated using Newton's second law, assuming a gravity acceleration value g of $9.81 m/s^2$.

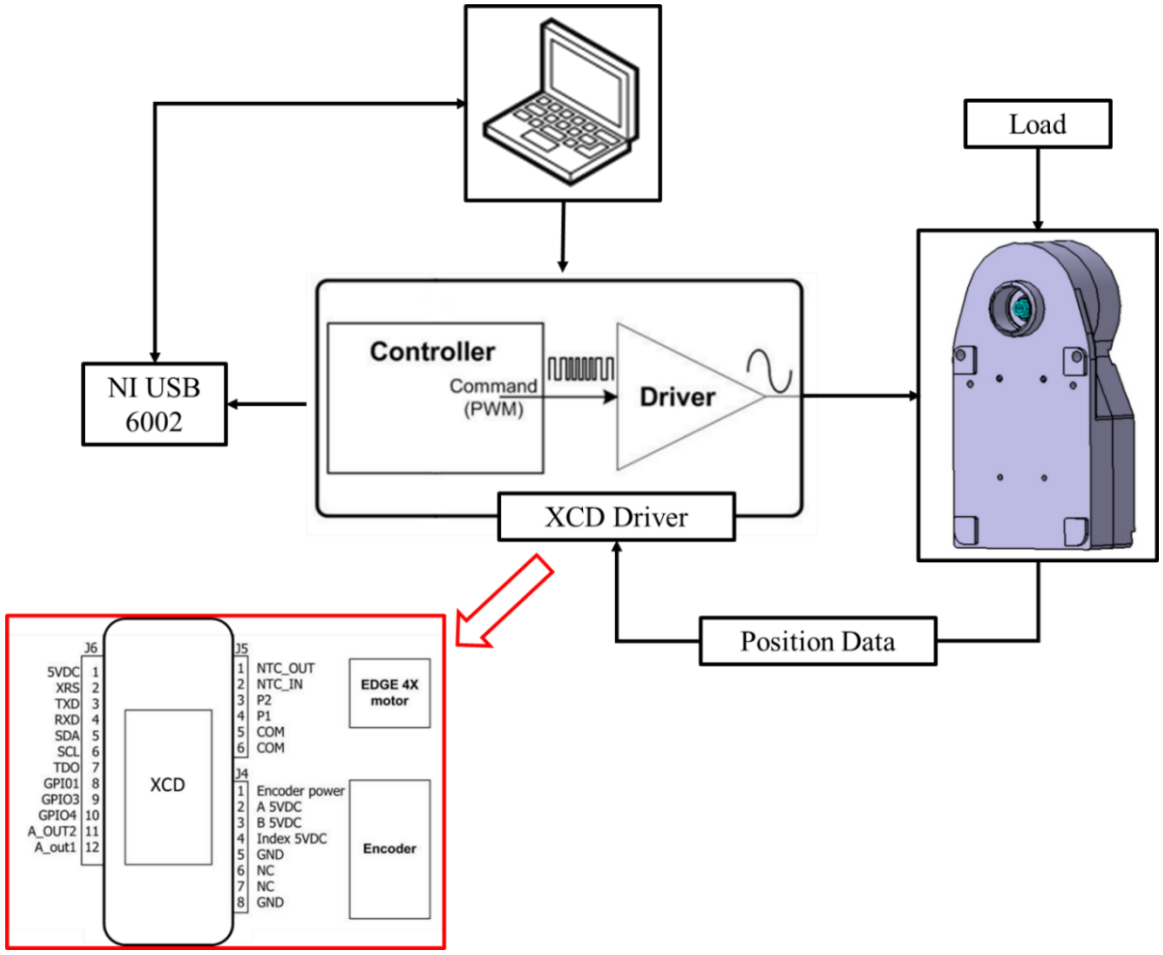

Figure V.5-1. Schema of the experimental set-up and detail of the XCD driver.

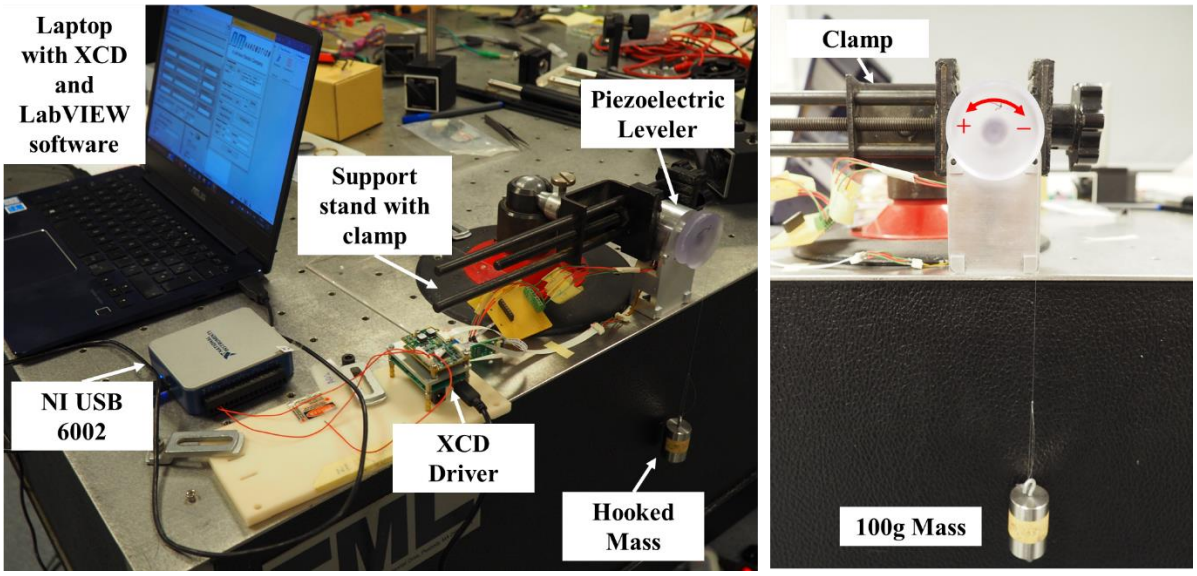

Figure V.5-2. Experimental set-up for measuring actuator performance under a given load.

V.5.1. L1 and B2 resonance frequencies

The XCD driver allows to modify the amplitude of the driving voltage by changing the duty cycle of a PWM, yet the frequency remains fixed. Figure V.5.1-1 shows an example of the output signal at 100% of duty cycle.

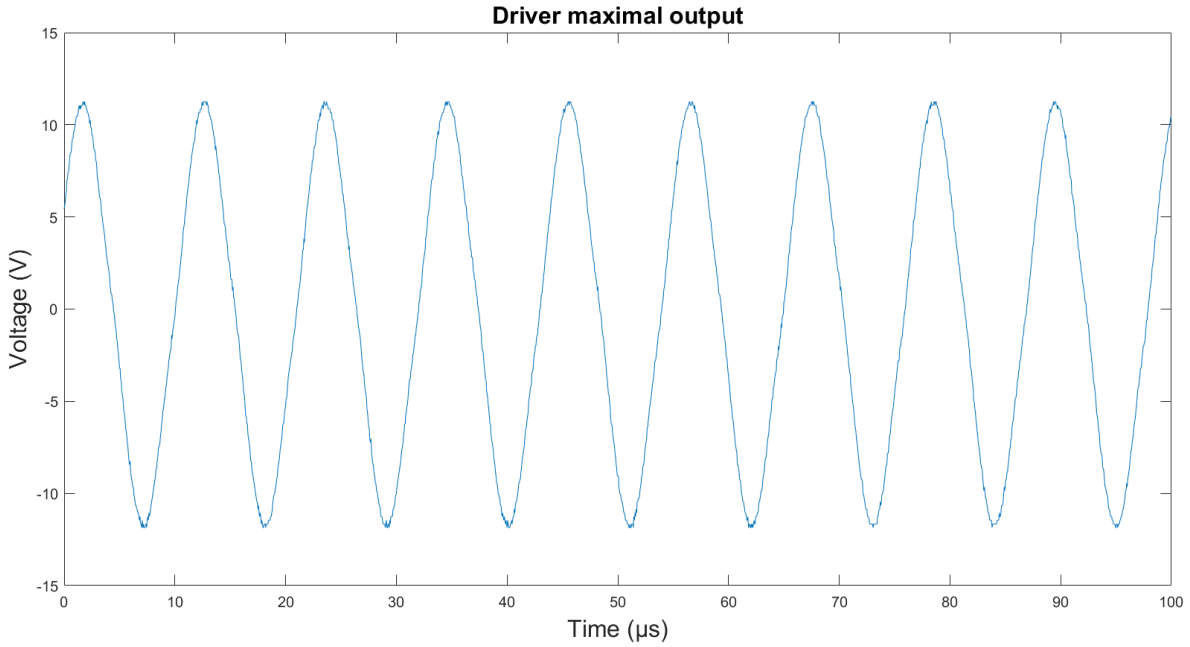

Figure V.5.1-1. Voltage output by the XCD driver at 100% of duty cycle.

We could take advantage of this for comparing the calculated frequency of the L1 and B2 modes f_L, f_B and the output frequency of the driver. By means of an oscilloscope Keysight 200MHz, we acquired the voltage output by the XCD driver at 100% of duty cycle and we got a first estimate about the order of magnitude of the frequency, around 90kHz. In order to obtain a more accurate result, we decided to compute its Fast Fourier Transform (FFT), so we could verify if it is really a single-frequency signal and what is its value.

The resolution of the Fourier transform depends on the sampling frequency which, according to the Nyquist–Shannon sampling theorem, must be greater than twice the frequency of the signal to be analyzed to avoid aliasing problems. After the first estimate obtained with the oscilloscope, we set the sampling frequency to 250kHz and sampled 0.2s of signal which corresponds to 50 thousand points, that corresponds to a resolution of 5Hz in the calculated frequency spectrum. The result is shown in Figure V.5.1-2.

This first analysis allows us to conclude that the piezoelectric is single-frequency excited by a voltage of 91055Hz which is a very close value to the ones we obtained when solving the generalized eigenvalue problem (see *Eq. IV.3.1.27* in chapter IV) f_L, f_B corresponding to the frequency of the L1 and B2 mode respectively.

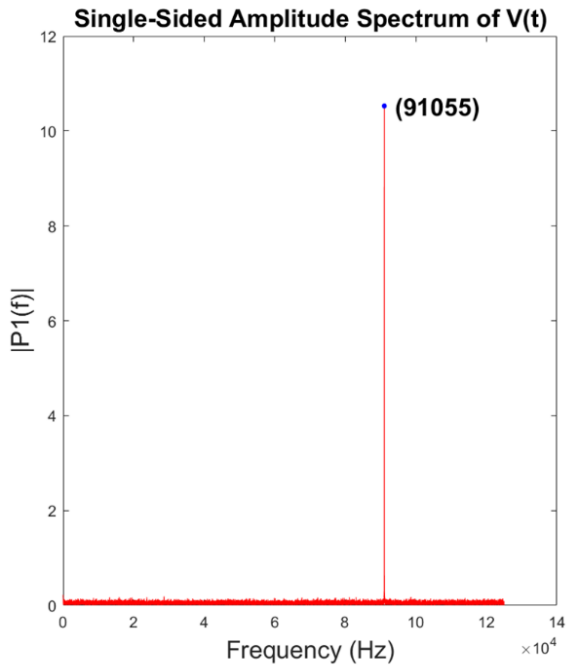

Figure V.5.1-2. Frequency spectrum of the signal output by the XCD driver.

The mean value of both frequencies is a good approach to excite both modes of vibration, so we assume that the experimental value obtained through Fourier analysis must be compared to the mean of f_L, f_B which will also be the value f we use in the simulations (see *Eq. V.4.1*)

Table V.5.1-1. Frequency analysis for the input voltage.

f_L (Hz)	f_B (Hz)	Mean value f (Hz)	Experimental (Hz)	Absolute error (Hz)	Relative Error
88146	89885	89015	91055	2040	2.2%

V.6. Performance evaluation of the actuator

As mentioned before, the simulations allow the evaluation of the performance of the piezo leveler for a given set of parameters. The dynamic model takes into account the material properties and dimensions of the piezoelectric vibrator and the friction interface, and we decided to simulate the leveler's output for different values of voltage amplitude and load as these are variables that we can experimentally define.

The voltage amplitude is related to a value of duty cycle that can be modified in the XCD driver.

Table V.6-1. Voltages used in the simulation.

Duty Cycle (%)	10	20	30	40	50	60	70	80	90	100
Voltage Amplitude V_{DC} (V)	2	3.3	4.5	5.7	7.1	8.3	9.34	10.15	10.65	10.75

The loads correspond to the torque that a hooked mass applies around the rotor's axis due to the effect of gravity and have been accordingly chosen so the leveler is able to rise the hooked mass up.

Table V.6-2. Experimental load torques.

Mass (g)	50	100	140	150	190	200	240
Torque (mNm)	9.8	19.6	27.4	29.4	37.2	39	47

Starting at the 0° position of the actuator, experimental data is acquired for every load torque at a sampling frequency of 10kHz and consist in series of 5 round trips $+10° \rightarrow -10° \rightarrow +10°$ as indicated in the flowchart of Figure V.6-1. The 0° position is defined by using the reference signal Z of the magnetic encoder, assuring that a 10° movement is possible in both directions before reaching the limit of the actuator. This is done for each duty cycle of Table V.6-3.

Table V.6-3. Voltages used in the experiments.

Duty Cycle (%)	60	70	80	90	100
Voltage Amplitude V_{DC} (V)	8.3	9.34	10.15	10.65	10.75

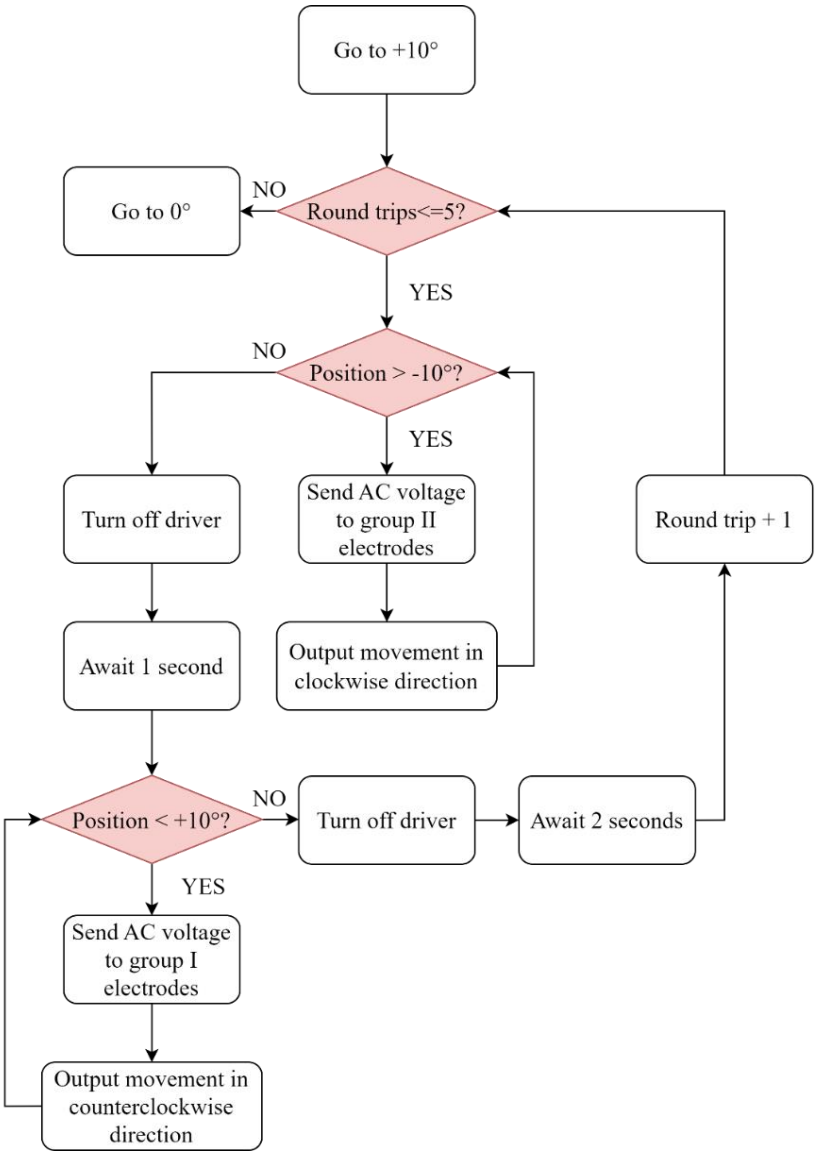

Figure V.6-1. Flowchart for the open-loop back and forth movement experimental data.

An example of the experimental data is shown in Figure V.6-2, corresponding to the no load, 100% duty cycle scenario.

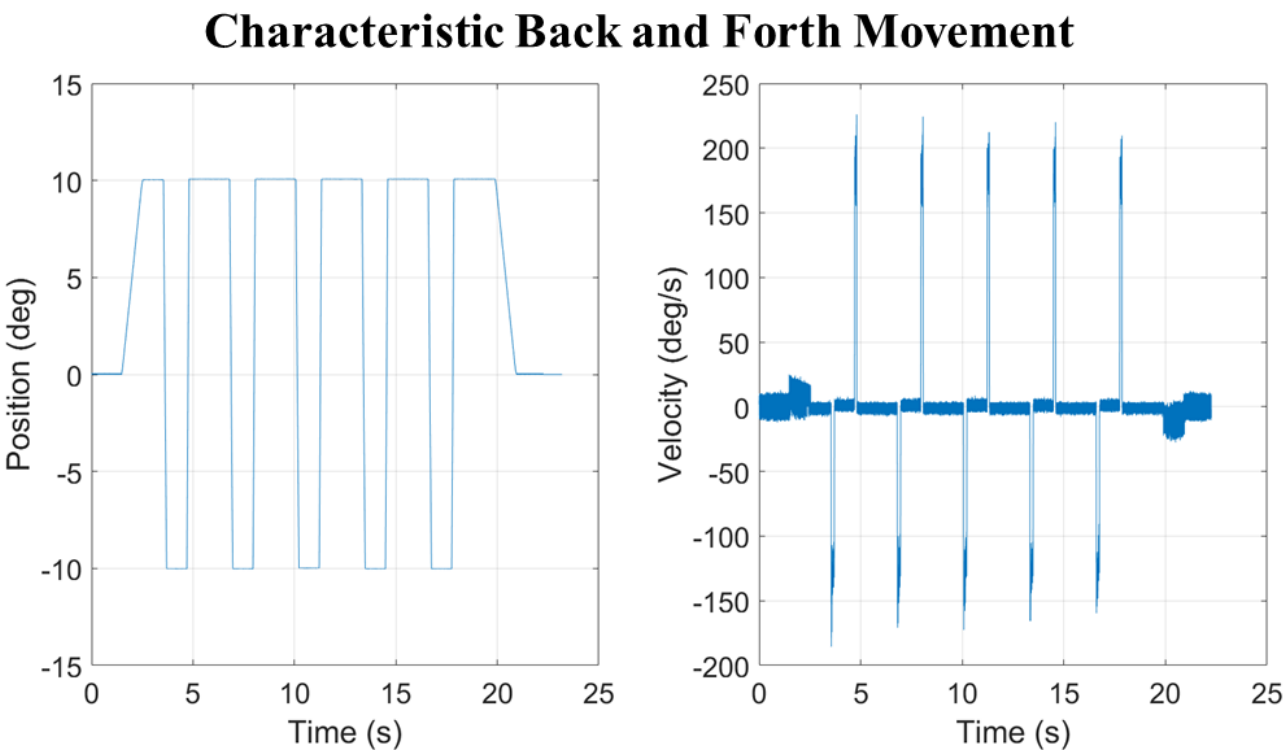

Figure V.6-2. Experimental data of the position and velocity of the rotor's leveler at 100% of duty cycle and no load applied.

The no-load experiment allows to evaluate the symmetry on the output of the actuator. Theoretically, there must be no difference between the clockwise and counterclockwise movement regarding the velocity plot of Figure V.6-2. Handling of the lateral springs during the USM assembly may have caused deformation on them and possible fabrication error of the piezo vibrator may also induce asymmetry on the output, for example misalignment of the electrode coating of the multilayer structure.

As a result, we evidence a difference between velocities depending on the direction of movement, being less efficient in the clockwise direction. This may due to deformation caused on the lateral springs while mounting them, defects on electrode placement in some of the layers of the piezo vibrator or misalignment between the axis of rotation and the axis of revolution of the friction interface. The simulated model does not take into account these effects hence we decided to take the position data from the movement in the positive direction (counterclockwise) for the comparisons made between the simulations and the experiments.

In Figure V.6-3.A, we can see that the duration of a single 20° movement is only about 100ms. The noise on the velocity data is tremendously multiplied after differentiation of the position data, which is proper to encoder measuring systems, so in order to maximize the reliability of the analysis, we decided to use the position data, under the assumption that, during the movement, the actuator moves at constant angular velocity. This corresponds to a constant slope value between the initial and final angular position and is supported by the fact that ultrasonic piezoelectric actuators exhibit settling time of a few tenths of milliseconds, as can be appreciated in the zoomed view at the starting time of the movement in Figure V.6-3.B.

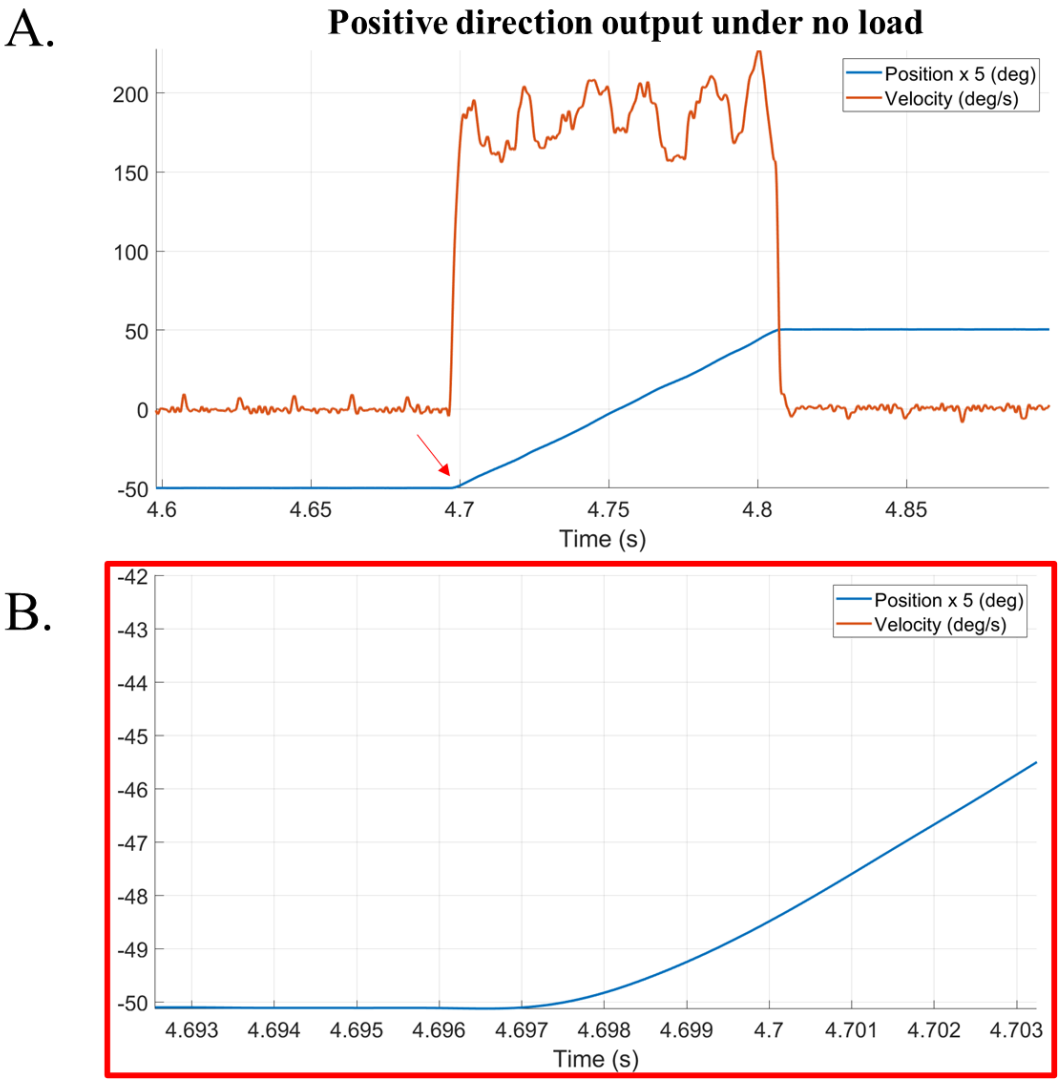

Figure V.6-3. Detail on the experimental data of the position and its derivative at 100% of duty cycle and no load applied.

V.6.1. Steady-state output of the actuator: simulation and experimental results

The simulation results of the steady-state output velocity of the actuator at 6 different values of load are contrasted to the $-10° \rightarrow +10°$ movements which corresponds to the actuator working against the weight of the hooked masses. This is shown in Figure V.6.1-1.

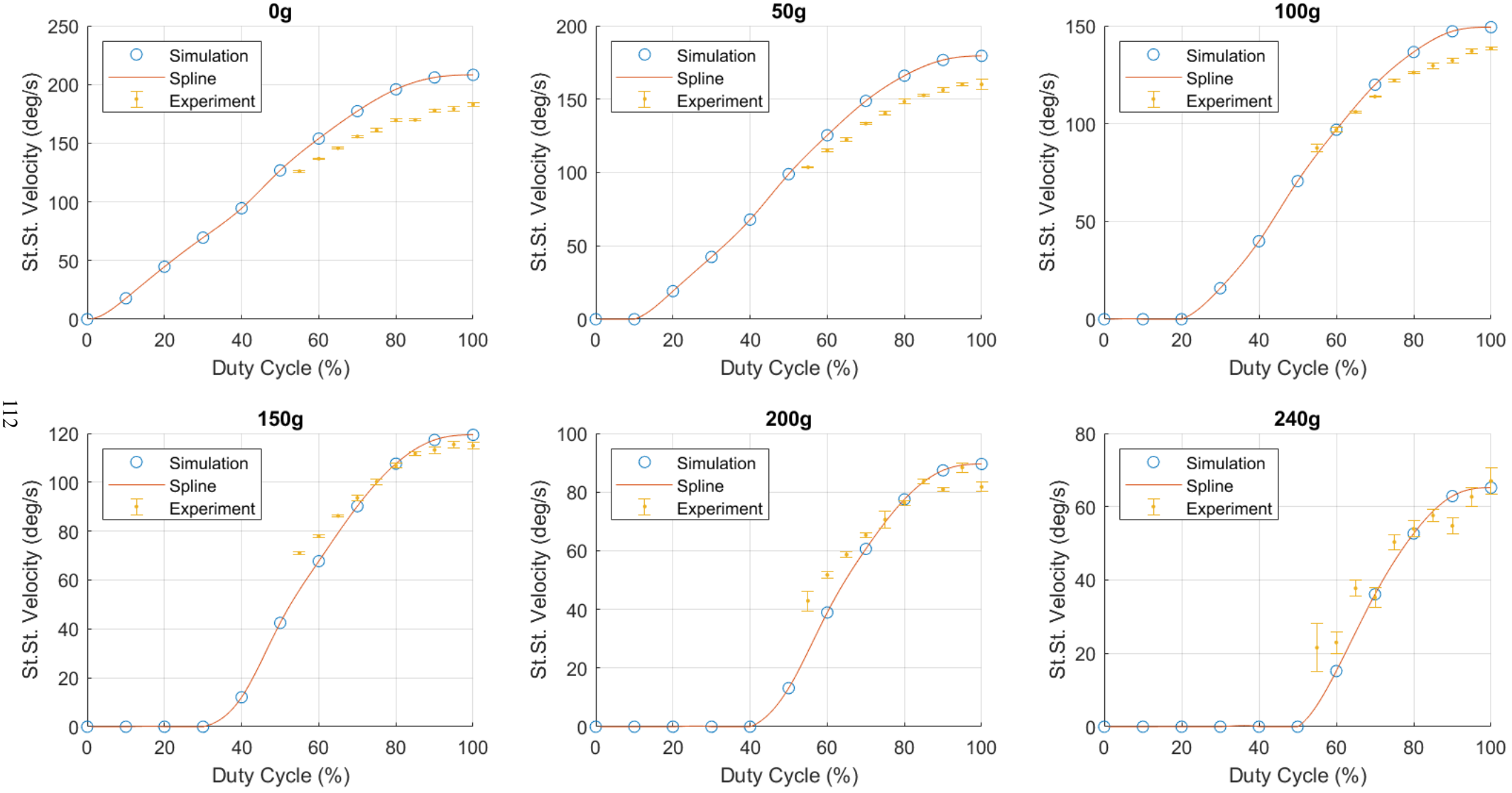

Figure V.6.1-1. Comparison of the steady-state output velocity of the actuator under different loads [0, 240]g at a fixed frequency of $f = 91070\ Hz$.

We can see that there is a good agreement between the simulated and the experimental results, especially for voltages corresponding to the 80% of duty cycle or lower, while for higher duty cycle values the steady-state velocity presents saturation as the corresponding voltage amplitude variation from this point is smaller. The external load does not seem to present a notorious influence on the voltage amplitude at which saturation occurs.

Other researchers [109], [110] have encountered the same saturation behavior when working with ultrasonic vibrators at high excitation voltage, as a result of amplitude saturation of the piezo vibrator, which is caused by nonlinear electro elasticity and augmentation of viscous friction coefficient. Our model does not take into account these effects then it predicts saturation at higher values of voltage compared to experimental data.

It is clear that the output steady-state velocity increases with the voltage amplitude yet there is a dead zone of zero output velocity associated to a start-up voltage. From this amplitude value, the tangential force of the hard tip is able to surpass the static friction with the friction interface which results in a non-zero net force, hence, rotor movement. This is a common characteristic to friction based piezoelectric actuators and is very important for precision control of ultrasonic motors, where the dead zone and start-up voltage predictions are critical for the controller design [111]. Of course, the start-up voltage will be higher when an external load is applied.

From the experimental data, we can also compare the steady-state velocity under different applied loads (Figure V.6.1-2) and the output power of the leveler (Figure V.6.1-3) for different voltage amplitudes. In Table V.6.1-1, we can see the experimental no-load speed, stall torque and maximal power output associated to each value of duty cycle, corresponding to a different voltage amplitude.

Table V.6.1-1. Experimental results.

	Duty Cycle				
	60%	70%	80%	90%	100%
No-Load Speed (deg/s)	136.7	155.7	169.4	177.8	182.9
Stall Torque (mNm)	52.3	59.3	64.5	67.9	68.5
Max Power (mW)	39.5	48.2	55.4	59.4	61.5

Besides the error observed by the differences between the simulation of an ideal Timoshenko beam and the actual piezo vibrator of the USM, the lower value of the experimental no-load speeds compared to the simulated results, can be explained because increasing the normal force necessary to obtain higher tangential forces and in consequence, higher output torques, comes with changes in the area of contact between the hard tip and the friction interface that we do not take into account in the simulation.

In general, this area of contact will increase proportionally to the normal force which causes the no-load speed to drop. This is one of the reasons why high-stiffness contact materials are preferred when choosing the materials for the couple hard tip-friction interface. In the designed leveler, we choose 304 stainless steel for the friction interface whose 200GPa stiffness is considerably lower than the 360GPa stiffness of the alumina hard tip.

In Figure V.6.1-2 we also see the parallel behavior of changing the voltage amplitude on the performance, which is a characteristic that has already been reported in other ultrasonic motors [94], [106], [112], [113].

Even though we simulated the piezo vibrator as an ideal Timoshenko beam, the previous simulated results show good resemblance when compared to the experimental data. Then, the developed model can be used to determine other characteristics of the actuator via simulation.

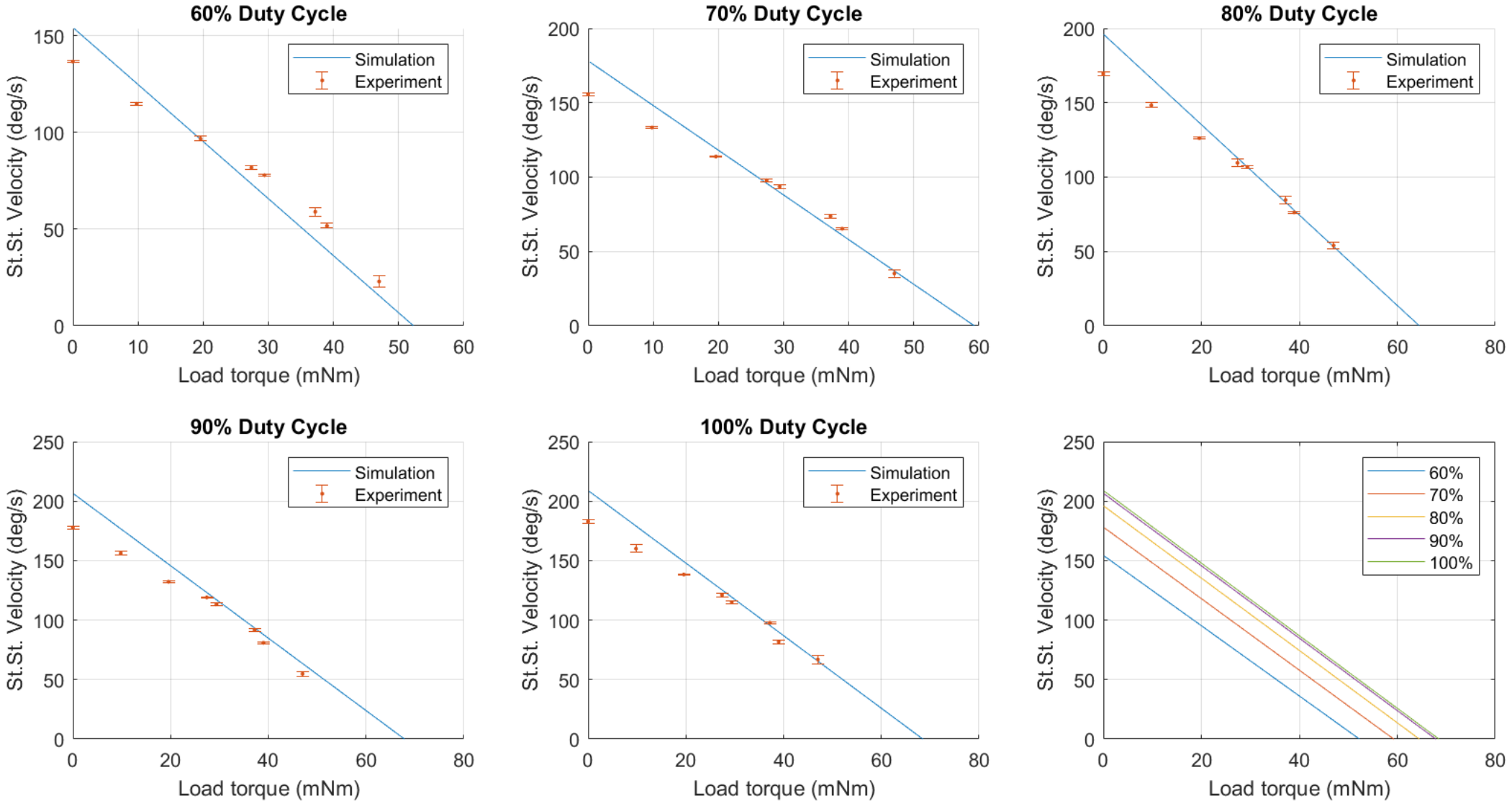

Figure V.6.1-2. Simulation and experimental results for the steady-state motor velocity under various applied torques at different input voltages.

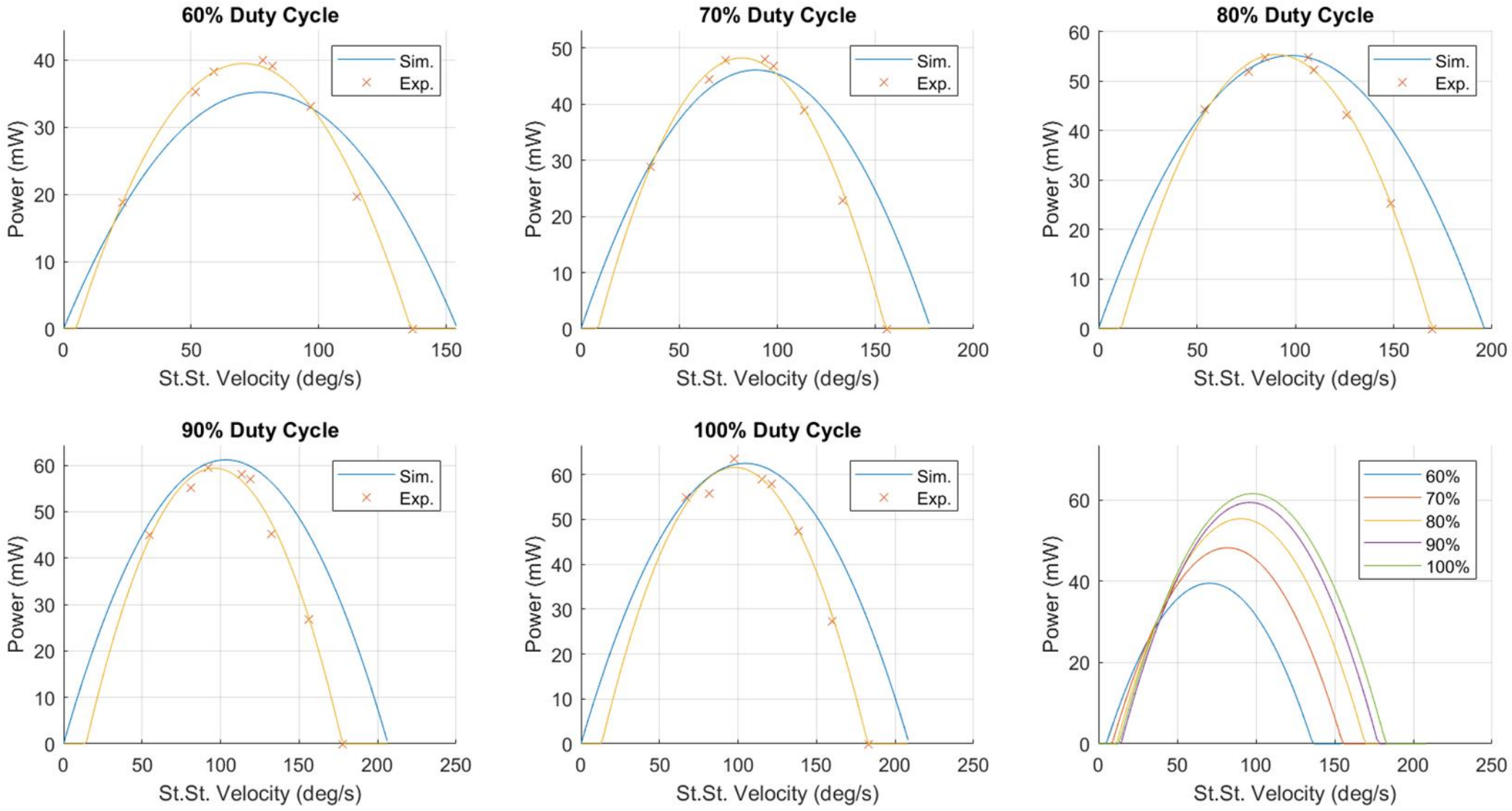

Figure V.6.1-3. The comparison of experimental and simulation results of the output power of the leveler.

V.6.2. Output velocity as a function of time

A constant duty cycle leads to a constant motor voltage rms: Associated to the duty cycle, the driver provides a command voltage to the driver's amplifier circuit, where the command voltage is translated into an AC high frequency voltage signal applied to the motor; thus, a constant duty cycle command leads to a constant rms voltage. Without loss of generality, the dead zone voltage can be defined as the minimum rms voltage to produce motion and translates accordingly into a minimum duty cycle value as it was seen before in Figure V.6.1-1.

When initially at rest, and applying a constant duty cycle command, higher than the dead zone voltage value, the angular velocity of the rotor ω as a function of time can be described by

$$\omega(t) = \omega_{max}\left(1 - e^{-\frac{\alpha\omega_{max}}{\tau_{max}}t}\right) \qquad \textit{Eq. V.6.2.1}$$

From the results exposed in Figure V.6.1-2, we know that it exists a linear inverse relationship between output steady-state velocity and available torque. Hence, for a given constant duty cycle (above dead zone) a leveler can apply a maximum torque τ_{max}, at zero angular velocity (also known as stall torque) or achieve a maximum angular velocity ω_{max} with zero available torque (also known as no-load velocity). The values of maximum torque and maximum angular velocity increase with increasing duty cycle command, until the absolute maximum torque and the absolute maximum angular velocity values are achieved at 100% duty cycle.

Figure V.6.2-1 shows the time-dependent function $\omega(t)$ at maximal duty cycle for three cases of external load and its comparison with the experimental angular velocity derived from the position data. The noise in the experimental position data is largely amplified after differentiation, especially in the steady-state phase, but still, we can see good agreement between the function $\omega(t)$ that describes the dynamics of the simulated model and the real actuator, especially in the acceleration phase.

Concerning the steady-state, it is reached around 10ms, which is a clear indicator of the high reactivity that the leveler exhibits. As it was said in chapter II, this is a desired characteristic for the application, because sudden changes in road conditions shall be quicky compensated by the leveler in order to maximize visibility at all times. This behavior is of interest for scanning, for example mapping applications made with Lidar sensors.

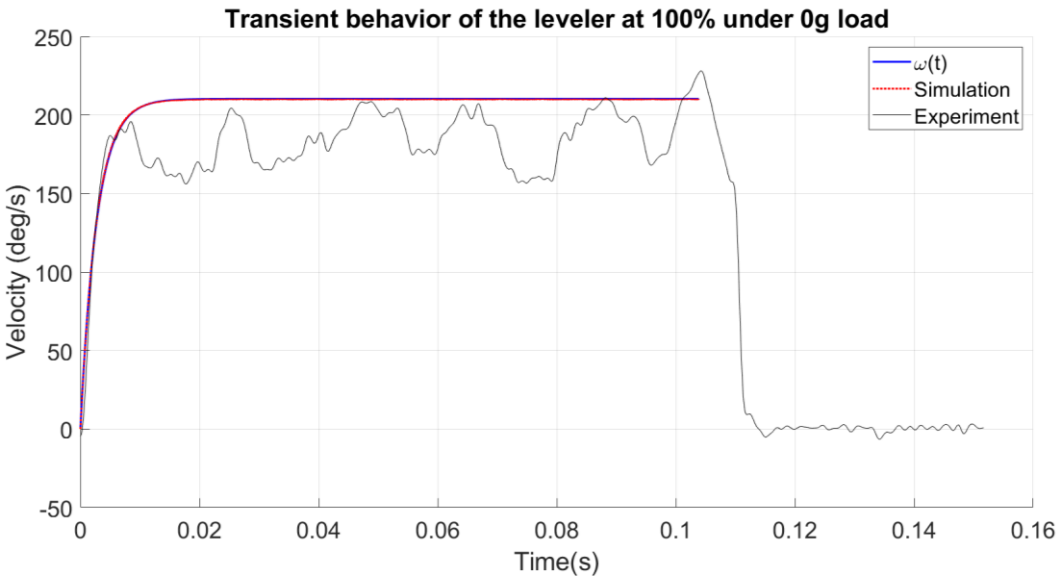

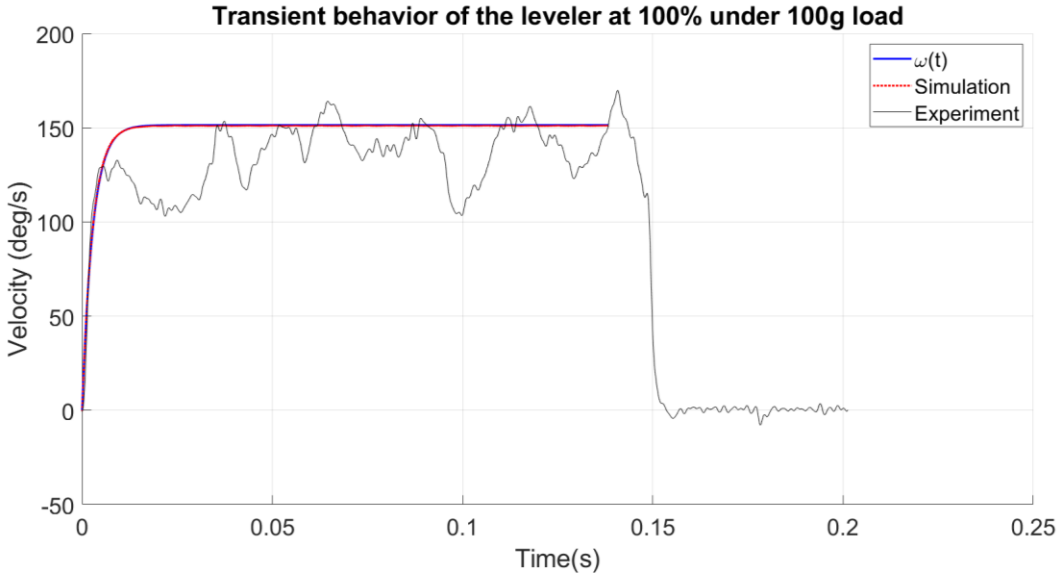

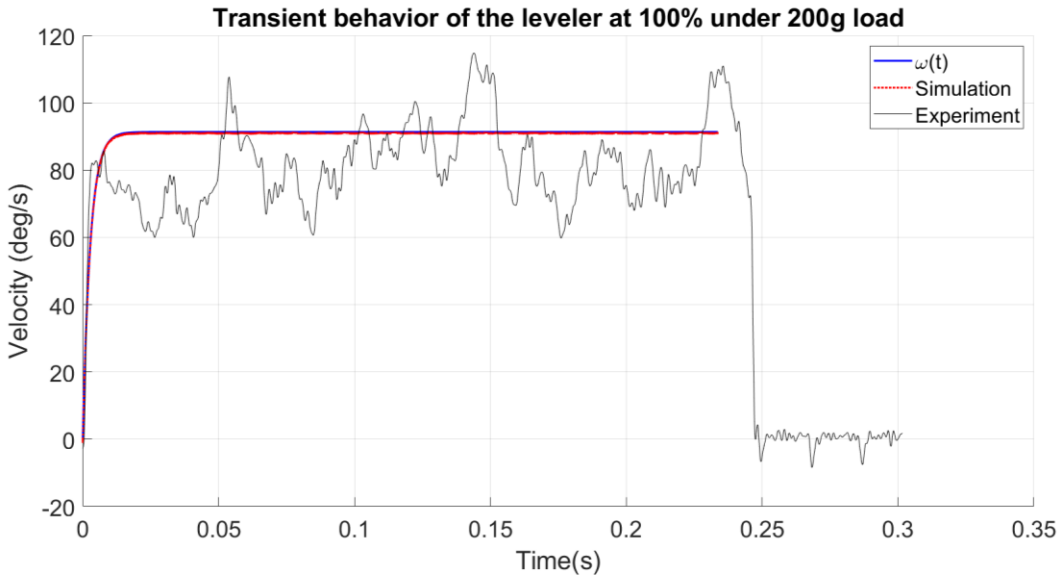

Figure V.6.2-1. Comparison of the transient behavior of the leveler.

V.6.3. Analysis of the steady-state trajectory at the driving tip

As it has been said along this thesis, the macroscopic output rotary movement is the result of cyclical contact between the hard tip and the friction interface as a result of the superposition of the L1 and B2 modes which generates an elliptic microscopic motion at the hard tip. Figure V.6.3-1 shows the output velocity of the leveler for three different values of load and the corresponding elliptic movement of the hard tip in steady-state at different values of voltage amplitude.

We can see that the trajectory of the hard tip describes an oblique ellipse in clockwise direction. In each case, points P1, P2, P3, P4 in Figure V.6.3-1 identify the minima and maxima of both the normal and tangential displacement when the leveler is excited at 60% of voltage amplitude. Similarly for points P5, P6, P7, P8 in the 100% duty cycle case. These values are shown in Table V.6.3-1.

Table V.6.3-1. Simulated results of elliptic amplitude.

Load (g)	Position (µm)	60% Duty Cycle				100% Duty Cycle			
		P1	P2	P3	P4	P5	P6	P7	P8
0	Tangential	0.535	-1.537	-0.481	1.577	0.536	-1.992	-0.526	2.043
	Normal	-0.19	-0.001	0.111	-0.099	-0.268	-0.003	0.18	-0.124
100	Tangential	0.511	-1.553	-0.466	1.597	0.531	-2.005	-0.496	2.063
	Normal	-0.19	0.005	0.111	-0.091	-0.268	-0.011	0.18	-0.113
200	Tangential	0.497	-1.567	-0.449	1.609	0.503	-2.021	-0.489	2.077
	Normal	-0.19	-0.005	0.111	-0.095	-0.268	-0.005	0.18	-0.106

	Tangential Amplitude (µm)		Normal Amplitude (µm)	
Load (g)	60%	100%	60%	100%
0	3.114	4.035	0.301	0.448
100	3.15	4.068	0.301	0.448
200	3.176	4.098	0.301	0.448

As it was previously explained, we do not simulate the tribology effects caused by the increase of the normal force due to the change on the contact area, the mechanical indentation or wear. For this reason, normal amplitude of the ellipse appears independent of the applied load. On the other hand, at higher voltages, both the tangential and the normal amplitude of the elliptic movement increases. From this result we can also see why ultrasonic actuators are characterized by output velocities in the range of hundreds of mm/s, as consequence of micrometer displacements of the hard tip at ultrasonic frequency.

We can evaluate the dependence of the elliptic movement on frequency. From Figure V.6.3-2, the output velocity of the leveler rapidly decreases when the frequency of the input voltage shifts from 89015Hz (the calculated value in Table V.5.1-1) and the corresponding elliptic movement of the hard tip contracts in tangential direction which implies, huge decrease in the tangential force F_T output by the hard tip. Then the output power by the leveler will be less than the results showed in Figure V.6.1-3 for the 100% DC case.

This result allows to understand the importance of the frequency of the input signal, as it has been clearly stated, it is important to be able to excite both modes L1 and B2 and moving away from their mean value results in loss of output power. This is especially relevant when designing (or selecting) a driver for the piezo leveler actuator.

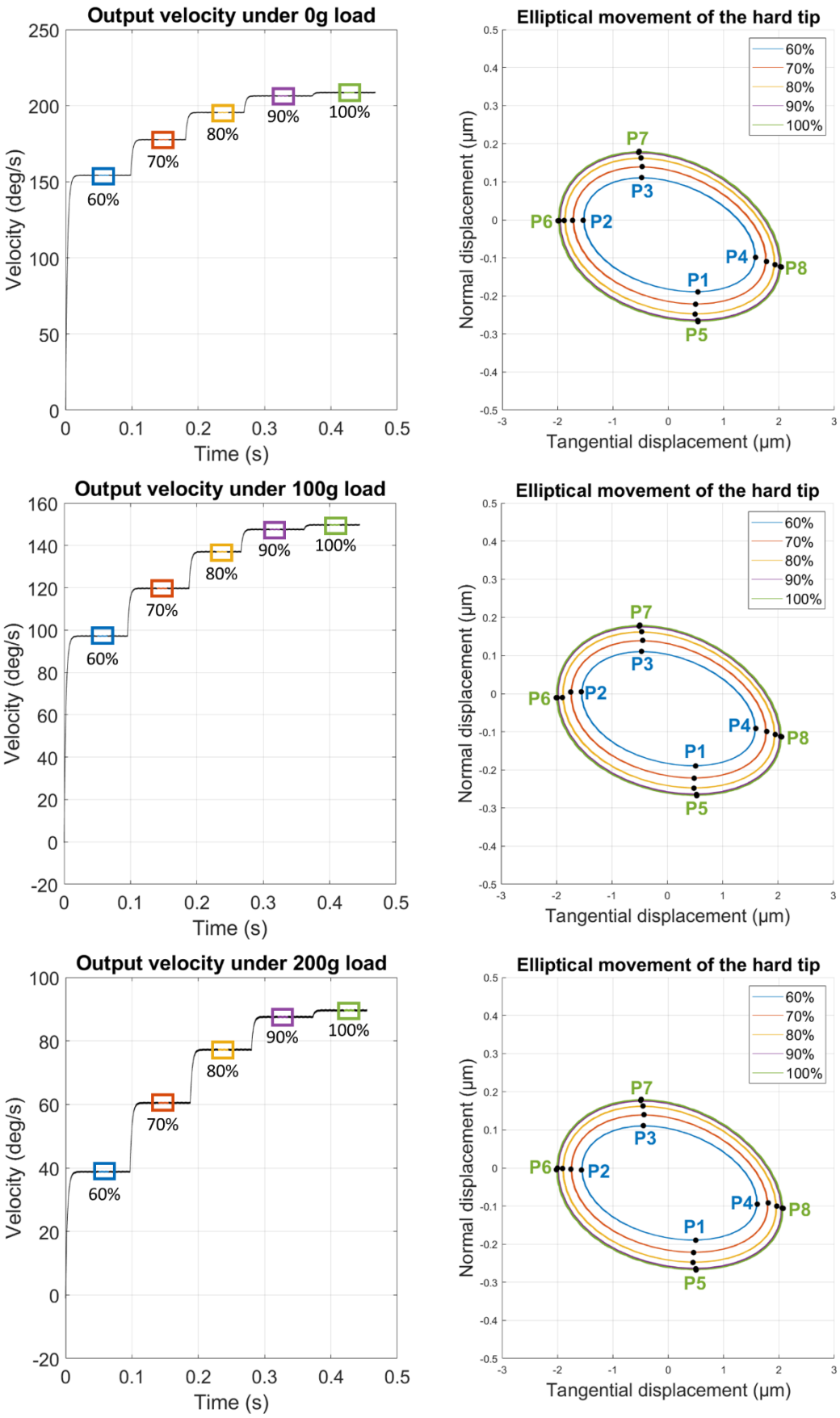

Figure V.6.3-1. Simulation of the trajectory of the hard tip under different loads and voltage amplitudes.

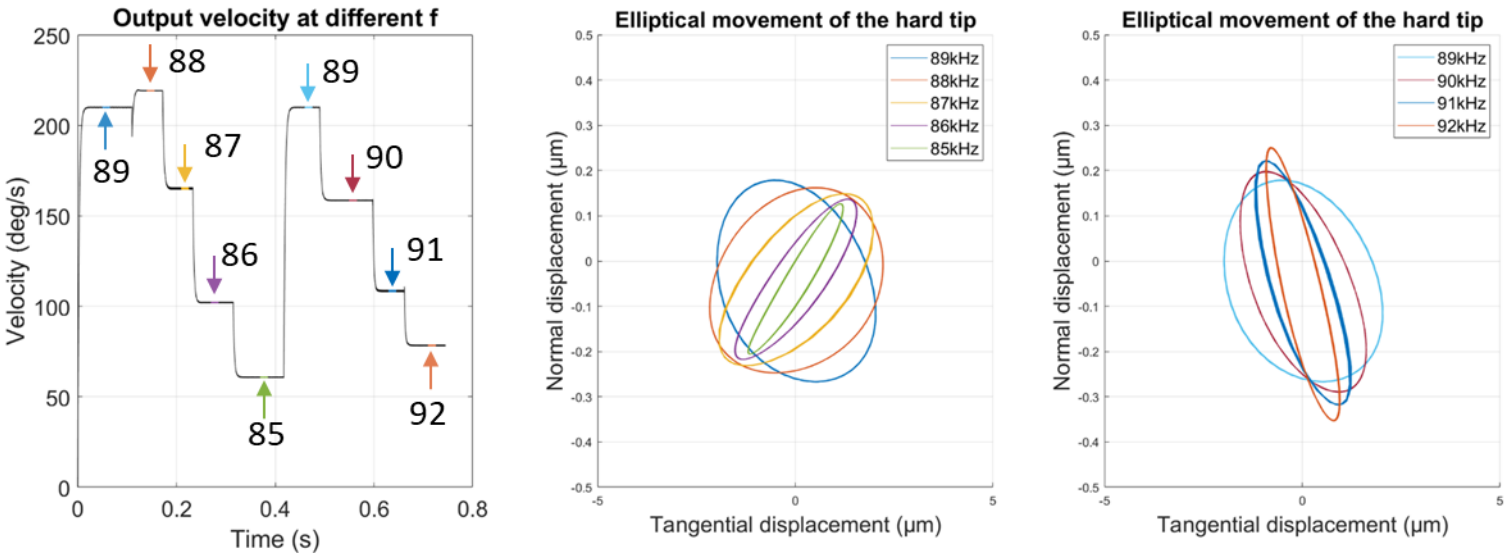

Figure V.6.3-2. Simulation of the trajectory of the hard tip under different frequencies at 100% DC.

V.6.4. Analysis of friction drive mechanism of the leveler

The output of the leveler being entirely based on the contact state of the hard tip of the USM with the friction interface, we will discuss the friction mechanism between these two parts and the effects of the contact state on the output of the leveler using the numerical results of the simulation in steady-state.

Figure V.6.4-1 shows the steady-state tangential force of the hard tip at 100% of duty cycle input under three different loads and the same preload force ($F_P = 4N$). This corresponds to the three cases indicated by a green square of Figure V.6.3-1. The periodic behavior of the friction contact allows us to analyze a single period, which corresponds to a single elliptic turn of the hard tip following the points P1àP2àP3àP4àP5 (clockwise direction).

We can see that the tangential force F_τ (solid purple line) is always comprised between the values of static friction as indicated in *Eq. V.4.7* (blue and red dotted lines)

$$|F_\tau(t)| < |\mu F_N(t)|, \text{ for every } t \geq 0$$

And its direction is defined by the relative velocity v_{rel} which is the difference between the hard tip tangential velocity $\dot{v}(x,t)$ and the rotor tangential velocity ωR. This means that the amount of force transmitted from the hard tip to the rotor depends on the amount of friction, which acts in two ways: contributes to the motion when the speed of the hard tip is greater than the rotor or opposes the motion when the speed of the drive tip is less than that the rotor [114].

The mean value of force within an elliptic cycle grows when the voltage is increased which indicates positive net work done by the hard tip, resulting in macroscopical positive rotation of the leveler's output. The elliptic cycle starting at P1 and ending in P5 comprises four moments:

- P1 to P2: $v_{rel} > 0$ and $\mu F_N(t) > 0$. The tangential force impulses the rotor.
- P2 to P3: $v_{rel} < 0$ and $\mu F_N(t) > 0$. Because the tangential velocity of the hard tip is lower than the velocity of the rotor, the tangential force cannot accelerate the rotor.

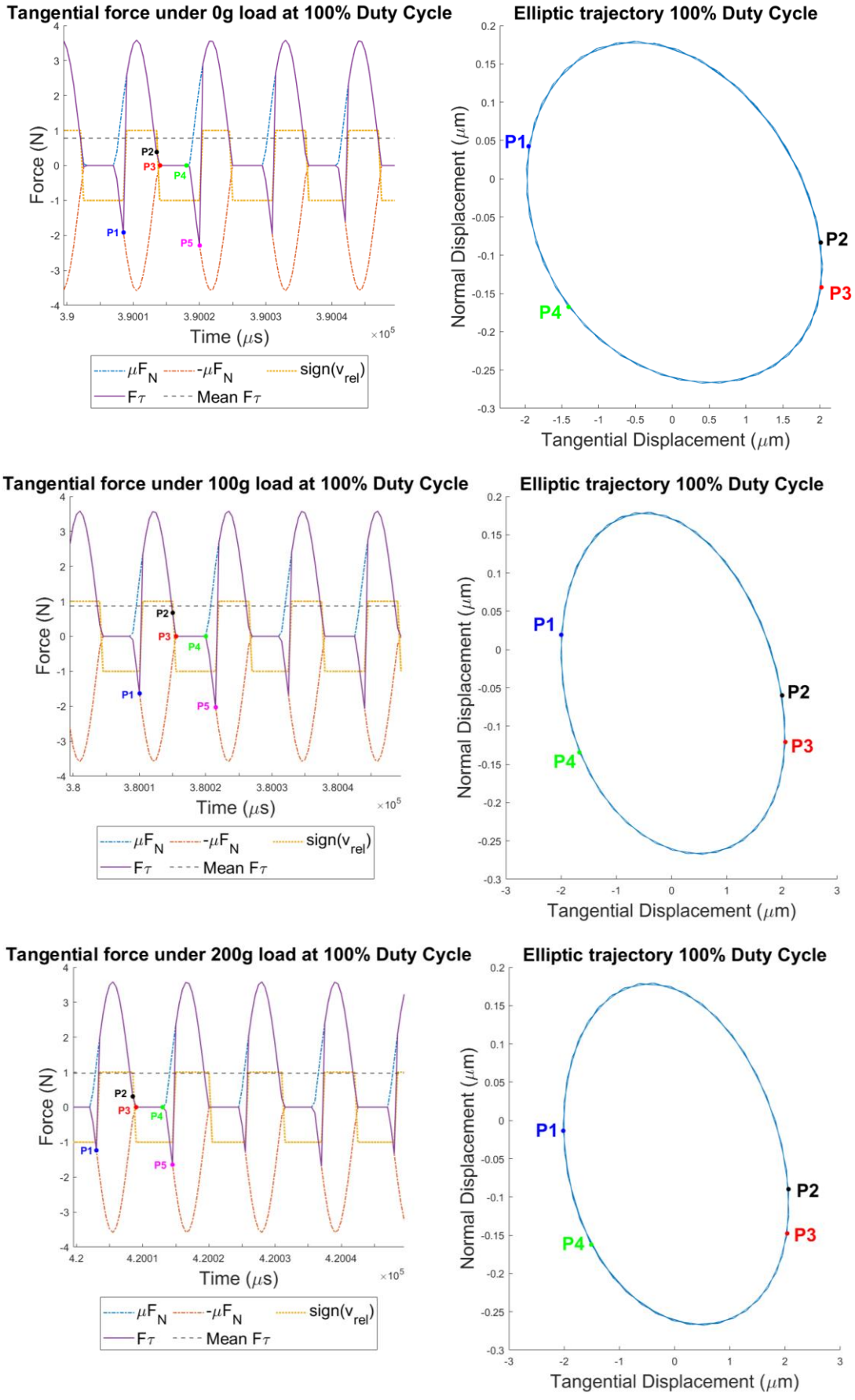

Figure V.6.4-1. Simulation of the trajectory of the tangential force.

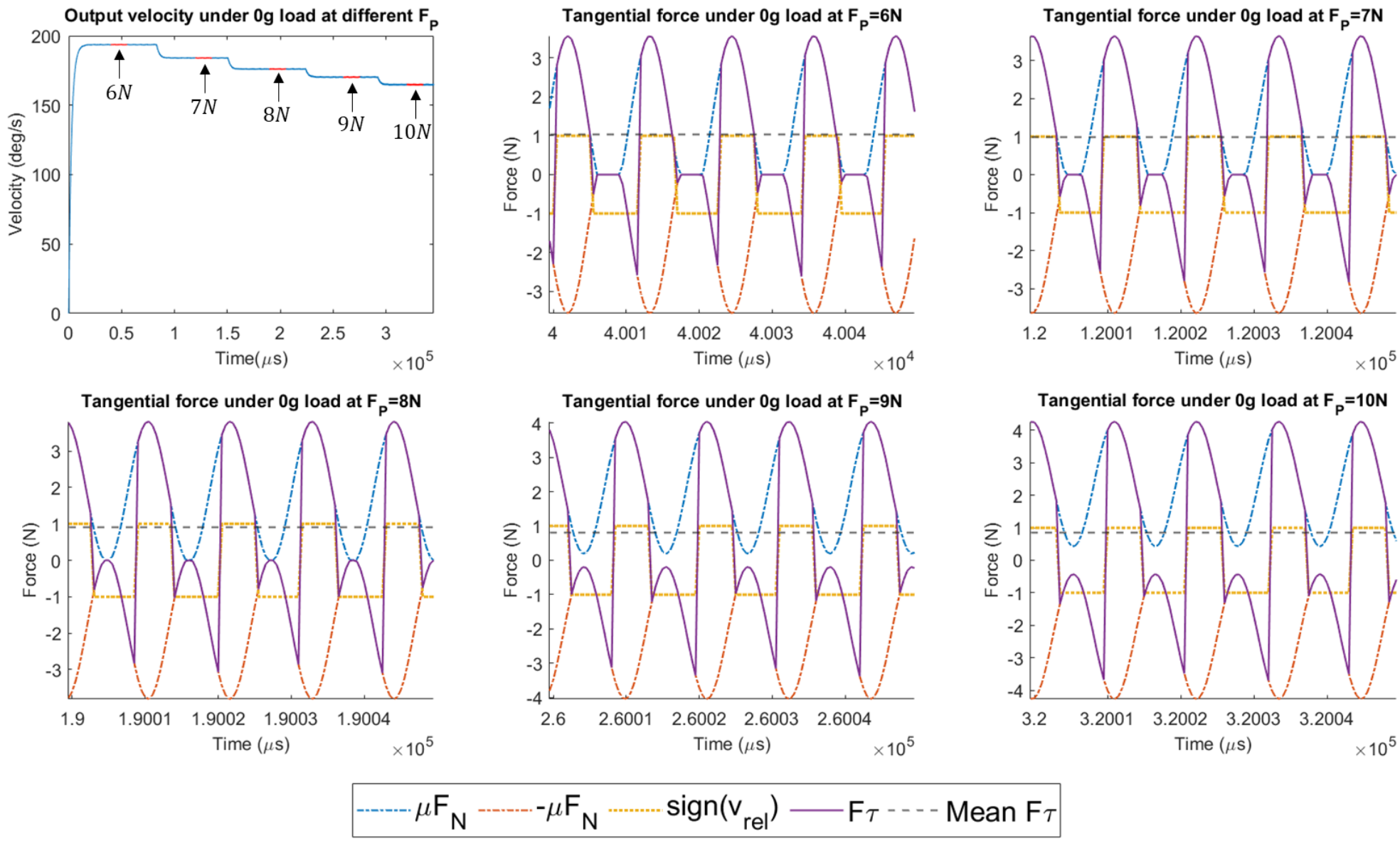

Figure V.6.4-2. Simulation of the output speed and force of the piezo leveler at different preload forces F_P.

- P3 to P4: $\mu F_N(t) = 0$. Since the normal force vanishes, as result of the separation of the hard tip from the friction interface, there is no driving force and the rotor continues its movement thanks to the inertia.

- P4 to P5: $v_{rel} < 0$ and $\mu F_N(t) < 0$. The tangential force exerts negative work on the rotor and acts as a breaking force. One elliptic turn is completed and the cycle restarts.

We can extend this analysis to compare the output at different values of preload F_P. In Figure V.6.4-2 we show the effect that different values of preload (from 6N to 10N) have in the output velocity of the piezo leveler ω and the detail of the tangential force F_T at steady-state.

Similar to the results for the experimental prototype case (at $F_P = 4N$), the magnitude of tangential force F_T is still enveloped by the maximal friction force μF_N, whose maximal and minimal values do not change for different values of load, i.e. since it depends on the amplitude of the normal displacement of the hard tip $u(t)$, as previously mentioned in Table V.6.3-1, the stall torque is independent of the external load.

On the other hand, the average value in a cycle of this friction force does change with F_P significantly increasing with the preload increase. Then, the stall torque τ_{max} is proportional to the voltage amplitude and the applied preload F_P.

$$\tau_{max} = \mu R \overline{F_N} = \frac{\mu R}{T} \int_0^T F_N(t) dt \propto V_{DC}, F_P \qquad \textit{Eq. V.6.4.1}$$

Nevertheless, this augmentation in stall torque comes at a cost. From the velocity curve, it is clear that the steady-state speed of the rotor decreases when increasing preload. This is due to the bias that F_P generates on the dynamic normal force F_N. The duration of the separation of the hard tip and the friction interface, indicated by the moments where the tangential force vanishes, tends to disappear when F_P surpasses a certain value, which in our case, happens at $F_P > 8$N when $V_{DC} = 100\%$. From this point, the hard tip cannot separate from the friction interface during the elliptic cycle. For lower values of voltage V_{DC}, this critical value will be lower, as the amplitude of the elliptic movement will also be lower and unable to generate enough force to separate from the friction interface. In Figure V.6.5-1, we show the case for $V_{DC} = 60\%$ and we can see that the critical preload is 6N.

Figure V.6.5-1 shows the five characteristic curves for the preload values of Figure V.6.4-2 and its comparison with the preload force ($4N$) applied on the designed prototype. From this, we can see that we can adapt the actuator depending on the conditions of the application. More precisely, in chapter III.2. *Application Requirements,* we stablished the difficulty of setting a value of moment of inertia I that single handedly describes the variety of projectors, as it is usual for this value to change from model to model. But from this analysis, we can set the exact same piezo leveler for different projectors by modifying the preload force parameter F_P through the modification of the preload distance d_P between the USM and the friction interface. This provides the designed actuator with a versatility that is of special interest regarding possible production of the parts at big scale, proper of the automotive industry.

V.6.5. Precision of the leveler

The use of piezoelectric actuators in the application is interesting for their high precision. In order to evaluate the precision of the piezo leveler, it is required to operate in closed loop mode. For this, we

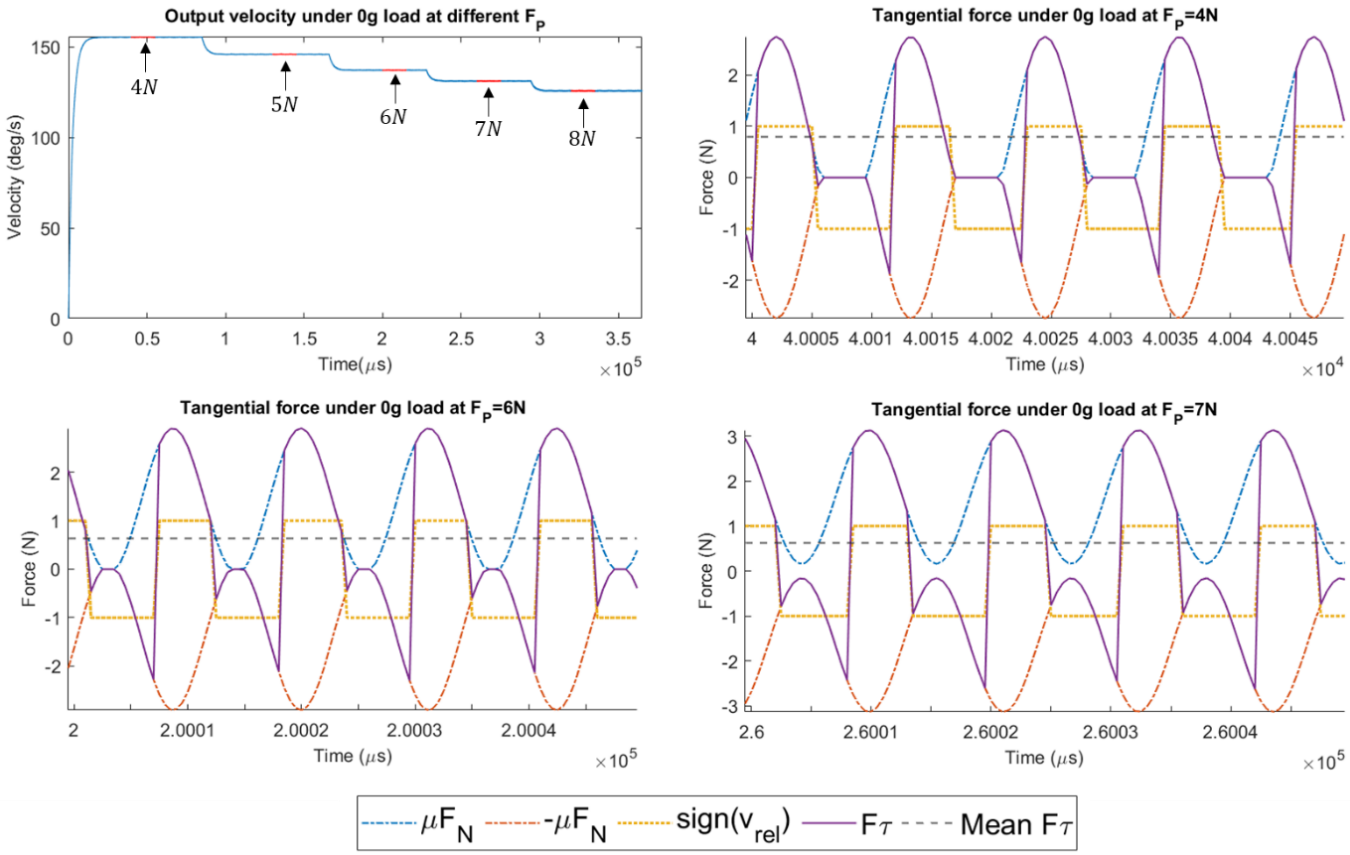

Figure V.6.5-1. Simulation of the output speed and force of the piezo leveler at 60% DC.

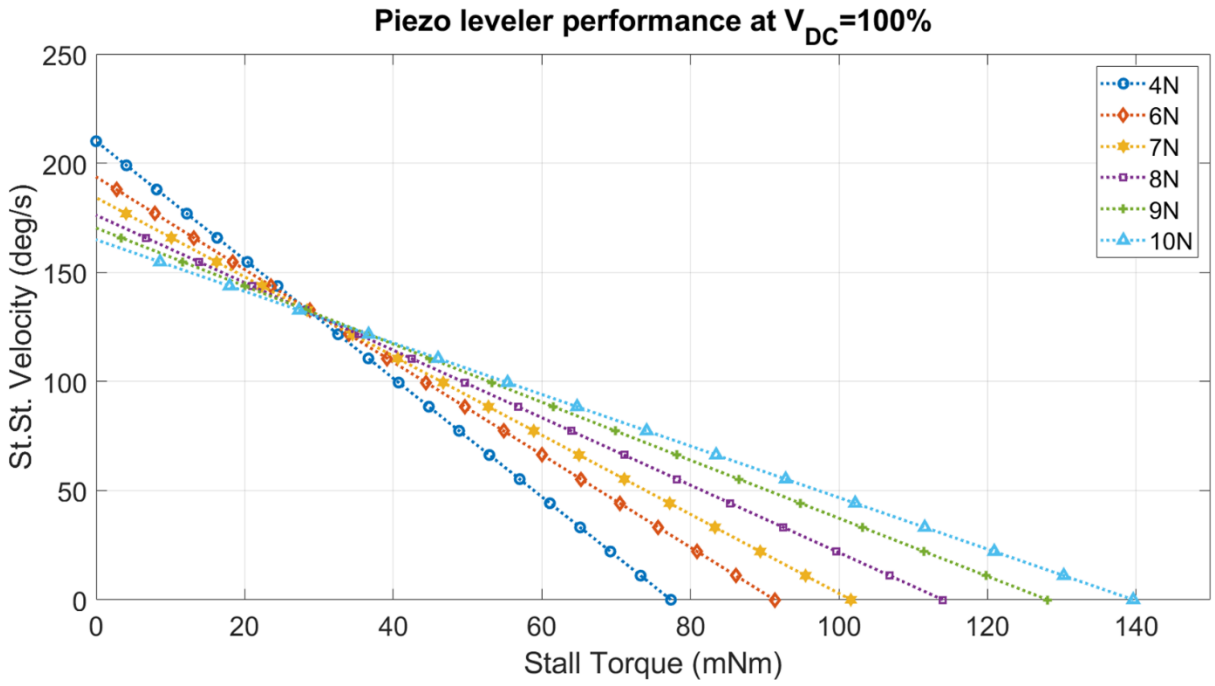

Figure V.6.5-2. Performance simulation at different values of F_P.

decided to use the controller integrated in the XCD driver, which is based on a standard PIV (position/velocity loop) controller. After defining a target position θ_f, an angular velocity ω_f and an angular acceleration α_f, the controller calculates a motion profile that includes a constant acceleration phase from 0 to t_a, a constant velocity phase from t_a to t_d, and a constant deceleration phase at t_d as shown in Figure V.6.5-3.

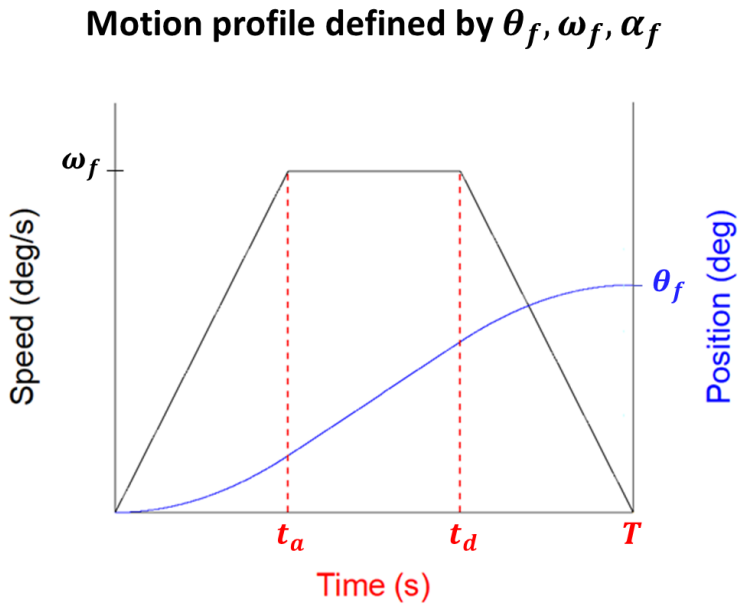

Figure V.6.5-3. Performance simulation

We analyzed the position of 30 series of back and forth movements in closed loop mode with no external load, where the values of final position ($+\theta_f$ or $-\theta_f$), angular velocity ω_f and acceleration α were chosen accordingly to the capabilities of the leveler and the requirements of a typical leveling application as shown in Figure V.6.5-4.

Variable		***Value***	***Units***
Constant Angular Acceleration	α	± 100	deg/s^2
Maximal Angular Velocity	ω_f	± 10	deg/s
Target Position	θ_f	± 10	deg
Back and Forth Movement			
$0 \rightarrow +\theta_f \rightarrow 0 \rightarrow -\theta_f \rightarrow 0$			

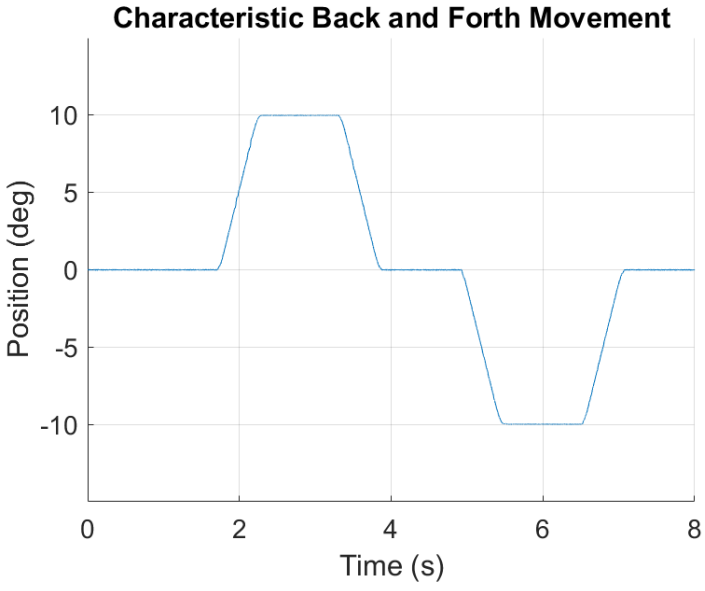

Figure V.6.5-4. Characteristic sample of the closed loop movement.

In the motion profile, we included a 1s delay once the target position is reached so we could take the mean value of $\pm\theta_f$ and evaluate the precision of the actuator in both directions of motion. This is different to the open loop analysis performance evaluation (sections V.6.1 - V.6.4) where the data was exclusively related to the positive direction. The asymmetry of the output does not affect the values of position taken in this section.

The distribution of the maximal and minimal value for the 30 samples taken are shown in the box plot of

Figure V.6.5-5.

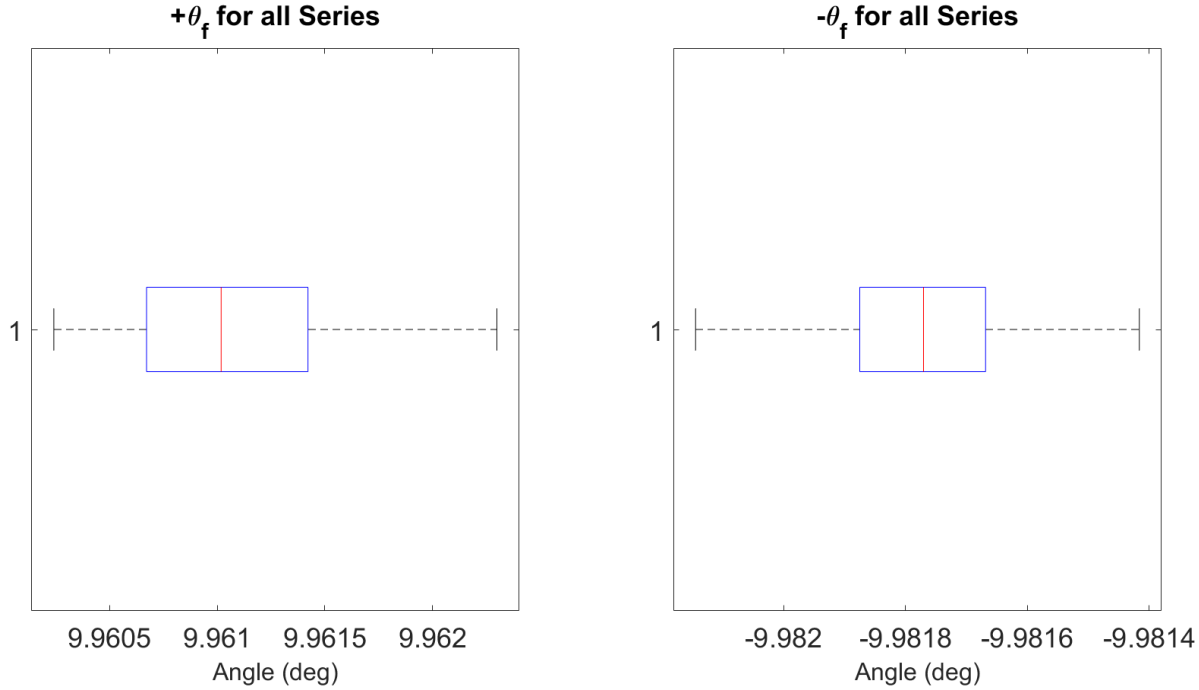

Variable	*Mean (deg)*	*Maximum absolute error (deg)*		*Repeatability (deg)*	
		Piezo	*Classic*	*Piezo*	*Classic*
$+\theta_f$	9.9611	0.0398	~0.1	$\pm 0.5 \times 10^{-3}$	~$\pm$0.1
$-\theta_f$	-9.9818	0.0179		$\pm 0.18 \times 10^{-3}$	

Figure V.6.5-5. Data distribution. Left, the distribution of $+\theta_f$. Right $-\theta_f$.

The calculated mean values represent the mean position reached by the leveler when turning in the direction of $+\theta_f, -\theta_f$ for the 30 series. We compare both the maximal error and the repeatability (described by the standard deviation of the data) of the designed piezo leveler and a classic electromagnetic leveler, and it is clear the advantage in favor of piezoelectric actuation regarding precision and repeatability. In this case, of about 100 times better.

V.7. Conclusion

In this chapter we evaluate the performance of the piezo leveler designed in chapter III both experimentally and numerically, based in the mathematical modeling developed in chapter IV.

For this, we started by showing the process of assembling the whole actuator, from its core, the SWUSM to the stator-rotor to its output, which complements the more theoretical part seen in chapter II. Giving a better sight of the internal components of the USM and the actuator's friction interface, rotor and sensor, we could show how is the transmission from microscopical elliptic cycles to macroscopic rotary movement through the setting of a preload distance d_P that ultimately defines the necessary preload force F_P for the piezo leveler to operate.

Then, from a base of parameters consisting in several geometric and material properties that describe our designed piezo leveler, we could numerically solve the equations obtained in chapter IV and compare the results with experimental data as we were interested in the validation of the dynamic model so we can analyze further the stick-slip movement of the USM and its influence on the output angular velocity. The model showed good agreement with the experimental data so we exploit it for performance evaluation at different scenarios of frequency and amplitude of the electric input $V(f,t)$, and preload force F_P.

The designed prototype has a footprint similar to other AML Systems ® leveling products, characterized by a no-load speed of 182.9 deg/s and stall torque of 68.5mNm when operating at $F_P = 4N$ and 100% DC. Nevertheless, we showed by simulation, that the output can be changed by setting a different preload value, so a taylor-made actuator can be satisfied without need of components redesign.

Lastly, we obtained the absolute error and repeatability of the actuator for a 10-degree movement in both directions and the results show great advantage when compared to the precision capabilities of a classical leveler based on electromagnetic actuators. From an economic point of view, the use of less performant sensors may be reasonable when such a precision is excessive for a given application.

VI. GENERAL CONCLUSION AND PERSPECTIVES

The main objective of this research is the design of a piezoelectric actuator for leveling applications which brings special interest to AML Systems as the use of piezoelectric materials for automotive lighting actuators has not been explored yet and this could be important towards closing the gap between illumination technologies and positioning actuators in the automotive context.

In the first chapter we give a background on headlamp actuation and how mechatronics has enabled its evolution. The constraints that glare imposes on the high illumination of the road traduces into a compromise between how far can the light source illuminate and how well can the light beam be positioned, in a context where high-intensity sources are today much more advanced than the actuators that control its position. This is what motivates the use of new technologies, and particularly piezoelectric actuators due to their great miniaturization capabilities, their tremendous precision compared to electric motors and the direct actuation possibilities where no gearbox is necessary.

Since there is no evidence of the use of piezoelectric actuators on automotive leveling, we needed to select the architecture that, from a dynamic point of view, approaches the best to the conditions of the application, specifically, a $\pm 10°$ movement.

For this reason, chapter II includes an extensive review about the different architectures of piezoelectric actuation, divided into three families: the internally, externally and frequency leveraged piezoelectric actuators. Each one of these groups includes itself a huge diversity of actuators all characterized by how the microscopic deformation of piezoelectric materials can be exploited. This allows to conclude that frequency leveraged piezoelectric actuators are the most suitable as the $\pm 10°$ movement, it is not realistic for internally leveraged, and the use of an externally leveraged would imply a compliant structure that exceeds by far the available space in a headlamp module. As they are only limited by the size of the guide they move on, frequency leveraged architectures are indeed the most convenient option.

In this group we find again two subgroups: the step motors and the ultrasonic motors. The first present better force capabilities but lacks in speed and reaction time compared to the seconds, which are two important requirements in leveling applications. For all these reasons, and in seek of maximizing synergy and industrial advantages, the vibrating body of an EDGE4X USM by Nanomotion was selected for being the core of the leveler to be designed.

It is a standing wave motor, where first longitudinal L1 and second bending mode B2 are excited to produce the elliptic movement, a characteristic that is shared in all ultrasonic actuators. As this is a rather small motor, we decided to redefine how the leveler should operate, so the actuator could support the moment of inertia of a projector without having to carry its mass. This traduces into moving from a linear output movement, which is how classically is done in today's levelers, towards a rotary output, directly operating on the axis of rotation of a projector.

This change of paradigm imposes new challenges, and a multidisciplinary approach, as piezoelectricity, vibration mechanics, tribology and rotary mechanisms are all merged while designing this ultrasonic actuator. A detailed description of the different parts that compose the actuator is made, starting from the very core, the L1B2 vibrating piezoelectric body, until how this is excited and integrated to the designed rotor in order to get a macroscopic rotary output that can be measured by a magnetic encoder: the closed loop operation is mandatory when working with piezoelectric actuators to maximize their precision and the result of the design process is shown in chapter III.

The designed prototype was delivered a patent during the realization of this thesis and stands out above previous expired patents that lack in detail and just mention the use of piezoelectrics without going further in the selection of a specific architecture, measuring system, rotor-stator configuration, driving technique, desired mechanical output, etc.

A dynamic model is explained in chapter IV. It describes the behavior of the designed actuator, including several geometric and material properties parameters that characterize the piezoelectric vibrating body and the force transmission by cyclical friction. Using an approach of interconnected systems, the driving circuit, the vibrating body, the stick slip contact, and the load; and under the assumption of a Timoshenko beam that vibrates in free-free condition, we deduced several equations that model each of these systems.

The objective was to numerically solve these equations to obtain a dynamic model that could be used for quick simulation and analysis of the impact of a set of parameters on the output behavior of the piezo leveler. In the final chapter, we abord this after, first, showing the process of assembly of the designed leveler, which complements chapter III. Then, in order to validate the model, we highlight the importance of compare it with experimental data.

The calculated excitation frequency and the simulation results of output velocity at different values of external load and voltage amplitude showed good agreement with the experimental data as it is depicted in the graphs of the steady-state speed versus load and the dead zone behavior of section V.6.1.

The confidence in the developed model allowed us to determine other characteristics of the actuator via simulation. We could give a better view of how the force transmission is done, the elliptic movement generated as consequence of the L1B2 excitation and the impact of other parameters on the output characteristics of the actuator, specifically, the frequency of excitation f, that if it is not properly choose can completely degenerate the behavior of the actuator; and the preload force F_P exerted on the piezo vibrator, a parameter that can completely change the torque and speed output by the piezo leveler and can be tuned to satisfy different demands without needing a whole redesign of the actuator but rather the modification of a single variable, the preload distance d_P.

As it closely represents the real-world behavior of the designed piezo leveler, the dynamic model developed in this research can provide a base for AML in the design of future rotative actuators based in similar piezoelectric architectures, i.e., Timoshenko-beam-type L1B2 standing wave ultrasonic motors. This includes among others, the use of piezoceramic materials of different piezoelectric, stiffness or permittivity constant, a beam of different large to width ratio (as long as its length is far greater than its thickness, so Timoshenko conditions are respected), the use of a different preload spring, a friction interface of different radius and material, or the use of a sinusoidal input of different amplitude or frequency.

Finally, chapter V concludes with the experimental obtaining of the precision of the designed prototype. This being the main interest of using piezoelectric materials for leveling applications, surpasses indeed the classical precision achieved with standard leveler based on electromagnetic motors in a factor of 100 when comparing the standard deviation an almost 2 when comparing the absolute error of position.

VI.1. PERSPECTIVES

The actuator and the proposed dynamic model are a good starting point for future iterations and upgrades. While working in this research, we find several aspects that are worth improvement and further exploration.

VI.1.1. The electrode and driver design

As it was said in thesis, the design of the driver did not make part of the scope of this research and as has been shown throughout the dynamic modeling and performance evaluation of the designed piezo leveler, it plays an important role for two mains reasons: it defines the control strategy to be used (by phase difference, by change of frequency, by change of amplitude) and must be in agreement with the excitation frequency of the vibrating body. This opens the door to different electric signal forms of excitation, for example, the use of square or saw signals, and how the mechanical oscillations can be changed for low-speed applications.

On the other hand, multilayer structures are the best solution to address the low voltages (<30V) required in the application, and this relates to two main things, which are, the design of the pattern that covers the surfaces for better and cleaner excitation modes maximizing the stiffness of the actuator and avoiding problems of uniformity in the geometry. It is frequent to use electrodes made of silver compounds, but this might not be an optimal choice regarding budget in automotive industry.

VI.1.2. The friction interface and the motor alimentation

The friction interface defines the rotational output of the leveler. Concerning its material, the use of steel is not an optimal solution regarding life expectancy of the leveler. The hard tip of the piezo vibrator needs always to be a ceramic material, and its elevated hardness starts to wear the friction interface which can produce changes in the preload distance, noise and undesirable vibrations.

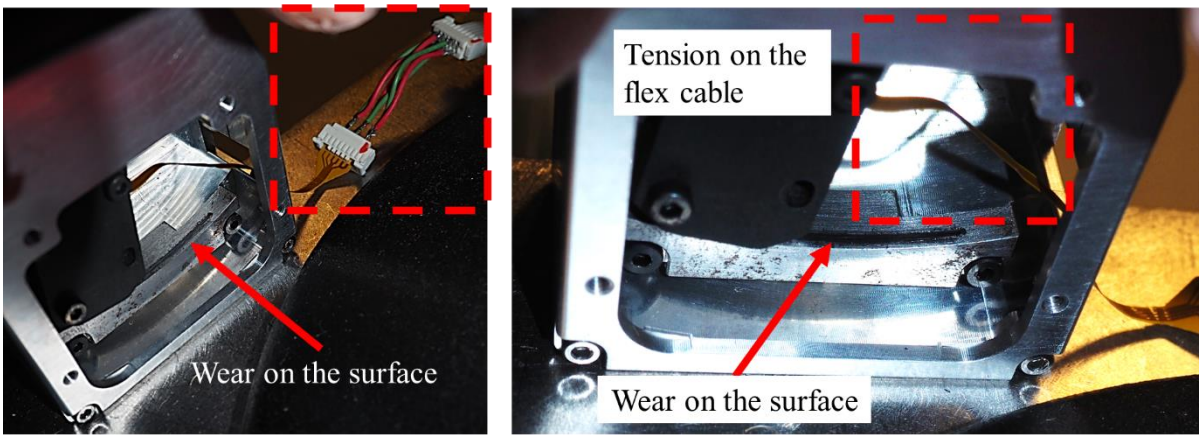

Figure VI.1.2-1. Detail on the friction interface wear.

In Figure VI.1.2-1 we also appreciate the tension that acts on the flex cable. Because the USM is integrated to the rotor, the flex cable moves with it and may cause tension if the driver is not close enough to the leveler. This tension if large enough can split the cable up.

VI.1.3. The modeling of the temperature effects

In the dynamic modeling we ignored the effects of temperature on the different material properties of the piezoelectric material. It is known that piezoelectric, permittivity and the elastic coefficients are sensible to temperature. Besides thermal expansion affects the dimensions of the piezo vibrator, resulting in changes on the resonance frequency, which, as we saw in section V.6.3, if deviates from the excitation frequency will result in a quick degeneration of the elliptic movement. Our Simulink numerical simulation based on interconnected subsystems can be adapted to include these effects.

VI.1.4. The use of other piezoelectric architectures

Other ultrasonic architectures are worth further exploration. A rotary USM based on transverse waves as the Sashida motor, or a motor based in torsional modes of vibration of a cylindrical body are interesting as their output is a rotational one and have been already used in aeronautics applications [112]. The use of lead-free materials for the vibrating body is also worth exploring, in a context of environment hazards and ecology sustainability.

BIBLIOGRAPHY

[1] X. Long *et al.*, “A review on light-emitting diode based automotive headlamps,” *Renewable and Sustainable Energy Reviews*, vol. 41, pp. 29–41, Jan. 2015, doi: 10.1016/J.RSER.2014.08.028.

[2] G. Helmers and K. Rumar, “High beam intensity and obstacle visibility,” *Lighting Research & Technology*, vol. 7, no. 1, pp. 35–42, Mar. 1975, doi: 10.1177/096032717500700105.

[3] B. Wördenweber, J. Wallaschek, P. Boyce, and D. Hoffman, *Automotive lighting and human vision*, 1st ed. Springer Berlin Heidelberg, 2007. doi: 10.1007/978-3-540-36697-3/COVER.

[4] K. Kosmas, J. Kobbert, and T. Q. Khanh, “Requirements for dynamic levelling devices to prevent headlamp glare blinding oncoming road users,” 2019.

[5] S. Venegas Bayona, H. Koulouh, A. Noronha, F. Lamarque, and C. Prelle, “Novel use of a piezoelectric ultrasonic motor for headlamp leveling,” in *IEEE/ASME International Conference on Advanced Intelligent Mechatronics, AIM*, Institute of Electrical and Electronics Engineers Inc., Jul. 2019, pp. 1299–1304. doi: 10.1109/AIM.2019.8868339.

[6] “Headlamps | HELLA.” Accessed: Nov. 14, 2022. [Online]. Available: https://www.hella.com/hella-com/en/Headlamps-620.html

[7] J. M. Sullivan, G. Adachi, M. L. Mefford, and M. J. Flannagan, “High-beam headlamp usage on unlighted rural roadways:,” *http://dx.doi.org/10.1191/1477153504li104oa*, vol. 36, no. 1, pp. 59–65, Aug. 2016, doi: 10.1191/1477153504LI104OA.

[8] “LED upgrade guide for D series projector headlight | 360 INTERNATIONAL GROUP LTD.” Accessed: Nov. 14, 2023. [Online]. Available: https://www.cn360led.com/news/D-Series-Projector-Headlight.html

[9] J. Wallaschek, H. Honsel, and M. Kleinkes, “Autonomous vehicle front lighting systems,” 2012.

[10] “XC90 Active bending lights | Volvo Support EN-TH.” Accessed: Nov. 14, 2023. [Online]. Available: https://www.volvocars.com/en-th/support/car/xc90/20w17/article/c41b4bca6fdc0b92c0a8015123829cb9

[11] “KIA HTML Manual.” Accessed: Nov. 14, 2023. [Online]. Available: https://www.kia.com/content/dam/kia2/in/en/content/ev6-manual/index.html

[12] U. N. E. C. f. Europe, *Addendum 47: Regulation No. 48*. 1995.

[13] A. L. Kholkin, N. A. Pertsev, and A. v. Goltsev, “Piezoelectricity and Crystal Symmetry,” in *Piezoelectric and Acoustic Materials for Transducer Applications*, E. K. Safari Ahmad and Akdoğan, Ed., Boston, MA: Springer US, 2008, pp. 17–38. doi: 10.1007/978-0-387-76540-2_2.

[14] K. Uchino, “Piezoelectric Actuator Renaissance,” *Energy Harvesting and Systems*, vol. 1, no. 1–2. Walter de Gruyter GmbH, pp. 45–56, 2014. doi: 10.1515/ehs-2013-0021.

[15] R. Dahiya and M. Valle, “Fundamentals of Piezoelectricity,” in *Robotic tactile sensing: Technologies and system*, 1st ed., Springer Dordrecht, 2014, pp. 195–210. doi: 10.1007/978-94-007-0579-1.

[16] C. Niezrecki, D. Brei, S. Balakrishnan, and A. Moskalik, “Piezoelectric Actuation: State of the Art.” [Online]. Available: http://www.fev-et.

[17] S. Mohith, A. R. Upadhya, K. P. Navin, S. M. Kulkarni, and M. Rao, “Recent trends in piezoelectric actuators for precision motion and their applications: a review,” *Smart Materials and Structures*, vol. 30, no. 1. IOP Publishing Ltd, Jan. 01, 2021. doi: 10.1088/1361-665X/abc6b9.

[18] C. A. Rogers and Z. Chaudhry, “Design of Displacement-Amplified Induced-Strain Actuators for Maximum Energy Output,” 1997. [Online]. Available: http://www.asme.org/about-asme/terms-of-use

[19] Physik Instrumente, “Physik Instrumente.” Accessed: Aug. 21, 2022. [Online]. Available: https://www.physikinstrumente.com/en/expertise/technology/piezo-technology/properties-piezo-actuators/forces-stiffnesses/

[20] G. Y. Gu, L. M. Zhu, C. Y. Su, H. DIng, and S. Fatikow, “Modeling and control of piezo-actuated nanopositioning stages: A survey,” *IEEE Transactions on Automation Science and Engineering*, vol. 13, no. 1, pp. 313–332, Jan. 2016, doi: 10.1109/TASE.2014.2352364.

[21] L. Wang, W. Chen, J. Liu, J. Deng, and Y. Liu, “A review of recent studies on non-resonant piezoelectric actuators,” *Mech Syst Signal Process*, vol. 133, Nov. 2019, doi: 10.1016/J.YMSSP.2019.106254.

[22] F. Callipari, M. Sabatini, F. Angeletti, P. Iannelli, and P. Gasbarri, “Active vibration control of large space structures: Modelling and experimental testing of offset piezoelectric stack actuators,” *Acta Astronaut*, Sep. 2022, doi: 10.1016/J.ACTAASTRO.2022.05.058.

[23] W. Wang and Z. Yang, “A compact piezoelectric stack actuator and its simulation in vibration control,” *Tsinghua Sci Technol*, vol. 14, no. S2, pp. 43–48, Mar. 2010, doi: 10.1016/S1007-0214(10)70029-8.

[24] J. Redmond and P. Barney, “Vibration Control of Stiff Beams and Plates Using Structurally Integrated PZT Stack Actuators:,” *J Intell Mater Syst Struct*, vol. 8, no. 6, pp. 525–535, Jul. 1997, doi: 10.1177/1045389X9700800605.

[25] M. Mohammadzaheri, S. Grainger, M. Bazghaleh, and P. Yaghmaee, “Intelligent modeling of a piezoelectric tube actuator,” *INISTA 2012 - International Symposium on INnovations in Intelligent SysTems and Applications*, 2012, doi: 10.1109/INISTA.2012.6246980.

[26] L. Li, C. X. Li, G. Gu, and L. Zhu, “Modified Repetitive Control Based Cross-Coupling Compensation Approach for the Piezoelectric Tube Scanner of Atomic Force Microscopes,” *IEEE/ASME Transactions on Mechatronics*, vol. 24, no. 2, pp. 666–676, Apr. 2019, doi: 10.1109/TMECH.2019.2893628.

[27] S. Y. Lee, B. Ko, and W. Yang, “Theoretical modeling, experiments and optimization of piezoelectric multimorph,” *Smart Mater Struct*, vol. 14, no. 6, p. 1343, Oct. 2005, doi: 10.1088/0964-1726/14/6/026.

[28] G. H. Haertling, “Rainbow actuators and sensors: a new smart technology,” *Smart Structures and Materials 1997: Smart Materials Technologies*, vol. 3040, pp. 81–92, Feb. 1997, doi: 10.1117/12.267101.

[29] S. Aimmanee, S. Chutima, and M. W. Hyer, “Nonlinear analysis of RAINBOW actuator characteristics,” *Smart Mater Struct*, vol. 18, no. 4, p. 045002, Mar. 2009, doi: 10.1088/0964-1726/18/4/045002.

[30] TFS, “Piezoelectric Micro Pumps - Takasago Fluidic Systems.” Accessed: Aug. 31, 2022. [Online]. Available: https://www.takasago-fluidics.com/pages/piezoelectric-micro-pumps

[31] M. B. Parkinson, B. D. Jensen, and K. Kurabayashl, “Design of compliant force and displacement amplification micro-mechanisms,” *Proceedings of the ASME Design Engineering Technical Conference*, vol. 2, pp. 741–748, 2001, doi: 10.1115/detc2001/dac-21089.

[32] S. Kota, J. Joo, Z. Li, S. M. Rodgers, and J. Sniegowski, “Design of Compliant Mechanisms: Applications to MEMS,” *Analog Integrated Circuits and Signal Processing 2001 29:1*, vol. 29, no. 1, pp. 7–15, Oct. 2001, doi: 10.1023/A:1011265810471.

[33] N. Jhawar and G. K. Ananthasuresh, “Cataloguing and Selection of Displacement-amplifying Compliant Mechanisms,” *ICORD 09: Proceedings of the 2nd International Conference on Research into Design, Bangalore, India 07.-09.01.2009*, pp. 26–34, 2009, Accessed: Sep. 03, 2022. [Online]. Available: https://www.designsociety.org/publication/32260/Cataloguing+and+Selection+of+Displacement-amplifying+Compliant+Mechanisms

[34] J. Hricko and Š. Havlík, “Compliant Mechanisms for Motion/Force Amplifiers for Robotics,” *Advances in Intelligent Systems and Computing*, vol. 980, pp. 26–33, 2020, doi: 10.1007/978-3-030-19648-6_4/COVER.

[35] S. Kota, J. Hetrick, Z. Li, and L. Saggere, “Tailoring unconventional actuators using compliant transmissions: design methods and applications,” *IEEE/ASME Transactions on Mechatronics*, vol. 4, no. 4, pp. 396–408, Dec. 1999, doi: 10.1109/3516.809518.

[36] Physik Instrumente, “P-604 Compact PiezoMove Linear Actuator.” Accessed: Sep. 06, 2022. [Online]. Available: https://www.physikinstrumente.com/en/products/linear-actuators/piezomove-lever-actuators/p-604-compact-piezomove-linear-actuator-202820/#downloads

[37] S. Wang, W. Rong, L. Wang, H. Xie, L. Sun, and J. K. Mills, “A survey of piezoelectric actuators with long working stroke in recent years: Classifications, principles, connections and distinctions,” *Mech Syst Signal Process*, vol. 123, pp. 591–605, May 2019, doi: 10.1016/J.YMSSP.2019.01.033.

[38] Y. B. Ham, W. S. Seo, W. Y. Cho, D. W. Yun, J. H. Park, and S. N. Yun, “Development of a piezoelectric pump using hinge-lever amplification mechanism,” *J Electroceram*, vol. 23, no. 2–4, pp. 346–350, Oct. 2009, doi: 10.1007/S10832-008-9461-Y/FIGURES/7.

[39] S. B. Choi, S. S. Han, Y. M. Han, and B. S. Thompson, “A magnification device for precision mechanisms featuring piezoactuators and flexure hinges: Design and experimental validation,” *Mech Mach Theory*, vol. 42, no. 9, pp. 1184–1198, Sep. 2007, doi: 10.1016/J.MECHMACHTHEORY.2006.08.009.

[40] A. Doğan and E. Uzgur, “Piezoelectric actuator designs,” *Piezoelectric and Acoustic Materials for Transducer Applications*, pp. 341–371, 2008, doi: 10.1007/978-0-387-76540-2_17/COVER.

[41] Physik Instrumente, “PiezoWalk® Walking Drives.” Accessed: Sep. 13, 2022. [Online]. Available: https://www.physikinstrumente.com/en/expertise/technology/piezoelectric-drives/piezowalk-piezo-motors/

[42] L. Wang, W. Chen, J. Liu, J. Deng, and Y. Liu, “A review of recent studies on non-resonant piezoelectric actuators,” *Mech Syst Signal Process*, vol. 133, Nov. 2019, doi: 10.1016/J.YMSSP.2019.106254.

[43] CEDRAT TECHNOLOGIES, “Mechatronic components for optronics - CEDRAT TECHNOLOGIES.” Accessed: Sep. 13, 2022. [Online]. Available: https://www.cedrat-technologies.com/en/products/piezo-motors/stepping-piezo-actuators/linear-stepping-piezo-actuators-lspa35xs.html

[44] Y. Peng, Y. Peng, X. Gu, J. Wang, and H. Yu, “A review of long range piezoelectric motors using frequency leveraged method,” *Sensors and Actuators, A: Physical*, vol. 235. Elsevier, pp. 240–255, Nov. 01, 2015. doi: 10.1016/j.sna.2015.10.015.

[45] P. Pertsch, “Piezoelectric Actuator Applications - Status 2018,” in *ACTUATOR 2018; 16th International Conference on New Actuators*, 2018, pp. 1–7.

[46] Newport, “Picomotor™ Piezo Linear Actuators.” Accessed: Sep. 13, 2022. [Online]. Available: https://www.newport.com/f/picomotor-piezo-linear-actuators?q=:relevance:npBrand:New Focus:allCategories:piezo-nanopositioning-actuators

[47] Physik Instrumente, “N-472 PiezoMike Linear Actuator.” Accessed: Sep. 13, 2022. [Online]. Available: https://www.physikinstrumente.com/en/products/linear-actuators/piezomike-for-long-term-stability/n-472-piezomike-linear-actuator-1000120/

[48] K. Spanner and B. Koc, “Piezoelectric motors, an overview,” *Actuators*, vol. 5, no. 1. MDPI AG, Mar. 01, 2016. doi: 10.3390/act5010006.

[49] SHINSEI Corporation, “SHINSEI Corporation|Technology.” Accessed: Sep. 18, 2022. [Online]. Available: http://www.shinsei-motor.com/English/techno/ultrasonic_motor.html

[50] P. Hagedorn and J. Wallaschek, “Travelling wave ultrasonic motors, Part I: Working principle and mathematical modelling of the stator,” *J Sound Vib*, vol. 155, no. 1, pp. 31–46, May 1992, doi: 10.1016/0022-460X(92)90643-C.

[51] M. Kuribayashi, S. Ueha, and E. Mori, “Excitation conditions of flexural traveling waves for a reversible ultrasonic linear motor,” *J Acoust Soc Am*, vol. 77, no. 4, p. 1431, Jun. 1998, doi: 10.1121/1.392037.

[52] W. Seemann, “A linear ultrasonic traveling wave motor of the ring type,” *Smart Mater Struct*, vol. 5, no. 3, p. 361, Jun. 1996, doi: 10.1088/0964-1726/5/3/015.

[53] B. Koc, S. Cagatay, and K. Uchino, “A piezoelectric motor using two orthogonal bending modes of a hollow cylinder,” *IEEE Trans Ultrason Ferroelectr Freq Control*, vol. 49, no. 4, pp. 495–500, Apr. 2002, doi: 10.1109/58.996568.

[54] M. K. Kurosawa, O. Kodaira, Y. Tsuchitoi, and T. Higuchi, “Transducer for high speed and large thrust ultrasonic linear motor using two sandwich-type vibrators,” *IEEE Trans Ultrason Ferroelectr Freq Control*, vol. 45, no. 5, pp. 1188–1195, 1998, doi: 10.1109/58.726442.

[55] Y. Liu, W. Chen, J. Liu, and S. Shi, “A high-power linear ultrasonic motor using longitudinal vibration transducers with single foot,” *IEEE Trans Ultrason Ferroelectr Freq Control*, vol. 57, no. 8, pp. 1860–1867, Aug. 2010, doi: 10.1109/TUFFC.2010.1625.

[56] Nanomotion, “HR1 Nanomotion Motor.” Accessed: Nov. 16, 2022. [Online]. Available: https://www.nanomotion.com/motion-product/hr1-nanomotion-motor/

[57] L. Yang and C. Zhao, “Optimum design for stress type hybrid ultrasonic motor using longitudinal and torsional vibration modes,” *Proceedings of the 2011 Symposium on Piezoelectricity, Acoustic Waves and Device Applications, SPAWDA 2011*, pp. 28–31, 2011, doi: 10.1109/SPAWDA.2011.6167183.

[58] CEDRAT TECHNOLOGIES, “Actionneur piezo amplifié - APA1000XL.” Accessed: Nov. 01, 2022. [Online]. Available: https://www.cedrat-technologies.com/fr/produits/produit/APA1000XL.html

[59] Physik Instrumente, “P-625.1U Linear Precision Positioner.” Accessed: Nov. 01, 2022. [Online]. Available: https://www.physikinstrumente.com/en/products/nanopositioning-piezo-flexure-stages/linear-piezo-flexure-stages/p-6211u-p-6251u-pihera-linear-precision-positioner-p-621-1u-p-625-1u#specification

[60] M. Ling, J. Cao, Z. Jiang, M. Zeng, and Q. Li, “Optimal design of a piezo-actuated 2-DOF millimeter-range monolithic flexure mechanism with a pseudo-static model,” *Mech Syst Signal Process*, vol. 115, pp. 120–131, Jan. 2019, doi: 10.1016/J.YMSSP.2018.05.064.

[61] R. D. Dsouza, K. P. Navin, T. Theodoridis, and P. Sharma, “Design, fabrication and testing of a 2 DOF compliant flexural microgripper,” *Microsystem Technologies*, vol. 24, no. 9, pp. 3867–3883, Sep. 2018, doi: 10.1007/S00542-018-3861-Y/FIGURES/19.

[62] Q. S. Pan, Y. Bin Liu, Y. H. Liu, L. J. Gong, L. G. He, and Z. H. Feng, “Design and fabrication of a large displacement piezoelectric actuator,” *Proceedings of the 2015 Symposium on Piezoelectricity, Acoustic Waves and Device Applications, SPAWDA 2015*, pp. 261–264, Dec. 2015, doi: 10.1109/SPAWDA.2015.7364485.

[63] D. Haller *et al.*, “Cymbal type Piezo-Polymer-Composite actuators for active cancellation of flow instabilities on airfoils,” *2011 16th International Solid-State Sensors, Actuators and Microsystems Conference, TRANSDUCERS’11*, pp. 494–497, 2011, doi: 10.1109/TRANSDUCERS.2011.5969617.

[64] M. Muraoka and S. Sanada, “Displacement amplifier for piezoelectric actuator based on honeycomb link mechanism,” *Sens Actuators A Phys*, vol. 157, no. 1, pp. 84–90, Jan. 2010, doi: 10.1016/J.SNA.2009.10.024.

[65] G. Peled, R. Yasinov, and N. Karasikov, “Performance and Applications of L1B2 Ultrasonic Motors,” *Actuators 2016, Vol. 5, Page 15*, vol. 5, no. 2, p. 15, Jun. 2016, doi: 10.3390/ACT5020015.

[66] C. Zhao, *Ultrasonic Motors*. Berlin, Heidelberg: Springer Berlin Heidelberg, 2011. doi: 10.1007/978-3-642-15305-1.

[67] J. J. Zhang, W. D. Diao, K. Fan, Z. Q. Wang, R. Q. Shi, and Z. H. Feng, “A miniature standing wave linear ultrasonic motor,” *Sens Actuators A Phys*, vol. 332, p. 113113, Dec. 2021, doi: 10.1016/J.SNA.2021.113113.

[68] A. Y. Le, “A Methodology for the Optimal Design of Linear Ultrasonic Actuators,” University of Toronto, 2015. [Online]. Available: https://tspace.library.utoronto.ca/handle/1807/69357

[69] X. Tian, Y. Liu, J. Deng, L. Wang, and W. Chen, “A review on piezoelectric ultrasonic motors for the past decade: Classification, operating principle, performance, and future work perspectives,” *Sens Actuators A Phys*, vol. 306, p. 111971, May 2020, doi: 10.1016/J.SNA.2020.111971.

[70] SHINSEI, “SHINSEI Corporation|products.” Accessed: Nov. 16, 2022. [Online]. Available: http://www.shinsei-motor.com/English/product/index.html

[71] O. Vyshnevskyy, S. Kovalev, and W. Wischnewskiy, “A novel, single-mode piezoceramic plate actuator for ultrasonic linear motors,” *IEEE Trans Ultrason Ferroelectr Freq Control*, vol. 52, no. 11, pp. 2047–2053, Nov. 2005, doi: 10.1109/TUFFC.2005.1561674.

[72] Physik Instrumente, “PILine® Ultrasonic Piezomotors.” Accessed: Nov. 16, 2022. [Online]. Available: https://www.physikinstrumente.com/en/expertise/technology/piezoelectric-drives/piline-ultrasonic-motors

[73] NANOMOTION, “EDGE4X motor - NANOMOTION.” Accessed: Nov. 16, 2022. [Online]. Available: https://www.nanomotion.com/product/edge4x-motor/

[74] New Scale Technologies, “Data Sheets - New Scale Technologies.” Accessed: Nov. 16, 2022. [Online]. Available: https://www.newscaletech.com/downloads/data-sheet/

[75] J. J. Zhang, W. D. Diao, K. Fan, Z. Q. Wang, R. Q. Shi, and Z. H. Feng, “A miniature standing wave linear ultrasonic motor,” *Sens Actuators A Phys*, vol. 332, p. 113113, Dec. 2021, doi: 10.1016/J.SNA.2021.113113.

[76] D. Lu, Q. Lin, B. Chen, C. Jiang, and X. Hu, “A single-modal linear ultrasonic motor based on multi vibration modes of PZT ceramics,” *Ultrasonics*, vol. 107, p. 106158, Sep. 2020, doi: 10.1016/J.ULTRAS.2020.106158.

[77] G. Wang, J. Tan, Z. Zhao, S. Cui, and H. Wu, “Mechanical and energetic characteristics of an energy harvesting type piezoelectric ultrasonic actuator,” *Mech Syst Signal Process*, vol. 128, pp. 110–125, Aug. 2019, doi: 10.1016/J.YMSSP.2019.03.029.

[78] S. Izuhara and T. Mashimo, “Design and evaluation of a micro linear ultrasonic motor,” *Sens Actuators A Phys*, vol. 278, pp. 60–66, Aug. 2018, doi: 10.1016/J.SNA.2018.05.022.

[79] V. Dabbagh, A. A. D. Sarhan, J. Akbari, and N. A. Mardi, “Design and manufacturing of ultrasonic motor with in-plane and out-of-plane bending vibration modes of rectangular plate with large contact area,” *Measurement*, vol. 109, pp. 425–431, Oct. 2017, doi: 10.1016/J.MEASUREMENT.2017.06.007.

[80] Y. Liu, X. Yang, W. Chen, and D. Xu, “A Bonded-Type Piezoelectric Actuator Using the First and Second Bending Vibration Modes,” *IEEE Transactions on Industrial Electronics*, vol. 63, no. 3, pp. 1676–1683, Mar. 2016, doi: 10.1109/TIE.2015.2492942.

[81] S. Zhou and Z. Yao, “Design and optimization of a modal-independent linear ultrasonic motor,” *IEEE Trans Ultrason Ferroelectr Freq Control*, vol. 61, no. 3, pp. 535–546, 2014, doi: 10.1109/TUFFC.2014.2937.

[82] S. Park and S. He, “Standing wave brass-PZT square tubular ultrasonic motor,” *Ultrasonics*, vol. 52, no. 7, pp. 880–889, Sep. 2012, doi: 10.1016/J.ULTRAS.2012.02.010.

[83] Y. Shi and C. Zhao, “A new standing-wave-type linear ultrasonic motor based on in-plane modes,” *Ultrasonics*, vol. 51, no. 4, pp. 397–404, May 2011, doi: 10.1016/J.ULTRAS.2010.11.006.

[84] Y. Wang, J. Jin, and W. Huang, “A compact ultrasonic motor using two in plane modes,” *Proceedings of the 2010 Symposium on Piezoelectricity, Acoustic Waves and Device Applications, SPAWDA10*, pp. 171–174, 2010, doi: 10.1109/SPAWDA.2010.5744297.

[85] O. Vyshnevskyy, S. Kovalev, and J. Mehner, “Coupled tangential-axial resonant modes of piezoelectric hollow cylinders and their application in ultrasonic motors,” *IEEE Trans Ultrason Ferroelectr Freq Control*, vol. 52, no. 1, pp. 31–36, Jan. 2005, doi: 10.1109/TUFFC.2005.1397348.

[86] Y. Tanoue and T. Morita, “Opposing preloads type ultrasonic linear motor with quadruped stator,” *Sens Actuators A Phys*, vol. 301, p. 111764, Jan. 2020, doi: 10.1016/J.SNA.2019.111764.

[87] G. Peled, R. Yasinov, and N. Karasikov, “Performance and Applications of L1B2 Ultrasonic Motors,” *Actuators 2016, Vol. 5, Page 15*, vol. 5, no. 2, p. 15, Jun. 2016, doi: 10.3390/ACT5020015.

[88] H. Saigoh, M. Kawasaki, N. Maruko, and K. Kanayama, “Multilayer piezoelectric motor using the first longitudinal and the second bending vibrations,” *Jpn J Appl Phys*, vol. 34, no. 5S, pp. 2760–2764, May 1995, doi: 10.1143/JJAP.34.2760/XML.

[89] Z. Chen, C. Yang, B. Gao, J. Wu, and T. Zhao, “A laminated ultrasonic motor operating in face expanding and face bending modes,” *Sens Actuators A Phys*, vol. 344, p. 113741, Sep. 2022, doi: 10.1016/J.SNA.2022.113741.

[90] T. Funakubo, T. Tsubata, Y. Taniguchi, K. Kumei, T. Fujimura, and C. Abe, “Ultrasonic linear motor using multilayer piezoelectric actuators,” *Jpn J Appl Phys*, vol. 34, no. 5S, pp. 2756–2759, May 1995, doi: 10.1143/JJAP.34.2756/XML.

[91] S. Yuan, Y. Zhao, X. Chu, C. Zhu, and Z. Zhong, “Analysis and Experimental Research of a Multilayer Linear Piezoelectric Actuator,” *Applied Sciences*, vol. 6, no. 8, 2016, doi: 10.3390/app6080225.

[92] S. Mukhopadhyay, B. Behera, and J. Kumar, “A brief review on the recent evolution in piezoelectric linear ultrasonic motors,” *Engineering Research Express*, vol. 3, no. 4, p. 042003, Dec. 2021, doi: 10.1088/2631-8695/AC3B73.

[93] J. Olofsson, S. Johansson, and S. Jacobson, “Influence from humidity on the alumina friction drive system of an ultrasonic motor,” *Tribol Int*, vol. 42, no. 10, pp. 1467–1477, Oct. 2009, doi: 10.1016/J.TRIBOINT.2009.05.010.

[94] Z. Chen, C. Yang, B. Gao, J. Wu, and T. Zhao, “A laminated ultrasonic motor operating in face expanding and face bending modes,” *Sens Actuators A Phys*, vol. 344, p. 113741, Sep. 2022, doi: 10.1016/J.SNA.2022.113741.

[95] Y. Shi, Y. Li, C. Zhao, and J. Zhang, “A New Type Butterfly-Shaped Transducer Linear Ultrasonic Motor,” *http://dx.doi.org/10.1177/1045389X11404955*, vol. 22, no. 6, pp. 567–575, Apr. 2011, doi: 10.1177/1045389X11404955.

[96] S. Yuan, Y. Zhao, X. Chu, C. Zhu, and Z. Zhong, “Analysis and Experimental Research of a Multilayer Linear Piezoelectric Actuator,” *Applied Sciences 2016, Vol. 6, Page 225*, vol. 6, no. 8, p. 225, Aug. 2016, doi: 10.3390/APP6080225.

[97] J. Zumeris, “Ceramic motor,” US5453653, Sep. 26, 1995

[98] NSK, “The ABC of Bearings.” Accessed: Sep. 02, 2022. [Online]. Available: https://www.nsk.com/services/basicknowledge/manual/abc/#

[99] Ringspann, “Star Spring Washers as ball bearing compensating discs for taking up free movement in bearings.” Accessed: Sep. 02, 2022. [Online]. Available: https://www.ringspann.fr/en/products/shaft-hub-connections/star-spring-washers

[100] RLS Encoders, “Miniature Incremental Magnetic Encoder Module.” Accessed: Nov. 01, 2022. [Online]. Available: https://www.rls.si/eng/rlc2ic-miniature-linear-and-rotary-pcb-level-incremental-magnetic-encoder#downloads|data-sheet

[101] Y. Shi, C. Zhao, and J. Zhang, “Contact analysis and modeling of standing wave linear ultrasonic motor,” *Journal Wuhan University of Technology, Materials Science Edition*, vol. 26, no. 6, pp. 1235–1242, Dec. 2011, doi: 10.1007/S11595-011-0396-9/METRICS.

[102] Z. Wan and H. Hu, “Modeling and experimental analysis of the linear ultrasonic motor with in-plane bending and longitudinal mode,” *Ultrasonics*, vol. 54, no. 3, pp. 921–928, Mar. 2014, doi: 10.1016/J.ULTRAS.2013.11.004.

[103] H. F. Tiersten, “Linear Piezoelectric Plate Vibrations,” *Linear Piezoelectric Plate Vibrations*, 1969, doi: 10.1007/978-1-4899-6453-3.

[104] S. S. Rao, *Mechanical vibrations*, 5th ed. Prentice Hall, 2011.

[105] F. Ma, M. Morzfeld, and A. Imam, “The decoupling of damped linear systems in free or forced vibration,” *J Sound Vib*, vol. 329, no. 15, pp. 3182–3202, Jul. 2010, doi: 10.1016/J.JSV.2010.02.017.

[106] X. Li, C. Kan, Y. Cheng, Z. Chen, and T. Ren, “Performance evaluation of a bimodal standing-wave ultrasonic motor considering nonlinear electroelasticity: Modeling and experimental validation,” *Mech Syst Signal Process*, vol. 141, p. 106475, Jul. 2020, doi: 10.1016/J.YMSSP.2019.106475.

[107] Plastics International, “Polypropylene Homopolymer.” Accessed: May 19, 2023. [Online]. Available: https://www.plasticsintl.com/shop-by-material/polypropylene-homopolymer

[108] Koyo Bearings, “Bearing mounting | Basic Bearing Knowledge.” Accessed: Jun. 24, 2023. [Online]. Available: https://koyo.jtekt.co.jp/en/support/bearing-knowledge/15-3000.html

[109] N. Aurelle, D. Guyomar, C. Richard, P. Gonnard, and L. Eyraud, “Nonlinear behavior of an ultrasonic transducer,” *Ultrasonics*, vol. 34, no. 2–5, pp. 187–191, Jun. 1996, doi: 10.1016/0041-624X(95)00077-G.

[110] X. Li, Z. Chen, and Z. Yao, “Contact analysis and performance evaluation of standing-wave linear ultrasonic motors via a physics-based contact model,” *Smart Mater Struct*, vol. 28, no. 1, p. 015032, Dec. 2018, doi: 10.1088/1361-665X/AAF11A.

[111] W. Shi, H. Zhao, J. Ma, and Y. Yao, “Dead-Zone Compensation of an Ultrasonic Motor Using an Adaptive Dither,” *IEEE Transactions on Industrial Electronics*, vol. 65, no. 5, pp. 3730–3739, May 2018, doi: 10.1109/TIE.2017.2760854.

[112] W. Szlabowicz, “Contribution au dimensionnement et à la réalisation d’actionneur piézoélectrique à rotation de mode fort couple pour applications aéronautiques,” 2006. Accessed: Nov. 23, 2021. [Online]. Available: http://www.theses.fr/2006INPT028H

[113] X. Li, Z. Yao, S. Zhou, Q. Lv, and Z. Liu, “Dynamic modeling and characteristics analysis of a modal-independent linear ultrasonic motor,” *Ultrasonics*, vol. 72, pp. 117–127, Dec. 2016, doi: 10.1016/J.ULTRAS.2016.07.018.

[114] J. K. K. Lau, “Development of a Linear Ultrasonic Motor with Segmented Electrodes,” Nov. 2012, Accessed: Nov. 23, 2023. [Online]. Available: https://tspace.library.utoronto.ca/handle/1807/42396

Appendix A

$$m_{11} = \frac{\rho A}{2}\int_0^l \phi_L^2 dx$$

$$m_{22} = \frac{\rho A}{2}\int_0^l \phi_B^2 dx$$

$$m_{33} = \frac{\rho A}{2}\int_0^l \phi_\psi^2 dx$$

$$k_{11} = \frac{c_{11} A}{2}\int_0^l {\phi_L'}^2 dx$$

$$k_{22} = \frac{c_{66} A}{2}\int_0^l {\phi_B'}^2 dx$$

$$k_{23} = -c_{66} A\int_0^l \phi_B' \phi_\psi dx$$

$$k_{33} = \frac{1}{2}\left(c_{11} I\int_0^l {\phi_\psi'}^2 dx + c_{66} A\int_0^l \phi_\psi^2 dx \right)$$

$$b_{11} = \frac{we_{31}}{2}\int_0^l \phi_L' dx$$

$$b_{31} = \frac{w^2 e_{31}}{8}\left(-\int_0^{l/2} \phi_\psi' dx + \int_{l/2}^l \phi_\psi' dx \right)$$

$$b_{12} = \phi_L(0) - \phi_L(L)$$

$$b_{23} = \phi_B(L)$$

$$b_{33} = L_2(\phi_\psi(L) - \phi_\psi(L_2))$$